UNIVERSTY OF CALIFORNIA SAN DIEGO

High Entropy Carbides: Modeling, Synthesis, and Properties

A dissertation submitted in partial satisfaction of the requirements
for the degree Doctor of Philosophy

in

Materials Science and Engineering

by

Tyler Harrington

Committee in charge:

Professor Kenneth Vecchio, Chair
Professor Emily Chin
Professor Javier Garay
Professor Jeffrey Gee
Professor Jian Luo
Professor Kesong Yang

2019

The Dissertation of Tyler Harrington is approved, and it is acceptable in quality and form for publication on microfilm and electronically:

_____

_____

_____

_____

_____

_____

Chair

University of California San Diego

2019

DEDICATION

To mom, dad, and the rest of the family. Your unwavering love and support never go unnoticed and I could not have done this without you.

EPIGRAPH

Before I came here, I was confused about this subject. Having listened to your lecture, I am still confused – but on a higher level.

Enrico Fermi

TABLE OF CONTENTS

LIST OF FIGURES

LIST OF TABLES

ACKNOWLEDGEMENTS

First and foremost, I would like to acknowledge Professor Kenneth Vecchio as my advisor and committee chair. Your advice has proven invaluable both in the production of this body of work and my development as a scientist, an engineer, and a person.

I would also like to acknowledge the staff of the NanoEngineering Materials Research Center: Wayne Neilson, Sabine Faulhaber, and Dr. Stephen Horvath for being available for discussion and aiding me in continuing my learning and development.

I would like to acknowledge the entire Vecchio research group, past and present: Kevin Kaufmann, Mojtaba Samiee, William Mellor, Chaoyi Zhu, Olivia Dippo, Cameron McElfresh, Matthew Quinn, Jordan Furlong, Laura Andersen, Haoren Wang, Sumin Shin, Cheng Zhang, Eduardo Marin, Lucas Borowski, Yu Wang, and Roxanne Afshari for help in operating and maintaining equipment that was vital to the production of this work and for countless hours of insightful scientific discussion.

I would like to acknowledge the Luo research group, past and present: Joshua Gild, Andrew Wright, Sicong Jiang, Mingde Qin, Yuanyao Zhang, Tao Hu, Naixie Zhou for guidance and many fruitful collaborations.

I would like to acknowledge the entire ONR-MURI collaboration group: Dr. Stefano Curtarolo, Dr. Cormac Toher, Corey Oses, Dr. Christina Rost, Dr. Pranab Sarker, Dr. Jon-Paul Maria, Trent Borman, Delower Hossain, Dr. Patrick Hopkins, Jeffrey Braun, Dr. Donald Brenner, Sam Daigle, Mina Lim, Dr. Elizabeth Opila, and Lavina Backman.

I would like to acknowledge Omar Cedillos Barazza at The University of Texas at El Paso and Davide Robba, Luka Vlahovic, Dario Manara, and Rudy Konings at the European Commission, Joint Research Centre, Institute for Transuranium Elements for help in conducting the melting temperature measurements.

Part 2, in full, is a reprint of the material "High-entropy high-hardness metal carbides discovered by entropy descriptors" as it appears in *Nature Communications*. Sarker, Pranab; Harrington, Tyler; Toher, Cormac; Oses, Corey; Samiee, Mojtaba; Maria, Jon-Paul; Brenner, Donald; Vecchio, Kenneth; Curtarolo, Stefano. The dissertation author was the primary investigator and co-author of this material.

Part 3, in full, is a reprint of the material "Phase stability and mechanical properties of novel high entropy transition metal carbides" in *Acta Materialia*. Harrington, Tyler; Gild, Joshua; Sarker, Pranab; Toher, Cormac; Rost, Christina; Dippo, Olivia; McElfresh, Carmeron; Kaufmann, Kevin; Marin, Eduardo; Borowski, Lucas; Hopkins, Patrick; Luo, Jian; Curtarolo, Stefano; Brenner, Donald; Vecchio, Kenneth. The dissertation author was the primary investigator and author of this material.

Part 4, in full, is currently in preparation for submission as "Fermi level engineering of tunable and ultra-tough entropy stabilized carbides", Harrington, Tyler; Oses, Corey; Toher, Cormac; Gild, Joshua; Mellor, William; Kaufmann, Kevin; Zhu, Chaoyi; Wright, Andrew; Luo, Jian Luo; Curtarolo, Stefano; Vecchio, Kenneth. The dissertation author was the primary investigator and author of this material.

Part 5, in part, is currently in preparation for submission as "Increased melting temperatures in high entropy carbides", Harrington, Tyler; Toher, Cormac; Oses, Corey; Gild, Joshua;

Kaufmann, Kevin; Mellor, William; Cedillos Barraza, Omar; Robba, Davide; Vlahovic, Luka; Manara Dario; Dippo, Olivia; Luo, Jian; Curtarolo, Stefano; Vecchio, Kenneth. The dissertation author was the primary investigator and author of this material.

VITA

2014 Bachelor of Science, University of California San Diego

2012-2019 Research Assistant, University of California San Diego

2017 Master of Science, University of California San Diego

2015-2016 Teaching Assistant, University of California San Diego

2019 Doctor of Philosophy, University of California San Diego

PUBLICATIONS

[1] J. Gild, J. Braun, K. Kaufmann, E. Marin, **T. Harrington**, P. Hopkins, K. Vecchio, J. Luo, A high-entropy silicide: (Mo0.2Nb0.2Ta0.2Ti0.2W0.2)Si2, J. Mater. (2019). doi:10.1016/J.JMAT.2019.03.002.

[2] **T.J. Harrington**, J. Gild, P. Sarker, C. Toher, C.M. Rost, O.F. Dippo, C. McElfresh, K. Kaufmann, E. Marin, L. Borowski, P.E. Hopkins, J. Luo, S. Curtarolo, D.W. Brenner, K.S. Vecchio, Phase stability and mechanical properties of novel high entropy transition metal carbides, Acta Mater. 166 (2019) 271–280. doi:10.1016/J.ACTAMAT.2018.12.054.

[3] E. Torresani, D. Giuntini, C. Zhu, **T. Harrington**, K.S. Vecchio, A. Molinari, R.K. Bordia, E.A. Olevsky, Anisotropy of Mass Transfer During Sintering of Powder Materials with Pore–Particle Structure Orientation, Metall. Mater. Trans. A. 50 (2019) 1033–1049. doi:10.1007/s11661-018-5037-x.

[4] C. Zhang, C. Zhu, **T. Harrington**, L. Casalena, H. Wang, S. Shin, K.S. Vecchio, Multifunctional Non-Equiatomic High Entropy Alloys with Superelastic, High Damping,

and Excellent Cryogenic Properties, Adv. Eng. Mater. 21 (2019) 1800941. doi:10.1002/adem.201800941.

[5] P. Sarker, **T. Harrington**, C. Toher, C. Oses, M. Samiee, J.-P. Maria, D.W. Brenner, K.S. Vecchio, S. Curtarolo, High-entropy high-hardness metal carbides discovered by entropy descriptors, Nat. Commun. 9 (2018) 4980. doi:10.1038/s41467-018-07160-7.

[6] C. Zhang, C. Zhu, **T. Harrington**, K. Vecchio, Design of non-equiatomic high entropy alloys with heterogeneous lamella structure towards strength-ductility synergy, Scr. Mater. 154 (2018) 78–82. doi:10.1016/J.SCRIPTAMAT.2018.05.020.

[7] C. Zhu, **T. Harrington**, G.T. Gray, K.S. Vecchio, Dislocation-type evolution in quasi-statically compressed polycrystalline nickel, Acta Mater. 155 (2018) 104–116. doi:10.1016/J.ACTAMAT.2018.05.022.

[8] J. Gild, M. Samiee, J.L. Braun, **T. Harrington**, H. Vega, P.E. Hopkins, K. Vecchio, J. Luo, High-entropy fluorite oxides, J. Eur. Ceram. Soc. 38 (2018) 3578–3584. doi:10.1016/J.JEURCERAMSOC.2018.04.010.

[9] C. McElfresh, **T. Harrington**, K.S. Vecchio, Application of a novel new multispectral nanoparticle tracking technique, Meas. Sci. Technol. 29 (2018) 065002. doi:10.1088/1361-6501/aab940.

[10] **T. Harrington**, C. McElfresh, K.S. Vecchio, Spark erosion as a high-throughput method for producing bimodal nanostructured 316L stainless steel powder, Powder Technol. 328 (2018) 156–166. doi:10.1016/J.POWTEC.2018.01.012.

[11] S. Jiang, T. Hu, J. Gild, N. Zhou, J. Nie, M. Qin, **T. Harrington**, K. Vecchio, J. Luo, A

new class of high-entropy perovskite oxides, Scr. Mater. 142 (2018) 116–120. doi:10.1016/J.SCRIPTAMAT.2017.08.040.

[12] L.M. Andersen, S. Faulhaber, **T. Harrington**, D.C. Hofmann, H. Cheng, K.S. Vecchio, An experimental investigation on the notch toughness of Cu-Zr-based bulk metallic glasses with in-situ crystallization, J. Non. Cryst. Solids. 469 (2017) 70–78. doi:10.1016/J.JNONCRYSOL.2017.04.040.

[13] J. Gild, Y. Zhang, **T. Harrington**, S. Jiang, T. Hu, M.C. Quinn, W.M. Mellor, N. Zhou, K. Vecchio, J. Luo, High-Entropy Metal Diborides: A New Class of High-Entropy Materials and a New Type of Ultrahigh Temperature Ceramics., Sci. Rep. 6 (2016) 37946. doi:10.1038/srep37946.

[14] C. Zhu, **T. Harrington**, V. Livescu, G.T. Gray, K.S. Vecchio, Determination of geometrically necessary dislocations in large shear strain localization in aluminum, Acta Mater. 118 (2016) 383–394. doi:10.1016/j.actamat.2016.07.051.

FIELDS OF STUDY

Major Field: Engineering

Studies in NanoEngineering

Studies in Materials Science and Engineering

Professor Kenneth Vecchio

ABSTRACT OF THE DISSERTATION

High Entropy Carbides: Modeling, Synthesis, and Properties

by

Tyler Harrington

Doctor of Philosophy in Materials Science and Engineering

University of California San Diego, 2019

Professor Kenneth Vecchio, Chair

Today's emerging technologies in high temperature applications are placing difficult demands on structural materials. These applications, including hypersonic flight and nuclear energy generation, are often limited by the maximum operating temperature of the structural and coating materials. The current list of materials that can withstand these extreme environments is short and a new material space must be explored to meet current and future demands. High entropy carbides, which comprise complex solid solution mixtures of five or more metals and carbon,

represent a new class of ultra-high temperature ceramics that allow for unique properties compared to the traditional binary carbides. In this work, five-component, rocksalt structured, transition metal carbides are synthesized in bulk via mechanical alloying and current and pressure assisted densification and homogenization. The carbides are investigated for phase composition in the pursuit of randomly mixed, single-phase, solid solutions. The effect of entropy on mixing is predicted via a newly formulated entropy descriptor, the Entropy Forming Ability (EFA), that is developed using experimental data and density functional theory. The EFA is then employed in choosing candidate compositions for experimental synthesis. In total, a list of 12 compositions are investigated with 9 forming single-phase and, therefore, high entropy carbides. Phase composition and the extent of mixing is investigated via electron microscopy with energy dispersive x-ray spectroscopy, transmission electron microscopy, x-ray diffraction, and x-ray absorption fine structure. These high entropy carbides allow for electronic structures that are not available to the binary or ternary carbides. Particularly, the use of entropy to stabilize single phase structures allows for the inclusion of elements that are not stable in the rocksalt structure at room temperature. In this work, the inclusion of molybdenum and tungsten into rocksalt structured carbides allows for more electron rich compositions that exhibit increased metallic character, which is described by the increased energy distance between the Fermi level and the pseudo-gap. This parameter is used to predict and tune mechanical properties and leads to the synthesis of compositions with enhanced plasticity and high fracture toughness. Elastic properties, hardness, and fracture toughness are investigated via acoustic wave speed, nanoindentation, and microindentation techniques.

Part 1 – Introduction

1.1 Motivation

Recently, the ever-increasing demands of technologies such as next generation nuclear reactors and hypersonic flight vehicles have begun to require materials that can operate at more extreme temperatures. The current list of materials that can withstand operating temperatures in excess of 3000°C is limited to just 14 materials, most of which comprise carbide and boride ceramics [1]. In newly developed atmospheric hypersonic vehicles, the temperatures generated via friction within the atmosphere cannot be withstood for long periods of time by any known materials. This means that current technologies employed in leading edges for hypersonic vehicles require that they can only be used a short time and that the shielding materials are replaced after a single use. In addition to the leading edges, the rocket nozzle structure and coatings must be made of materials that can withstand the temperature as well as the chemical environment. As all of these components comprise a structural part, the mechanical properties must also be taken into careful consideration, which is why rocket nozzles are often still made of metallic alloys such as nickel 718. Obviously, an ultra-high temperature ceramic material would be a better fit for these parts when considering the temperatures involved, however ceramics are simply too brittle for the construction of structural aerospace components and are thus usually reserved for coatings of the bulk metallic alloy parts.

In energy generation from simple combustion engines to nuclear reactors a common theme is present – the higher the operating temperature, the higher the efficiency. In fact, the output of combustion engines and nuclear reactors alike is still limited by the operating temperature that can be withstood by the materials that contain combustion/radioactive fuel. Next generation reactors

that are necessary to fulfill the ever-increasing energy demands must be lined with materials that can withstand ultra-high temperatures, extremely high thermal gradients, and irradiation without breaking down or failing mechanically. Clearly, a new direction is needed that will enable the development and understanding of novel materials for these future applications.

1.2 Background and Objective

Traditional metallurgy generally relies on the addition of small fractions of alloying elements to a base element in order to change the properties to fulfill application needs (e.g. enhance strength). This way of thinking has been carried from the bronze age all the way to the modern age of steels, aluminum, and titanium alloys. This means, when considering complex phase diagrams of two or more elements, minor alloying techniques focus on the corners and edges rather than the vast space in the center. These complex phase spaces remain largely unexplored and represents an immense number of possible material compositions. In a simple calculation Cantor [2] outlines that using, conservatively, 40 metals on the periodic table and mixing them in in variations of, again conservatively, integer percent, the number of possible compositions is 10^{78}. For perspective there are an estimated 10^{66} atoms in the milky way galaxy. Clearly, there must be materials that lie in the center of these complex phase diagrams that have advantageous properties. With recent advances in computational modeling techniques, these vast phase spaces have come under consideration and an increasing amount of research is going into the modeling and experimental techniques to study and understand these materials. These alloys, which employ mixing multiple components in near equiatomic amounts, were initially called high entropy alloys (HEA) but are now being classified into the broader categories of multi principle element alloys (MPEA) or complex concentrated alloys (CCA). High entropy alloys, however, remain an

important subset of MPEAs and have been the subject of research in recent years where many have been discovered to have highly advantageous properties.

The exploration into the modern research field of high entropy alloys was initiated by the separate works of Cantor [3], Yeh *et al.*, [4], and Ranganathan [5]. The insights of Cantor revealed that, when five or more elements were mixed together in near equiatomic amounts, the number of phases in the resulting microstructure was typically one or two, which is much fewer than is possible by Gibbs phase rule [2]. Original theories arose that, in equiatomic alloys with five or more components, the high configurational entropy, S, of the mixed solid solution phase ($S = RlnQ$, where $R=8.314\ J\cdot mol^{-1}\cdot K^{-1}$ and Q is the number of components) stabilized it against the formation of thermodynamically competing intermetallic phases [6]. Hence, single-phase, randomly mixed, solid solution alloys containing five or more principle elements were called high entropy alloys. Since their initial conception, debate has arisen over the theory of entropic stabilization, as it has been proven a false theory in many systems, and many alloys that were not single-phase solid solutions were called HEAs simply because they compositionally occupied a space near the center of a complex phase diagram. For this reason, in this work, we define three separate material spaces: MPEAs or CCAs that only require that there are five or more elements in near equiatomic amounts (i.e. is near the center of a phase diagram), a subset of MPEAs - high entropy alloys that require that the elements are mixed in a single phase randomly ordered solid solution (i.e. actually have a high configurational entropy), and a subset of high entropy alloys - entropy stabilized alloys (ESAs) that require that the single phase solid solution is stabilized by the high configurational entropy (i.e. has a positive enthalpy of formation). Regardless of definitions, driven by the original work in HEAs, the exploration of these complex alloy spaces

has accelerated rapidly in recent years and research has branched from metal systems to ceramics containing separate anion and cation lattices.

The first entropy stabilized ceramic material, $(Mg_{0.2}Co_{0.2}Ni_{0.2}Cu_{0.2}Zn_{0.2})O$, was synthesized by Rost *et al*., [7,8] and was proven to demonstrate a truly randomly ordered solid solution that was stabilized by its high configurational entropy. This oxide sparked an interest in high entropy and entropy stabilized ceramics and until date high entropy oxides, carbides, borides, nitrides, and carbonitrides have been investigated [9–15]. These materials have been aimed at applications from ultra-high temperature ceramics for hypersonic flight leading edges to dielectrics and electrolytes for energy storage and conversion and both interesting and advantageous properties have been achieved [10,16,17]. Given the vast number of material compositions, investigation into high entropy ceramics, their stability, and their properties is still in its infancy.

In the realm of ultra-high temperature ceramics (UHTCs) the number of materials that are eligible for use is very slim as there are just fourteen known materials with melting temperatures greater than 3000°C [1]. The question then arises; is there any room in the high temperature space to develop new materials? Here, we turn to the field of high entropy alloys in looking towards the center of phase diagrams for new phases or new complex single-phase systems that can exploit properties that are not available to the binary ceramics. In particular, the carbides of group IVB, VB, and VIB transition metals are of interest in the UHTC community for their high melting temperatures, good corrosion resistance, and high strength and hardness [19]. The individual binary carbides such as HfC and TaC have the highest melting temperatures of any known materials, as well as good corrosion resistance and high strength and hardness [18,19]. Thus, these carbides serve as good starting points for investigations into complex alloys that may have advantageous properties. The carbides also are known to have tunable mechanical properties that

depend on their electronic structure, which can enable tunable mechanical properties based on alloying in complex systems [20–24].

The objective behind this work is to expand the recent research of high entropy alloys and entropy stabilized ceramics into ultra-high temperature ceramic materials with a focus on transition metal carbides. Through the development of modeling techniques and descriptors, we aim to advance the understanding of the fundamental thermodynamics behind material stability and the atomic scale physics behind their mechanical, thermal, and thermomechanical properties and further the ability to predict new materials. Through the introduction of new material compositions and theories of mechanical properties that depend on the electronic structures achieved in these complex compositions, we hope to introduce ultra-high temperature ceramics with enhanced and tunable mechanical properties. Further, through applied experimental synthesis and characterization, we aim to introduce a new class of ultra-high temperature ceramics that can direct future research towards possible materials to fill current voids in engineering applications where the available materials are the limiting factor.

References

[1] E. Wuchina, E. Opila, M. Opeka, W. Fahrenholtz, I. Talmy, UHTCs: ultra-high temperature ceramics for extreme environment applications, Electrochem. Soc. Interface. 16 (2007) 30.

[2] B. Cantor, Multicomponent and High Entropy Alloys, Entropy. 16 (2014) 4749–4768. doi:10.3390/e16094749.

[3] B. Cantor, I.T.H. Chang, P. Knight, A.J.B. Vincent, Microstructural development in equiatomic multicomponent alloys, Mater. Sci. Eng. A. 375–377 (2004) 213–218. doi:10.1016/J.MSEA.2003.10.257.

[4] J.-W. Yeh, S.-K. Chen, S.-J. Lin, J.-Y. Gan, T.-S. Chin, T.-T. Shun, C.-H. Tsau, S.-Y. Chang, Nanostructured High-Entropy Alloys with Multiple Principal Elements: Novel Alloy Design Concepts and Outcomes, Adv. Eng. Mater. 6 (2004) 299–303. doi:10.1002/adem.200300567.

[5] S. Ranganathan, Alloyed pleasures: Multimetallic cocktails, (2003).

[6] D.B. Miracle, O.N. Senkov, A critical review of high entropy alloys and related concepts, Acta Mater. 122 (2017) 448–511. doi:10.1016/j.actamat.2016.08.081.

[7] C.M. Rost, E. Sachet, T. Borman, A. Moballegh, E.C. Dickey, D. Hou, J.L. Jones, S. Curtarolo, J.-P. Maria, Entropy-stabilized oxides, Nat. Commun. 6 (2015) 8485. doi:10.1038/ncomms9485.

[8] C. Rost, Entropy-Stabilized Oxides: Explorations of a Novel Class of Multicomponent Materials., Dissertation, (2016).

[9] S. Jiang, T. Hu, J. Gild, N. Zhou, J. Nie, M. Qin, T. Harrington, K. Vecchio, J. Luo, A new class of high-entropy perovskite oxides, Scr. Mater. 142 (2018) 116–120. doi:10.1016/J.SCRIPTAMAT.2017.08.040.

[10] J. Gild, Y. Zhang, T. Harrington, S. Jiang, T. Hu, M.C. Quinn, W.M. Mellor, N. Zhou, K. Vecchio, J. Luo, High-Entropy Metal Diborides: A New Class of High-Entropy Materials and a New Type of Ultrahigh Temperature Ceramics., Sci. Rep. 6 (2016) 37946. doi:10.1038/srep37946.

[11] J. Gild, M. Samiee, J.L. Braun, T. Harrington, H. Vega, P.E. Hopkins, K. Vecchio, J. Luo, High-entropy fluorite oxides, J. Eur. Ceram. Soc. 38 (2018) 3578–3584. doi:10.1016/J.JEURCERAMSOC.2018.04.010.

[12] K. Vecchio, J. Luo, J. Gild, M. Samiee, O. Dippo, T. Harrington, S. Curtarolo, P. Sarker, C. Toher, Modelling and synthesis of high-entropy refractory carbides, nitrides and carbonitrides, Ultra-High Temp. Ceram. Mater. Extrem. Environ. Appl. IV. (2017).

[13] P. Sarker, T. Harrington, C. Toher, C. Oses, M. Samiee, J.-P. Maria, D.W. Brenner, K.S. Vecchio, S. Curtarolo, Novel high-entropy high-hardness metal carbides discovered by entropy descriptors, (2018).

[14] J. Dusza, P. Švec, V. Girman, R. Sedlák, E.G. Castle, T. Csanádi, A. Kovalčíková, M.J. Reece, Microstructure of (Hf-Ta-Zr-Nb)C high-entropy carbide at micro and nano/atomic level, J. Eur. Ceram. Soc. 38 (2018) 4303–4307. doi:10.1016/J.JEURCERAMSOC.2018.05.006.

[15] E. Castle, T. Csanádi, S. Grasso, J. Dusza, M. Reece, Processing and Properties of High-Entropy Ultra-High Temperature Carbides, Sci. Rep. 8 (2018) 8609. doi:10.1038/s41598-018-26827-1.

[16] D. Bérardan, S. Franger, A.K. Meena, N. Dragoe, Room temperature lithium superionic conductivity in high entropy oxides, J. Mater. Chem. A. 4 (2016) 9536–9541. doi:10.1039/C6TA03249D.

[17] D. Bérardan, S. Franger, D. Dragoe, A.K. Meena, N. Dragoe, Colossal dielectric constant in high entropy oxides, Phys. Status Solidi - Rapid Res. Lett. 10 (2016) 328–333. doi:10.1002/pssr.201600043.

[18] O. Cedillos-Barraza, D. Manara, K. Boboridis, T. Watkins, S. Grasso, D.D. Jayaseelan, R.J.M. Konings, M.J. Reece, W.E. Lee, Investigating the highest melting temperature materials: A laser melting study of the TaC-HfC system, Sci. Rep. 6 (2016) 37962. doi:10.1038/srep37962.

[19] L. Toth, Transition Metal Carbides and Nitrides., Elsevier Science, 1971.

[20] H. Yu, M. Bahadori, G.B. Thompson, C.R. Weinberger, Understanding dislocation slip in stoichiometric rocksalt transition metal carbides and nitrides, J. Mater. Sci. 52 (2017) 6235–6248. doi:10.1007/s10853-017-0857-4.

[21] N. De Leon, X. Yu, H. Yu, C.R. Weinberger, G.B. Thompson, Bonding Effects on the Slip Differences in the B 1 Monocarbides, Phys. Rev. Lett. 114 (2015) 165502. doi:10.1103/PhysRevLett.114.165502.

[22] C.J. Smith, X.-X. Yu, Q. Guo, C.R. Weinberger, G.B. Thompson, Phase, hardness, and deformation slip behavior in mixed HfxTa1-xC, Acta Mater. 145 (2018) 142–153. doi:10.1016/J.ACTAMAT.2017.11.038.

[23] D. Edström, D.G. Sangiovanni, L. Hultman, I. Petrov, J.E. Greene, V. Chirita, Elastic properties and plastic deformation of TiC- and VC-based pseudobinary alloys, Acta Mater. 144 (2018) 376–385. doi:10.1016/J.ACTAMAT.2017.10.047.

[24] T. Das, S. Deb, A. Mookerjee, Study of electronic structure and elastic properties of transition metal and actinide carbides, Phys. B Condens. Matter. 367 (2005) 6–18. doi:10.1016/J.PHYSB.2005.05.041.

Part 2

High-entropy high-hardness metal carbides discovered by entropy descriptors

Pranab Sarker,[1,†] Tyler J. Harrington,[2,3,†] Cormac Toher,[1] Corey Oses,[1] Mojtaba Samiee,[2] Jon-Paul Maria,[4] Donald W. Brenner,[5] Kenneth S. Vecchio[2,3,*] Stefano Curtarolo,[6,*]

[1]Department of Mechanical Engineering and Materials Science, Duke University, Durham, NC 27708, USA
[2]Materials Science and Engineering Program, University of California San Diego, La Jolla, CA 92093, USA
[3]Department of NanoEngineering, University of California San Diego, La Jolla, CA 92093, USA
[6]Department of Materials Science and Engineering, North Carolina State University, Raleigh, NC 27695, USA
[5]Materials Science, Electrical Engineering, Physics and Chemistry, Duke University, Durham, NC 27708, USA
† These authors contributed equally
** Corresponding author(s)*

ABSTRACT

High-entropy materials have attracted considerable interest due to the combination of useful properties and promising applications. Predicting their formation remains the major hindrance to the discovery of new systems. Here we propose a descriptor—entropy forming ability—for addressing synthesizability from first principles. The formalism, based on the energy distribution spectrum of randomized calculations, captures the accessibility of equally-sampled states near the ground state and quantifies configurational disorder capable of stabilizing high-entropy homogeneous phases. The methodology is applied to disordered refractory 5-metal carbides—promising candidates for high-hardness applications. The descriptor correctly predicts the ease with which compositions can be experimentally synthesized as rock-salt high-entropy

homogeneous phases, validating the ansatz, and in some cases, going beyond intuition. Several of these materials exhibit hardness up to 50% higher than rule of mixtures estimations. The entropy descriptor method has the potential to accelerate the search for high-entropy systems by rationally combining first principles with experimental synthesis and characterization.

2.1 Introduction

High-entropy materials having a highly disordered homogeneous crystalline single phase (potentially stabilized entirely by entropic contributions) continue to attract a great deal of research interest [1,2,3]. Remarkable properties have been reported: high strength (yield stress >1 GPa) combined with ductility [4-11], hardness [5,12,13], superconductivity [14], colossal dielectric constant [15], and superionic conductivity [16]. Entropy is thought to play a key-stabilizing role in high-entropy alloys [1], entropy-stabilized oxides [17,18] , high-entropy borides [19], and high-entropy carbides [20-23]. The latter three classes consist of disordered metal cation sublattices with several species at equi-concentration combined with oxide [15,17,18,24], boride [19], or carbide [20-23] anion sublattices. These systems offer the potential to combine excellent thermo-mechanical properties and resilient thermodynamic stability given by entropy stabilization with the higher oxidation resistance of ceramics [25]. The resistance of disordered carbides to extreme heat [26-28], oxidation [23], and wear makes them promising ultra-high-temperature ceramics for thermal protection coatings in aerospace applications [29], and as high-hardness, relatively low-density high-performance drill bits and cutting tools in mining and industry.

Super-hard transition metal carbides have been known since the 1930s to exhibit significant levels of solid solution [26,30,31], and to display high melting temperatures [26,27]. $Ta_xHf_{1-x}C$ forms a homogeneous solid solution across all composition ranges [28,32,33], with Ta_4HfC_5

exhibiting one of the highest experimentally reported melting points (T_m ~ 4263K [26,27])). In this case, the two refractory metals randomly populate one of the two rock-salt sublattices [28]. More recent measurements indicate that the maximum melting point of 4232 K occurs without Ta at the composition $HfC_{0.98}$ [34]. Investigation of new carbide compositions will help elucidate the high temperature behavior of these materials and will provide an avenue to settle the discrepancies in the experimental literature. To discover materials with even more advantageous properties, including increased thermal stability, enhanced strength and hardness, and improved oxidation resistance [23], more species and configurations have to be considered. Unfortunately, the lack of a rational, effective, and rapid method to find and characterize the disordered crystalline phase makes it impossible to pinpoint the right combination of species/compositions and the discovery continues by slow and relatively expensive trial and error.

Computationally, the hindrance in in-silico disordered materials development can be attributed to entropy—a very difficult quantity to parameterize when searching through the immense space of candidates (even with efficient computational methods, e.g., Monte Carlo and ab-initio lattice energies in the Wang-Landau [35] or nested sampling [36] formalisms). CALPHAD has also been applied successfully [2,13,37-39], although it is dependent on the availability of sufficient experimental data. This is the perfect challenge for ab-initio high-throughput computing [40] as long as reasonable entropy descriptors—the set of parameters capturing the underlying mechanism of a materials property—can be found.

In this article, we undertake the challenge by formulating an entropy-forming-ability (EFA) descriptor. It captures the relative propensity of a material to form a high-entropy single-phase crystal by measuring the energy distribution (spectrum) of configurationally randomized

calculations up to a given unit-cell size. A narrow spectrum implies a low energy cost for accessing metastable configurations, hence promoting randomness (i.e., entropy) into the system (high-EFA) at finite temperature. In contrast, a wide spectrum suggests a composition with a high energy barrier for introducing different configurations (low-EFA), and thus with a strong preference for ordered phases. The method is benchmarked by the matrix of possible carbides. Given a set of eight refractory metals (Hf, Nb, Mo, Ta, Ti, V, W, and Zr) plus carbon, the formalism predicts the matrix of synthesizable five-metal high-entropy carbides. Candidates are then experimentally prepared, leading to a novel class of systems. In particular, it is demonstrated that the descriptor is capable of reliably distinguishing between the compositions that easily form homogeneous single phases and the ones that do not, including identifying compositions that form single phases despite incorporating multiple binary carbide precursors with different structures and stoichiometric ratios. Note that because of the differing stoichiometries of the non-rock-salt phase binary carbide precursors Mo_2C and W_2C, the compositions listed in this work are nominal. There are extensive carbon vacancies in the anion sublattice in the synthesized materials, further contributing to the configurational entropy. Several of these materials display enhanced mechanical properties, e.g., Vickers hardness up to 50% higher than predicted by a rule of mixtures (ROM). Thus, this class of materials has strong potential for industrial uses where dense and wear-resistant impactors are needed, particularly for extreme temperature applications. The successful outcome demonstrates the strength of the synergy between thermodynamics, high-throughput computation, and experimental synthesis.

2.2 Results

2.2.1 EFA formalism

To accelerate the search in the chemical space, the entropy content of a compound is estimated from the energy distribution spectrum of metastable configurations above the zero-temperature ground state. At finite *T*, any disordered state can be present with a probability given by the Boltzmann distribution and the state's degeneracy. Note that configurations are randomly sampled up to a given unit-cell size: the larger the size, the more accurately the spectrum represents the real thermodynamic density of states.

The energy distribution (H_i) spectrum can be quantitatively characterized by its standard deviation σ, so that the σ becomes the descriptor for *S*: the smaller σ, the larger *S*. The descriptor for an *N*-species system, called the EFA, is defined as the inverse of the σ of the energy spectrum above the ground state of the *N*-system at zero temperature:

$$EFA(N) = \{\sigma[spectrum(H_i(N))]_{T=0}\}^{-1} \quad (1)$$

where

$$\sigma\{H_i(N)\} = \sqrt{\frac{\sum_{i=1}^{n} g_i(H_i - H_{mix})^2}{\left(\sum_{i=1}^{n} g_i\right) - 1}} \quad (2)$$

where n is the total number of sampled geometrical configurations and g_i are their degeneracies. H_{mix} is the mixed-phase enthalpy approximated by averaging the enthalpies H_i of the sampled configurations:

$$H_{mix} = \frac{\sum_{i=1}^{n} g_i H_i}{\sum_{i=1}^{n} g_i} \quad (3)$$

The broader the spectrum, the more energetically expensive it will be to introduce configurational disorder into the system, and thus the lower the EFA. EFA is measured in $(\text{eV/atom})^{-1}$.

2.2.2 EFA calculation

A total of 56 five-metal compositions can be generated using the eight refractory metals (8!/5!3! = 56) of interest (Hf, Nb, Mo, Ta, Ti, V, W, and Zr). For each composition, the Hermite normal form superlattices of the Automatic FLOW (AFLOW) partial occupation (AFLOW-POCC) method [41] generate 49 distinct 10-atom-cell configurations, resulting in a total of 2744 configurations needed to determine the EFA of this composition space (Methods section). The ab-initio calculated EFA values for the full set of 56 five-metal compositions are provided in Table 2.1. Nine candidates are chosen from this list for experimental synthesis and investigation: (i) the three candidates with the highest value of EFA ($MoNbTaVWC_5$ (EFA = 125 $(\text{eV/atom})^{-1}$), $HfNbTaTiZrC_5$ (EFA = 100 $(\text{eV/atom})^{-1}$), $HfNbTaTiVC_5$ (EFA = 100 $(\text{eV/atom})^{-1}$), high probability of forming high-entropy single phases), (ii) the two candidates with the lowest value of EFA ($HfMoVWZrC_5$ (37 $(\text{eV/atom})^{-1}$), $HfMoTiWZrC_5$ (38 $(\text{eV/atom})^{-1}$), low probability of forming high-entropy single phases), and (iii) four chosen at random with intermediate EFA ($NbTaTiVWC_5$ (77 $(\text{eV/atom})^{-1}$), $HfNbTaTiWC_5$ (67 $(\text{eV/atom})^{-1}$), $HfTaTiWZrC_5$ (50 $(\text{eV/atom})^{-1}$), and $HfMoTaWZrC_5$ (45 $(\text{eV/atom})^{-1}$)). Figure 2.1a shows the energy distribution and EFA values obtained ab initio from configurations generated with AFLOW for the nine chosen systems. For $MoNbTaVWC_5$, $HfNbTaTiZrC_5$, and $HfNbTaTiVC_5$, most of the configurations are within 20 meV/atom of the lowest energy state, and the distributions have an EFA of at least 100

$(eV/atom)^{-1}$. Therefore, at finite temperature, most of the configurations should have a high probability of being formed, so that a high level of configurational randomness is expected to be accessible in the three systems, making them promising candidates to form a high-entropy homogeneous single phase. Achieving a similar level of configurational randomness would be progressively more difficult in $NbTaTiVWC_5$, $HfNbTaTiWC_5$, and $HfTaTiWZrC_5$ as the different configurations display a broader energy distribution, with EFAs ranging from 50 to 77 $(eV/atom)^{-1}$. A higher energy cost is needed to incorporate configurational entropy into these three compositions, so forming a homogeneous single phase will be more difficult. For $HfMoTaWZrC_5$, $HfMoTiWZrC_5$, and $HfMoVWZrC_5$, the spread of energies for the configurations is very wide, with EFA values from 45 down to 37 $(eV/atom)^{-1}$. These materials would be expected to be very difficult to synthesize as a homogeneous single phase.

Table 2.1: Results for the calculated entropy-forming-ability (EFA) descriptor, energetic distance from six-dimensional convex hull (ΔH_f) and vibrational free energy at 2000 K (ΔF_{vib}) for the five-metal carbide systems, arranged in descending order of EFA.

System	EFA	ΔH_f	ΔF_{vib}	Exp.	ε	System	EFA	ΔH_f	ΔF_{vib}	Exp.	ε	System	EFA	ΔH_f	ΔF_{vib}	Exp.	ε
$MoNbTaVWC_5$	125	156	−14	S	0.063	$HfNbTaVWC_5$	67	110				$TaTiVWZrC_5$	50	96			
$HfNbTaTiZrC_5$	100	19	−12	S	0.094	$HfMoTaTiVC_5$	67	82				$NbTiVWZrC_5$	50	93			
$HfNbTaTiVC_5$	100	56	−31	S	0.107	$HfMoNbTiZrC_5$	67	53				$HfMoTiVZrC_5$	50	96			
$MoNbTaTiVC_5$	100	82				$MoNbTaWZrC_5$	63	133				$HfMoTaVZrC_5$	50	92			
$NbTaTiVZrC_5$	83	64				$HfMoTaTiZrC_5$	63	55				$HfMoNbVZrC_5$	50	89			
$HfMoNbTaTiC_5$	83	48				$NbTaTiWZrC_5$	59	61				$MoTaVWZrC_5$	48	148			
$NbTaTiVWC_5$	77	92	−19	S	0.124	$MoTaTiVZrC_5$	59	92				$MoTaTiWZrC_5$	48	94			
$MoNbTaTiWC_5$	77	111				$MoNbTiVZrC_5$	59	87				$MoNbVWZrC_5$	48	146			
$MoNbTiVWC_5$	71	122				$MoNbTaVZrC_5$	59	108				$MoNbTiWZrC_5$	48	89			
$MoNbTaTiZrC_5$	71	57				$HfNbTiVWC_5$	59	81				$HfMoNbWZrC_5$	48	101			
$HfTaTiVZrC_5$	71	73				$HfNbTaWZrC_5$	59	53				$HfTiVWZrC_5$	45	99			
$HfNbTiVZrC_5$	71	73				$NbTaVWZrC_5$	56	119				$HfNbVWZrC_5$	45	94			
$HfMoNbTiVC_5$	71	77				$HfTaTiVWC_5$	56	84				$HfMoTiVWC_5$	45	97			
$HfMoNbTaZrC_5$	71	48				$HfMoTaVWC_5$	56	139				$HfMoTaWZrC_5$	45	105		M	0.271
$HfMoNbTaWC_5$	71	126				$HfMoNbVWC_5$	56	137				$HfTaVWZrC_5$	43	97			
$HfMoNbTaVC_5$	71	99				$HfNbTiWZrC_5$	53	56				$MoTiVWZrC_5$	40	107			
$HfNbTaTiWC_5$	67	53	~0	S	0.171	$HfMoTaTiWC_5$	53	84				$HfMoTiWZrC_5$	38	83		M	0.315
$MoTaTiVWC_5$	67	128				$HfMoNbTiWC_5$	53	81				$HfMoVWZrC_5$	37	141		M	0.325
$HfNbTaVZrC_5$	67	60				$HfTaTiWZrC_5$	50	59	~0	S	0.169						

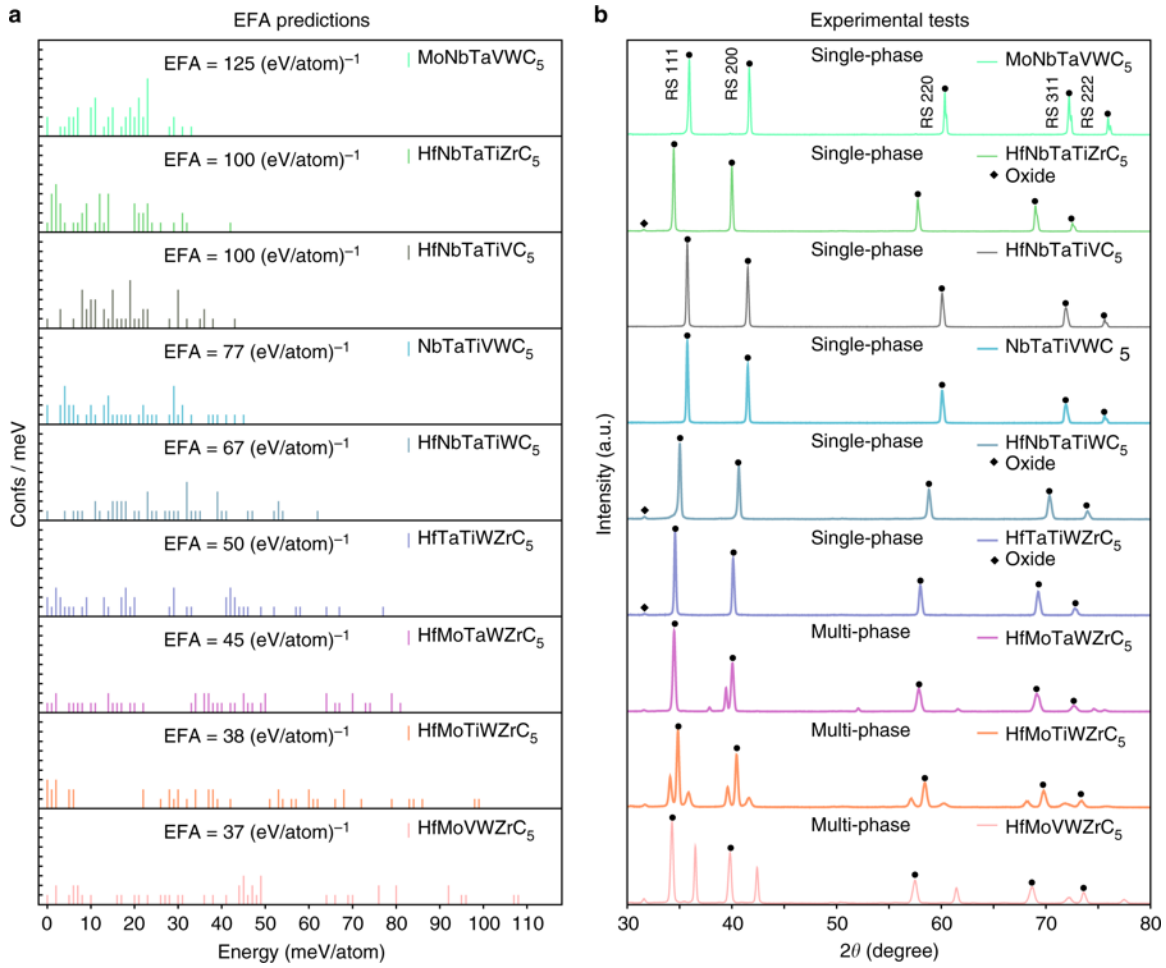

Figure 2.1: Schematics of high-entropy carbides predictions. **a** The energy distribution of different configurations of the 9 five-metal carbides: $MoNbTaVWC_5$, $HfNbTaTiZrC_5$, $HfNbTaTiVC_5$, $NbTaTiVWC_5$, $HfNbTaTiWC_5$, $HfTaTiWZrC_5$, $HfMoTaWZrC_5$, $HfMoTiWZrC_5$, and $HfMoVWZrC_5$; spectrum is shifted so that the lowest energy configuration for each composition is at zero. The energy spectrum for each composition indicates its propensity to form the high-entropy single phase: the narrower the distribution, the more likely it is to form a high-entropy single phase at finite *T*. **b** The X-ray diffraction patterns for the same 9 five-metal carbides, where the first six compositions exhibit only the desired fcc structure peaks, whereas the additional peaks for remaining three compositions indicate the presence of secondary phases. The small peaks at $2\theta = 31.7°$, marked by the diamond symbol in the spectra of $HfNbTaTiZrC_5$, $HfNbTaTiWC_5$ and $HfTaTiWZrC_5$, are from the (111) plane of a monoclinic $(Hf,Zr)O_2$ phase that remains due to processing.

2.2.3 Competing ordered phases

The phase diagrams for the five-metal carbide systems were generated to investigate the existence of binary and ternary ordered structures that could compete with the formation of the high-entropy single phase. First, prototypes for experimentally reported binary and ternary carbide structures [42,43] are used to calculate the formation enthalpies of additional ordered phases for the AFLOW database. The results are used to generate the convex hull phase diagrams for all 56 compositions using the AFLOW-CHULL module [44]. The relevant binary and ternary convex hulls are illustrated in Supplementary Figures 1–36. The distance along the enthalpy axis of the lowest energy AFLOW-POCC configuration from the convex hull, ΔH_f, is listed in Table 2.1 (the decomposition reaction products are summarized in Supplementary Table 2). A rough estimation of the synthesis temperature T_s (see the analogous Entropy-Stabilized Oxides case, Fig. 2 of ref. [17])—can be calculated by dividing ΔH_f by the ideal configuration entropy (Supplementary Table 1, with the ideal entropy per atom evaluated as $0.5k_B \times \log 0.2$, since $k_B \times \log 0.2$ is the entropy per metal carbide atomic pair). A precise characterization of the disorder requires more expensive approaches, such as the LTVC method [45], and is beyond the scope of this article. The highest temperature is 2254 K, which is less than the synthesis temperature of 2200°C (2473 K), indicating that during sintering the disordered phases are thermodynamically accessible with respect to decomposition into ordered compounds. In analogy to the formation of metallic glasses where energetic confusion obstructs crystalline growth [46,47] once the temperature is reduced, systems with high EFA remain locked into ensembles of highly degenerate configurations, retaining the disorder achieved at high temperature. Hence, EFA provides a measure of the relative synthesizability of the disordered composition.

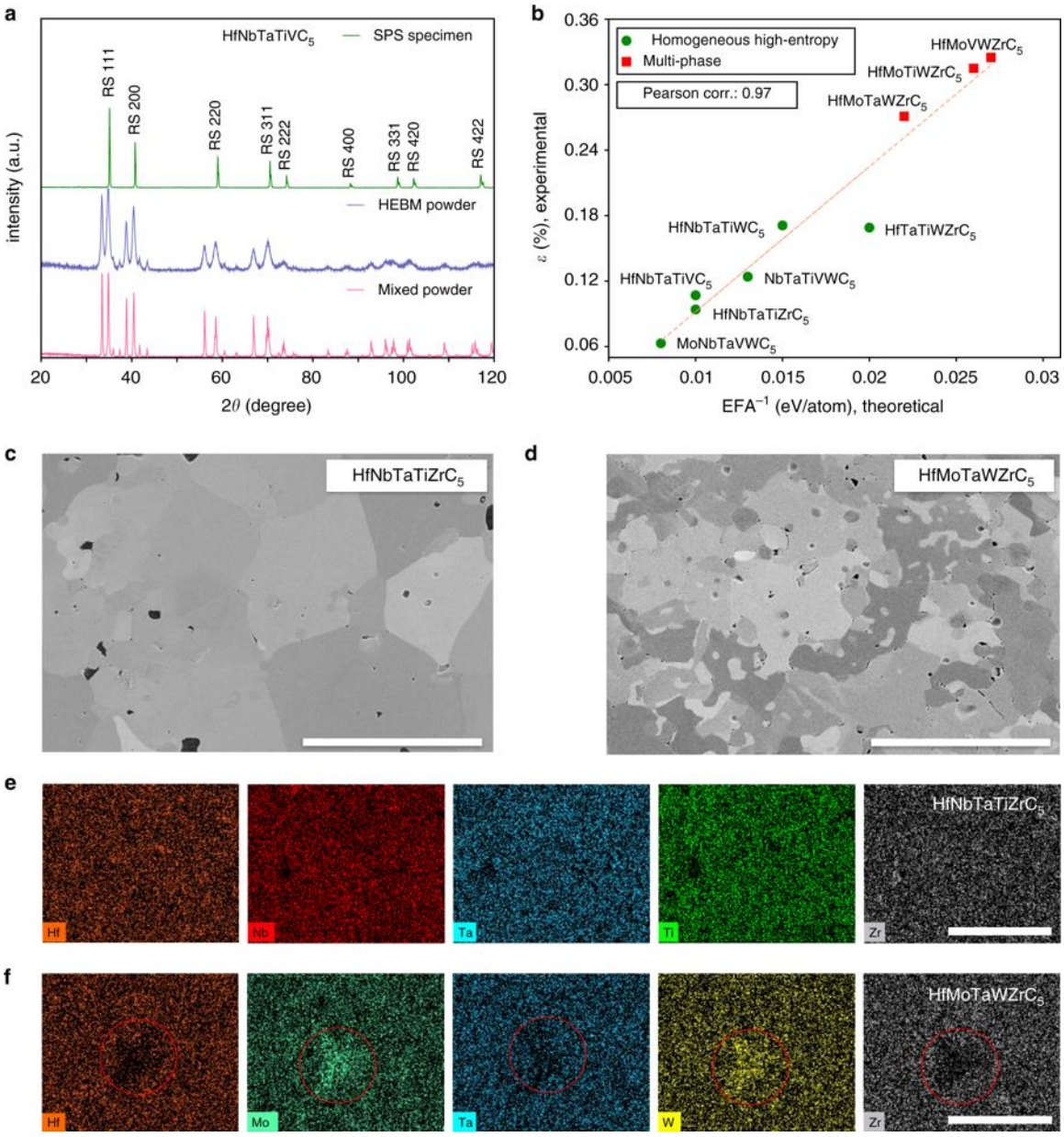

Figure 2.2: Experimental results for high-entropy carbides synthesis and characterization. **a** Progression of a sample of $HfNbTaTiVC_5$ through each processing step: hand mixing (magenta spectrum, bottom), ball milling (blue spectrum, center), and spark plasma sintering (green spectrum, top), depicting the evolution towards the desired rock-salt crystal structure ($a_{exp} = 4.42$ Å). **b** Linear relationship between EFA^{-1} and the distortion of experimental lattice parameters ε. Green circles and red squares indicate homogeneous high-entropy single- and multi-phase compounds, respectively. **c**, **d** Electron micrographs of single-phase $HfNbTaTiZrC_5$ and multi-phase $HfMoTaWZrC_5$ specimens. **e**, **f** Selected EDS compositional maps of the $HfNbTaTiZrC_5$ and $HfMoTaWZrC_5$ specimens. The micrographs show the presence of the secondary phase in $HfMoTaWZrC_5$ (circles) that is also present in XRD results, which is revealed to be a W- and Mo-rich phase. Scale bars, 10 μm (**c**–**f**).

2.2.4 From enthalpy to entropy

It is important to consider that the metal carbide precursors have very strong covalent/ionic bonds, and are therefore enthalpy stabilized [48]. However, the same might not be the case for their mixture. In fact, a statistical analysis of the AFLOW.org enthalpies [44] indicates that the gain in formation enthalpy by adding mixing species, $\Delta H_f(N+1) - \Delta H_f(N)$, decreases with N, and can easily be overcome by the monotonic increase in entropy-gain for the disordered systems (to go from order to complete or partial disorder). In the AFLOW analysis, the threshold between low- and high-entropy systems is around four mixing species. To have completely entropy-stabilized materials, five mixing species are required (similar to the Entropy-Stabilized Oxides [17]). For carbides in which only the metal-sublattice is randomly populated, five metals should be enough to achieve carbide entropy stabilization, especially at equi-composition. Notably, if other sublattices were also allowed to contain disorder, (e.g., reciprocal systems like $Ta_xHf_{1-x}C_{1-y}$)[26,27], then the overall number of species might reduce. In this example, entropy was increased by introducing point defects (vacancies)—a promising strategy to improve high temperature performance. In HfC_{1-x}, the reduction of C to sub-stoichiometry enhances the stabilizing effect of the configurational entropy on the solid phase, offsetting its Gibbs free energy (vacancies can only exist in the solid phase) leading to an overall increase in melting point (see ref. [28]).

2.2.5 Experimental results

To validate the predictions, the nine chosen carbides are experimentally synthesized and characterized (see Methods section). The chemical homogeneity of each sample is measured using energy-dispersive X-ray spectroscopy (EDS), whereas the crystalline structure is determined via X-ray diffraction (XRD).

An example of the evolution of a sample of composition $HfNbTaTiVC_5$ through each processing step is given in Fig. 2.2a, demonstrating the densification and homogenization into a single rock-salt structure. At least three distinct precursor phases are distinguishable in the mixed powder pattern. Following ball milling, the individual phases are still present, however, the peaks are considerably broadened, which is due to particle size reduction and mechanical alloying. Following the final spark plasma sintering (SPS) step at 2200 °C, the sample consolidates into a bulk solid pellet of the desired single rock-salt phase indicating the successful synthesis of a high-entropy homogeneous carbide.

Results of XRD analysis for each sample following SPS at 2200 °C, presented in Fig. 2.1b, demonstrate that compositions $MoNbTaVWC_5$, $HfNbTaTiZrC_5$, $HfNbTaTiVC_5$, $HfNbTaTiWC_5$, $NbTaTiVWC_5$, and $HfTaTiWZrC_5$ (the top 6) only exhibit single fcc peaks of the desired high-entropy phase (rock-salt), whereas $HfMoTaWZrC_5$, $HfMoTiWZrC_5$, and $HfMoVWZrC_5$ (the bottom 3) show multiple structures. The small peaks at $2\theta = 31.7°$, marked by the diamond symbol in the spectra of $HfNbTaTiZrC_5$, $HfNbTaTiWC_5$, and $HfTaTiWZrC_5$ in Fig. 2.1b, are from the (111) plane of a monoclinic (Hf, Zr)O_2 phase that remains due to processing. The volume fraction of this phase is <5% and does not significantly alter the composition of the carbide phase. The distinguishable second phase in $HfMoTaWZrC_5$ is identified as a hexagonal phase. One and two

secondary fcc phases are observed for $HfMoVWZrC_5$ and $HfMoTiWZrC_5$, respectively. Microstructure analysis and selected elemental mapping (Figs. 2.2c–d) confirm that the systems displaying single phases are chemically homogeneous, whereas the multi-phase samples undergo chemical segregation. For example, only grain orientation contrast is present in the $HfNbTaTiZrC_5$ microstructure, and no indication of notable clustering or segregation is visible in its compositional maps. On the contrary, a clear chemical phase contrast is observable in the microstructure of the multi-phase $HfMoTaWZrC_5$ sample, and the compositional maps demonstrate that the secondary phase, apparent in XRD, is W- and Mo-rich.

2.2.6 Homogeneity analysis

Peak broadening in XRD patterns (Fig. 2.1b) is used to quantify the level of structural homogenization achieved in the samples. According to the Williamson–Hall formulation [49], broadening in XRD is principally due to crystallite size ($\propto 1/\cos\theta$, θ = Bragg angle) and lattice strain ($\propto 1/\tan\theta$). For multi-component systems, significant broadening is expected to occur due to local lattice strains and variations in the interplanar spacings throughout the sample [50]. The latter can be attributed to the inhomogeneous distribution of the elements, the extent of which can be evaluated by applying the analysis to a multi-component system, which has only a single lattice structure and is assumed strain free [50].

The lattice distortion of the rock-salt phase in the single-phase materials (or the most prevalent in the multi-phase ones) is determined by using the relationship between broadening β_S and Bragg angle θ (Methods section):

$$\beta_S \cos\theta = 4\varepsilon \sin\theta + \frac{K\lambda}{D} \quad (4)$$

where ε is the lattice strain or variation in interplanar spacing due to chemical inhomogeneity, K is a constant (dependent on the grain shape), λ is the incident X-ray wavelength, and D is the crystallite size. Since materials are assumed strain free, ε—obtained by inverting Eq. 4—represents the relative variation of the lattice parameter due to inhomogeneity. Thus, ε is both a measure of homogeneity and of the effective mixing with respect to the ideal scenario. The results for the EFA descriptor, the experimental characterization, as well as the values for ε for all nine carbides compositions are given in Table 2.1. The values for ε range from 0.063% for $MoNbTaVWC_5$ and 0.094% for $HfNbTaTiZrC_5$ (the most homogeneous materials) to 0.325% for $HfMoVWZrC_5$ (the least homogeneous material). Overall, the experimental findings agree well with the predictions of EFA descriptor, validate its ansatz and indicate a potential threshold for our model of five-metal carbides: EFA ~ $50(eV/atom)^{-1}$ ⇒ homogeneous disordered single phase (high entropy).

2.2.7 High-entropy synthesizability

The comparison between the EFA predictions and the homogeneity of the samples is analyzed in Fig. 2.2b. Although the Williamson–Hall formalism does not provide particularly accurate absolute values of ε, it is effective for comparing similarly processed samples, determining the relative homogeneity. The lattice distortion ε (capturing homogeneity) decreases linearly with the increase of EFA. The Pearson (linear) correlation of EFA^{-1} with ε is 0.97, whereas the Spearman (rank order) correlation is 0.98. As such, the EFA takes the role of an effective high-entropy synthesizability descriptor.

Three facts are relevant. (i) Intuitively, several of the carbide compositions that easily form a highly homogeneous phase, particularly $HfNbTaTiVC_5$ and $HfNbTaTiZrC_5$, come from binary precursors having the same structure and ratio of anions to cations as the final high-entropy

material. (ii) Counterintuitively, the highest-EFA and most homogeneous phase $MoNbTaVWC_5$ is made with two precursors having different structures and stoichiometric ratios from the high-entropy material, specifically orthorhombic α-Mo_2C and hexagonal α-W_2C, leading to a final sub-stoichiometric $MoNbTaVWC_{5-x}$. The additional disorder provided by the presence of vacancies in the C-sublattice is advantageous: it allows further entropy stabilization, potentially increasing the melting point vis-à-vis the stoichiometric composition [28]. An investigation of the effect of carbon stoichiometry is clearly warranted, although it is outside of the scope of this study. (iii) For tungsten and molybdenum, metal-rich carbides are used because of the difficulties in obtaining molybdenum monocarbide (MoC) powder, or tungsten monocarbide (WC) powder in the particle sizes compatible with the other precursors, hindering consistent mixing, sintering and homogenization. It should be noted that additional samples of $MoNbTaVWC_5$ were also synthesized using hexagonal WC with a smaller particle size, and the homogeneous rock-salt phase was again successfully obtained (see Supplementary Figure 37). The existence of phase-pure $MoNbTaVWC_5$ indicates that, similar to the rock-salt binary carbides, the multi-component carbide is stable over a range of stoichiometry. From experimental/phenomenological grounds, the formation of such a phase is surprising. The equi-composition binary carbides MoC and WC have hexagonal ground states, and their rock-salt configurations have significantly higher formation enthalpy [51]. Considering these facts, there are no experimental indications that adding Mo and W would contribute to stabilizing the most homogeneous rock-salt five-metal carbide that was predicted by the EFA and later validated experimentally. The arguments demonstrate the advantage of a descriptor that quantifies the relative EFA over simple empirical/phenomenological rules, in that it correctly identifies this composition as having a high propensity to form a single

phase, while simultaneously correctly predicting that several other systems having both Mo and W subcomponents undergo phase separation.

2.2.8 Mechanical properties

The Vickers hardness, H_V, and elastic modulus, E, of both the binary carbide precursors and the synthesized five-metal single-phase compositions are measured using nanoindentation, where the properties are extracted from load-displacement curves (see Supplementary Figure 38(a)). The binary precursor samples for these measurements are prepared and analyzed using the same protocol to ensure the validity of the comparisons (see Methods section for more details). The results for the five-metal compositions are in Table 2.2, whereas those for the binary carbides are listed in Table 2.3. It is found that, for the five-metal compositions, the measured H_V and E values exceed those predicted from a ROM based on the binary precursor measurements. The enhancement of the mechanical properties is particularly strong in the case of $HfNbTaTiZrC_5$, where the measured E and H_V exceed the ROM predictions by 10 and 50%, respectively (see Supplementary Figure 38(b) for a comparison between the H_V results obtained from calculation, experiment, and ROM). Mass disorder is one possible source of the enhanced hardness: deformation is caused by dislocation movements and activation energy is absorbed and released at each lattice step. An ideal ordered system can be seen as a dislocation-wave-guide with matched (uniform) impedance along the path: propagation occurs without any relevant energy reflection and/or dispersion. This is not the case for disordered systems: mass inhomogeneity causes impedance mismatch, generating reflections and disturbing the transmission by dispersing (scattering) its group energy. Macroscopically the effect is seen as increased resistance to plastic deformations—more mechanical work is required—i.e., increase of hardness. Other possible

causes of increased hardness include solid solution hardening [5,13,20], where the atomic size mismatch results in lattice distortions, limiting the motion of dislocations necessary for plastic deformation; and changes in the slip systems and the ease with which slip can occur [20,52].

Table 2.2: Results for mechanical properties (bulk: *B*, shear: *G*, and elastic moduli: *E*, and Vickers hardness: H_V) for six single-phase high-entropy carbides.

	B		***G***		***E***		$H_{v,Chen}$	$H_{v,Teter}$	$H_{v,Tian}$	$H_{v,exp}$
System	**AFLOW (ROM)**	**Exp. (ROM)**	**AFLOW (ROM)**	**Exp. (ROM)**	**AFLOW (ROM)**	**Exp. (ROM)**	**AFLOW (ROM)**	**AFLOW (ROM)**	**AFLOW (ROM)**	**Exp. (ROM)**
$MoNbTaVWC_5$	312 (321)	278 (−)	183 (183)	226 (−)	460 (459)	533 ± 32 (−)	20 (20)	28 (28)	20 (20)	27 ± 3 (−)
$HfNbTaTiZrC_5$	262 (267)	235 (232)	192 (165)	188 (184)	464 (455)	443 ± 40 (436 ± 30)	27 (25)	29 (28)	27 (25)	32 ± 2 (23 ± 2)
$HfNbTaTiVC_5$	276 (279)	267 (239)	196 (196)	212 (189)	475 (476)	503 ± 40 (449 ± 30)	26 (26)	30 (30)	26 (26)	29 ± 3 (24 ± 2)
$HfNbTaTiWC_5$	291 (296)	252 (−)	203 (186)	205 (−)	493 (459)	483 ± 24 (−)	26 (22)	31 (28)	26 (22)	31 ± 2 (−)
$NbTaTiVWC_5$	305 (304)	253 (−)	199 (189)	206 (−)	490 (460)	485 ± 36 (−)	24 (22)	30 (29)	24 (23)	28 ± 2 (−)
$HfTaTiWZrC_5$	274 (280)	246 (−)	191 (178)	200 (−)	466 (438)	473 ± 26 (−)	25 (21)	29 (27)	25 (21)	33 ± 2 (−)

Elastic properties are calculated using AFLOW [41,53] for the five-metal compositions $MoNbTaVWC_5$, $HfNbTaTiZrC_5$, $HfNbTaTiVC_5$, $HfNbTaTiWC_5$, $NbTaTiVWC_5$, and $HfTaTiWZrC_5$ (Table 2.2) and their precursors. In general, results are within the experimentally reported ranges for the binary carbides (Table 2.3 in the Methods section). H_V values are estimated from the bulk and shear moduli using the models introduced by Chen et al. [54], Teter [55], and Tian et al. [56]. Computational models do not consider plastic deformation mechanisms in inhomogeneous systems and thus H_V predictions underestimate experiments, leading to results consistent with the ROM of binary carbides (Table 2.2). The outcome further corroborates that the experimentally observed enhancement of the mechanical properties is due to disorder.

Table 2.3: Results for mechanical properties (bulk: *B*, shear: *G*, and elastic: *E*, moduli, and Vickers hardness: H_V) for eight rock-salt structure binary carbides.

	B			***G***			***E***			***H*** $_V$				
System	**AFLOW**	**Exp.**	**Exp.[a]**	**AFLOW**	**Exp.**	**Exp.[a]**	**AFLOW**	**Exp.**	**Exp.[a]**	**Chen**	**Teter**	**Tian**	**Exp.**	**Exp.[a]**
HfC	239	241	223	186	179–193	181	443	316–461	428 ± 32	29	28	28	19–25	25 ± 2
MoC	335	—	—	152	—	—	396	—	—	12	23	13	27–83[b]	—
NbC	297	296–378	246	199	197–245	177	488	330–537	429 ± 46	25	30	25	19–25	17 ± 3
TaC	326	248–343	219	213	215–227	184	525	241–722	431 ± 44	25	32	25	16–23	14 ± 2
TiC	251	241	255	181	186	207	438	447–451	489 ± 13	26	27	25	32	31 ± 2
VC	283	389	250	199	157	196	484	268–420	465 ± 13	26	30	26	20–29	29 ± 1
WC	365	—	—	153	—	—	403	—	—	11	23	12	> 28[c]	—
ZrC	221	220	216	157	172	169	381	385–406	402 ± 13	23	28	22	23–25	24 ±

2.2.9 Vibrational contribution to formation free energy

The vibrational contributions to the formation Gibbs free energy, ΔF_{vib}, at 2000 K are listed in Table 2.1 for the six compositions synthesized as a single phase. The vibrational free energies, F_{vib}, are calculated using the Debye–Grüneisen model implemented in the AFLOW–Automatic GIBBS Library (AGL) module [57], using the Poisson ratio calculated with AFLOW–Automatic Elasticity Library (AEL) [53]. The average F_{vib} for the five-metal compositions are calculated, weighted according to the Boltzmann distribution at 2000 K. The vibrational contribution to the formation Gibbs free energy, ΔF_{vib}, for each composition is obtained from the difference between its average F_{vib} and the average F_{vib} of its component binary carbides. ΔF_{vib} at 2000 K ranges from ~0 meV/atom for $HfNbTaTiWC_5$ to −31 meV/atom for $HfNbTaTiVC_5$, which are significantly less than the total entropy contribution (mostly configurational plus vibrational) required to overcome the values of 50 meV/atom to 150 meV/atom for the formation enthalpy ΔH_f. These results are in agreement with previous observations that the vibrational formation entropy is generally an order of magnitude smaller than the configuration entropy [39,58].

2.3 Discussion

In this article, an EFA descriptor has been developed for the purpose of capturing synthesizability of high-entropy materials. The framework has been applied to refractory metal carbides, leading to the prediction and subsequent experimental discovery of homogeneous high-entropy single phases. The method is able to quantitatively predict the relative propensity of each composition to form a homogeneous single phase, thus identifying the most promising candidates for experimental synthesis. In particular, the experiments validate the prediction that the composition $MoNbTaVWC_5$ should have a very high propensity to form a homogeneous single phase, despite incorporating both Mo_2C and W_2C, which have different structures (hexagonal and/or orthorhombic instead of rock-salt) and stoichiometric ratios from the five-metal high-entropy material.

Furthermore, it is demonstrated that disorder enhances the mechanical properties of these materials: $HfNbTaTiZrC_5$ and $HfTaTiWZrC_5$ are measured to have hardness of 32 GPa (almost 50% higher than the ROM prediction) and 33 GPa, respectively, suggesting a new avenue for designing super-hard materials. The formalism could become the long-sought enabler of accelerated design for high-entropy functional materials with enhanced properties for a wide range of different technological applications.

2.4 Methods

2.4.1 Spectrum generation

The different possible configurations required to calculate the energy spectrum are generated using the AFLOW-POCC algorithm [41] implemented within the AFLOW computational materials design framework [51,59,60]. The algorithm initially generates a superlattice of the minimum size necessary to obtain the required partial occupancies within some user-specified accuracy. For each unique superlattice, the AFLOW-POCC algorithm then generates the complete set of possible supercells using Hermite normal form matrices [41]. Non-unique supercell combinations are eliminated from the ensemble by first estimating the total energies of all configurations using a Universal Force Field [41,61] based method, and then identifying duplicates from their identical energies.

2.4.2 Structure generation

In the case of the high-entropy carbide [17] systems investigated here, the AFLOW-POCC algorithm starts with the rock-salt crystal structure (spacegroup: $Fm\bar{3}m, \#225$; Pearson symbol: cF8; AFLOW Prototype: AB_cF8_225_a_b [62]) as the input parent lattice. Each anion site is occupied with a C atom (occupancy probability of 1.0), whereas the cation site is occupied by five different refractory metal elements, with a 0.2 occupancy probability for each. The AFLOW-POCC algorithm then generates a set of configurations (49 in total in the case of the rock-salt based five-metal carbide systems, once structural duplicates are excluded), each containing 10 atoms: one atom of each of the metals, along with five carbon atoms. This is the minimum cell size necessary to accurately reproduce the required stoichiometry. All configurations have $g_i = 10$,

except for one where $g_i = 120$, so that $\sum_{i=1}^{n} g_i = 600$ for the rock-salt-based five-metal carbide systems. Note that computational demands increase significantly with the number of elements: AFLOW-POCC generates 522, 1793, and 7483 for six-, seven-, and eight-metal carbide compositions, respectively.

2.4.3 Energies calculation

The energy of each configuration is calculated using density functional theory (Vienna Ab-initio Simulation Package [63]) within the AFLOW framework [59] and the standard settings [60]. Each configuration is fully relaxed using the Perdew, Burke, Ernzerhof (PBE) parameterization of the generalized gradient approximation exchange-correlation functional [64], projector augmented wave potentials, at least 8000 **k**-points per reciprocal atom (KPPRA), and a plane-wave cut-off of at least 1.4 times the cut-off values of constituent species' pseudopotentials [60]. The formation enthalpy (H_f) of each configuration along with the link to AFLOW.org entry page is provided in Supplementary Tables 4–10.

2.4.4 Mechanical properties

Elastic properties are calculated using the AEL module [53] of the AFLOW framework, which applies a set of independent directional normal and shear strains to the structure, and fits the resulting stress tensors to obtain the elastic constants. From this, the bulk: *B*, and shear: *G*, moduli are calculated in the Voigt, Reuss and Voigt-Reuss-Hill (VRH) approximations, with the average being used for the purposes of this work. The elastic or Young's modulus: *E*, is calculated using the approximation $E = 9BG/(3B + G)$, which can be derived starting from the expression for Hooke's Law in terms of *E* and the Poisson ratio, *v*: $\varepsilon_{11} = 1/E[\sigma_{11} - v(\sigma_{22} + \sigma_{33})]$ [65], and similarly

for ε_{22} and ε_{33}. For a cubic system, $\varepsilon_{11} = S_{11}\sigma_{11} + S_{12}\sigma_{22} + S_{12}\sigma_{33}$ (similarly for ε_{22} and ε_{33}), where S_{ij} are the elements of the elastic compliance tensor, so that $1/E = S_{11}$ and $-\nu/E = S_{12}$. For a cubic system, the bulk modulus is $B = 1/[3(S_{11} + 2S_{12})] = E/[3(1 - 2\nu)]$. The Poisson ratio can be written as $\nu = (3B - 2G)/(6B + 2G)$, and combining with the expression for B and rearranging gives the required $E = 9BG/(3B + G)$.

The elastic properties for the five-metal compositions are first calculated for each of the 49 configurations generated by AFLOW-POCC. The VRH approximated values of B and G for these configurations are listed in Supplementary Table 3, along with the AFLOW-POCC ensemble averaged electronic density of states (see Supplementary Figure 39). The average elastic moduli are then obtained, weighted according to the Boltzmann distribution at a temperature of 2200 °C (the experimental sintering temperature). These calculated values are compared with those obtained using a ROM (average of the binary components, weighted according to fractional composition in the sample).

Three different models are used for predicting the Vickers hardness based on the elastic moduli: Chen et al. ($H_V = 2(k^2G)^{0.585} - 3$; $k = G/B$)[54], Teter ($H_V = 0.151G$)[55], and Tian et al. ($H_V = 0.92k^{1.137}G^{0.708}$; $k = G/B$)[56]. Note, however, that these models are based on the elastic response of the materials, and do not take into account phenomena such as plastic deformation, slip planes, and lattice defects.

2.4.5 Sample preparation

Initial powders of each of the eight binary precursor carbides (HfC, NbC, TaC, TiC, Mo_2C, VC, W_2C, ZrC) are obtained in >99% purity and −325 mesh (<44 μm) particle size (Alfa Aesar). Samples are weighed out in 15 g batches and mixed to achieve the desired five-metal carbide compositions. To ensure adequate mixing, each sample is ball milled in a shaker pot mill for a total of 2 h in individual 30-min intervals intersected by 10-min rest times to avoid heating and consequent oxide formation. All milling is done in tungsten carbide-lined stainless steel milling jars with tungsten carbide grinding media.

Bulk sample pellets are synthesized via solid-state processing routes. The field-assisted sintering technique (FAST), also called SPS, is employed to simultaneously densify and react the compositions into single-phase materials. For all samples, sintering is done at 2200 °C with a heating rate of 100 °C/min, 30 MPa uniaxial pressure, and a 5-min dwell at temperature. Samples are heated in vacuum atmosphere to 1300 °C followed by flowing argon to 2200 °C. All sintering is done in 20 mm graphite die and plunger sets with graphite foil surrounding the samples to prevent reaction with the die.

2.4.6 Sample analysis

Elemental analysis is performed using an FEI Quanta 600 SEM equipped with a Bruker e-Flash EDS detector at an accelerating voltage of 20 kV. Microstructural scanning electron microscope (SEM) imaging is carried out using an FEI Apreo FE-SEM at an accelerating voltage of 5 kV, with a combination of secondary and back-scattered electron detectors to show phase contrast. Crystal phase analysis is performed using a Rigaku Miniflex X-ray Diffractometer with

a stepsize of 0.02° and 5-s dwells, using Cu Kα radiation (wavelength $\lambda = 1.54059$ Å) for all measurements and calculation of the lattice parameter. All sample patterns are fitted in Materials Data Incorporated's (MDI) Jade 9 software [66] with a residual of fit $R < 8\%$. Lattice parameter, a_{exp}, values of 4.353 Å, 4.500 Å, 4.415 Å, 4.434 Å, 4.355 Å, 4.502 Å, 4.506 Å, 4.534 Å, and 4.476 Å were measured for $MoNbTaVWC_5$, $HfNbTaTiZrC_5$, $HfNbTaTiVC_5$, $HfNbTaTiWC_5$, $NbTaTiVWC_5$, $HfTaTiWZrC_5$, $HfMoTaWZrC_5$, $HfMoVWZrC_5$, and $HfMoTiWZrC_5$, respectively (for multi-phase samples, a_{exp} refers to the primary cubic phase).

For analysis of sample peak broadening β_S, instrumental broadening β_I must first be determined. For this, a NIST 660b LaB_6 standard is run under the same conditions as each carbide sample. The instrumental profile is then fitted, and β_I is determined to vary with Bragg angle θ as:

$$\beta_I = 0.1750985 - 0.0015606260\theta + 0.0000112534202\theta^2 \quad (5)$$

β_S is determined by subtracting β_I from the measured broadening β_M: $\beta_S=\beta_M-\beta_I$. β_M is measured as a function of θ, and x is a constant between 1.0 and 2.0. In the current analysis, x is set to 2.0 due to the Gaussian-like shape of the instrument peaks, as this value leads to the lowest standard deviation of linear fits to the peak broadening data.

Both crystallite size and lattice strain contribute to β_S [49,67,68]

$$\beta_s = 4\varepsilon \tan\theta + \frac{K\lambda}{D\cos\theta} \quad (6)$$

where ε is the lattice strain or variation in interplanar spacing due to chemical inhomogeneity, K is a constant (dependent on the grain shape), λ is the incident X-ray wavelength and D is the crystallite size. Rearranging Eq. 6 gives:

$$\beta_S \cos\theta = 4\varepsilon \sin\theta + \frac{K\lambda}{D} \quad (7)$$

The slope of a linear fit to the plot of $\beta_S \cos\theta$ against $\sin\theta$ is equal to the strain, or lattice distortion, whereas the *y*-intercept of a linear fit with zero slope determines the crystallite size.

2.4.7 Mechanical testing

Mechanical properties of each of the single-phase compositions are tested using a Keysight NanoIndenter G200 with a Berkovich indenter tip. To rule out indentation size effects, testing is carried out at loads of both 50 mN and 300 mN, and no significant deviation in hardness or modulus is observed. To allow valid cross-comparison, each of the high entropy carbides is compared with the binary carbides, which were hot-pressed and indentation tested under identical conditions. For the reported values, tests are carried out according to the standard method outlined in ISO 14577 using a maximum load of 50 mN. Values are calculated as an average of 40 indents, and are reported with errors of plus or minus one standard deviation. A fused crystal silica standard is run prior to each test to ensure proper equipment calibration is maintained. Samples are polycrystalline with grain sizes between 10 μm and 30 μm. Prior to indentation testing each sample is vibratory polished using 0.05 μm colloidal silica for 12 h to ensure minimal surface roughness. All tests are carried out at a temperature of 27 °C ± 0.5 °C. Indentation data are analyzed according to the methods of Oliver and Pharr [69,70]. The elastic (i.e., Young's) modulus is determined using $1/E_{\text{eff}}=(1-\nu^2)/E+(1-\nu_{2\text{I}})/E_{\text{I}}$, where E_{eff} is the effective modulus (sometimes called the reduced modulus) obtained from nanoindentation, E and ν are the Young's modulus and Poisson's ratio, respectively, for the specimen, whereas E_{I} and ν_{I} are the same parameters for the indenter. A Poisson's ratio for each of the binary carbides is obtained from literature [71] where available. For

five-metal carbide samples where data for each of the constituents is available, the value used for Poisson's ratio is taken as the average of the constituent binaries. If this average is unavailable (i.e., when Mo and/or W are present), Poisson's ratio is assumed to be equal to 0.18.

Acknowledgements

The authors acknowledge support by DOD-ONR (N00014-15-1-2863, N00014-17-1-2090, N00014-16-1-2583, N00014-17-1-2876) and by Duke University—Center for Materials Genomics—for computational support. S.C. acknowledges the Alexander von Humboldt Foundation for financial support. C.O. acknowledges support from the National Science Foundation Graduate Research Fellowship under grant no. DGF1106401. The authors thank Axel van de Walle, Matthias Scheffler, Claudia Draxl, Ohad Levy, Yoav Lederer, Amir Natan, Omar Cedillos Barraza, Joshua Gild, Olivia Dippo, and Cameron McElfresh for helpful discussions.

Part 2, in full, is a reprint of the material "High-entropy high-hardness metal carbides discovered by entropy descriptors" as it appears in *Nature Communications*. Sarker, Pranab; Harrington, Tyler; Toher, Cormac; Oses, Corey; Samiee, Mojtaba; Maria, Jon-Paul; Brenner, Donald; Vecchio, Kenneth; Curtarolo, Stefano. The dissertation author was the primary investigator and co-author of this material.

References

[1] Gao, M. C, Yeh, J. W, Liaw, P. K. & Zhang, Y.High-Entropy Alloys: Fundamentals and Applications. (Springer, Cham, Switzerland, 2016).

[2] Senkov, O. N., Miller, J. D., Miracle, D. B. & Woodward, C. Accelerated exploration of multi-principal element alloys with solid solution phases. Nat Commun. 6, 6529 (2015).

[3] Widom, M. Modeling the structure and thermodynamics of high-entropy alloys. J. Mater. Res.33, 2881–2898 (2018).

[4] Lim, X. Mixed-up metals make for stronger, tougher, stretchier alloys. Nature 533, 306–307 (2016).

[5] Ye, Y. F., Wang, Q., Lu, J., Liu, C. T. & Yang, Y. High-entropy alloy: challenges and prospects. Mater. Today 19, 349–362 (2016).

[6] Gludovatz, B., Hohenwarter, A., Catoor, D., Chang, E. H., & George, E. P. A fracture-resistant high-entropy alloy for cryogenic applications. Science 345, 1153–1158 (2014).

[7] Gali, A. & George, E. P. Tensile properties of high- and medium-entropy alloys. Intermetallics 39, 74–78 (2013).

[8] Senkov, O. N., Wilks, G. B., Scott, J. M. & Miracle, D. B. Mechanical properties of $Nb_{25}Mo_{25}Ta_{25}W_{25}$and $V_{20}Nb_{20}Mo_{20}Ta_{20}W_{20}$refractory high entropy alloys. Intermetallics 19, 698–706 (2011).

[9] Li, Z., Pradeep, K. G., Deng, Y., Raabe, D. & Tasan, C. C. Metastable high-entropy dual-phase alloys overcome the strength-ductility trade-off. Nature 534, 227–230 (2016).

[10] Tsao, T.-K., Yeh, A., Kuo, C. M.,, Kakehi, K., Murakami, H., Yeh, J. W., & Jian, S. R.. The high temperature tensile and creep behaviors of high entropy superalloy. Sci. Rep. 7, 12658 (2017).

[11] Li, Z., Tasan, C. C., Springer, H., Gault, B. & Raabe, D. Interstitial atoms enable joint twinning and transformation induced plasticity in strong and ductile high-entropy alloys. Sci. Rep. 7, 40704 (2017).

[12] Senkov, O. N., Wilks, G. B., Miracle, D. B., Chuang, C. P. & Liaw, P. K. Refractory high-entropy alloys. Intermetallics 18, 1758–1765 (2010).

[13] Senkov, O. N., Senkova, S. V., Woodward, C. & Miracle, D. B. Low-density, refractory multi-principal element alloys of the Cr-Nb-Ti-V-Zr system: microstructure and phase analysis. Acta Mater. 61, 1545–1557 (2013).

[14] von Rohr, F., Winiarski, M. J., Tao, J., Klimczuk, T. & Cava, R. J. Effect of electron count and chemical complexity in the Ta-Nb-Hf-Zr-Ti high-entropy alloy superconductor. Proc. Natl Acad. Sci. USA113, E7144–E7150 (2016).

[15] Bérardan, D., Franger, S., Dragoe, D., Meena, A. K. & Dragoe, N. Colossal dielectric constant in high entropy oxides. Phys. Status Solidi RRL10, 328–333(2016).

[16] Bérardan, D., Franger, S., Meena, A. K. & Dragoe, N. Room temperature lithium superionic conductivity in high entropy oxides. J. Mater. Chem. A4,9536–9541 (2016).

[17] Rost, C. M., Sachet, M., Borman, T., Moballegh, A., Dickey, E. C., Hou, D., Jones, J. L ., & Curtarolo, S. Entropy-stabilized oxides. Nat Commun.6, 8485 (2015).

[18] Rak, Z., Rost, C. M., Lim, M., Sarker, P., Toher, C., Maria, J.-P., & Brenner, D. W. Charge compensation and electrostatic transferability in three entropy-stabilized oxides: results from density functional theory calculations. J. Appl. Phys. 120, 095105 (2016).

[19] Gild, J., Zhang, Y., Harrington, T., Jiang, S., Hu, T., Quinn, M. C., Mellor, W. M., Zhou, N., Vecchio, K., & Luo, J. High-entropy metal diborides: a new class of high-entropy materials and a new type of ultrahigh temperature ceramics. Sci. Rep. 6, 37946 (2016).

[20] Castle, E., Csanádi, T., Grasso, S., Dusza, J. & Reece, M. Processing and properties of high-entropy ultra-high temperature carbides. Sci. Rep. 8, 8609 (2018).

[21] Dusza, J., Svec, P., Girman, V., Sedlak, R., Castle, E. G., Csanadi, T., Kovalcikova, A., & Reece, M. J. Microstructure of (Hf-Ta-Zr-Nb)C high-entropy carbide at micro and nano/atomic level. J. Eur. Ceram. Soc. 38, 4303–4307 (2018).

[22] Yan, X., Constantin, L., Lu, Y., Silvain, J., Nastasi, M., &Cui, B. (Hf0.2Zr0.2Ta0.2Nb0.2Ti0.2)C high-entropy ceramics with low thermal conductivity. J. Am. Ceram. Soc. 101, 4486–4491 (2018).

[23] Zhou, J., Zhang, J., Zhang, F., Niu, B., Lei, L., % Wang, W. High-entropy carbide: a novel class of multicomponent ceramics. Ceramics Int. 44, 22014–22018 (2018).

[24] Meisenheimer, P. B., Kratofil, T. J. & Heron, J. T. Giant enhancement of exchange coupling in entropy-stabilized oxide heterostructures. Sci. Rep. 7,13344 (2017).

[25] Rohrer, G. S., Affatigato, M., Backhaus, M., Bordia, R., Chan, H. M., Curtarolo, S., Demkov, A., Eckstein, J. N., Faber, K. T., Garay, J. E., Gogotsi, Y., Huang, L., Jones, L. E., Kalinin, S. V., Lad, R. J., Levi, C. G., Levy, J., Maria, J.-P., Mattos Jr, Louis, Navrotsky, A., Orlovskayaya, N., Pantano, C., Stebbins, J. F., Sudarshan, T. S., Tani, T. & Weil, K. S. Challenges in ceramic science: a report from the workshop on emerging research areas in ceramic science. J. Am. Ceram. Soc.95,3699–3712 (2012).

[26] Agte, C. & Alterthum, H. Untersuchungen über systeme hochschmelzendercarbide nebst beiträgen zum problem der kohlenstoffschmelzung [Investigations of high-melting point carbide systems and their contribution to the problem of carbon fusion]. Z. Tech. Phys. 11, 182–191 (1930).

[27] Andrievskii, R. A., Strel'nikova, N. S., Poltoratskii, N. I., Kharkhardin, E. D. &Smirnov, V. S. Melting point in systems ZrC-HfC, TaC-ZrC, TaC-HfC.Poroshk. Metall. 1, 85–88 (1967).

[28] Hong, Q.-J. & van de Walle, A. Prediction of the material with highest known melting point from ab initio molecular dynamics calculations. Phys. Rev. B92,020104 (2015).

[29] Wuchina, E., Opila, E., Opeka, M., Fahrenholtz, W. & Talmy, I. UHTCs: ultra-high temperature ceramic materials for extreme environment applications. Electrochem. Soc. Interface 16, 30–36 (2007).

[30] Rudy, E. Ternary Phase Equilibria in Transition Metal-Boron-Carbon-Silicon Systems. Part II. Ternary Systems. (Air Force Materials Laboratory, Wright-Patterson Air Force Base, Ohio, USA, 1965).

[31] Rudy, E. Ternary Phase Equilibria in Transition Metal-Boron-Carbon-Silicon Systems. Part V. Compendium of Phase Diagram Data. (Air Force Materials Laboratory, Wright-Patterson Air Force Base, Ohio, USA, 1969).

[32] Gusev, A. I. Phase diagrams of the pseudo-binary TiC-NbC, TiC-TaC, ZrC-NbC, ZrC-TaC, and HfC-TaC carbide systems. Russ. J. Phys. Chem. 59, 336–340 (1985).

[33] Cedillos-Barraza, O. et al. Sintering behaviour, solid solution formation and characterisation of TaC, HfC and TaC-HfC fabricated by spark plasma sintering. J. Eur. Ceram. Soc. 36, 1539–1548 (2016).

[34] Cedillos-Barraza, O., Grasso, S., Al Nasiri, N., Jayaseelan, D. D., Reece, M. J., & Lee, W. E. Investigating the highest melting temperature materials: a laser melting study of the TaC-HfC system. Sci. Rep. 6, 37962 (2016).

[35] Landau, D. P., Tsai, S.-H. & Exler, M. A new approach to Monte Carlo simulations in statistical physics: Wang-Landau sampling. Am. J. Phys. 72, 1294–1302 (2004).

[36] Baldock, R. J. N., Pártay, L. B., Bartók, A. P., Payne, M. C. & Csányi, G. Determining pressure-temperature phase diagrams of materials. Phys. Rev. B 93, 174108 (2016).

[37] Gao, M. C. & Alman, D. E. Searching for next single-phase high-entropy alloy compositions. Entropy 15, 4504–4519 (2013).

[38] Zhang, F., Zhang, C., Chen, S. L., Zhu, J., Cao, W. S., & Kattner, U. R.. An understanding of high entropy alloys from phase diagram calculations. Calphad 45, 1–10 (2014).

[39] Gao, M. C. et al. Thermodynamics of concentrated solid solution alloys. Curr. Opin. Solid State Mater. Sci.21, 238–251 (2017).

[40] Curtarolo, S., Hart, G. L. W., Nardelli, M. B., Mingo, N., Sanvito, S., & Levy, O. The high-throughput highway to computational materials design. Nat. Mater. 12, 191–201 (2013).

[41] Yang, K., Oses, C. & Curtarolo, S. Modeling off-stoichiometry materials with a high-throughpu tab-initio approach. Chem. Mater. 28, 6484–6492 (2016).

[42] Bergerhoff, G., Hundt, R., Sievers, R. & Brown, I. D. The inorganic crystal structure data base. J. Chem. Inf. Comput. Sci. 23, 66–69 (1983).

[43] Massalski, T. B., Okamoto, H., Subramanian, P. R. & Kacprzak, L. Binary Alloy Phase Diagrams. (ASM International, Materials Park, Ohio, USA, 1990).

[44] Oses, C., Gossett, E., Hicks, D., Rose, F., Mehl, M. J., Perim, E., Takeuchi, I., Sanvito, S., Scheffler, M., Lederer, Y., Levy, O., Toher, C., & Curtarolo, C. AFLOW-CHULL: cloud-oriented platform for autonomous phase stability analysis. J. Chem. Inf. Model. https://doi.org/10.1021/acs.jcim.8b00393 (2018).

[45] Lederer, Y., Toher, C., Vecchio, K. S. & Curtarolo, S. The search for high entropy alloys: a high-throughput ab-initio approach. Acta Mater. 159, 364–383 (2018).

[46] Perim, E., Lee, D., Liu, Y., Toher, C., Gong, P., Li, Y., Neal Simmons, W., Levy, O., Vlassak, J. J., Schroers, J., & Curtarolo, S. Spectral descriptors for bulk metallic glasses based on the thermodynamics of competing crystalline phases. Nat. Commun. 7, 12315 (2016).

[47] Greer, A. L. Confusion by design. Nature 366, 303–304 (1993).

[48] Kuo, K. & Hägg, G. A new molybdenum carbide. Nature 170, 245–246 (1952).

[49] Williamson, G. K. & Hall, W. H. X-ray line broadening from filed aluminium and wolfram. Acta Metall. 1, 22–31 (1953).

[50] Freudenberger, J., Rafaja, D., Geissler, D., Giebeler, L., Ullrich, C., Kauffmann, A., Heilmaier, M., & Nielsch K. Face centred cubic multi-component equiatomic solid solutions in the Au-Cu-Ni-Pd-Pt system. Metals 7, 135 (2017).

[51] Curtarolo, S. et al. AFLOWLIB.ORG: a distributed materials properties repository from high-throughput ab initio calculations. Comput. Mater. Sci. 58, 227–235 (2012).

[52] Smith, C. J., Yu, X.-X., Guo, Q., Weinberger, C. R. & Thompson, G. B. Phase, hardness, and deformation slip behavior in mixed HfxTa1−xC. Acta Mater. 145, 142–153 (2018).

[53] Toher, C., Oses, C., Plata, J. J., Hicks, D., Rose, F., Levy, O., Jong, M., Asta, M., Fornari, M., Nardelli, M. B., & Curtarolo, S. Combining the AFLOW GIBBS and elastic libraries

to efficiently and robustly screen thermomechanical properties of solids. Phys. Rev. Mater.1, 015401 (2017).

[54] Chen, X.-Q., Niu, H., Li, D. & Li, Y. Modeling hardness of polycrystalline materials and bulk metallic glasses. Intermetallics 19, 1275–1281 (2011).

[55] Teter, D. M. Computational alchemy: the search for new superhard materials. MRS Bull. 23, 22–27 (1998).

[56] Tian, Y., Xu, B. & Zhao, Z. Microscopic theory of hardness and design of novel superhard crystals. Int. J. Refract. Met. Hard Mater. 33, 93–106 (2012).

[57] Toher, C., Plata, J. J., Levy, O., Jong, M., Asta, M., Nardelli, M. B., & Curtarolo, S. High-throughput computational screening of thermal conductivity, Debye temperature, and Grüneisen parameter using a quasiharmonic Debye model. Phys. Rev. B90, 174107 (2014).

[58] van de Walle, A. & Ceder, G. The effect of lattice vibrations on substitutional alloy thermodynamics. Rev. Mod. Phys. 74, 11–45 (2002).

[59] Curtarolo, S., Setyawan, W., Hart, G. L. W., Jahnatek, M., Chepulskii, R. V., Taylor, R. H., Wang, S., Xue, J., Yang, K., Levy, O., Mehl, M. J., Stokes, H. T., Demchenko, D. O. & Morgan, D. AFLOW: an automatic framework for high-throughput materials discovery. Comput. Mater. Sci. 58, 218–226 (2012).

[60] Calderon, C. E., Plata, J. J., Toher, C., Oses, C., Levy, O., Fornari, M., Natan, A., Mehl, M. J., Hart, G., Nardelli, M. B., & Curtarolo, S. The AFLOW standard for high-throughput materials science calculations. Comput. Mater. Sci.108 Part A, 233–238 (2015).

[61] Rappe, A. K., Casewit, C. J., Colwell, K. S., Goddard, W. A. III & Skiff, W. M.UFF, a full periodic table forcefield for molecular mechanics and molecular dynamics simulations. J. Am. Chem. Soc. 114, 10024–10035 (1992).

[62] Mehl, M. J., Hicks, D., Toher, C., Levy, O., Hanson, R. M., Hart, G. & Curtarolo, S. The AFLOW library of crystallographic prototypes: part 1. Comput. Mater. Sci.136,S1–S828 (2017).

[63] Kresse, G. & Furthmüller, J. Efficient iterative schemes for ab initio total-energy calculations using a plane-wave basis set. Phys. Rev. B54, 11169–11186 (1996).

[64] Perdew, J. P., Burke, K. & Ernzerhof, M. Generalized gradient approximation made simple. Phys. Rev. Lett.77, 3865–3868 (1996).

[65] Suh, N. P. & Turner, A. P. L. Elements of the Mechanical Behavior of Solids (McGraw-Hill, New York, 1975).

[66] Materials Data, Inc. Jade 9. https://materialsdata.com/prodjd.html (Materials Data Inc., 2016).

[67] Cullity, B. D. Elements of X-Ray Diffraction. (Addison-Wesley, Reading, MA, USA, 1956).

[68] Mote, V. D., Purushotham, Y. & Dole, B. N. Williamson-Hall analysis in estimation of lattice strain in nanometer-sized ZnO particles. J. Theor. Appl. Phys. 6, 6 (2012).

[69] Oliver, W. C. & Pharr, G. M. An improved technique for determining hardness and elastic modulus using load and displacement sensing indentation experiments. J. Mater. Res. 7, 1564–1583 (1992).

[70] Oliver, W. C. & Pharr, G. M. Measurement of hardness and elastic modulus by instrumented indentation: advances in understanding and refinements to methodology. J. Mater. Res. 19, 3–20 (2004).

[71] Kral, C., Lengauer, W., Rafaja, D. & Ettmayer, P. Critical review on the elastic properties of transition metal carbides, nitrides and carbonitrides. J. Alloy. Compd. 265, 215–233 (1998).

[72] American Society for Metals. ASM Engineered Materials Reference Book (ASM International, Materials Park, Ohio, USA, 1989).

[73] Oyama, S. T. (ed.) The Chemistry of Transition Metal Carbides and Nitrides (Blackie Academic & Professional, Glasgow, UK, 1996).

[74] Dubitsky, G. A., Blank, V. D., Buga, S. G., Semenova, E. E., Serebryanaya, N. R., Aksenenkov, V. V., Prokhorov, V. M., Kul'bachinski, V. A., Krechetov, A. V. & Kytin, V. G. Superhard superconductor composites obtained by sintering of diamond, c-BN and C60 powders with superconductors. Z. Naturforsch. B61, 1541–1546 (2006).

[75] Caron, P. & Tremblay, A. Method for treating tungsten carbide particles.US patent 7981394 B2 (2011).

[76] Rose, F., Toher, C., Gossett, E., Oses, C., Nardelli, M., Fornari, M. & Curtarolo, S. AFLUX: The LUX materials search API for the AFLOW data repositories. Comput. Mater. Sci. 137, 362–370 (2017).

Part 3

Phase stability and mechanical properties of novel high entropy transition metal carbides

Tyler J. Harrington,[1,2] Joshua Gild,[2] Pranab Sarker,[3] Cormac Toher,[3] Christina M. Rost,[4] Olivia F. Dippo,[2] Cameron McElfresh[1], Kevin Kaufmann,[1] Eduardo Marin,[1] Lucas Borowski,[1] Patrick E. Hopkins[4], Jian Luo,[1,2] Stefano Curtarolo,[5] Donald W. Brenner,[6] Kenneth S. Vecchio[1,2,*]

[1]*Department of NanoEngineering, University of California San Diego, La Jolla, CA 92093, USA*
[2]*Materials Science and Engineering Program, University of California San Diego, La Jolla, CA 92093, USA*
[3]*Department of Mechanical Engineering and Materials Science, Duke University, Durham, NC 27708, USA*
[4]*Department of Mechanical and Aerospace Engineering, University of Virginia, Charlottesville, VA 22904, USA*
[5]*Materials Science, Electrical Engineering, Physics and Chemistry, Duke University, Durham, NC 27708, USA*
[6]*Department of Materials Science and Engineering, North Carolina State University, Raleigh, NC 27695, USA*

ABSTRACT

Twelve different equiatomic five-metal carbides of group IVB, VB, and VIB refractory transition metals are synthesized via high-energy ball milling and spark plasma sintering. Implementation of a newly developed *ab initio* entropy descriptor aids in selection of candidate compositions for synthesis of high entropy and entropy stabilized carbides. Phase formation and composition uniformity are analyzed via XRD, EDS, S/TEM-EDS, and EXAFS. Nine of the twelve candidates form true single-phase materials with the rocksalt (B1) structure when sintered at 2473K and can therefore be investigated as high entropy carbides (HECs). The composition $(V_{0.2}Nb_{0.2}Ta_{0.2}Mo_{0.2}W_{0.2})C$ is presented as a likely candidate for further investigation as an entropy

stabilized carbide. Seven of the carbides are examined for mechanical properties via nanoindentation. The HECs show significantly enhanced hardness when compared to a rule of mixtures average of the constituent binary carbides and to the highest hardness of the binary constituents. The mechanical properties are correlated to the electronic structure of the solid solutions, offering a future route to tunability of the mechanical properties of carbide ceramics via exploration of a new complex composition space.

3.1 Introduction

Ultra-high temperature materials are generally defined as materials with melting temperatures ≥3300K - a quality that is currently limited to a list of about 15 elements or compounds [1,2]. Of these, the carbides, nitrides, oxides, and borides comprise a class of materials called ultra-high temperature ceramics (UHTCs). Recently, driven by the increasingly more demanding operating conditions in structural applications, such as next generation nuclear reactors, rocket nozzles, and hypersonic vehicle leading edges, there has been a resurgence in the research and development of UHTCs. Owing to their high hardness, good corrosion resistance, and high melting temperature, the carbides of group IVB, VB, and VIB transition metals are promising candidates for the aforementioned applications [1,3,4]. Of the short list of the known UHTCs, tantalum carbide and hafnium carbide have two of the highest melting temperatures of any known materials with T_m = 4041 K and T_m = 4232 K, respectively; however, they are prone to oxidation at intermediate temperatures [1]. The diborides of Hf and Zr are therefore generally considered as the state of the art in UHTCs when operating in oxidizing environments, even though they melt at lower temperatures than the carbides [1]. As application demands increase, the short list of current UHTCs cannot fulfill all the necessary requirements and new material composition

spaces must be explored. In this regard, ceramics development has begun to follow metallurgy in the investigation of high entropy systems.

The newly developed field of high entropy alloys (HEAs) has garnered much research interest in recent years. In the original theory of HEAs, the high configurational entropy of chemically complex solid solution phases stabilizes them into a single crystalline phase against the formation of the thermodynamically competing intermetallics. According to this theory, when the constituent elements are present in equiatomic amounts in a single phase, the maximum molar configurational entropy of $S = R\,lnN$ is obtained, where R is the gas constant, 8.314 $J \cdot mol^{-1} \cdot K^{-1}$, and N is the number of components [5,6]. It is somewhat generally accepted that this molar configurational entropy becomes significant when there are five or more components, which gives $S \geq 1.61R$ [7]. Thus, HEA compositions typically comprise five or more chemical species mixed in equimolar (or close to equimolar) concentrations. It should be noted, however, that there remains significant debate over the term "high entropy alloy" regarding the actual role that entropy plays in the stability of the system, as opposed to simply being higher than systems with fewer components [8]. For instance, a five-component equiatomic system that displays a single-phase is not necessarily "entropy stabilized" (i.e., it can be enthalpically stable as well). Further, the entropy value of $1.61R$ for a five-component system implies that all the elements are present in an approximately random solid solution phase that is mixed on a first nearest neighbor scale, which means that any material that is not homogeneous or that forms multiple phases is not a HEA; thus the terms multi-principle element alloy (MPEA) and complex concentrated alloy (CCA) have been recently applied to these systems [7,9]. For this work, we deem it important to differentiate between a high entropy material and an entropy stabilized material. A high entropy material implies only that the configurational entropy is significant, meaning that the elements are present

in a random solid solution phase. An entropy stabilized material implies that the solid solution phase only exists due to the high configurational entropy (i.e. the molar heat of mixing is positive). Regardless of the "role of entropy" debate, the exploration of the high entropy material space is growing rapidly and significant developments are being made, which are quickly advancing the understanding of these materials on a fundamental level and accelerating their development for applications as structural materials [7,8]. To date, a myriad of HEA compositions have been synthesized and studied, and many have demonstrated exceptional mechanical and physical properties including high hardness and strength, good corrosion resistance, and high-temperature stability [6,7,10–14]. The work has also extended into the field of ceramics, where studies of oxides, carbides, borides, and nitrides are beginning to show promise for applications such as ultra-high temperature structural materials, extreme environments, and electronics [15–18].

The first bulk, crystalline, entropy stabilized ceramic $(Co_{0.2}Cu_{0.2}Mg_{0.2}Ni_{0.2}Zn_{0.2})O$, was fabricated by Rost *et al.* [16], illustrating the high temperature entropic stabilization as it required quenching from sufficiently high temperatures for a single phase to occur, and the transformation was endothermic on heating. This study also marks one of the first and only works to present a systematic investigation of the role that entropy plays in forcing the formation of a solid solution [19]. Thus, it provides valuable insight for resolution of the aforementioned "role of entropy" debate. Since the original work, the $(Co_{0.2}Cu_{0.2}Mg_{0.2}Ni_{0.2}Zn_{0.2})O$ system and those based on it $(Mg_{0.2}Co_{0.2}Ni_{0.2}Cu_{0.2}Zn_{0.2})_{1-x-y}Ga_yA_xO$ (where A = Li, Na, or K), have demonstrated colossal dielectric constants and room temperature lithium superionic conductivity [17,18]. Recently, in the field of UHTCs, Gild *et al.* [20] demonstrated successful fabrication of several crystalline, stoichiometric, high entropy diborides of group IVB, VB, and VIB refractory transition metals. The diborides showed a single hexagonal phase, which consisted of alternating layers of metal and

boron nets. There has also been investigation into a variety of carbide and nitride films, which exhibit superior hardness, wear resistance and oxidation resistance compared to individual constituents [21–27]. The majority of these nitride and carbide films, while exhibiting exceptional properties, are far from the equiatomic compositions that optimize entropic stabilization and often possess an amorphous structure [7]. Yeh *et al.* [6] reported fabrication of a single phase bulk $(Cr_{0.2}Nb_{0.2}Ti_{0.2}V_{0.2}W_{0.2})C$ high entropy carbide via mechanical alloying and solid-state sintering, but little information is given on the properties of the material. Recent work done by Castle *et al.* [28,29], demonstrated that the four component carbides $(Hf_{0.25}Ta_{0.25}Zr_{0.25}Ti_{0.25})C$ and $(Hf_{0.25}Ta_{0.25}Zr_{0.25}Nb_{0.25})C$ could be fabricated in bulk, although $(Hf_{0.25}Ta_{0.25}Zr_{0.25}Nb_{0.25})C$ more easily formed a single phase. The four component carbides demonstrated significant hardness enhancements over the expected values from rule of mixtures [28]. The work of Dusza *et al.* [29] showed that the $(Hf_{0.25}Ta_{0.25}Zr_{0.25}Nb_{0.25})C$ material was single phase with no detectable segregation at the micro/nanoscale level. Following the work of the present authors [30], the bulk five component carbide $(Hf_{0.2}Nb_{0.2}Ta_{0.2}Ti_{0.2}Zr_{0.2})C$ was fabricated by Yan *et al.* [31], which demonstrated low thermal conductivity and a high elastic modulus and hardness.

Here we present a systematic study of phase stability and mechanical properties in twelve bulk, equiatomic, five-metal high entropy carbides, of which eleven have never been reported. Specifically, introduction of elements from group VIB, none of which demonstrate cubic monocarbides at room temperature, allows for insight into the role of entropy in the stability of the single phase. Phase purity is examined through XRD, EDS, S/TEM, and EXAFS. Mechanical properties are presented in terms of hardness and modulus measured from nanoindentation testing and compared with rule-of-mixtures predictions based on the five constituent binary carbides as well as their relationship to electronic structure through the valence electron concentration (VEC).

The study of a range of compositions spanning group IVB, VB, and VIB transition metals leads to a series of materials with different electronic structures, which allows for analysis of trends relating mechanical properties to electronic structure that can be valuable in future materials design.

3.2 Methods

3.2.1 Predicting High Entropy Compositions

An *ab initio* technique for determining the effective role of entropy was employed to identify compositions with a high or low propensity to form a single phase. A thorough discussion of the technique by the current authors is presented in Ref. [32] and is outside of the scope of this study, which focuses primarily on the experimental synthesis and characterization of high entropy carbides. In short, the model employs an entropy descriptor, which allows for the determination of an Entropy Forming Ability (EFA) for each material composition. To calculate the EFA, a set of 49 configurations is generated using the partial occupation (POCC) module [33] of the AFLOW (Automatic FLOW) framework [34]. The energy distributions of these sets of configurations are calculated using density functional theory as implemented in the VASP package [35], with the PBE parameterization of the generalized gradient approximations (GGA) exchange-correlation functional [36], and the AFLOW standard settings [37]. A narrow distribution indicates a low energy cost to introduce metastable configurations (and thus disorder) into the material, whereas a broad distribution implies a high energy barrier to add configurations. The EFA descriptor is inversely proportional to the width of the energy distribution, so that a high EFA value corresponds to a composition that should easily form a single phase.

3.2.2 Synthesis and Sintering

For each of the candidate compositions listed in Table 3.1, starting powders of each of the individual carbide compounds (TiC, ZrC, HfC, $VC_{0.88}$, NbC, TaC, Mo_2C, W_2C) (Alfa Aesar, >99.5% purity, -325mesh) were weighed out in batches of 50 g and hand mixed. Following hand mixing, the powders were high energy ball milled (HEBM) in a Spex 8000D shaker pot high energy ball mill (SpexCertPrep, NJ, USA) using tungsten carbide lined stainless steel jars and 10 mm tungsten carbide milling media for 2 hours in 12 g batches with 0.1 g stearic acid as lubricant. The milling was performed in 30-minute segments with 10-minute cool-off periods to minimize overheating and oxide formation; all milling was performed in an argon atmosphere. The milled powders were consolidated in 12 g batches via spark plasma sintering (SPS) at 2473 K under a uniaxial load of 30 MPa for 10 min, into 20 mm pellets using a Thermal Technologies 3000 series SPS (Thermal Technologies, CA, USA). The entire sintering process was carried out in a vacuum environment at an initial value of less than 20 mTorr; final sintered pellets measured approximately 4 mm in thickness. A heating rate of 100 K/min was used throughout the entire ramp to 2473 K for each SPS run, and samples were left to cool to room temperature in argon following the 10-minute dwell at the sintering temperature. All SPS steps were carried out in graphite die and plunger sets lined with graphite foil.

3.2.3 X-ray Diffraction and Electron Microscopy

XRD was done on a Rigaku Miniflex diffractometer at 30 kV and 15 mA over a 2θ range of 20°-120° with 0.02° steps. SEM and EDS analyses were conducted on a Thermo Scientific Apreo electron microscope at an accelerating voltage of 20 kV. TEM sample preparation was carried out on a Thermo Scientific Scios Dual Beam FIB. S/TEM characterization was performed on a Thermo Scientific Talos S/TEM at an accelerating voltage of 200 kV.

3.2.4 Extended X-ray Absorption Fine Structure

The extended x-ray absorption fine structure (EXAFS) data for V, Nb, Mo, and W was collected on the APS beamline 12-BM at Argonne National Laboratory (Lemont, IL). Tantalum was not scanned as the tantalum L absorption edges (Ta_{L1} = 11,682 eV, Ta_{L2} = 11,136 eV, Ta_{L3} = 9,881 eV) lie too close to the tungsten L-edges (W_{L1} = 12,100 eV, W_{L2} = 11,544 eV, W_{L3} = 10,207 eV), making the EXAFS region for Ta inaccessible when W is also within a sample composition. The V data was collected using the vanadium K-edge at 5,465 eV, molybdenum using the K-edge at 20,000 eV, niobium using the K-edge at 18,986 eV and tungsten using the L3-edge at 10,207 eV [38]. To reduce noise, each absorber was scanned a minimum of eight runs, and the reported data is the average after 'glitch' removal and background fitting. Initial raw data processing was carried out in the Athena software package [38]; data fitting to the theoretical model was conducted using Artemis [38].

3.2.5 Hardness Testing

Hardness and modulus testing was conducted via nanoindentation on a KLA-tencor G200 Nanoindenter (KLA-tencor, CA, USA). Hardness measurements were performed according to ISO 14577 under a maximum load of 300 mN. In order to produce more statistically relevant data from the nanoindentation measurements, the KLA-tencor Express Test software module was employed. This testing method allows for modulus and hardness measurements at a rate of approx. 1 per second, thereby enabling very large datasets to be generated. For analysis of indentation size effects (ISE), which are known to be present in B1 transition metal carbides [39], an investigation of the hardness of a 99% dense sample of composition $(Ti_{0.2}Zr_{0.2}Hf_{0.2}Nb_{0.2}Ta_{0.2})C$ was done under different loading conditions. The results of the load and indentation depth dependence of the hardness measurements is given in Supplementary Figure 40. The hardness exhibits increased values for measurements made with a max load under 50 mN (resulting indentation depth of 326 nm). A load over 50 mN leads to indents large enough to be free of indentation size effects. Indents above 300 mN show significant scatter due to crack formation and therefore cannot be used to calculate the modulus and hardness according to the standard methods of Oliver and Pharr [40]. A load of 300 mN was selected for testing of the carbide materials in this study. Nanoindentation was done on each of the binary carbides synthesized in the same manner as the HECs in this study for generation of rule of mixture moduli and hardness. Tabulated values for each of the binaries in included in Supplementary Table 1. Elastic and hardness data for rocksalt structured MoC was take from theoretical treatments presented in Ref. [41], modulus data for rocksalt WC from calculated values in Ref. [42], and hardness for rocksalt WC from experimental values in Ref. [43] and [44].

3.2.6 Carbon Combustion Analysis

Analysis of the carbon content in each of four samples: $(Ti_{0.2}Hf_{0.2}V_{0.2}Nb_{0.2}Ta_{0.2})C$, $(Ti_{0.2}V_{0.2}Nb_{0.2}Ta_{0.2}W_{0.2})C$, $(Ti_{0.2}Zr_{0.2}Hf_{0.2}Ta_{0.2}W_{0.2})C$, and $(Ti_{0.2}Hf_{0.2}Nb_{0.2}Ta_{0.2}W_{0.2})C$ was done on a Perkin Elmer 2400 Series II CHNS/O Analyzer with a combustion time of 30 seconds at 975°C. Prior to testing, each sample was hand ground and sifted to ≤ 45 μm powder, tests were run in 5 mg powder batches and the given values are an average of eight runs per sample. A $VC_{0.88}$ standard was run four times between each sample composition. The results are presented in Supplementary Table .

3.3 Results

3.3.1 Phase Formation and EFA Predictions

The compositions listed in Table 3.1 are given along with their calculated EFA values. Compositions with an EFA ≥ 50 are shown to form phase pure high entropy ceramics, while the three compositions with EFA ≤ 45 exhibit multiple phases after sintering at 2473 K, suggesting that the cutoff for single phase formation for five component carbides at 2473 K lies between EFA values of 45 and 50.

Table 3.1: List of compositions studied, their calculated entropy forming ability, determination of phase composition following experimental synthesis, and lattice parameter from XRD measurements. If multiple phases were present, reported lattice parameter corresponds to the highest intensity cubic phase.

Composition	EFA	Phase Composition	Secondary Phase	Lattice Parameter, a, (Å)
$(Ti_{0.2}Zr_{0.2}Hf_{0.2}Nb_{0.2}Ta_{0.2})C$	100	Single Phase	-	4.51(8)
$(Ti_{0.2}Hf_{0.2}V_{0.2}Nb_{0.2}Ta_{0.2})C$	100	Single Phase	-	4.42(1)
$(Ti_{0.2}V_{0.2}Nb_{0.2}Ta_{0.2}W_{0.2})C$	77	Single Phase	-	4.36(2)
$(Ti_{0.2}Zr_{0.2}Hf_{0.2}Ta_{0.2}W_{0.2})C$	50	Single Phase	-	4.48(7)
$(Ti_{0.2}Hf_{0.2}Nb_{0.2}Ta_{0.2}W_{0.2})C$	67	Single Phase	-	4.44(2)
$(Ti_{0.2}V_{0.2}Nb_{0.2}Ta_{0.2}Mo_{0.2})C$	100	Single Phase	-	4.36(1)
$(Ti_{0.2}Zr_{0.2}Hf_{0.2}Ta_{0.2}Mo_{0.2})C$	63	Single Phase	-	4.49(4)
$(Ti_{0.2}Hf_{0.2}Nb_{0.2}Ta_{0.2}Mo_{0.2})C$	83	Single Phase	-	4.44(3)
$(V_{0.2}Nb_{0.2}Ta_{0.2}Mo_{0.2}W_{0.2})C$	125	Single Phase	-	4.34(0)
$(Zr_{0.2}Hf_{0.2}Ta_{0.2}Mo_{0.2}W_{0.2})C$	45	Multiple Phases	$(Mo_xW_y)C$ (orth)	4.51(6)
$(Ti_{0.2}Zr_{0.2}Hf_{0.2}Mo_{0.2}W_{0.2})C$	38	Multiple Phases	$(Mo_xW_y)C$ (rs)	4.45(9)
$(Zr_{0.2}Hf_{0.2}V_{0.2}Mo_{0.2}W_{0.2})C$	37	Multiple Phases	$(Mo_xW_y)C$ (rs)	4.52(6)

3.3.2 Structure Determination

Initial determination of phase purity is carried out through X-ray diffraction (XRD) analysis. An example of a detailed investigation of phase progression in a sample of composition $(Ti_{0.2}Hf_{0.2}V_{0.2}Nb_{0.2}Ta_{0.2})C$ follows. This sample composition is used as the example for analysis in XRD, SEM, and S/TEM-EDS throughout. All other compositions were analyzed in a similar manner with results located in the Supplementary Information. The X-ray diffraction patterns of a specimen processed via hand mixing, HEBM, and SPS, collected after each processing step (i.e. hand mixed powder, high energy ball milled powder, and spark plasma sintered pellet) are shown in Figure 3.1a. Five distinct cubic phases that correlate to the individual precursor powders are observed in the hand mixed powder specimen in Figure 3.1b. After high energy ball milling, similar but broader peaks are observed, which can be attributed to the particle size reduction and mechanical alloying resulting from the milling. After spark plasma sintering, only the peaks from a single rocksalt phase are observed, indicating that the system has progressed toward a solid

solution with a uniform lattice parameter. The final diffraction pattern is representative of a homogeneous single phase, to the extent that this can be determined in a laboratory diffractometer. The reflections are: (a) narrow in 2-theta (2θ) space, (b) demonstrate clear $K\alpha_2$ splitting in higher order peaks, and (c) free of shoulders, reinforcing the conclusion of a chemically homogeneous structure with a single lattice parameter. The relative intensities for the final patterns of each single-phase carbide match well with the structure factor calculations for a fully mixed rocksalt phase. Reitveld refinement (Supplementary Figure 41) shows a single lattice parameter of 4.42(1) Å with a χ^2 of 3.3, indicating a good degree of fitting to the calculated, chemically mixed phase.

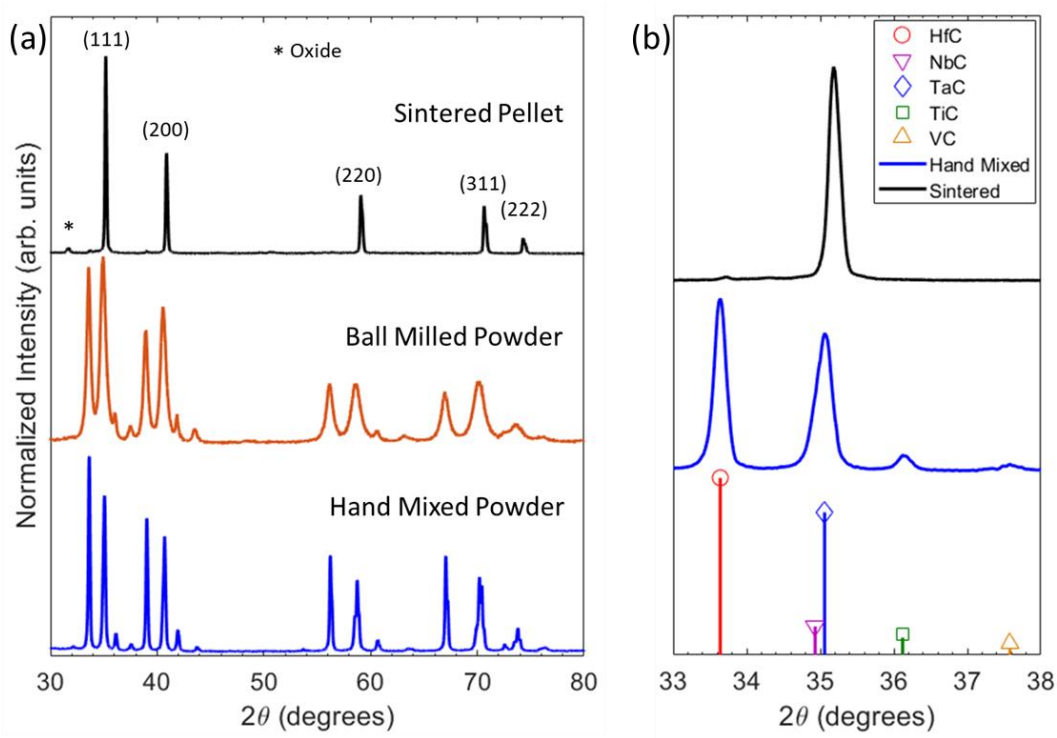

Figure 3.1: X-ray diffraction patterns for the example composition $(Ti_{0.2}Hf_{0.2}V_{0.2}Nb_{0.2}Ta_{0.2})C$, through (a) each processing step: hand mixed, ball milled, and sintered demonstrating the progression into a single phase rocksalt material (lattice parameter: *a=4.42* Å; space group: $Fm\bar{3}m$, #225; Pearson Symbol: cF8) and (b) high magnification of the {111} peak of each of the hand mixed precursor powders and sintered product showing the final carbide with the approximate average lattice parameter of the constituents.

XRD patterns for each of the nine single phase carbide compositions are shown in Figure 3.2a, and for the three multiple phase compositions in Figure 3.2b. The compositions that contain only group IVB and VB transition metals each demonstrate a single phase following sintering at 2473 K. Similarly, materials that contain four species from groups IVB and VB and a single group VIB show only a cubic phase. Three of the four compositions that contain three group IVB and VB and two group VIB (i.e. both W and Mo) show multiple phases, however, of particular interest is $(V_{0.2}Nb_{0.2}Ta_{0.2}Mo_{0.2}W_{0.2})C$, which shows a single phase despite having both Mo and W in equiatomic amounts. The second phase present in each of the multiple phase compositions is a Mo and W rich phase. In $(Zr_{0.2}Hf_{0.2}Ta_{0.2}Mo_{0.2}W_{0.2})C$, this second phase is a hexagonal $(Mo_xW_y)C$ phase, while $(Ti_{0.2}Zr_{0.2}Hf_{0.2}Mo_{0.2}W_{0.2})C$ exhibits the primary mixed rocksalt phase and two secondary cubic phases, and $(Zr_{0.2}Hf_{0.2}V_{0.2}Mo_{0.2}W_{0.2})C$ exhibits the primary mixed rocksalt and a single secondary cubic phase. It should be noted that the secondary phase present in the three samples are distinct and not representative of the hexagonal WC or orthorhombic Mo_2C powder.

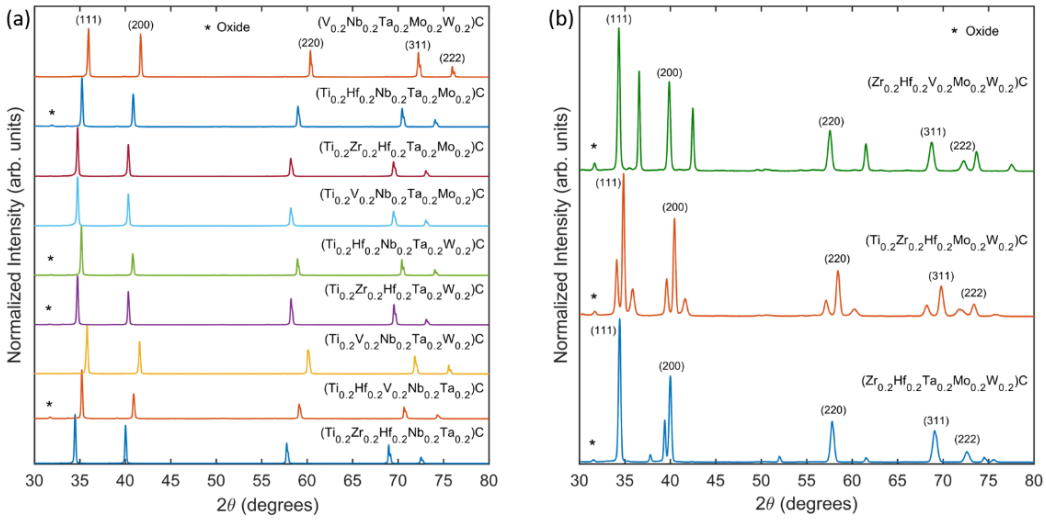

Figure 3.2: X-ray diffraction patterns for (a) nine single phase compositions and (b) three multi-phase compositions. Note that the secondary (and tertiary) phases that form in the multi-phase specimens are different in each of the three compositions.

3.3.3 Determining Homogeneity - Microstructure and S/TEM

Following structure determination in XRD, microscale homogeneity must be determined via SEM microstructural imaging. Example SEM micrographs of the example single-phase $(Ti_{0.2}Hf_{0.2}V_{0.2}Nb_{0.2}Ta_{0.2})C$ and a multi-phase $(Zr_{0.2}Hf_{0.2}Ta_{0.2}Mo_{0.2}W_{0.2})C$ sample are given in Figure 3.3. Microstructure images for all twelve compositions are presented in Supplementary Figure 42. The microstructure of the multi-phase sample shows clear grain boundary phase precipitation, while the single-phase sample demonstrates only orientation contrast and no indications of secondary phases, grain boundary or otherwise, supporting the conclusion that the rocksalt phase is mixed and homogeneous.

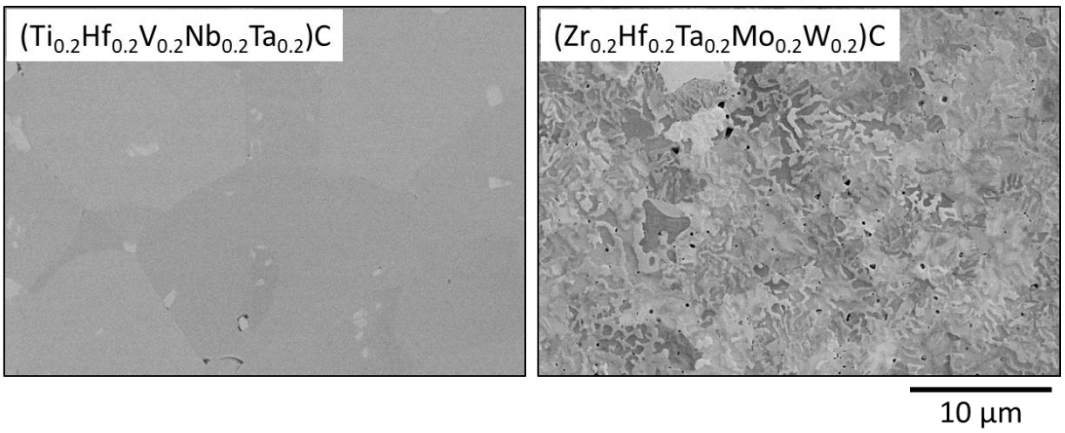

Figure 3.3: Backscattered electron micrographs from (left) a single-phase specimen of composition $(Ti_{0.2}Hf_{0.2}V_{0.2}Nb_{0.2}Ta_{0.2})C$ and (right) the example multi-phase specimen of composition $(Zr_{0.2}Hf_{0.2}Ta_{0.2}Mo_{0.2}W_{0.2})C$.

For nano/atomic level microstructure information, example TEM and STEM-EDS for composition $(Ti_{0.2}Hf_{0.2}V_{0.2}Nb_{0.2}Ta_{0.2})C$ is given in Figure 3.4. The selected area electron diffraction (SAED) pattern for $(Ti_{0.2}Hf_{0.2}V_{0.2}Nb_{0.2}Ta_{0.2})C$ shows no signs of ordering and no additional spots, indicative of a secondary phase. The STEM-EDS exhibits no indication of elemental clustering or phase segregation. While none of the individual techniques fully prove the existence of a fully mixed single-phase material, the combination of XRD with STEM-EDS and TEM strongly supports that a true high entropy phase-pure material is formed in both cases.

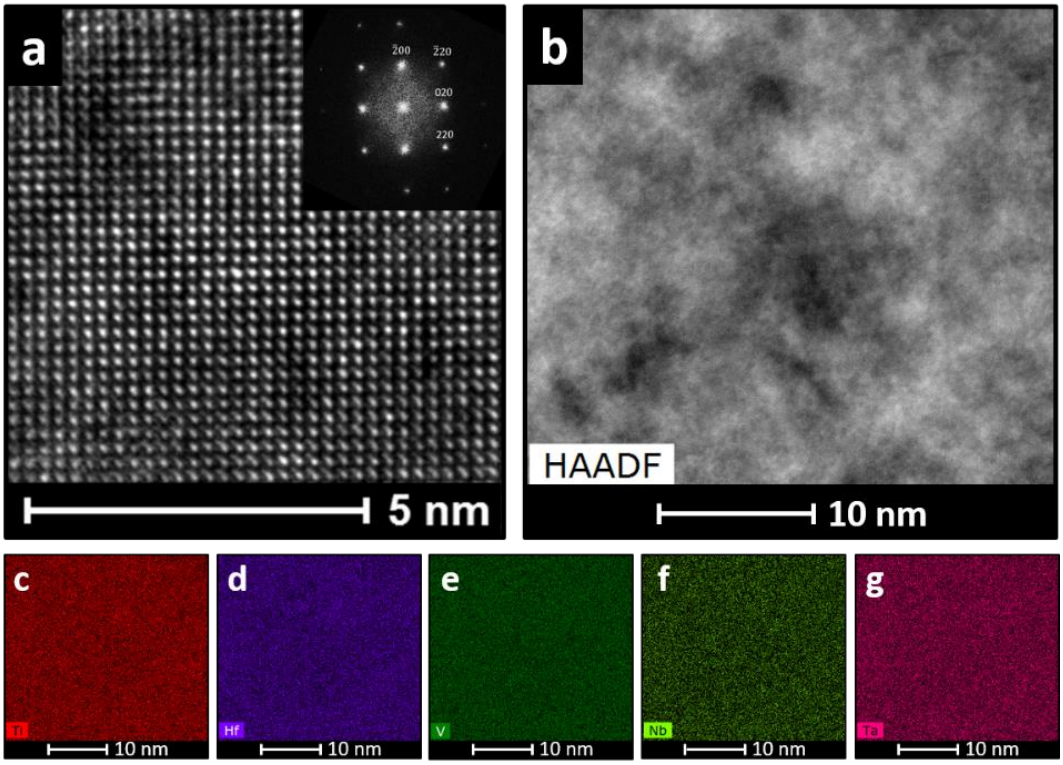

Figure 3.4: (a) TEM and inset selected area electron diffraction (SAED) pattern, (b) STEM high angle annular dark field (HAADF) image and corresponding selected compositional maps from EDS for a sample of composition $(Ti_{0.2}Hf_{0.2}V_{0.2}Nb_{0.2}Ta_{0.2})C$. The SAED pattern is free of any additional points from secondary phases or long-range ordering. The compositional maps for (c) Ti, (d) Hf, (e) V, (f) Nb, and (g) Ta each appear homogeneous on the nanoscale and show no signs of chemical clustering.

3.3.4 Determining Homogeneity – EXAFS

For entropy to be a significant contributing factor to the stability of the disordered phase, the structure must be an approximately ideally mixed and disordered, chemically homogeneous solid solution. To prove this, it must be demonstrated that only a single crystal structure exists, and that it is homogeneous on any length scale. XRD probes the d-spacing of crystals on a sample global scale, but in complex systems it offers little information about the local chemical distribution. EDS probes the chemical distribution, but it does so on a micrometer length scale when carried out in a SEM environment. S/TEM and STEM-EDS studies test the chemical

distribution on the angstrom length scale; however, only a very small amount of the sample can be studied, and therefore these results may not always be representative of the bulk sample. To determine the angstrom scale local environment of each element globally in the sample, EXAFS is the ideal characterization technique.

The results from an EXAFS study of composition $(V_{0.2}Nb_{0.2}Ta_{0.2}Mo_{0.2}W_{0.2})C$ are presented in Figure 3.5. The $k^2\ \chi(k)$ intensity for each of the V, Nb, and Mo absorbers looks very similar, indicating that each of the metals has similar local surroundings [16]. Results for W and Ta are not given due to the aforementioned issues with absorption edge overlap.

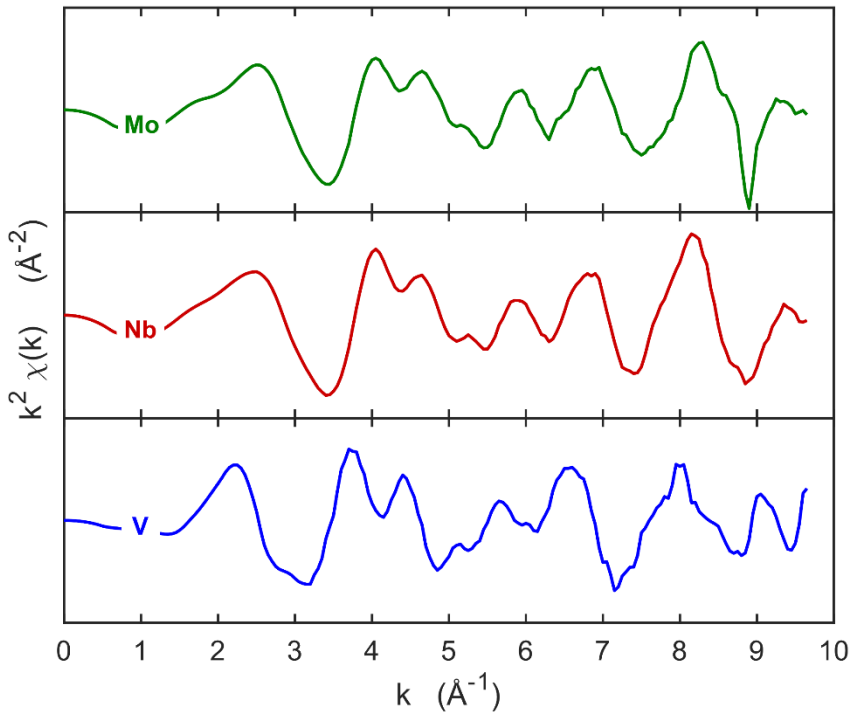

Figure 3.5: XAFS for three of the metal absorbers in a sample of $(V_{0.2}Nb_{0.2}Ta_{0.2}Mo_{0.2}W_{0.2})C$, measured at the Advanced Photon Source beamline 12-BM after energy normalization and fitting. The oscillations appear at similar reciprocal spacings and with similar intensity.

Given the complex nature of HECs, verification of the local structure from measured EXAFS data relies on fitting to a theoretical structure model [45]. For a theoretical model of a disordered material, the degeneracy of the scattering paths can be used to simulate the random occupancy. In the EXAFS of a rocksalt carbide, the first nearest neighbor shell of each metal is carbon with a coordination number of six, and the second nearest neighbor shell is another metal atom with a coordination number of 12. The scattering paths in EXAFS have a degeneracy, D equal to the coordination number of that atom, therefore for a rocksalt carbide the single scattering path of the absorber to a metal in the second nearest neighbor shell would have a degeneracy of 12. For example, if one were to simulate a V-edge absorber within a vanadium monocarbide lattice, two single-scattering paths would be considered – first the single scattering event from the vanadium absorber to the surrounding carbon atoms with a degeneracy of 6, then the single scattering path from the vanadium absorber to the second nearest neighbor vanadium with a degeneracy of 12. These two scattering paths would make up the majority of the signal for the first and second shells in the radial distribution function (RDF). By simulating a theoretical structure with the scattering path containing multiple different atoms and changing the degeneracy of each to fractions of the total degeneracy, partial occupancy can be represented. To do this, five separate single scattering paths from the vanadium absorber to the metal are added to the simulation. Geometrically they are all equivalent, however they assume that the metal atom is a different species. Each of the paths is weighted so that the total scattering path weight is D=12 (i.e. D_V=2, D_{Nb}=2.5, D_{Ta}=2.5, D_{Mo}=2.5, D_W=2.5). Each of the non-absorbing atoms are set to 2.5, while the absorber is set to 2 to simulate true mixing the absorber would be surrounded by atoms other than itself. This is carried out with the results shown in Figure 3.6, wherein the plots show the averaged experimental data from eight runs of the vanadium K-edge absorber in blue and the

attempted fits to theoretical data in red. The second nearest neighbor shell was simulated as each of the elements, and then the mixed degeneracy from all five elements. The theoretical data is only shown to match the experimental data well when the metal shell is mixed occupancy and demonstrates significant error when it is modeled as any single metallic species.

3.3.5 Mechanical Properties

The experimental elastic modulus and hardness results for five of the single- phase high entropy carbides are reported in Figure 3.7 against their valence electron concentration (VEC) and rule of mixtures (RoM) expected values (tabulated values can be found in Supplementary Table 1). All HECs show significant hardness enhancements of the RoM predicted values. The hardness of transition metal carbides, nitrides and carbonitrides with the B1 structure is maximized when the VEC is equal to 8.4 [46–48]. An approximately monotonic correlation can be seen between the hardness and modulus and the VEC in the range from 8.4 – 9.4. As the VEC increases, the hardness decreases and the elastic modulus increases. A Pearson (linear) correlation coefficient of $r = -0.75$ and a Spearman's (rank) correlation coefficient of $\rho = -0.85$ demonstrate a negative correlation between hardness and VEC. Conversely, a Pearson correlation coefficient of $r = 0.78$ and Spearman's coefficient of $\rho = 0.65$ for modulus and VEC demonstrates a positive correlation. Supplementary Figure 43 outlines a comparison of HECs in this study with the results of a comprehensive theoretical calculation from Ref. [48]. A comparison of strengthening and VEC is given in Supplementary Figure 44(a) where strengthening is defined as measured hardness minus the rule of mixtures predicted hardness. The results show that there is a correlation between the strengthening and the overall electronic structure of the final solid solution. Supplementary Figure

44(b) compares the strengthening to the carbon stoichiometry for four compositions, which demonstrates no noticeable relationship between the carbon content and the hardness increases.

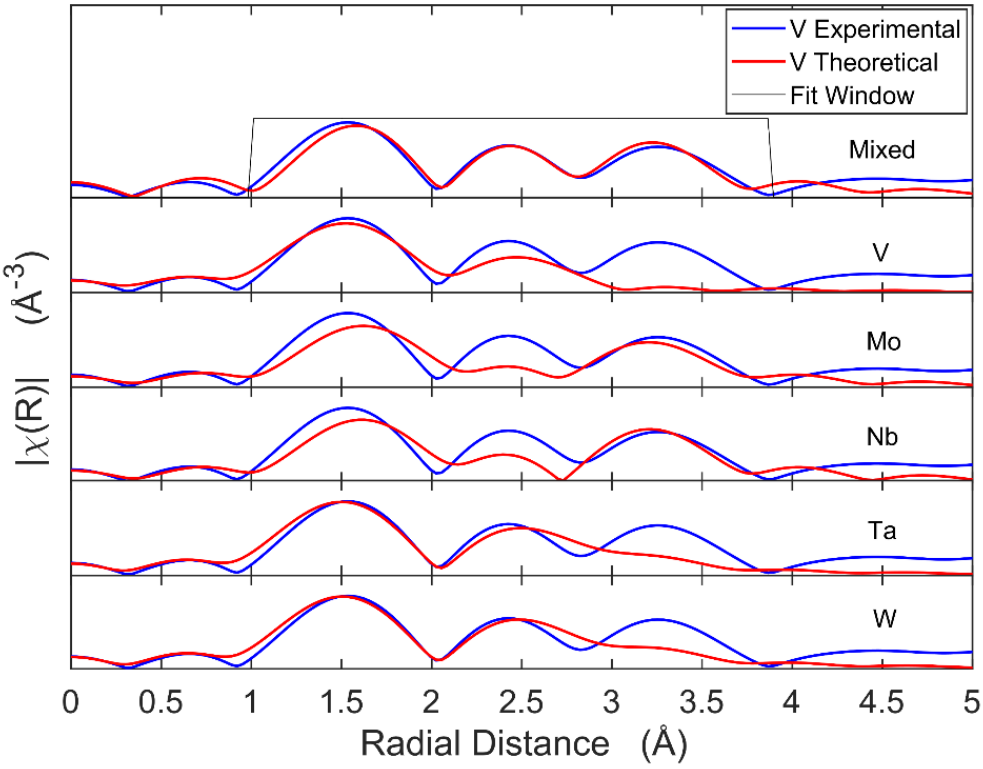

Figure 3.6: Pseudo-radial distribution function from EXAFS measurements made on a vanadium absorber in a sample of composition $(V_{0.2}Nb_{0.2}Ta_{0.2}Mo_{0.2}W_{0.2})C$. The second nearest neighbor shell has a coordination number of 12, and therefore a degeneracy of 12 for the single scattering path. The theoretical fits (red) are attempted for the experimental data (blue) assuming the second nearest neighbor is a single metal species (W, Ta, Nb, Mo, V, from bottom to top) and then when the scattering path is weighted to be a combination of the five different metal species (mixed), which simulates a random distribution of nearest neighbors in the metal lattice. Note that the theoretical model only fits the data when the metal lattice is modeled as mixed and randomly oriented.

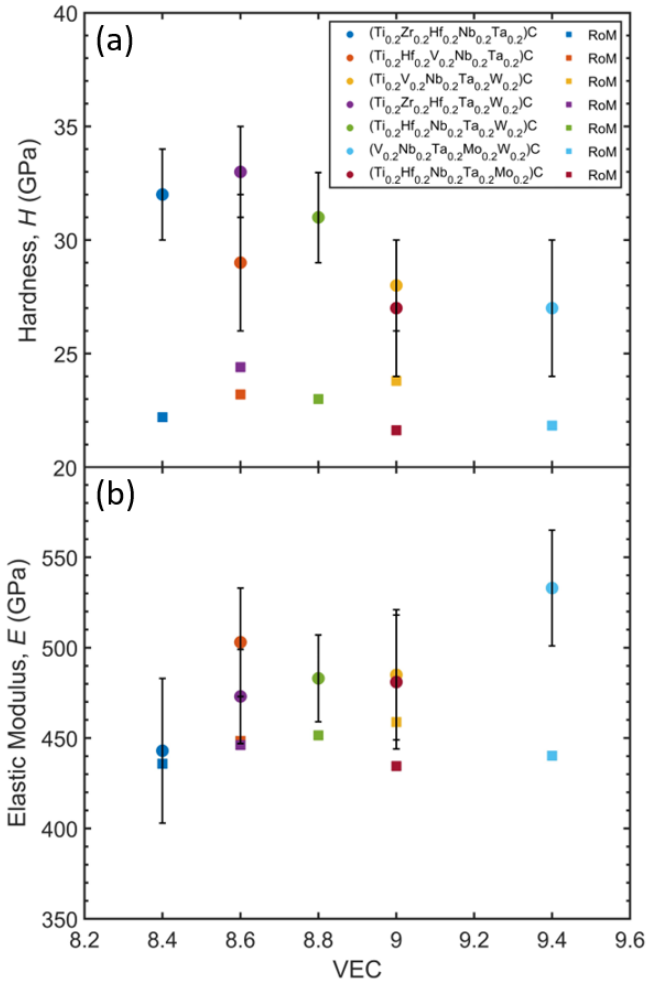

Figure 3.7: (a) Hardness and (b) elastic moduli (circle markers) from nanoindentation on seven high entropy carbide compositions along with rule of mixture (RoM) values (square markers) against valence electron concentration (VEC). RoM values were calculated from experimental data in the current study and theoretical and experimental treatments in Ref. [41–44] for MoC and WC. Error bars are one standard deviation from 100 indents per sample.

3.4 Discussion

3.4.1 Phase Formation

Given the list of compositions presented and the known solubilities of the group IVB, VB and VIB transition metal carbides, many of the compositions that exhibit single-phase materials are not surprising. It is well known that the group IVB and group VB carbides all exhibit extended mutual solid substitutional solubility [4]. It may be argued that mixing five B1 carbides that are all known to mix, amounts to no significant discovery when they are shown to do so. Hence, the compositions that contain only elements from group IVB and VB are likely enthalpically stable and are termed high entropy carbides, but not entropy stabilized carbides. However, the inclusion of the group VIB elements, which show limited solubility within the group IVB and VB metal carbides allows for a study of the effect of entropy in stabilizing the single phase. The EFA value for the composition $(V_{0.2}Nb_{0.2}Ta_{0.2}Mo_{0.2}W_{0.2})C$ is high indicating that the material should have a high entropic contribution and should easily form a single phase despite having both W and Mo. The inclusion of these two elements likely drives the system to instability on an enthalpic basis, so the formation of a single phase shows evidence for entropic stabilization. Experimental synthesis shows that $(V_{0.2}Nb_{0.2}Ta_{0.2}Mo_{0.2}W_{0.2})C$ does in fact easily form a random solid solution, providing evidence that the phase stability is a result of the high configurational entropy overcoming a positive enthalpy of formation, making this a true entropy stabilized material in the vein of the $(Co_{0.2}Cu_{0.2}Mg_{0.2}Ni_{0.2}Zn_{0.2})O$ oxide [16,45]. Further investigation of this composition is warranted and ongoing, including a so called "N-1" study, which involves removing a single element and determining if the four component systems maintain single phase stability, and calorimetry for determination of an endothermic phase transformation. As W and Mo are clearly the elements that drive up the enthalpy of formation of the rocksalt solid solution and destabilize

it, it can be argued that the precursors used (hexagonal W_2C and orthorhombic Mo_2C) are more stable than their rocksalt analogues, and therefore would not undergo a phase transformation. This is likely not the case when considering the phases present in the final multi-phase specimens. The secondary and ternary phases are not the original hex-W_2C and Mo_2C that are present in the precursor. In two cases there are only cubic phases present, however these are in addition to the desired single rocksalt phase. This suggests that the thermodynamic equilibrium of the system at 2473 K (sintering temperature) consists of multiple phases rather than simply the W_2C and Mo_2C precursors remaining as remnant phases. The phase stability in each composition containing Mo and W is determined by the ability of the positive configurational entropy overcoming the positive enthalpy of formation of the solid solution. In $(V_{0.2}Nb_{0.2}Ta_{0.2}Mo_{0.2}W_{0.2})C$ the contribution is significant enough to overcome the enthalpy at 2473 K, where in $(Zr_{0.2}Hf_{0.2}Ta_{0.2}Mo_{0.2}W_{0.2})C$, $(Ti_{0.2}Zr_{0.2}Hf_{0.2}Mo_{0.2}W_{0.2})C$, and $(Zr_{0.2}Hf_{0.2}V_{0.2}Mo_{0.2}W_{0.2})C$ it is not. The final carbon stoichiometry for four of the compositions in Supplementary Table 2 are all within the range of 0.85 and 0.95, which suggests that the carbon content is not heavily dependent on the initial carbon content of the precursors, but in a carbon rich sintering environment above 2273 K each of the compositions approaches an equilibrium stability.

3.4.2 Mechanical Properties

The hardness enhancement in high entropy carbides has been reported in the preliminary works by the present authors [30,32,49], Castle *et al.*, [28], and Yan *et al.*, [31]. Solid solution strengthening undoubtedly has an effect on the mechanical performance of the alloys, however certain alloys display significant enhancements over the rule of mixtures predicted values, which cannot be fully explained by traditional solid solution strengthening mechanisms (i.e. dislocation

inhibition by solute atoms). The complex nature of the d-orbital bonding in the transition metal nitrides and carbides is still not fundamentally well understood, which makes a true calculation of solid solution strengthening effects unattainable [50]. It has even been suggested in transition metal carbides and nitrides with the B1 structure, that the mechanical properties, such as hardness, depend more significantly on the nature of the bonding than on the microstructural features [3,46–48]. This implies that the hardness of the solid solution of five transition metal carbides will likely demonstrate dependence both on the mechanical properties of the individual constituents within the solid solution, and on the overall electronic structure of the final phase. Hence, a comparison of the hardness and modulus of each of the carbides to the VEC can reveal the contribution of the electronic mechanism behind the hardness enhancements. The results show agreement with the *ab initio* study in reference [48], that the hardness of carbides decreases as a function of VEC from 8.4 – 9.4. The modulus of the HECs is shown to increase with VEC, which is seemingly in contrast to what is normally reported, however the comparison to the modulus data (Supplementary Figure 43) shows that the modulus of the ternary nitrides and carbonitrides increases for most materials up to a maximum near VEC 9 then decreases to a VEC of 11. Further characterization of HECs with VEC greater than 9.4 (the maximum in this study) could determine whether the modulus begins to decrease. It has also been shown both experimentally and through theoretical investigations that the toughness of B1 structured transition metal carbides and nitrides increases with increasing VEC [51,52]. This is demonstrated in studies that explore the different deformation mechanisms that lead to the mechanical properties of HfC and TaC. HfC and TaC are similarly structured and bonded ceramics, yet TaC shows significant plasticity and dislocation formation and motion when deformed at room temperature, while HfC shows very little plasticity by comparison [53,54]. The work of De Leon *et al.* in reference [35] attributes this to the difference

in electronic structure that leads to an intrinsic stacking fault in TaC, which promotes dissociation of dislocations into partials on the {111} and causes the dominant slip system to be the a/2<110>{111}, while in HfC the a/2<110>{110} system is dominant. The work of Castle *et al*. [28] agrees that comparison of the hardness of four component solid solution carbides to the rule of mixtures average of the binary constituents is not warranted, as different electronic structures lead to different slip conditions. The experimental results across the five component compositions in this study reveal that the high entropy carbides do show a general trend of decreasing hardness and increasing modulus with increasing VEC, however there also exists significant deviations amongst multiple systems with the same VEC. For instance, the compositions $(Ti_{0.2}Hf_{0.2}V_{0.2}Nb_{0.2}Ta_{0.2})C$ and $(Ti_{0.2}Zr_{0.2}Hf_{0.2}Ta_{0.2}W_{0.2})C$ each have a VEC of 8.6, while their hardness values are 29 GPa and 33 GPa, respectively. This suggests that the deformation mechanisms and, therefore, mechanical properties are at least partially dependent on the electronic structure, but the VEC parameter may be an over-simplification of the electronic density of states, which depends on the structure and bonding characteristics of each of the constituent elements and carbon. Further, as also suggested by Castle *et al.,* traditional solid solution strengthening likely does have an effect on the overall hardness measured in high entropy carbides and an analysis of trends over a range of VECs as well as trends over a range of compositions with the same VEC can allow for isolation of hardness increases from solid solution effects and hardness increases from electronic effects. Although a clear model for solid solution strengthening is a difficult task in HECs, since they are all five-component, equiatomic solid solutions we can justify that they would all show similar strengthening over the rule of mixtures average of the binaries regardless of the electronic structure. When comparing strengthening to VEC (Supplementary Figure 5a), however, there is a clear relationship, which reinforces that there is more than just solid solution

strengthening effects and that different solutions exhibit different deformation mechanics that are dependent on the average electronic structure of the solid solution. Clearly, further work regarding the complete electronic density of states of each complex composition and its relationship to the deformation mechanisms is warranted and ongoing. The dependence of the mechanical properties on the electronic state of the material, however, gives a route to further tunability of mechanical properties of carbides and the exploration of the high entropy composition space gives access to a new library of electronic states that may be inaccessible via simply binary and ternary carbides.

3.5 Conclusion

This study explores phase formation in twelve different five-metal high entropy carbide ceramic compositions. Nine of the twelve compositions are determined to be single-phase solid solutions when sintered at 2473 K. We conclude that:

- These materials represent an exploration of a new composition space in ceramics that may lead to improved UHTCs.
- Addition of tungsten and molybdenum into systems with three group IVB or VB transition metals lowers the chance of forming a single phase, however systems can be synthesized that form a single phase with both Mo and W.
- The phase stability depends on a trade-off between enthalpy and entropy, and we find evidence for entropic stabilization (rather than simply high entropy) in the composition $(V_{0.2}Nb_{0.2}Ta_{0.2}Mo_{0.2}W_{0.2})C$, which warrants further investigation.
- Single-phase materials were homogeneous on multiple length scales from characterization in XRD, SEM-EDS, S/TEM-EDS, and EXAFS analysis.

- The high entropy transition metal carbides show significantly enhanced hardness over the weighted average of the binary constituents. Comparison to the average of the binary constituent carbides is ineffective in predicting hardness enhancements.
- The mechanical properties follow theories of electronic structure mechanisms in carbides and nitrides, and support trends of hardness decreasing with increasing valence electron concentration.
- Evidence shows that enhanced mechanical properties are not dependent on entropic stabilization and can be exploited as long as the material is randomly mixed (a true high entropy) material (i.e. they must be high entropy rather than just multicomponent, but do not necessarily need to be entropy stabilized). However, the discovery of entropically-stabilized phases may lead to enhanced properties previously unattainable at high temperatures.

Acknowledgements

The authors acknowledge support through the Office of Naval Research ONR-MURI (grant No. N00014-15-1-2863). This research used resources of the Advanced Photon Source, a U.S. Department of Energy (DOE) Office of Science User Facility operated for the DOE Office of Science by Argonne National Laboratory under Contract No. DE-AC02-06CH11357. K. Kaufmann was supported by the Department of Defense (DoD) through the National Defense Science & Engineering Graduate Fellowship (NDSEG) Program. K. Kaufmann would also like to acknowledge the generous support of the ARCS Foundation, San Diego Chapter. The authors thank APS BM-12B beamline scientist Dr. Benjamin Reinhart for aid in EXAFS data collection,

and Lavina Backman, Jeffrey Braun, Trent Borman, Dr. Jon-Paul Maria and Dr. Elizabeth Opila for guidance and helpful scientific discussion.

Part 3, in full, is a reprint of the material “Phase stability and mechanical properties of novel high entropy transition metal carbides” in *Acta Materialia*. Harrington, Tyler; Gild, Joshua; Sarker, Pranab; Toher, Cormac; Rost, Christina; Dippo, Olivia; McElfresh, Carmeron; Kaufmann, Kevin; Marin, Eduardo; Borowski, Lucas; Hopkins, Patrick; Luo, Jian; Curtarolo, Stefano; Brenner, Donald; Vecchio, Kenneth. The dissertation author was the primary investigator and author of this material.

References

[1] E. Wuchina, E. Opila, M. Opeka, W. Fahrenholtz, I. Talmy, UHTCs: ultra-high temperature ceramics for extreme environment applications, Electrochem. Soc. Interface. 16 (2007) 30.

[2] O. Cedillos-Barraza, D. Manara, K. Boboridis, T. Watkins, S. Grasso, D.D. Jayaseelan, R.J.M. Konings, M.J. Reece, W.E. Lee, Investigating the highest melting temperature materials: A laser melting study of the TaC-HfC system, Sci. Rep. 6 (2016) 37962. doi:10.1038/srep37962.

[3] L. Toth, Transition Metal Carbides and Nitrides., Elsevier Science, 1971.

[4] H.O. Pierson, Handbook of refractory carbides and nitrides : properties, characteristics, processing, and applications, Noyes Publications, 1996.

[5] B.S. Murty, High-entropy alloys, Butterworth-Heinemann, 2014.

[6] M.-H. Tsai, J.-W. Yeh, High-Entropy Alloys: A Critical Review, Mater. Res. Lett. 2 (2014) 107–123. doi:10.1080/21663831.2014.912690.

[7] D.B. Miracle, O.N. Senkov, A critical review of high entropy alloys and related concepts, Acta Mater. 122 (2017) 448–511. doi:10.1016/J.ACTAMAT.2016.08.081.

[8] D.B. Miracle, Critical Assessment 14: High entropy alloys and their development as structural materials, Mater. Sci. Technol. 31 (2015) 1142–1147. doi:10.1179/1743284714Y.0000000749.

[9] F. Otto, Y. Yang, H. Bei, E.P. George, Relative effects of enthalpy and entropy on the phase stability of equiatomic high-entropy alloys, Acta Mater. 61 (2013) 2628–2638. doi:10.1016/J.ACTAMAT.2013.01.042.

[10] Y. Zhang, T.T. Zuo, Z. Tang, M.C. Gao, K.A. Dahmen, P.K. Liaw, Z.P. Lu, Microstructures and properties of high-entropy alloys, Prog. Mater. Sci. 61 (2014) 1–93. doi:10.1016/J.PMATSCI.2013.10.001.

[11] É. Fazakas, V. Zadorozhnyy, L.K. Varga, A. Inoue, D.V. Louzguine-Luzgin, F. Tian, L. Vitos, Experimental and theoretical study of Ti20Zr20Hf20Nb20X20 (X=V or Cr) refractory high-entropy alloys, Int. J. Refract. Met. Hard Mater. 47 (2014) 131–138. doi:10.1016/j.ijrmhm.2014.07.009.

[12] O.N. Senkov, G.B. Wilks, D.B. Miracle, C.P. Chuang, P.K. Liaw, Refractory high-entropy alloys, Intermetallics. 18 (2010) 1758–1765. doi:10.1016/J.INTERMET.2010.05.014.

[13] A. Poulia, E. Georgatis, A. Lekatou, A.E. Karantzalis, Microstructure and wear behavior of a refractory high entropy alloy, Int. J. Refract. Met. Hard Mater. 57 (2016) 50–63. doi:10.1016/J.IJRMHM.2016.02.006.

[14] O.N. Senkov, G.B. Wilks, J.M. Scott, D.B. Miracle, Mechanical properties of Nb25Mo25Ta25W25 and V20Nb20Mo20Ta20W20 refractory high entropy alloys, Intermetallics. 19 (2011) 698–706. doi:10.1016/J.INTERMET.2011.01.004.

[15] J. Gild, M. Samiee, J.L. Braun, T. Harrington, H. Vega, P.E. Hopkins, K. Vecchio, J. Luo, High-entropy fluorite oxides, J. Eur. Ceram. Soc. 38 (2018) 3578–3584. doi:10.1016/J.JEURCERAMSOC.2018.04.010.

[16] C.M. Rost, E. Sachet, T. Borman, A. Moballegh, E.C. Dickey, D. Hou, J.L. Jones, S. Curtarolo, J.-P. Maria, Entropy-stabilized oxides, Nat. Commun. 6 (2015) 8485. doi:10.1038/ncomms9485.

[17] D. Bérardan, S. Franger, A.K. Meena, N. Dragoe, Room temperature lithium superionic conductivity in high entropy oxides, J. Mater. Chem. A. 4 (2016) 9536–9541. doi:10.1039/C6TA03249D.

[18] D. Bérardan, S. Franger, D. Dragoe, A.K. Meena, N. Dragoe, Colossal dielectric constant in high entropy oxides, Phys. Status Solidi - Rapid Res. Lett. 10 (2016) 328–333. doi:10.1002/pssr.201600043.

[19] D.B. Miracle, High-Entropy Alloys: A Current Evaluation of Founding Ideas and Core Effects and Exploring "Nonlinear Alloys," JOM. 69 (2017) 2130–2136. doi:10.1007/s11837-017-2527-z.

[20] J. Gild, Y. Zhang, T. Harrington, S. Jiang, T. Hu, M.C. Quinn, W.M. Mellor, N. Zhou, K. Vecchio, J. Luo, High-Entropy Metal Diborides: A New Class of High-Entropy Materials and a New Type of Ultrahigh Temperature Ceramics., Sci. Rep. 6 (2016) 37946. doi:10.1038/srep37946.

[21] C.-H. Lai, S.-J. Lin, J.-W. Yeh, S.-Y. Chang, Preparation and characterization of AlCrTaTiZr multi-element nitride coatings, Surf. Coatings Technol. 201 (2006) 3275–3280. doi:10.1016/j.surfcoat.2006.06.048.

[22] T.K. Chen, T.T. Shun, J.W. Yeh, M.S. Wong, Nanostructured nitride films of multi-element high-entropy alloys by reactive DC sputtering, Surf. Coatings Technol. 188–189 (2004) 193–200. doi:10.1016/j.surfcoat.2004.08.023.

[23] T.-T. Shun, Y.-C. Du, Age hardening of the Al0.3CoCrFeNiC0.1 high entropy alloy, J. Alloys Compd. 478 (2009) 269–272. doi:10.1016/j.jallcom.2008.12.014.

[24] H. Fager, J.M. Andersson, J. Jensen, J. Lu, L. Hultman, Thermal stability and mechanical properties of amorphous coatings in the Ti-B-Si-Al-N system grown by cathodic arc evaporation from TiB_2, $Ti_{33}Al_{67}$, and $Ti_{85}Si_{15}$ cathodes, J. Vac. Sci. Technol. A Vacuum, Surfaces, Film. 32 (2014) 061508. doi:10.1116/1.4897170.

[25] V.F. Gorban', A.A. Andreyev, G.N. Kartmazov, A.M. Chikryzhov, M. V. Karpets, A. V. Dolomanov, A.A. Ostroverkh, E. V. Kantsyr, Production and mechanical properties of high-entropic carbide based on the TiZrHfVNbTa multicomponent alloy, J. Superhard Mater. 39

(2017) 166–171. doi:10.3103/S1063457617030030.

[26] A. Vladescu, I. Titorencu, Y. Dekhtyar, V. Jinga, V. Pruna, M. Balaceanu, M. Dinu, I. Pana, V. Vendina, M. Braic, In Vitro Biocompatibility of Si Alloyed Multi-Principal Element Carbide Coatings, PLoS One. 11 (2016) e0161151. doi:10.1371/journal.pone.0161151.

[27] V. Braic, A. Vladescu, M. Balaceanu, C.R. Luculescu, M. Braic, Nanostructured multi-element (TiZrNbHfTa)N and (TiZrNbHfTa)C hard coatings, Surf. Coatings Technol. 211 (2012) 117–121. doi:10.1016/J.SURFCOAT.2011.09.033.

[28] E. Castle, T. Csanádi, S. Grasso, J. Dusza, M. Reece, Processing and Properties of High-Entropy Ultra-High Temperature Carbides, Sci. Rep. 8 (2018) 8609. doi:10.1038/s41598-018-26827-1.

[29] J. Dusza, P. Švec, V. Girman, R. Sedlák, E.G. Castle, T. Csanádi, A. Kovalčíková, M.J. Reece, Microstructure of (Hf-Ta-Zr-Nb)C high-entropy carbide at micro and nano/atomic level, J. Eur. Ceram. Soc. 38 (2018) 4303–4307. doi:10.1016/J.JEURCERAMSOC.2018.05.006.

[30] K. Vecchio, J. Luo, J. Gild, M. Samiee, O. Dippo, T. Harrington, S. Curtarolo, P. Sarker, C. Toher, Modelling and synthesis of high-entropy refractory carbides, nitrides and carbonitrides, Ultra-High Temp. Ceram. Mater. Extrem. Environ. Appl. IV. (2017). http://dc.engconfintl.org/uhtc_iv/32 (accessed July 5, 2018).

[31] X. Yan, L. Constantin, Y. Lu, J.-F. Silvain, M. Nastasi, B. Cui, ($Hf_{0.2}Zr_{0.2}Ta_{0.2}Nb_{0.2}Ti_{0.2}$)C high-entropy ceramics with low thermal conductivity, J. Am. Ceram. Soc. (2018). doi:10.1111/jace.15779.

[32] P. Sarker, T. Harrington, C. Toher, C. Oses, M. Samiee, J.-P. Maria, D.W. Brenner, K.S. Vecchio, S. Curtarolo, High-entropy high-hardness metal carbides discovered by entropy descriptors, Nat. Commun. 9 (2018) 4980. doi:10.1038/s41467-018-07160-7.

[33] K. Yang, C. Oses, S. Curtarolo, Modeling Off-Stoichiometry Materials with a High-Throughput Ab-Initio Approach, Chem. Mater. 28 (2016) 6484–6492. doi:10.1021/acs.chemmater.6b01449.

[34] S. Curtarolo, W. Setyawan, G.L.W. Hart, M. Jahnatek, R. V. Chepulskii, R.H. Taylor, S. Wang, J. Xue, K. Yang, O. Levy, M.J. Mehl, H.T. Stokes, D.O. Demchenko, D. Morgan, AFLOW: An automatic framework for high-throughput materials discovery, Comput. Mater. Sci. 58 (2012) 218–226. doi:10.1016/J.COMMATSCI.2012.02.005.

[35] G. Kresse, J. Furthmüller, Efficient iterative schemes for *ab initio* total-energy calculations using a plane-wave basis set, Phys. Rev. B. 54 (1996) 11169–11186. doi:10.1103/PhysRevB.54.11169.

[36] J.P. Perdew, K. Burke, M. Ernzerhof, Generalized Gradient Approximation Made Simple, Phys. Rev. Lett. 77 (1996) 3865–3868. doi:10.1103/PhysRevLett.77.3865.

[37] C.E. Calderon, J.J. Plata, C. Toher, C. Oses, O. Levy, M. Fornari, A. Natan, M.J. Mehl, G. Hart, M. Buongiorno Nardelli, S. Curtarolo, The AFLOW standard for high-throughput materials science calculations, Comput. Mater. Sci. 108 (2015) 233–238. doi:10.1016/J.COMMATSCI.2015.07.019.

[38] B. Ravel, M. Newville, ATHENA, ARTEMIS, HEPHAESTUS: data analysis for X-ray absorption spectroscopy using IFEFFIT, J. Synchrotron Radiat. 12 (2005) 537–541.

[39] A. Nino, A. Tanaka, S. Sugiyama, H. Taimatsu, Indentation Size Effect for the Hardness of Refractory Carbides, Mater. Trans. 51 (2010) 1621–1626. doi:10.2320/matertrans.M2010110.

[40] W.C. Oliver, G.M. Pharr, An improved technique for determining hardness and elastic modulus using load and displacement sensing indentation experiments, J. Mater. Res. 7 (1992) 1564–1583. doi:10.1557/JMR.1992.1564.

[41] Y. Liu, Y. Jiang, J. Feng, R. Zhou, Elasticity, electronic properties and hardness of MoC investigated by first principles calculations, Phys. B Condens. Matter. 419 (2013) 45–50. doi:10.1016/J.PHYSB.2013.03.016.

[42] D. V. Suetin, I.R. Shein, A.L. Ivanovskii, Elastic and electronic properties of hexagonal and cubic polymorphs of tungsten monocarbide WC and mononitride WN from first-principles calculations, Phys. Status Solidi. 245 (2008) 1590–1597. doi:10.1002/pssb.200844077.

[43] A.A. Voevodin, J.P. O'Neill, S. V. Prasad, J.S. Zabinski, Nanocrystalline WC and WC/a-C composite coatings produced from intersected plasma fluxes at low deposition temperatures, J. Vac. Sci. Technol. A Vacuum, Surfaces, Film. 17 (1999) 986. doi:10.1116/1.581674.

[44] Y. Pauleau, P. Gouy-Pailler, Characterization of tungsten-carbon layers deposited on stainless steel by reactive magnetron sputtering, J. Mater. Res. 7 (1992) 2070–2079. doi:10.1557/JMR.1992.2070.

[45] C. Rost, Entropy-Stabilized Oxides: Explorations of a Novel Class of Multicomponent Materials., Dissertation, (2016).

[46] S.-H. Jhi, J. Ihm, S.G. Louie, M.L. Cohen, Electronic mechanism of hardness enhancement in transition-metal carbonitrides, Nature. 399 (1999) 132–134. doi:10.1038/20148.

[47] V. Richter, A. Beger, J. Drobniewski, I. Endler, E. Wolf, Characterisation and wear behaviour of TiN- and TiCxN1-x-coated cermets, Mater. Sci. Eng. A. 209 (1996) 353–357. doi:10.1016/0921-5093(95)10109-8.

[48] K. Balasubramanian, S. V. Khare, D. Gall, Valence electron concentration as an indicator for mechanical properties in rocksalt structure nitrides, carbides and carbonitrides, Acta Mater. 152 (2018) 175–185. doi:10.1016/J.ACTAMAT.2018.04.033.

[49] P. Sarker, T. Harrington, C. Toher, C. Oses, M. Samiee, J.-P. Maria, D.W. Brenner, K.S.

Vecchio, S. Curtarolo, Novel high-entropy high-hardness metal carbides discovered by entropy descriptors, (2018).

[50] F. Gao, Hardness of cubic solid solutions, Sci. Rep. 7 (2017) 40276. doi:10.1038/srep40276.

[51] D.G. Sangiovanni, V. Chirita, L. Hultman, Electronic mechanism for toughness enhancement in Ti x M 1 − x N (M = Mo and W), Phys. Rev. B. 81 (2010) 104107. doi:10.1103/PhysRevB.81.104107.

[52] D.G. Sangiovanni, L. Hultman, V. Chirita, Supertoughening in B1 transition metal nitride alloys by increased valence electron concentration, Acta Mater. 59 (2011) 2121–2134. doi:10.1016/J.ACTAMAT.2010.12.013.

[53] N. De Leon, X. Yu, H. Yu, C.R. Weinberger, G.B. Thompson, Bonding Effects on the Slip Differences in the B 1 Monocarbides, Phys. Rev. Lett. 114 (2015) 165502. doi:10.1103/PhysRevLett.114.165502.

[54] S. Kiani, J.-M. Yang, S. Kodambaka, Nanomechanics of Refractory Transition-Metal Carbides: A Path to Discovering Plasticity in Hard Ceramics, J. Am. Ceram. Soc. 98 (2015) 2313–2323. doi:10.1111/jace.13686.

Part 4

Fermi level engineering of tunable and ultra-tough entropy stabilized carbides

Tyler J. Harrington,[1,2,†] Corey Oses,[3,†] Cormac Toher,[3] Joshua Gild,[2] William Mellor,[2] Kevin Kaufmann,[1] Andrew Wright,[2] Jian Luo,[1,2] Stefano Curtarolo,[4,*] Kenneth Vecchio[1,2,*]

[1]*Department of NanoEngineering, University of California San Diego, La Jolla, CA 92093, USA*
[2]*Materials Science and Engineering Program, University of California San Diego, La Jolla, CA 92093, USA*
[3]*Department of Mechanical Engineering and Materials Science, Duke University, Durham, NC 27708, USA*
[4]*Materials Science, Electrical Engineering, Physics and Chemistry, Duke University, Durham, NC 27708, USA*
† These authors contributed equally
** Corresponding author(s)*

ABSTRACT

Mechanical properties of a range of high entropy, rocksalt (B1) structured, carbide ceramics are investigated. The elastic constants, hardness, and fracture toughness of the high entropy carbides depend on the electronic structure, which is explained via the relationship with the valence electron concentration (VEC), electronic density of states at the Fermi level ($DOS(E_F)$), and the Fermi level to pseudo-gap energy difference ($|E_F-E_{pg}|$). The parameter $|E_F-E_{pg}|$ correlates best to the modeled and experimentally determined mechanical properties and is introduced as the parameter on which to base mechanical property tuning. As the high entropy carbides progress from low to high electron abundance, the Fermi level shifts further above the pseudo-gap leading to more overall metallic bonding character. The composition $MoNbTaVWC_5$

presents a VEC of 9.4 and a $|E_F-E_{pg}|$ of 2.36 eV, which are higher than is attainable via binary and ternary carbides that maintain the rockalt structure. Entropic stabilization allows $MoNbTaVWC_5$ to form a single-phase solid solution of the rocksalt structure through a large temperature range and, due to its high electron abundance, it demonstrates increased plasticity and a high fracture toughness.

4.1 Introduction

The B1 structured monocarbides of group IVB, VB, and VIB transition metals demonstrate high hardness and elastic modulus, good corrosion resistance, and some of the highest melting temperatures of any materials, making them good candidates for applications in future technologies such as reactor linings and hypersonic vehicle leading edges [1,2]. When designing for these extreme environment applications, the mechanical properties of the carbides is an important factor. In particular, the transition metal carbides (TMCs) demonstrate little to no plastic flow and lack any dislocation mechanism to dissipate stress, which leads to failure by brittle fracture [3]. It has been shown, however, that the TMCs have tailorable mechanical, thermomechanical, and thermophysical properties based on their electronic structure [1,4,5]. It can even be argued that, since the Peierls stresses are so high and the hardness depends on the movement of dislocations, the hardness may depend more on the difficulty of nucleating dislocations in the inherent lattice than on the difficulty of moving them through microstructural features [6,7]. This implies that the tunability of mechanical properties may be more successful through control of the bonding (i.e. electronic density of states (DOS)) via compositional control and alloying, than through traditional microstructural engineering (i.e. Hall-Petch or precipitate strengthening).

Most works have focused on compositional control of the carbon stoichiometry to tune the mechanical properties of individual binary carbides; however, some recent work has been done on alloy systems that include two or more transition metals [5,8]. The specific transition metal that forms the rocksalt structure with carbon is important in the determination of its final mechanical properties, as the different atomic species will result in unique bonding states. This is apparent in the variations in mechanical properties of HfC and TaC, which are both stable in the B1 structure and have similar bonding enthalpy (evidenced by their similar ultra-high melting temperatures), yet HfC is brittle, while TaC allows for significant plasticity via dislocations, when both are deformed at room temperature [9]. An increasing number of electrons in the system increases the overall metallic character of the bonds and allows for additional ductility. Additionally, the increase in valence electron concentration (VEC) from Hf to Ta leads to different active slip systems; the primary slip system in tantalum carbide is the $\{111\}\langle 110\rangle$, while in the rest of the rocksalt structured carbides the primary system is the $\{110\}\langle 1\bar{1}0\rangle$ [4,9,10]. The higher availability of slip systems, without thermal activation, allows for plasticity, which gives TaC the highest room temperature toughness of any of the rocksalt structured TMCs [11]. Recent *ab initio* work on these carbides, and some nitrides with the B1 structure, has elucidated that the deformation mechanisms (i.e. active slip planes) are dependent on the VEC; however, the VEC alone may be an oversimplification of the true electronic density of states [4–6,12–15]. TaC and NbC, for instance, have the same VEC, yet NbC does not demonstrate slip on the {111} at room temperature. De Leon *et al.* have demonstrated that TaC possesses an intrinsic stacking fault, which is what allows it access to the {111} and is a detail that is not captured by the simple VEC parameter. The work of Sangiovanni *et al*. [3,13,15] uses the VEC to predict the toughness enhancement of carbides and nitrides, finding that the ductility and, therefore, toughness increase with increasing VEC. The

ab initio work of Jhi *et al.* [6] demonstrated that the carbides possess the highest hardness at a VEC of 8.4, which is attributed to the complete filling of the *pd* σ bonding states between the metal $d_{x^2-y^2}$ orbitals and the carbon p_x and p_y orbitals, which are extremely resistive to shear. Once the electron population increases beyond a VEC of 8.4, metallic character increases, and the much more deformable metal t_{2g} derived states dominate the density of states. Since the nitrides are inherently more electron abundant than the carbides, investigations into increasing ductility and toughness usually involve the nitrides, as the binary monocarbides are only stable in the B1 configuration up to a VEC of 9.0. Thus, work in the carbides is typically focused on compositional control to engineer a VEC equal to 8.4 to maximize hardness [6].

To develop a better understanding than the VEC parameter can provide, Das *et al*. [16] compared the electronic density of states (DOS) of the transition metals carbides of Sc, Ti, V, Zr and Hf. Each of the TMCs demonstrates a characteristic bonding/anti-bonding structure with a pseudo-gap that arises from the dominating covalent-like bonding between the transition metal t_{2g} orbitals and the C p orbitals [16,17]. For the group IIIB metal (Sc) the Fermi energy lies below the pseudo-gap, while for the group IVB metals (Zr, Ti, Hf) the Fermi energy lies directly in the center of the pseudo-gap, and for the group VB metals (V) the Fermi energy lies above the pseudo-gap [16]. Das *et* al. [16] state that for TiC and ZrC, one may expect that they exhibit strong bonding because the E_F sits at the center of the pseudo-gap where the DOS is low and, in agreement, the TMCs of group IV metals demonstrate the highest hardness values [6,12]. In more complex alloy systems, through choice of alloying elements, the relationship between the pseudo-gap and the Fermi level can be tuned, allowing control over mechanical properties.

Theoretically, if a carbide can be synthesized that is stable in the rocksalt structure at room temperature and has a higher valence electron concentration than 9.0, it would exhibit significant

plasticity and an increased fracture toughness over the binary TMCs. Theoretical works into alloys of group VIB transition metals (i.e. W and Mo) with group VB TMCs have demonstrated that these materials should indeed demonstrate significantly enhanced plasticity [3]. However, experimentally, alloys of WC and MoC are only stable in the rocksalt structure at elevated temperatures, or in low concentrations of Mo and W at low temperatures. Recent work by the present authors [18,19] demonstrated the synthesis of high entropy carbides (HECs) that contain a high atomic fraction (10 at%) of both Mo and W and demonstrated, at the atomic scale, a single phase rocksalt structure. In particular, the synthesis of the equiatomic high entropy compound $MoNbTaVWC_5$ employs entropic stabilization, which allows for the material to exhibit a single, randomly ordered rocksalt phase and a VEC of 9.4.

Here we demonstrate the tunability of mechanical properties in high entropy carbides through control of composition, which determines electronic structure. We relate the elastic properties and hardness to the electronic structure through the VEC, the electronic density of states at the Fermi level ($DOS(E_F)$), and the pseudo-gap to Fermi level difference ($|E_F-E_{pg}|$). This theory allows for precise tunability of mechanical properties and, through entropic stabilization, the development of a highly stable HEC that demonstrates a higher fracture toughness than any of the binary TMCs.

4.2 Results

4.2.1 Modeling

The list of HEC compositions chosen in this work are given in Table 4.1 along with their calculated VEC, $|E_F-E_{pg}|$, and DOS(E_F). Compositions were chosen in order to provide a spread of HECs ranging from low to high electron population. The lowest valence electron density composition, consisting of three group IVB and two group VB transition metals is $HfNbTaTiZrC_5$, while the highest, comprising three group VB and two group VIB is $MoNbTaVWC_5$. The total spread of VEC ranges from 8.4 to 9.4. The full electronic density of states, from which DOS(E_F) and $|E_F-E_{pg}|$ were determined, for each of the carbide compositions are shown in Supplementary Figure 45. The electronic density of states for each of the HECs shows a pseudo-gap, which is characteristic of rocksalt structured transition metal carbides [16]. All of the compositions investigated have a Fermi level, E_F, greater than the pseudo-gap energy, E_{pg}.

Table 4.1: List of compositions and corresponding valence electron concentration (VEC), Fermi level pseudo-gap difference ($|E_F-E_{pg}|$), and electronic density of states at the Fermi level (DOS(E_F)) taken from density functional theory.

Composition	VEC	$\|E_F-E_{pg}\|$ (eV)	DOS(E_F) (states/eV)
$HfNbTaTiZrC_5$	8.4	1.122	2.88
$HfNbTaTiVC_5$	8.6	1.353	3.85
$HfTaTiWZrC_5$	8.6	1.425	3.06
$HfNbTaTiWC_5$	8.8	1.733	3.00
$NbTaTiVWC_5$	9	1.984	4.56
$MoNbTaVWC_5$	9.4	2.357	5.09

Figure 4.1a depicts the correlation between the VEC and the DOS(E_F), which does not show a strong correlation. Figure 4.1b shows the energy spread between the pseudo-gap and the Fermi level ($|E_F-E_{pg}|$) against the valence electron configuration for each of the compositions,

where a linear relationship is demonstrated. Due to the linear correlation, it can be determined that in the case of rocksalt structured high entropy carbides, the parameter $|E_F-E_{pg}|$ may function as a better descriptor of metallic character of bonding and, therefore, as a better parameter on which to base tuning of mechanical properties than $DOS(E_F)$.

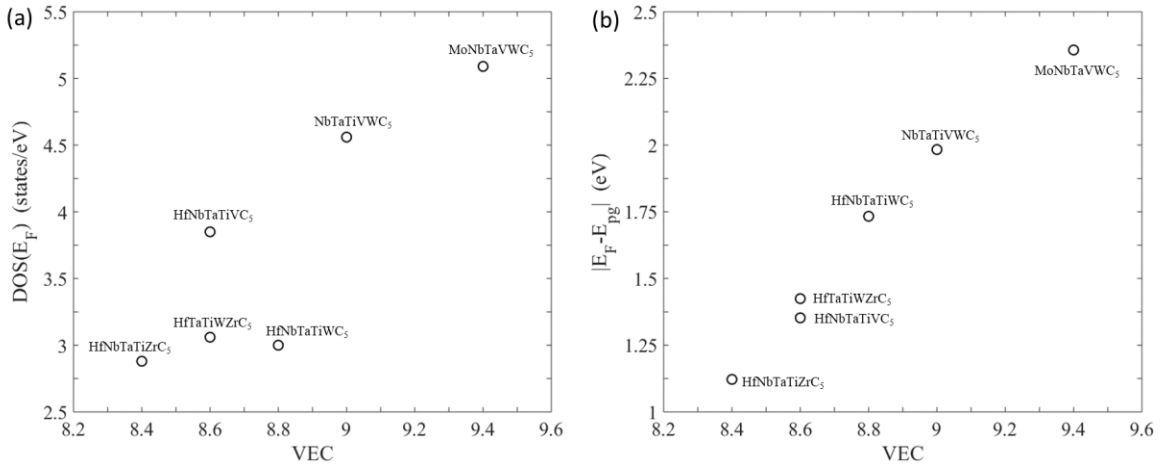

Figure 4.1: (a) The electronic density of states at the Fermi energy ($DOS(E_F)$) against the valence electron configuration (VEC) and **(b)** the energy gap between the Fermi energy and the pseudo-gap ($|E_F-E_{pg}|$) against the VEC for six solid solution high entropy carbides.

Figure 4.2 demonstrates the correlation between the VEC (a-c), $DOS(E_F)$ (d-f), and $|E_F-E_{pg}|$ (g-i) parameters and the predicted elastic properties. The VEC parameter demonstrates a strong positive correlation with bulk modulus (Figure 4.2a) with a Pearson correlation coefficient of 0.96. The Fermi-pseudo-gap parameter, $|E_F-E_{pg}|$, and B also demonstrate a positive correlation with a Pearson coefficient of 0.98. The $DOS(E_F)$ does not, however, demonstrate as strong of a correlation to the predicted bulk modulus with a Pearson coefficient of 0.835, again enforcing that the $DOS(E_F)$ is not the most suitable parameter on which to base the tuning of elastic properties. For both increasing VEC and increasing $|E_F-E_{pg}|$, the shear and bulk moduli demonstrate a trend of first increasing and then steadily decreasing, in agreement with previous theoretical work on

binary carbides and nitrides [12] and previous results in high entropy carbides [18]. The maximum for shear modulus is near a VEC of 9 or $|E_F-E_{pg}|$ equal to ~1.7, which is the maximum attainable for any stable rocksalt binary carbide.

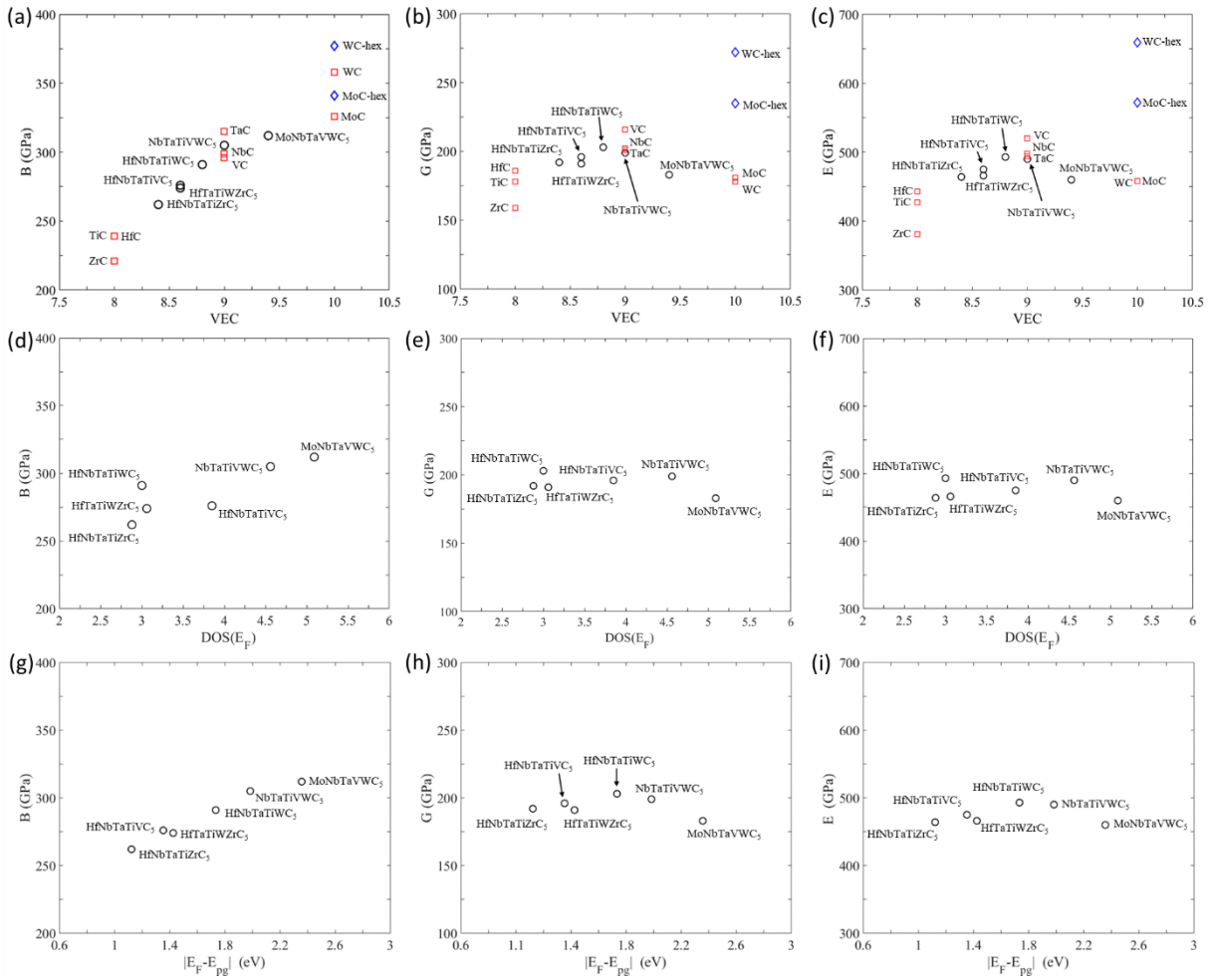

Figure 4.2: (a-c) Bulk (B), shear (G), and elastic (E) modulus against valence electron concentration (VEC) for each of the high entropy carbides (HECs) and binary carbides, **(d-f)** bulk (B), shear (G), and elastic (E) modulus against the electronic density of states at the Fermi energy ($DOS(E_F)$) for each of the HEC compositions, and **(g-i)** bulk (B), shear (G), and elastic (E) modulus against the energy difference from the minimum point of the pseudo-gap and the Fermi energy ($|E_F-E_{pg}|$).

In order to predict the ductility of any material composition, the simple formulation of Pugh [20] can be applied, where the plastic properties of metals are linked to their elastic moduli [3,12,21]. If the ratio of shear modulus to bulk modulus is less than 0.5 ($G/B < 0.5$), the material will behave in a ductile manner, otherwise in a brittle manner [20,21]. Thus, theoretical prediction of the relationship of the moduli and a relevant electronic parameter can help to predict the formation of a ductile material based on compositional control of alloying elements. Figure 4.3a shows the relationship between Pugh's modulus ratio (G/B) and the parameter $|E_F-E_{pg}|$. The Pearson (linear) correlation coefficient between G/B and $|E_F-E_{pg}|$ is -0.96, demonstrating a strong negative correlation. Thus, as the elements used in alloying HECs move the overall configuration to a more valence electron rich region, the ductility of the alloy increases. The composition $MoNbTaVWC_5$ demonstrates the lowest predicted Pugh's modulus ratio of 0.587 and should therefore demonstrate the highest ability to deform plastically under an applied stress and lead to an increased fracture toughness over any of the binary carbides. Since G/B is not less than 0.5, $MoNbTaVWC_5$ is not expected to behave as a ductile material, but should accommodate an increased amount of plasticity that, in a brittle material, should still manifest on the macroscale as an increase in toughness. A second method of determining ductility from predicted elastic parameters is the formulation of Pettifor [22] developed for intermetallic systems, in which the angular character of bonding can be used to determine mechanical properties. Since Cauchy pressure is defined as $C_{12} - C_{44}$ (where C_{12} and C_{44} are components of the stiffness tensor), if the bonding is simple pair-wise potentials, then the Cauchy pressure will be zero [23]. If the Cauchy pressure is negative, then the bonding is more angular and the orbitals will resist deformation in response to stress (i.e. brittle) [22]. If the bonding is more metallic, where each atom is more spherical and overlapping into the free electron sea of the surrounding system, then the Cauchy

pressure will be positive. Thus, a positive Cauchy pressure denotes a more metallic and, therefore, more ductile material. Figure 4.3b shows the Cauchy pressure ($C_{12} - C_{44}$) against the $|E_F\text{-}E_{pg}|$ parameter. The Cauchy pressure increases with increasing $|E_F\text{-}E_{pg}|$ with a Pearson (linear) correlation coefficient of 0.92 indicating a positive linear correlation. As with the Pugh's modulus ratio trend, the Cauchy pressure shows a more drastic rate of increase following $|E_F\text{-}E_{pg}|$ of ~1.7. These trends suggest that with the use of entropic stabilization, which allows for stable rocksalt structured compositions containing group VIB metals, even more significant enhancements in ductility can be achieved than when moving from group IVB to VB binary carbides.

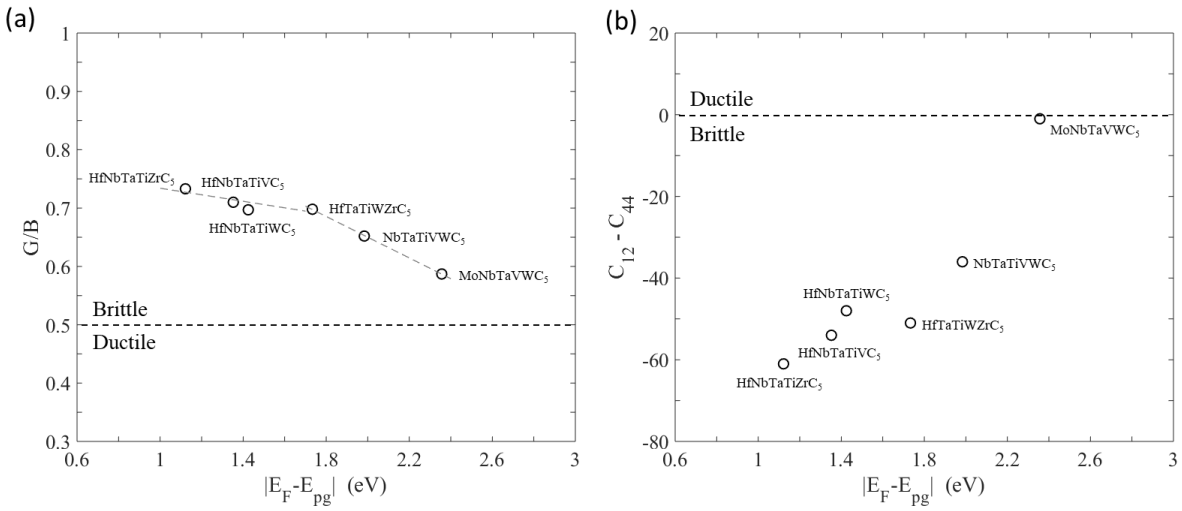

Figure 4.3: (a) The relationship between predicted Pugh's modulus ratio (G/B) and $|E_F\text{-}E_{pg}|$ and **(b)** the relationship between Cauchy pressure (C_{12}-C_{44}) and $|E_F\text{-}E_{pg}|$ for each of the six HEC compositions of interest demonstrating the trend towards the ductile regions with increasing electronic population.

Figure 4.4 presents a plot of Pugh's modulus ratio against Cauchy pressure, which is common in determination of material ductility [3]. Here the most ductile materials should fall in the furthest bottom right corner of the plot and the composition $MoNbTaVWC_5$ is again the closest to that region with a Cauchy pressure of -1, which is almost in satisfaction of ductility parameters put forth by Pettifor [22]. Supplementary Figure 46 shows the calculated Pugh's modulus ratio

(2a) and the Cauchy pressure (2b) against the VEC of the HECs along with the rocksalt structured binary carbides of group IVB, and VB transition metals, and rocksalt structured and hexagonal structured binary carbides of group VIB transition metals. Note that WC and MoC in the rocksalt structure fall well into the ductile region for both ductility criterion, however the hexagonal structures for both WC and MoC fall well within the brittle region. Since these binaries are only stable as rocksalts at high temperatures [2], the most ductile material, even when considering all of the rocksalt binaries, should be the high entropy composition $MoNbTaVWC_5$.

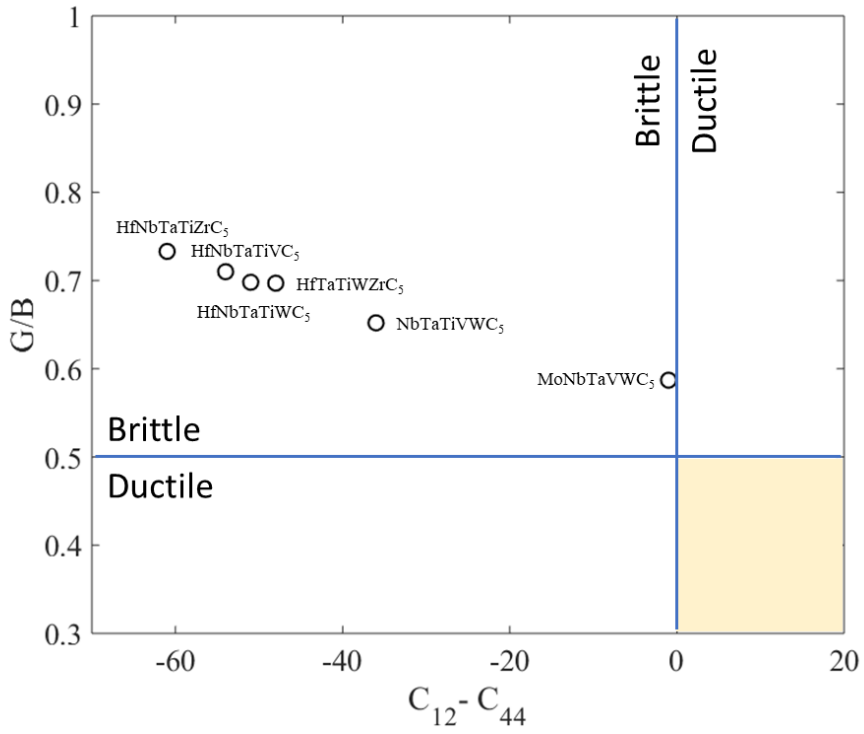

Figure 4.4: Calculated Pugh's modulus ratio and Cauchy pressure for each of the six HEC compositions. A ductile material would have a Pugh's modulus ratio below 0.5 and a positive Cauchy pressure, indicated by the shaded region in the bottom right corner of the plot.

4.2.2 Experimental Mechanical Properties

For experimental verification of predicted properties, each of the high entropy carbides was synthesized in bulk form. Figure 4.5 shows the trend of experimentally measured bulk moduli (3.5a), shear moduli (3.5b), elastic moduli (3.5c), and Pugh's modulus ratios (3.5d) against the $|E_F-E_{pg}|$ parameter. The moduli are in good agreement with the predicted values from DFT and demonstrate the expected relationships with increasing $|E_F-E_{pg}|$. All of the experimentally measured moduli from experiments show slight negative deviations from predicted values, which is likely due to sample imperfections such as porosity, impurities, and oxide inclusions. Since Pugh's ductility criteria is a modulus ratio and the imperfections in the experimental samples lead to low measurements for both bulk and shear moduli, the experimental measurements of Pugh's modulus ratios are less affected by the imperfections and agree well with predicted values despite the low measurements for each of the individual moduli. By Pugh's criteria, the most ductile HEC should be the highest $|E_F-E_{pg}|$ composition - $MoNbTaVWC_5$.

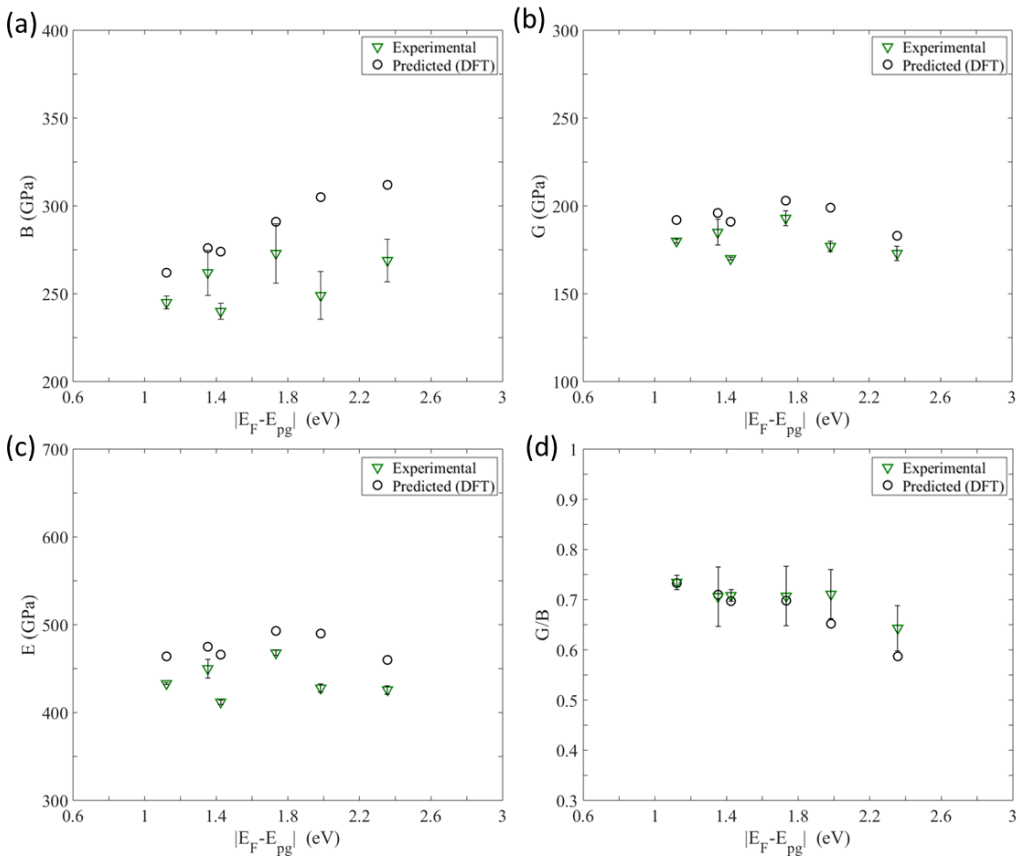

Figure 4.5: Predicted and experimental **(a)** bulk moduli, **(b)** shear moduli, **(c)** elastic moduli, and **(d)** Pugh's modulus ratios for each of the HEC compositions. Individual composition labels are left off for clarity in showing trends, however the compositions are, from left to right: $HfNbTaTiZrC_5$, $HfNbTaTiVC_5$, $HfNbTaTiWC_5$, $HfTaTiWZrC_5$, $NbTaTiVWC_5$, and $MoNbTaVWC_5$.

In order to design a high toughness material, the ideal composition would demonstrate both high hardness and ductility. The experimental and calculated Vickers hardness for each of the high entropy carbide compositions are shown in Figure 4.6. Each of the measured hardness values are lower than that calculated from DFT, which, as with the moduli, is likely due to imperfections in the experimental samples. The hardness displays the expected trend of decreasing with increasing $|E_F\text{-}E_{pg}|$, indicating softening of the materials as they increase in electron abundance and metallic character. However, the hardness of the most ductile, entropy stabilized composition – $MoNbTaVWC_5$, remains at the relatively high value of 19.2 GPa ± 1.4 GPa. The high hardness

obtained in HECs coupled with the increase in plasticity should allow for the electron rich compositions to comprise high toughness materials.

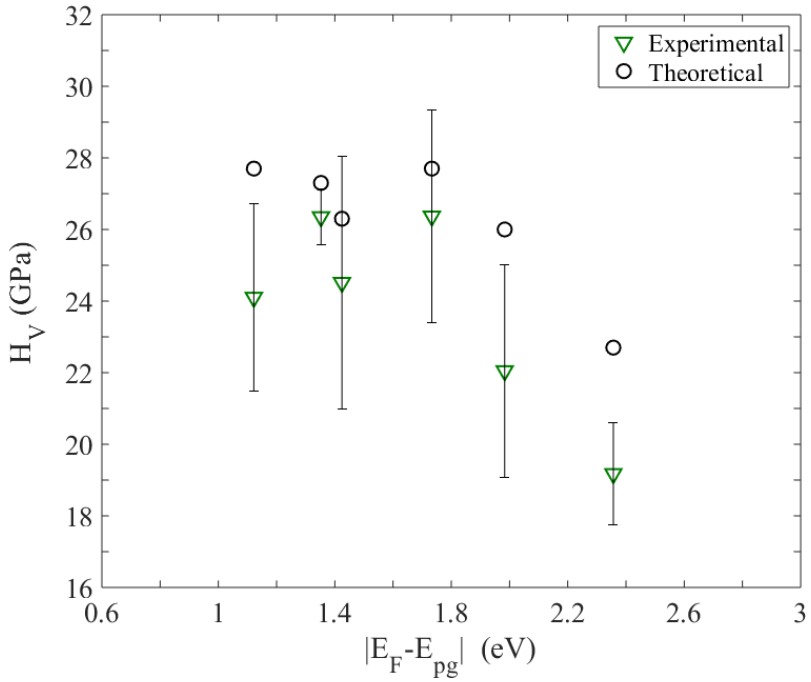

Figure 4.6: Calculated and experimental Vickers hardness, H_V, of each of the six high entropy carbides. Individual composition labels are left off for clarity in showing trends, however the compositions are, from left to right: $HfNbTaTiZrC_5$, $HfNbTaTiVC_5$, $HfNbTaTiWC_5$, $HfTaTiWZrC_5$, $NbTaTiVWC_5$, and $MoNbTaVWC_5$. Reported errors are ± 1 standard deviation from measurements on a minimum of 10 indents.

Since the main goal of designing high entropy carbides that can exhibit significant plasticity is to increase toughness, the indentation fracture toughness, K_{ifr}, of each of the compositions is given against $|E_F-E_{pg}|$ in Figure 4.7. The expected trend is seen where the HECs demonstrate an increase in fracture toughness with increasing $|E_F-E_{pg}|$, indicating that the use of group VIB elements in a high atomic fraction in HECs can effectively increase the metallic character of the bonding in the system and lead to increased ductility and fracture toughness.

Further, the trend shows a much more drastic rate of increase as the metallic character increases beyond $|E_F-E_{pg}|$ of ~1.7 (VEC = 9).

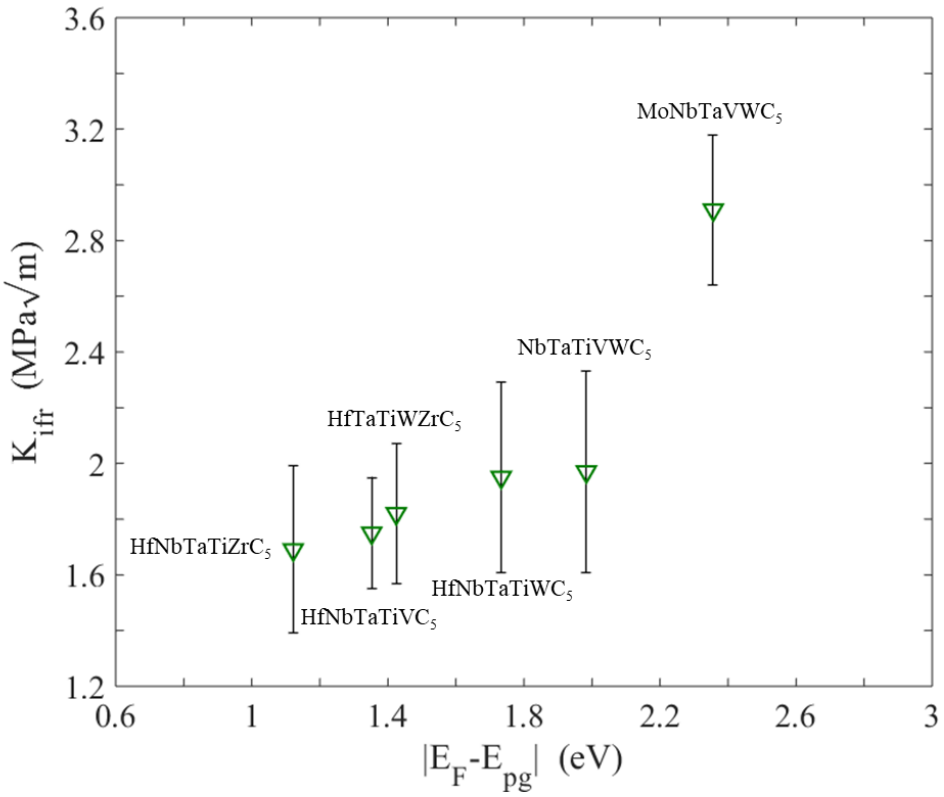

Figure 4.7: Experimental indentation fracture toughness, K_{ifr}, of each of the six high entropy carbide compositions against the $|E_F-E_{pg}|$ electronic parameter. Reported errors are ± 1 standard deviation from measurements on a minimum of 10 indents that satisfy the conditions for fracture toughness outlined in the Methods (section 4.5.6).

To determine whether the carbides are in fact deforming by plasticity (i.e. dislocations), Figure 4.8 presents transmission SEM (t-SEM) (4.8a) bright field and (4.8b) high angle annular dark field images and (4.8c and d) transmission Kikuchi diffraction (TKD) of a cross section of a deformation region below an indent made in a sample of $HfNbTaTiZrC_5$. A plastic strain field consisting of extensive dislocation networks is apparent in t-SEM imaging. The orientation map in Figure 4.8d shows significant orientation change, indicating a large change in the crystal rotation tensor and, therefore, an accommodating geometrically necessary dislocation density. The

decrease in band contrast surrounding the indent edges is expected and indicative of large plastic strain in the lattice, which reduces symmetry within the diffracting area and, as a result, decreases the pattern quality and band contrast of the Kikuchi patterns.

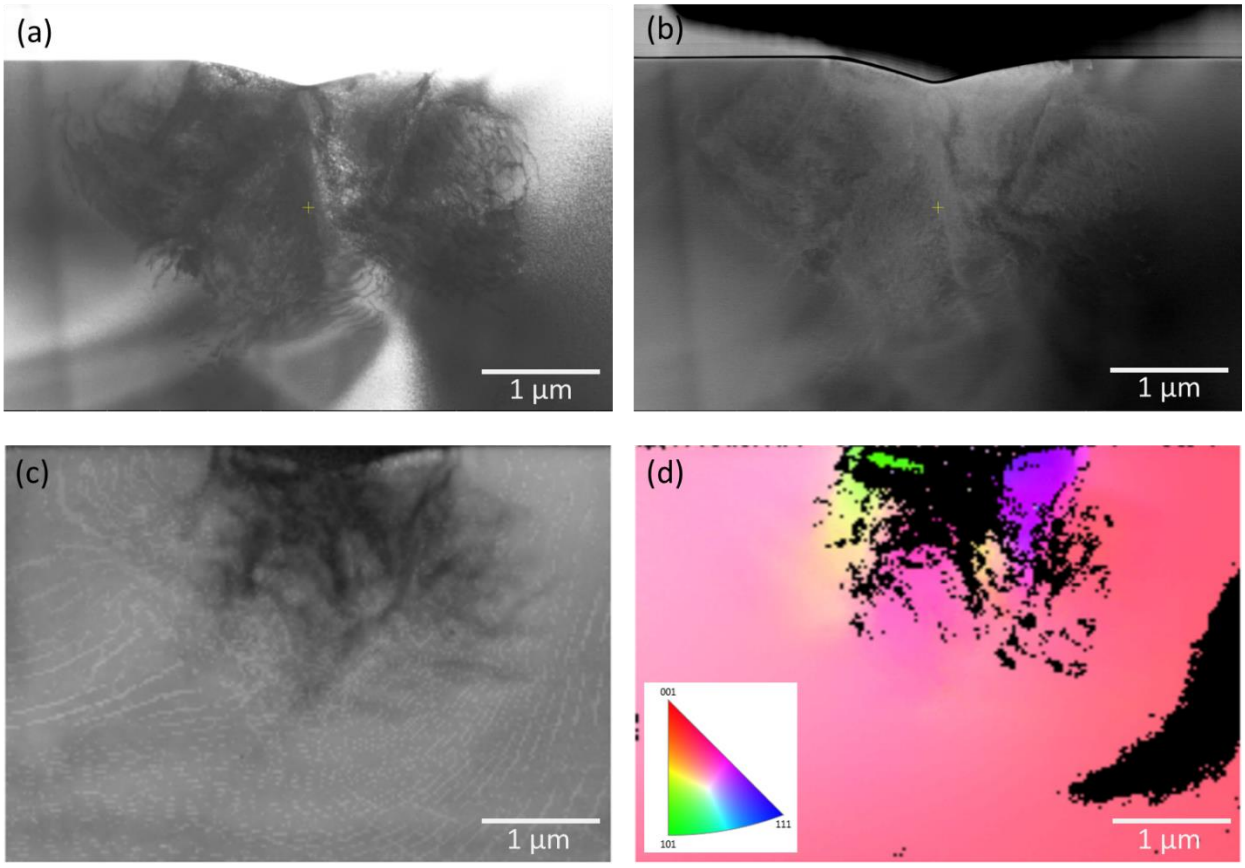

Figure 4.8: Transmission SEM (t-SEM) bright field **(a)**, high angle annular dark field **(b)** images of a cross section of an indent made in a sample of $HfNbTaTiZrC_5$ using a Berkovich indenter and 150 mN force and the corresponding band contrast map **(c)** and y-direction inverse pole figure map **(d)**. The y-direction corresponds to the surface normal loading direction in indentation.

4.3 Discussion

4.3.1 Modeling

The increase in the parameter $|E_F-E_{pg}|$ directly shows the movement of E_F to higher energies as the transition metal d-states are filled with more electrons. Specifically, the octahedral t_{2g}-derived bonding states of the metals contribute more to the overall density of states, indicating a more metallic bonding character [16]. Thus, the $|E_f-E_{pg}|$ parameter suffices as a simple descriptor of metallic character in rocksalt carbides and can be used to predict and tune mechanical properties. Theoretically, since Pugh's ductility criterion depends on decreasing G/B, a high bulk modulus and low shear modulus are desirable to maximize ductility. The bulk modulus increases linearly with increasing $|E_F-E_{pg}|$ whereas the shear modulus increases up to a $|E_F-E_{pg}| = 1.7$ (VEC=9.0) and then begins to decrease. The increase in plasticity in binary carbides with increasing VEC up to 9.0 is dependent on the increase in bulk modulus, rather than a decrease in shear modulus, as shear modulus also increases up to a VEC of 9.0. If we can move further than group VB transition metals, however, the shear modulus begins to decrease, indicating that G/B will decrease even faster than when considering the low VEC materials because both an increasing B and decreasing G can be exploited rather than just B increasing at a faster rate than G. This is demonstrated in Figure 3.3, where G/B is fitted linearly before and after a VEC of 9 ($|E_F-E_{pg}| = 1.7$) and is clearly shown to decrease at a higher rate after 1.7. The Cauchy pressure also demonstrates a strong trend of increasing with increasing $|E_F-E_{pg}|$, denoting that the carbides should become more metallic in nature with increasing electron abundance. The decrease in angular bonding in the system and increase in metallic character should be accompanied by an increase in plasticity and toughness. Since, as previously discussed, the Fermi level engineering parameter $|E_F-E_{pg}|$ can be used to determine mechanical properties of carbides, a new route to development of ultra-tough materials

is presented here. The use of entropic stabilization and the development of single-phase high entropy carbides gives access to a vast new composition space and a resulting new library of electronic density of states that can be searched for parameters such as $|E_F-E_{pg}|$ in order to find compositions with desirable properties such as hardness and ductility.

4.3.2 Mechanical Properties

It has been well established that the binary carbides demonstrate more significant plasticity as the number of valence electrons in the system increases beyond 8.4, however the synthesis of carbides that are more electron rich than TaC remains difficult as they are then more stable in a hexagonal or orthorhombic structure. Here, through entropic stabilization, we can stabilize a composition that contains 20 at% each of WC and MoC (10 at% Mo, 10 at% W), which allows for a VEC of 9.4 to be attained. The randomly ordered solid solution is entropy stabilized and therefore, demonstrates a single phase through a large temperature range from <700°C to T_m [Supplementary Figure 47]. The compositions with the highest metallic character via VEC and $|E_F-E_{pg}|$ parameters demonstrate the lowest hardness and highest fracture toughness of any of the compositions. This theory lays the groundwork for the use of alloying in high entropy carbides to produce ultra-tough rocksalt structured carbide, nitride, and carbonitride materials, that were previously unattainable. The entropically stabilized materials realm gives access to a new library of electronic density of states of materials, which can be mined for parameters such as $|E_F-E_{pg}|$, in the case of carbides, to result in desirable mechanical properties.

4.4 Conclusion

High entropy carbides are shown to increase in ductility with increasing VEC and $|EF-E_{pg}|$. Analogous to what is done in semiconductors, Fermi-level engineering via adjusting the $|E_F-E_{pg}|$ parameter through element choice is determined to be an effective method for predicting and tuning the metallic character of bonding and resultant mechanical properties in high entropy carbides. The composition $MoNbTaVWC_5$ employs entropic stabilization and Fermi-level engineering to allow for a single-phase rocksalt structured high entropy carbide that demonstrates a higher electron abundance and high toughness.

4.5 Methods

4.5.1 AFLOW of High Entropy Crystals

The different possible configurations required to calculate the energy spectrum are generated using the AFLOW-POCC algorithm [24] implemented within the AFLOW computational materials design framework. The algorithm initially generates a superlattice of the minimum size necessary to obtain the required partial occupancies within some user-specified accuracy. For each unique superlattice, the AFLOW-POCC algorithm then generates the complete set of possible supercells using Hermite normal form matrices. Non-unique supercell combinations are eliminated from the ensemble by first estimating the total energies of all configurations using a Universal Force Field [25] based method, and then identifying duplicates from their identical energies.

For structure generation in the case of the high-entropy carbide systems investigated here, the AFLOW-POCC algorithm starts with the rock-salt crystal structure (spacegroup: Fm3m, #225;

Pearson symbol: cF8; AFLOW Prototype: AB_cF8_225_a_b) as the input parent lattice. Each anion site is occupied with a C atom (occupancy probability of 1.0), while the cation site is occupied by 5 different refractory metal elements, with a 0.2 occupancy probability for each. The AFLOW-POCC algorithm then generates a set of configurations (49 in total in the case of the rock-salt based 5-metal carbide systems, once structural duplicates are excluded), each containing 10 atoms: one atom of each of the metals, along with 5 carbon atoms. This is the minimum cell size necessary to accurately reproduce the required stoichiometry.

From each high entropy carbides, for calculation of $|E_F-E_{pg}|$ from the total electronic density of states, E_F is the Fermi level and E_{pg} is taken as the energy of the minimum value of the total density of states in states/eV above the band gap.

4.5.2 Calculating Elastic Constants

Elastic properties, including the elastic constants and moduli, are calculated using the Automatic Elasticity Library (AEL) module [26] of the AFLOW framework, which applies a set of independent directional normal and shear strains to the structure, and fits the resulting stress tensors to obtain the elastic constants. From this, the bulk: B, and shear: G, moduli are calculated in the Voigt, Reuss, and Voigt-Reuss-Hill (VRH) approximations, with the VRH average being used for the purposes of this work.

The elastic properties for the 5-metal compositions are first calculated for each of the 49 configurations generated by AFLOW-POCC. The average elastic constants moduli are then obtained and weighted according to the Boltzmann distribution at a temperature of 2200°C (2473 K, the experimental sintering temperature).

Ductility is modeled using the Pugh's modulus ratio: k = G/B; and the Cauchy pressure: C_{12} - C_{44}. Three different models are used for predicting the Vickers hardness based on the elastic moduli:

Chen *et al.* $\left(H_v = 2(k^2G)^{0.585} - 3 \text{ where } k = \frac{G}{B}\right)$ [27],

Teter $(H_V = 0.151G)$ [28], and

Tian *et al.* $(H_V = 0.92k^{1.137}G^{0.708})$ [29].

Note, however, that these models are based on the elastic response of the materials, and do not take into account phenomena such as plastic deformation, slip planes, and lattice defects.

4.5.3 Experimental Synthesis

Each of the carbide compositions is weighed out in 24 g batches using binary carbide powders (TiC, ZrC, HfC, VC, NbC, TaC, Mo_2C, WC, C; Alfa Aesar, USA). Powders are hand mixed and high energy ball milled in a shaker pot ball mill for a total of 2 hours in 30-minute increments intersected by 10-minute rests to avoid overheating. Samples are sintered using current and pressure assisted densification (CAPAD) in a vacuum environment. The temperature and pressure profile for each sample is as follows: heat to 2200°C at 100°C/min under 5 MPa uniaxial load; hold for 9 minutes; increase load to 80 MPa at 75 MPa/min while at 2200°C; hold for 15 minutes; cool under ambient conditions. The initial vacuum is less than 20 mtorr prior to heating. Whenever the vacuum exceeds 100 mtorr the heating and pressure profile is held until the vacuum again reaches less than 20 mtorr. All sintering is done in graphite die and plunger sets. Each sample is ground and polished to 0.04 um colloidal silica on both sides to remove any remaining carbon.

4.5.4 Experimental Elastic Constants from Acoustic Wave Speed

All moduli are obtained following ASTM standard E494-15. Sample dimensions are on average 20 mm diameter and 3 mm in height cylindrical pucks. Both sides of samples are ground and polished, and then placed on an acoustically isolated substrate to ensure no interference from the local surroundings. Using a piezoelectric transducer coupled with an oscilloscope, the reverberating sound waves are measured and recorded. For each sample, a total of four longitudinal and four shear waves at different intervals are recorded in order to calculate the respective velocities. After determination of the velocities, Poisson's ratio: ν, Young's modulus: E, shear modulus: G, and bulk modulus: B are determined using equations 8 – 11 below.

$$\nu = \frac{V_L^2 - 2V_S^2}{2(V_L^2 - V_S^2)} \tag{8}$$

$$E = 2V_S^2\rho(1+\nu) \tag{9}$$

$$G = \rho(V_S^2) \tag{10}$$

$$K = \frac{E}{3(1-2\nu)} \tag{11}$$

where V_L and V_S are the longitudinal wave velocity and shear wave velocity, respectively.

4.5.5 Hardness and Fracture Toughness from Indentation

Samples are polished and mounted in preparation for Vickers microhardness following ASTM standard E92-17. A Leco micro-indentor is used to create Vickers hardness indents in each sample. A total of 20 indents are done on each sample, and their location subsequently marked on the sample. After indentation, the samples are then loaded into an FEI Apreo scanning electron

microscope and the indents are individually imaged and size of the indents measured. The Vickers hardness (H_V) values are determined using the cross-diagonal measurements obtained from SEM imaging via Equation 12 below.

$$H_V = \frac{P}{d_1 d_2} \tag{12}$$

Fracture toughness is calculated in according to the methods laid out by Anstis *et al.*, [30]. Crack lengths are measured simultaneously upon measuring the hardness values of each individual indent. Criteria for viable indents are as follows: cracks measured must be propagating from the corners of the indent, the indent must be uniform and in accordance with ASTM standards for hardness calculation, crack paths must be devoid of obstructions such as pores in the sample. After obtaining crack lengths, fracture toughness is computed via equation 13 [30] below:

$$K_{ifr} = 0.016 \left(\frac{E}{HV}\right)^{\frac{1}{2}} \frac{P}{c^{\frac{3}{2}}} \tag{13}$$

where E and H_V are in units of GPa, P is the load force in N, and c is the crack length from the center of the indent in units of m. Fracture toughness values are determined using H_V and c for each individual indent and the final reported K_{ifr} is taken as the average across all viable measurements (minimum of 10) for a given sample.

Acknowledgements

The authors acknowledge support by DOD-ONR (N00014-15-1-2863, N00014-17-1-2090, N00014-16-1-2583, N00014-17-1-2876) and by Duke University—Center for Materials Genomics—for computational support. S.C. acknowledges the Alexander von Humboldt Foundation for financial support. C.O. acknowledges support from the National Science

Foundation Graduate Research Fellowship under grant no. DGF1106401. K. Kaufmann acknowledges support by the Department of Defense (DoD) through the National Defense Science and Engineering Graduate Fellowship (NDSEG) Program. K. Kaufmann would also like to acknowledge the financial support of the ARCS Foundation. The authors thank, Christina Rost, Olivia Dippo, Lavina Backman, Jeffrey Braun, Trent Borman, Delower Hossain, Sam Daigle, Mina Lim, Dr. Donald Brenner, Dr. Patrick Hopkins, Dr. Jon-Paul Maria and Dr. Elizabeth Opila for guidance and helpful scientific discussion.

Part 4, in full, is currently in preparation for submission as “Fermi level engineering of tunable and ultra-tough entropy stabilized carbides”, Harrington, Tyler; Oses, Corey; Toher, Cormac; Gild, Joshua; Mellor, William; Kaufmann, Kevin; Zhu, Chaoyi; Wright, Andrew; Luo, Jian; Curtarolo, Stefano; Vecchio, Kenneth. The dissertation author was the primary investigator and author of this material.

References

[1] E. Wuchina, E. Opila, M. Opeka, W. Fahrenholtz, I. Talmy, UHTCs: ultra-high temperature ceramics for extreme environment applications, Electrochem. Soc. Interface. 16 (2007) 30.

[2] L. Toth, Transition Metal Carbides and Nitrides., Elsevier Science, 1971.

[3] D. Edström, D.G. Sangiovanni, L. Hultman, I. Petrov, J.E. Greene, V. Chirita, Elastic properties and plastic deformation of TiC- and VC-based pseudobinary alloys, Acta Mater. 144 (2018) 376–385. doi:10.1016/J.ACTAMAT.2017.10.047.

[4] N. De Leon, X. Yu, H. Yu, C.R. Weinberger, G.B. Thompson, Bonding Effects on the Slip Differences in the B 1 Monocarbides, Phys. Rev. Lett. 114 (2015) 165502. doi:10.1103/PhysRevLett.114.165502.

[5] C.J. Smith, X.-X. Yu, Q. Guo, C.R. Weinberger, G.B. Thompson, Phase, hardness, and deformation slip behavior in mixed HfxTa1-xC, Acta Mater. 145 (2018) 142–153. doi:10.1016/J.ACTAMAT.2017.11.038.

[6] S.-H. Jhi, J. Ihm, S.G. Louie, M.L. Cohen, Electronic mechanism of hardness enhancement in transition-metal carbonitrides, Nature. 399 (1999) 132–134. doi:10.1038/20148.

[7] A. (Anthony) Kelly, N.H. (Norman H. Macmillan, Strong solids, Clarendon Press, Oxford [Oxfordshire] :, 1986.

[8] X.-X. Yu, G.B. Thompson, C.R. Weinberger, Influence of carbon vacancy formation on the elastic constants and hardening mechanisms in transition metal carbides, J. Eur. Ceram. Soc. 35 (2015) 95–103. doi:10.1016/j.jeurceramsoc.2014.08.021.

[9] D.D. Rowcliffe, G.E. Hollox~, Plastic Flow and Fracture of Tantalum Carbide and Hafnium Carbide at Low Temperatures, J. Mater. Sci. 6 (1971) 1261–1269.

[10] S.-H. Jhi, S.G. Louie, M.L. Cohen, J.W. Morris, Mechanical Instability and Ideal Shear Strength of Transition Metal Carbides and Nitrides, Phys. Rev. Lett. 87 (2001) 075503. doi:10.1103/PhysRevLett.87.075503.

[11] A. Nieto, D. Lahiri, A. Agarwal, Graphene NanoPlatelets reinforced tantalum carbide consolidated by spark plasma sintering, Mater. Sci. Eng. A. 582 (2013) 338–346. doi:10.1016/J.MSEA.2013.06.006.

[12] K. Balasubramanian, S. V. Khare, D. Gall, Valence electron concentration as an indicator for mechanical properties in rocksalt structure nitrides, carbides and carbonitrides, Acta Mater. 152 (2018) 175–185. doi:10.1016/J.ACTAMAT.2018.04.033.

[13] D.G. Sangiovanni, L. Hultman, V. Chirita, Supertoughening in B1 transition metal nitride alloys by increased valence electron concentration, Acta Mater. 59 (2011) 2121–2134.

doi:10.1016/J.ACTAMAT.2010.12.013.

[14] H. Yu, M. Bahadori, G.B. Thompson, C.R. Weinberger, Understanding dislocation slip in stoichiometric rocksalt transition metal carbides and nitrides, J. Mater. Sci. 52 (2017) 6235–6248. doi:10.1007/s10853-017-0857-4.

[15] D.G. Sangiovanni, V. Chirita, L. Hultman, Electronic mechanism for toughness enhancement in Ti x M 1 − x N (M = Mo and W), Phys. Rev. B. 81 (2010) 104107. doi:10.1103/PhysRevB.81.104107.

[16] T. Das, S. Deb, A. Mookerjee, Study of electronic structure and elastic properties of transition metal and actinide carbides, Phys. B Condens. Matter. 367 (2005) 6–18. doi:10.1016/J.PHYSB.2005.05.041.

[17] A. Pasturel, C. Colinet, P. Hicter, Strong chemical interactions in disordered alloys, Phys. B+C. 132 (1985) 177–180. doi:10.1016/0378-4363(85)90062-2.

[18] T.J. Harrington, J. Gild, P. Sarker, C. Toher, C.M. Rost, O.F. Dippo, C. McElfresh, K. Kaufmann, E. Marin, L. Borowski, P.E. Hopkins, J. Luo, S. Curtarolo, D.W. Brenner, K.S. Vecchio, Phase stability and mechanical properties of novel high entropy transition metal carbides, Acta Mater. 166 (2019) 271–280. doi:10.1016/J.ACTAMAT.2018.12.054.

[19] P. Sarker, T. Harrington, C. Toher, C. Oses, M. Samiee, J.-P. Maria, D.W. Brenner, K.S. Vecchio, S. Curtarolo, Novel high-entropy high-hardness metal carbides discovered by entropy descriptors, (2018).

[20] S.F. Pugh, XCII. Relations between the elastic moduli and the plastic properties of polycrystalline pure metals, London, Edinburgh, Dublin Philos. Mag. J. Sci. 45 (1954) 823–843. doi:10.1080/14786440808520496.

[21] K. Chen, L.R. Zhao, J. Rodgers, J.S. Tse, Alloying effects on elastic properties of TiN-based nitrides, J. Phys. D. Appl. Phys. 36 (2003) 2725–2729. doi:10.1088/0022-3727/36/21/021.

[22] D.G. Pettifor, Theoretical predictions of structure and related properties of intermetallics, Mater. Sci. Technol. 8 (1992) 345–349. doi:10.1179/mst.1992.8.4.345.

[23] R.A. Johnson, Analytic nearest-neighbor model for fcc metals, Phys. Rev. B. 37 (1988) 3924–3931. doi:10.1103/PhysRevB.37.3924.

[24] K. Yang, C. Oses, S. Curtarolo, Modeling Off-Stoichiometry Materials with a High-Throughput Ab-Initio Approach, Chem. Mater. 28 (2016) 6484–6492. doi:10.1021/acs.chemmater.6b01449.

[25] A.K. Rappe, C.J. Casewit, K.S. Colwell, W.A. Goddard, W.M. Skiff, UFF, a full periodic table force field for molecular mechanics and molecular dynamics simulations, J. Am. Chem. Soc. 114 (1992) 10024–10035. doi:10.1021/ja00051a040.

[26] C. Toher, C. Oses, J.J. Plata, D. Hicks, F. Rose, O. Levy, M. de Jong, M. Asta, M. Fornari, M. Buongiorno Nardelli, S. Curtarolo, Combining the AFLOW GIBBS and elastic libraries to efficiently and robustly screen thermomechanical properties of solids, Phys. Rev. Mater. 1 (2017) 015401. doi:10.1103/PhysRevMaterials.1.015401.

[27] X.-Q. Chen, H. Niu, D. Li, Y. Li, Modeling hardness of polycrystalline materials and bulk metallic glasses, Intermetallics. 19 (2011) 1275–1281. doi:10.1016/J.INTERMET.2011.03.026.

[28] D.M. Teter, Computational Alchemy: The Search for New Superhard Materials, MRS Bull. 23 (1998) 22–27. doi:10.1557/S0883769400031420.

[29] Y. Tian, B. Xu, Z. Zhao, Microscopic theory of hardness and design of novel superhard crystals, Int. J. Refract. Met. Hard Mater. 33 (2012) 93–106. doi:10.1016/J.IJRMHM.2012.02.021.

[30] G.R. Anstis, P. Chantikul, B.R. Lawn, D.B. Marshall, A Critical Evaluation of Indentation Techniques for Measuring Fracture Toughness: I, Direct Crack Measurements, J. Am. Ceram. Soc. 64 (1981) 533–538. doi:10.1111/j.1151-2916.1981.tb10320.x.

Part 5 - Future directions in high entropy carbides

5.1 Testing increased melting temperatures in high entropy ultra-high temperature carbides

5.1.1 Introduction

High entropy and entropy stabilized ceramics are a new field of ceramic materials that contain a mixture of five or more metals occupying a randomly ordered lattice and a separate ordered anion lattice containing one or two chemical species. The first entropy stabilized ceramic was synthesized by Rost *et al.* [1–3] and comprised five constituent oxides, which mixed to form a single phase randomly ordered solid solution. Since this initial inception, research has grown to include the field of high entropy ultra-high temperature ceramics (UHTCs) and a multitude of high entropy oxides, carbides, borides, nitrides, carbonitrides, and silicides have been successfully synthesized [4–9]. Although high entropy alloys typically exhibit BCC, FCC, and rarely HCP structures, the increased diversity of bonding in ceramics allows them to form many more complex structures, and high entropy ceramics have already been shown to exhibit different cubic (i.e. rocksalt, perovskite, fluorite), and hexagonal crystal structures [5,6,8,10].

Traditional engineering for high temperature tolerant systems begins with searching for materials that have a very large negative enthalpy, which is why most UHTCs comprise carbides, borides, and nitrides of group IVB, VB, and VIB transition metals. However, the well-known Gibbs free energy function: $G=H-TS$, where H is enthalpy, T is temperature, and S is entropy, which dictates material stability, suggests that at sufficiently high temperatures, a large entropy,

S, can effectively stabilize a solid solution phase. The original theory of high entropy alloys stated that this entropy stabilized the single phase against the formation of other competing phases, such as intermetallics. Although this theory has not been proven correct in many cases of metallic systems, it has been proven in ceramics [1,3]. If this concept is correct, then it stands to reason that the increase in entropy of the solid can also stabilize the material against the formation of the liquid. Since melting is an entropically driven phase transformation, an increase in the configurational entropy of the solid solution phase should result in a decrease in the energetic driving force for melting, leading to an increased melting temperature.

Of all the high temperature materials, the rocksalt carbides of hafnium and tantalum have the highest melting temperatures of any known materials at 4232 K and 4041 K, respectively [11]. TaC, HfC, and the remaining carbides of group IVB, and VB transition metals form stable rocksalt structures throughout a large temperature range, from room temperature to melting, and are well known to accommodate a large carbon stoichiometry range. The most stable carbide (with the highest melting temperature) is often a slightly substoichiometric phase [12,13]. Hong *et al.* argue that the reason for the higher stability of the substoichiometric phases is that the carbon vacancies can be regarded as another species, which leads to an increased configurational entropy when they are present [13]. If this proves true, then it further strengthens the case for the investigation of the effect of high entropy solid solutions on melting temperatures. Figure 5.1 outlines the expected effect of an increase entropy on melting temperature. When considering Gibbs free energy curves, the enthalpy is the y-intercept of the curve, while the entropy is the slope of the curve with respect to temperature. Because it is the slope of the curve, at ultra-high temperatures entropy can arguably have a more drastic effect on stabilizing a solid than enthalpy.

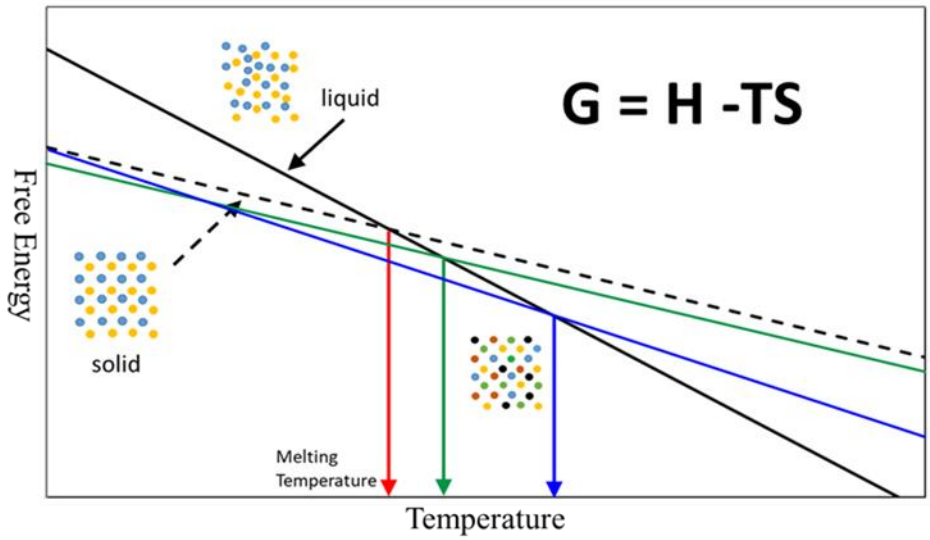

Figure 5.1: A simplified Gibbs free energy curve demonstrating the variation in melting temperature with changes in enthalpy and entropy of the solid phase. Note that the entropy is the slope of the Gibbs free energy curve, while the enthalpy is the y-intercept.

5.1.2 Preliminary Results

Preliminary results for melting temperatures of a series of HECs are given in Table 5.1. Melting temperatures were tested via a laser heating vacuum melting apparatus outlined in Ref. [14,15]. Samples of TaC and HfC were melting in the same apparatus to ensure accurate results. The results indicate that the HECs demonstrate increased melting temperatures over the rule of mixtures average for each composition. Relating the melting temperatures to the EFA values, which can be used to describe the extent of entropic stabilization in HECs [4] reveals that the most entropically stabilized composition, $MoNbTaVWC_5$, demonstrates the largest increase in Tm over the rule of mixtures average. These results, although preliminary show promise for the ability to use entropic stabilization to increase the stability of carbides at ultra-high temperatures and perhaps

even allow the synthesis of materials that demonstrate higher melting temperatures than any materials currently known.

Table 5.1: Table of compositions tested along with calculated entropy forming ability (EFA) from Ref. [4], experimentally tested melting temperature from this study, the rule of mixtures (RoM) average melting temperature of the binary carbides, and the difference between the measured melting temperature and the RoM average melting temperature denoted ΔT_m.

Composition	EFA*	T_m (K) (exp)	T_m (K) (RoM)**†	ΔT_m
$(V_{0.2}Nb_{0.2}Ta_{0.2}Mo_{0.2}W_{0.2})C$	125	3791	3443	348
$(Ti_{0.2}Hf_{0.2}V_{0.2}Nb_{0.2}Ta_{0.2})C$	100	3874	3799	75
$(Ti_{0.2}Nb_{0.2}Ta_{0.2}V_{0.2}W_{0.2})C$	77	3786	3552	234
$(Ti_{0.2}Hf_{0.2}Nb_{0.2}Ta_{0.2}W_{0.2})C$	67	3812	3807	5
$(Ti_{0.2}Zr_{0.2}Hf_{0.2}Ta_{0.2}W_{0.2})C$	50	3944	3771	173
HfC	NA	4377	NA	NA
TaC	NA	4302	NA	NA

* Ref. [4]
** Ref. [16]
† For HfC and TaC T_m (exp) from the current study were used in calculating T_m (RoM)

5.2 Irradiation resistance of high entropy carbides

Since irradiation damage depends on the formation and diffusion of defects in crystalline materials, high entropy alloys and ceramics are expected to show an increased resistance to irradiation damage. Very little work has been done in the field of high entropy alloys, with none currently undertaken in high entropy carbides, which should be under consideration as they are ultra-high temperature stable materials that may see application in future nuclear reactor systems.

5.3 High entropy composite materials and multi-anion systems

The successful fabrication of carbides, nitrides, and borides separately lays groundwork for the exploration of systems that contain more than a single anion species. Compositions of borides and carbides can be expected to form two phase composite materials, with each phase comprising a high entropy solid solution. These composites can be chemically tuned via the individual constituents of each of the solutions as well as phase fraction of each to give desired properties.

In the case of a system containing both nitrogen and carbon as anions, it can be expected to form a single phase carbonitride solid solution as both form many rocksalt structured binary compounds with transition metals. Investigation into these materials has yielded a few single phase compounds [9], but little work has been done investigating their properties. These materials could allow for even further entropic stabilization to be achieved via additional disorder in the anion lattice, leading to increased stabilities and elevated melting temperatures. Further, these compounds could allow for access to an even more extensive library of electronic density of states allowing further tuning and selecting of compounds with enhanced ductility as outlined in Part 4 of this work.

Acknowledgements

The authors acknowledge support through the Office of Naval Research ONR-MURI (grant No. N00014-15-1-2863). K. Kaufmann was supported by the Department of Defense (DoD) through the National Defense Science & Engineering Graduate Fellowship (NDSEG) Program. K. Kaufmann would also like to acknowledge the generous support of the ARCS Foundation, San Diego Chapter. The authors thank Lavina Backman, Jeffrey Braun, Trent Borman, Dr. Jon-Paul

Maria and Dr. Elizabeth Opila for guidance and helpful scientific discussion. The authors would like to acknowledge Rudy Konings for help in conducting melting temperature experiments.

Part 5, in part, is currently in preparation for submission as “Increased melting temperatures in high entropy carbides”, Harrington, Tyler; Toher, Cormac; Oses, Corey; Gild, Joshua; Kaufmann, Kevin; Mellor, William; Cedillos Barraza, Omar; Robba, Davide; Vlahovic, Luka; Manara Dario; Dippo, Olivia; Luo, Jian; Curtarolo, Stefano; Vecchio, Kenneth.

References

[1] C.M. Rost, E. Sachet, T. Borman, A. Moballegh, E.C. Dickey, D. Hou, J.L. Jones, S. Curtarolo, J.-P. Maria, Entropy-stabilized oxides, Nat. Commun. 6 (2015) 8485. doi:10.1038/ncomms9485.

[2] C.M. Rost, Z. Rak, D.W. Brenner, J.-P. Maria, Local structure of the $Mg_x Ni_x Co_x Cu_x Zn_x O$ (x =0.2) entropy-stabilized oxide: An EXAFS study, J. Am. Ceram. Soc. 100 (2017) 2732–2738. doi:10.1111/jace.14756.

[3] C. Rost, Entropy-Stabilized Oxides: Explorations of a Novel Class of Multicomponent Materials., (2016).

[4] P. Sarker, T. Harrington, C. Toher, C. Oses, M. Samiee, J.-P. Maria, D.W. Brenner, K.S. Vecchio, S. Curtarolo, High-entropy high-hardness metal carbides discovered by entropy descriptors, Nat. Commun. 9 (2018) 4980. doi:10.1038/s41467-018-07160-7.

[5] J. Gild, Y. Zhang, T. Harrington, S. Jiang, T. Hu, M.C. Quinn, W.M. Mellor, N. Zhou, K. Vecchio, J. Luo, High-Entropy Metal Diborides: A New Class of High-Entropy Materials and a New Type of Ultrahigh Temperature Ceramics., Sci. Rep. 6 (2016) 37946. doi:10.1038/srep37946.

[6] J. Gild, M. Samiee, J.L. Braun, T. Harrington, H. Vega, P.E. Hopkins, K. Vecchio, J. Luo, High-entropy fluorite oxides, J. Eur. Ceram. Soc. 38 (2018) 3578–3584. doi:10.1016/J.JEURCERAMSOC.2018.04.010.

[7] Y. Qin, J.-X. Liu, F. Li, X. Wei, H. Wu, G.-J. Zhang, A high entropy silicide by reactive spark plasma sintering, J. Adv. Ceram. 8 (2019) 148–152. doi:10.1007/s40145-019-0319-3.

[8] S. Jiang, T. Hu, J. Gild, N. Zhou, J. Nie, M. Qin, T. Harrington, K. Vecchio, J. Luo, A new class of high-entropy perovskite oxides, Scr. Mater. 142 (2018) 116–120. doi:10.1016/J.SCRIPTAMAT.2017.08.040.

[9] K. Vecchio, J. Luo, J. Gild, M. Samiee, O. Dippo, T. Harrington, S. Curtarolo, P. Sarker, C. Toher, Modelling and synthesis of high-entropy refractory carbides, nitrides and carbonitrides, Ultra-High Temp. Ceram. Mater. Extrem. Environ. Appl. IV. (2017). http://dc.engconfintl.org/uhtc_iv/32 (accessed July 5, 2018).

[10] Y. Liu, Y. Jiang, R. Zhou, J. Feng, First principles study the stability and mechanical properties of MC (M = Ti, V, Zr, Nb, Hf and Ta) compounds, J. Alloys Compd. 582 (2014) 500–504. doi:10.1016/j.jallcom.2013.08.045.

[11] O. Cedillos-Barraza, D. Manara, K. Boboridis, T. Watkins, S. Grasso, D.D. Jayaseelan, R.J.M. Konings, M.J. Reece, W.E. Lee, Investigating the highest melting temperature materials: A laser melting study of the TaC-HfC system, Sci. Rep. 6 (2016) 37962. doi:10.1038/srep37962.

[12] L. Toth, Transition Metal Carbides and Nitrides., Elsevier Science, 1971.

[13] Q.-J. Hong, A. van de Walle, Prediction of the material with highest known melting point

from *ab initio* molecular dynamics calculations, Phys. Rev. B. 92 (2015) 020104. doi:10.1103/PhysRevB.92.020104.

[14] O. Cedillos-Barraza, D. Manara, K. Boboridis, T. Watkins, S. Grasso, D.D. Jayaseelan, R.J.M. Konings, M.J. Reece, W.E. Lee, Investigating the highest melting temperature materials: A laser melting study of the TaC-HfC system, Sci. Rep. 6 (2016) 37962. doi:10.1038/srep37962.

[15] H.F. Jackson, D.D. Jayaseelan, D. Manara, C.P. Casoni, W.E. Lee, Laser Melting of Zirconium Carbide: Determination of Phase Transitions in Refractory Ceramic Systems, J. Am. Ceram. Soc. 94 (2011) 3561–3569. doi:10.1111/j.1551-2916.2011.04560.x.

[16] H.O. Pierson, Handbook of refractory carbides and nitrides : properties, characteristics, processing, and applications, Noyes Publications, 1996.

SUPPLEMENTARY INFORMATION PART 2

High-entropy high-hardness metal carbides discovered by entropy descriptors

Pranab Sarker,[1,*] Tyler Harrington,[2,*] Cormac Toher,[1] Corey Oses,[1] Mojtaba Samiee,[2]
Jon-Paul Maria,[3] Donald W. Brenner,[3] Kenneth S. Vecchio,[2,4,†] and Stefano Curtarolo[5,6,‡]

[1] *Department of Mechanical Engineering and Materials Science, Duke University, Durham, NC 27708, USA*
[2] *Materials Science and Engineering Program, University of California, San Diego, La Jolla, CA 92093, USA*
[3] *Department of Materials Science and Engineering, North Carolina State University, Raleigh, NC 27695, USA*
[4] *Department of NanoEngineering, University of California, San Diego, La Jolla, CA 92093, USA*
[5] *Materials Science, Electrical Engineering, Physics and Chemistry, Duke University, Durham NC, 27708, USA*
[6] *Fritz-Haber-Institut der Max-Planck-Gesellschaft, 14195 Berlin-Dahlem, Germany*

(Dated: October 16, 2018)

SUPPLEMENTARY NOTE 1: CONTENT

The supplementary information includes: **i.** the binary and ternary convex hull phase diagrams for all component carbide systems; **ii.** the energetic distance from the convex hull, ΔH_{f}, for the lowest energy configuration and the corresponding decomposition reaction products for all 56 5-metal carbide compositions; **iii.** a comparison of XRD spectra for $MoNbTaVWC_{5-x}$ synthesized using both WC and W_2C precursors; **iv.** the elastic response during the mechanical testing for $HfNbTaTiZrC_5$; **v.** a comparison between the Vickers hardness results obtained from calculation, experiment, and rule of mixtures for the 6 single-phase 5-metal carbides; **vi.** the bulk and shear moduli for each configuration of the 6 single-phase 5-metal carbides; **vii.** the electronic density of states for the 9 synthesized 5-metal carbides; **viii.** the formation enthalpies for each configuration of all 56 5-metal carbides; and **ix.** the atomic geometry for all configurations used to calculate the EFA for $HfNbTaTiZrC_5$.

SUPPLEMENTARY NOTE 2: COMPETING ORDERED PHASES

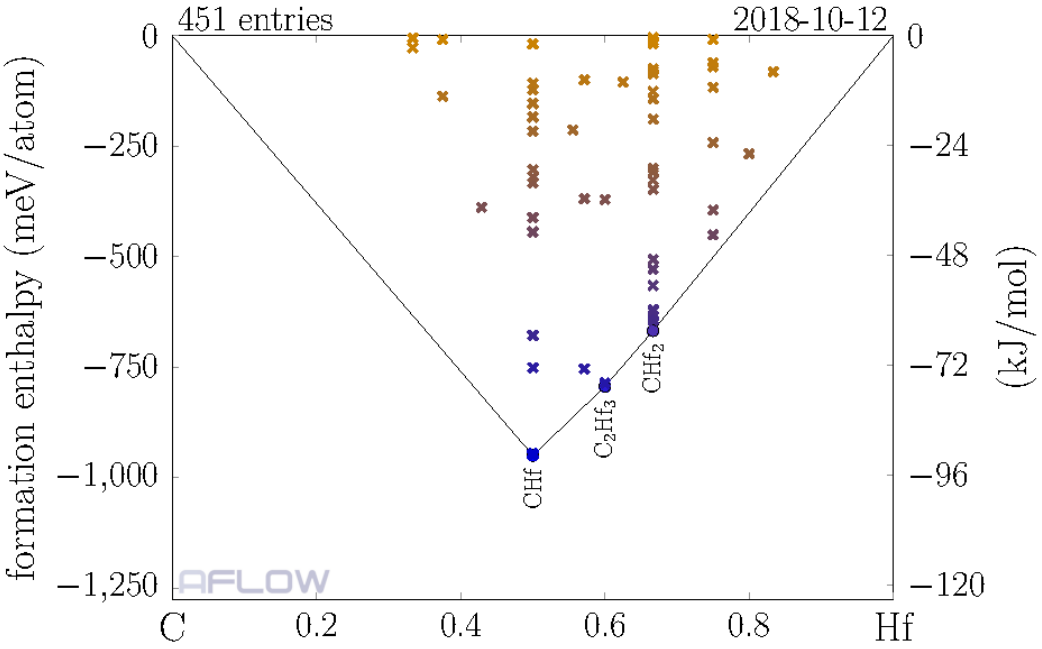

Supplementary Figure 1. CHf binary hull as calculated with AFLOW-CHULL.

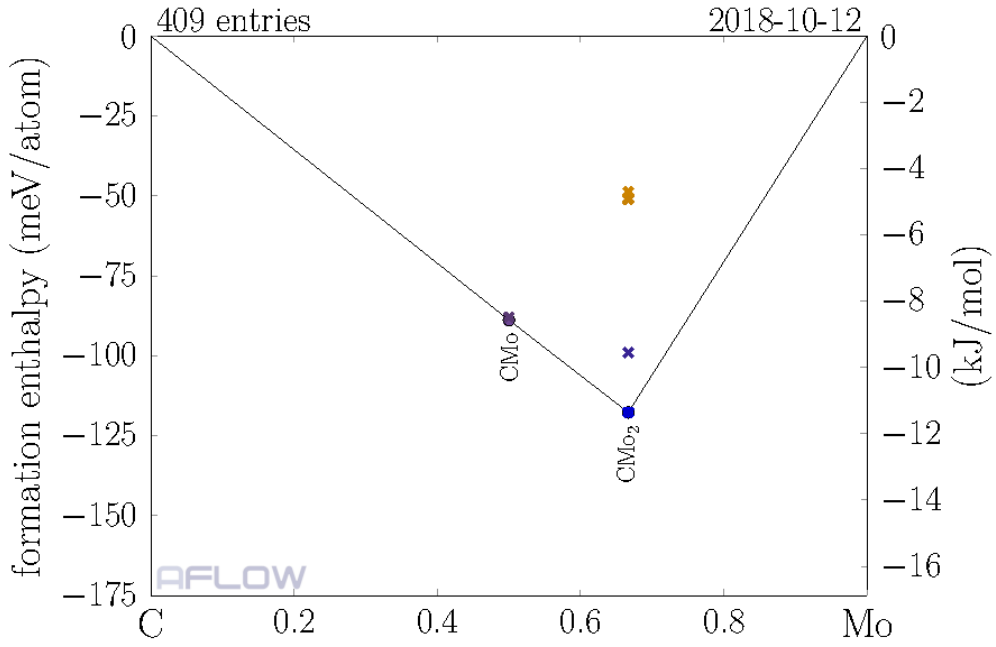

Supplementary Figure 2. CMo binary hull as calculated with AFLOW-CHULL.

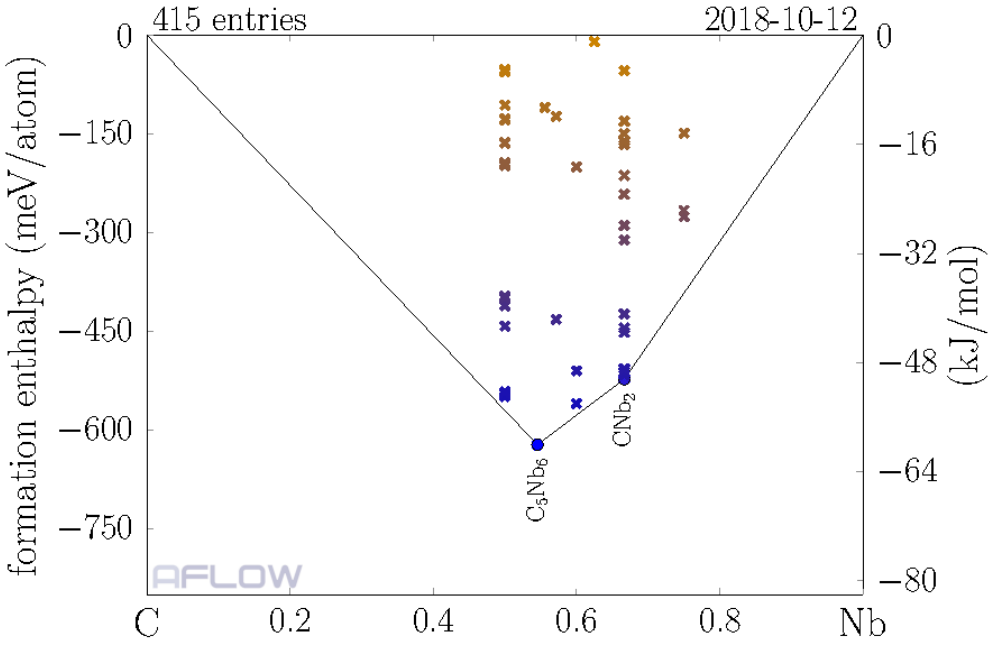

Supplementary Figure 3. CNb binary hull as calculated with AFLOW-CHULL.

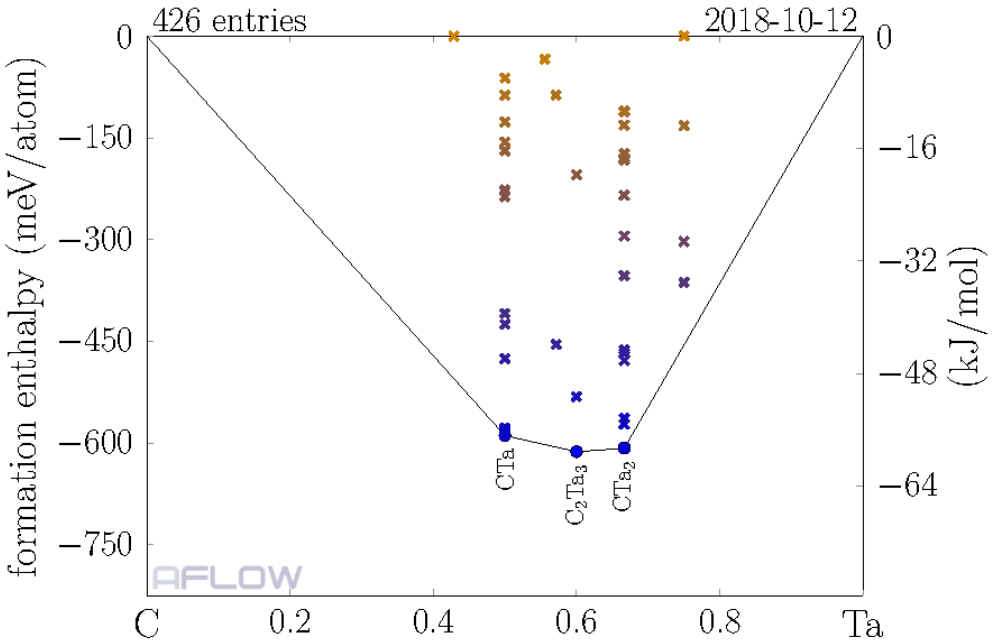

Supplementary Figure 4. CTa binary hull as calculated with AFLOW-CHULL.

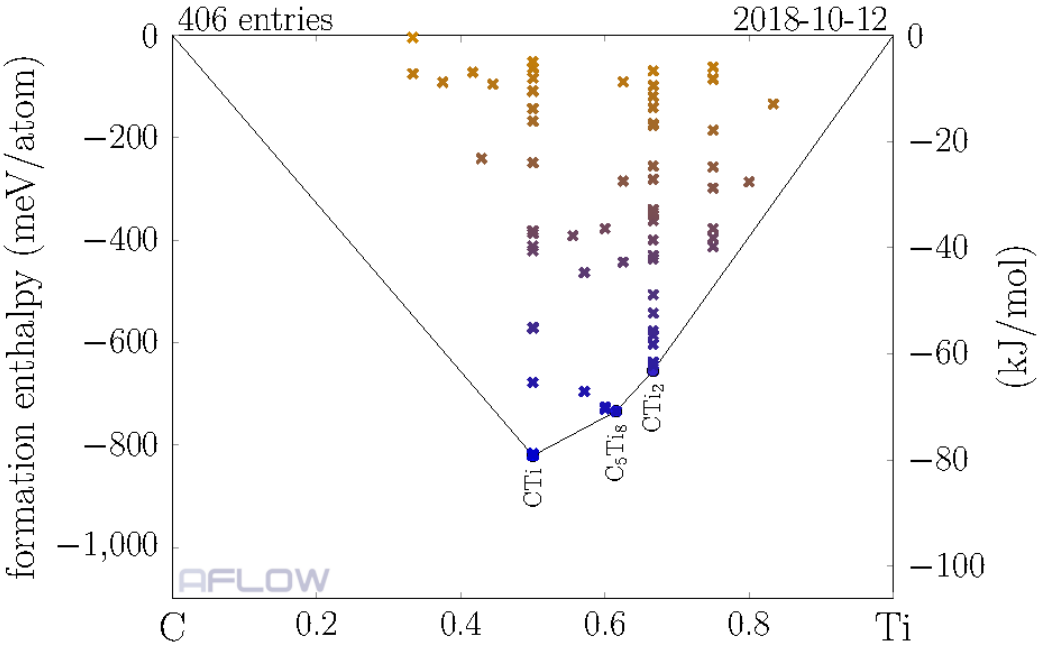

Supplementary Figure 5. CTi binary hull as calculated with AFLOW-CHULL.

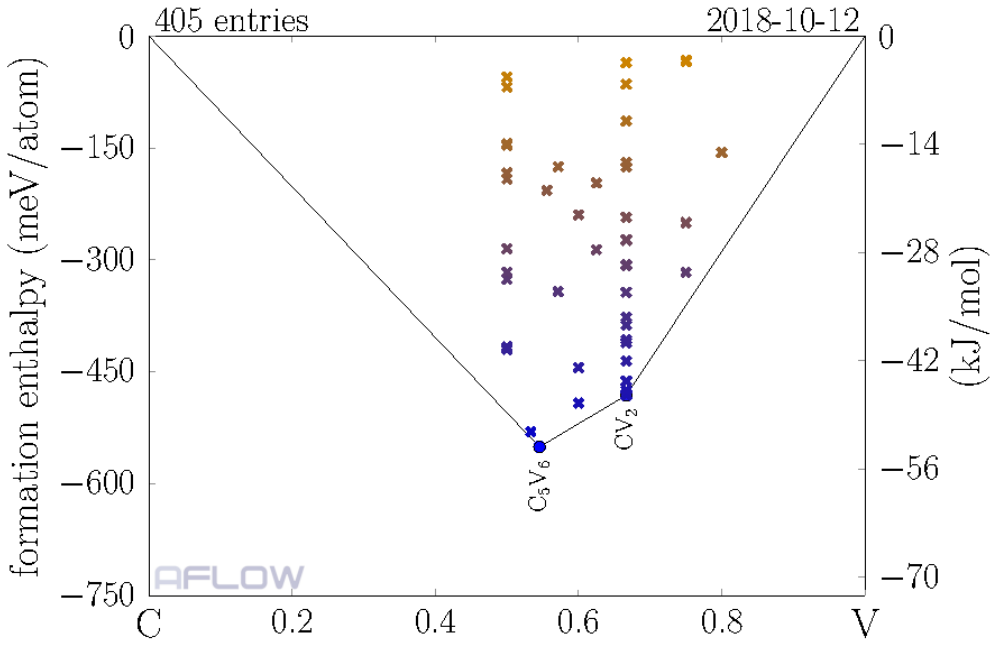

Supplementary Figure 6. CV binary hull as calculated with AFLOW-CHULL.

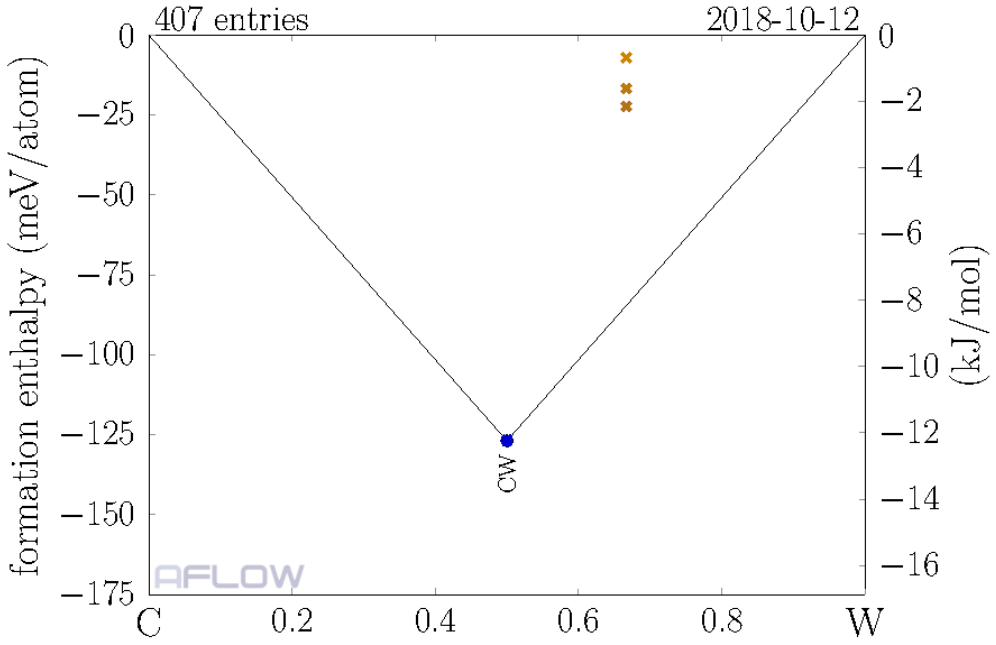

Supplementary Figure 7. CW binary hull as calculated with AFLOW-CHULL.

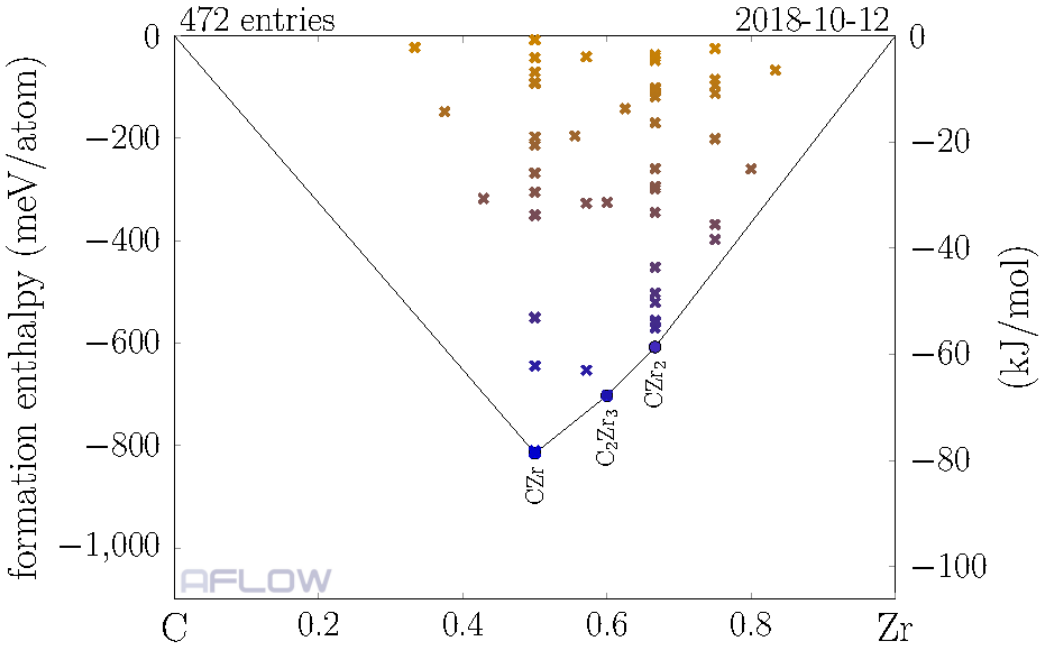

Supplementary Figure 8. CZr binary hull as calculated with AFLOW-CHULL.

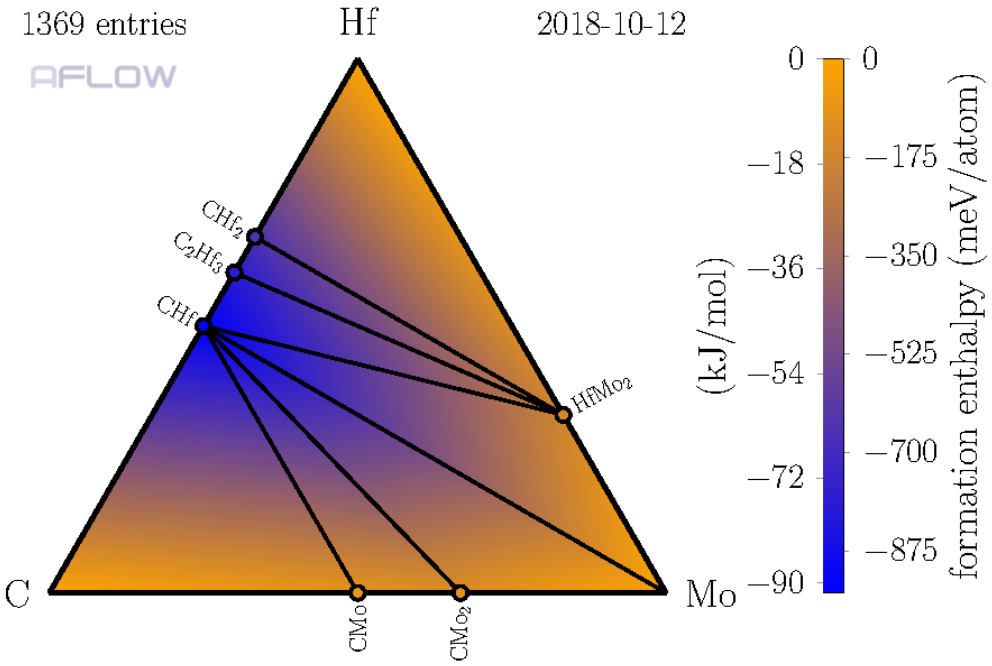

Supplementary Figure 9. CHfMo ternary hull as calculated with AFLOW-CHULL.

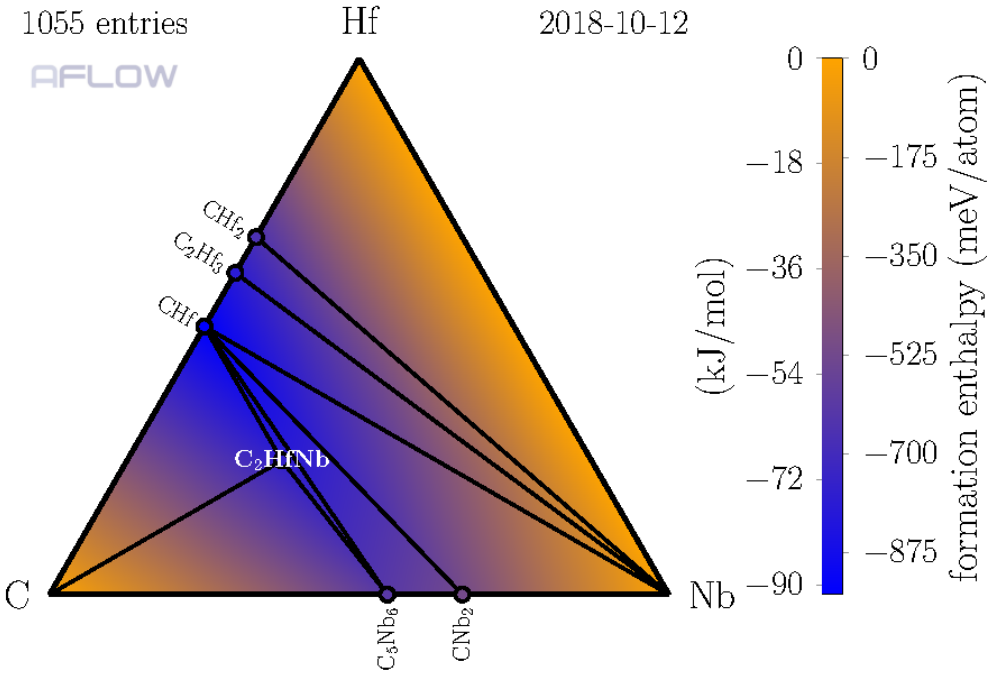

Supplementary Figure 10. CHfNb ternary hull as calculated with AFLOW-CHULL.

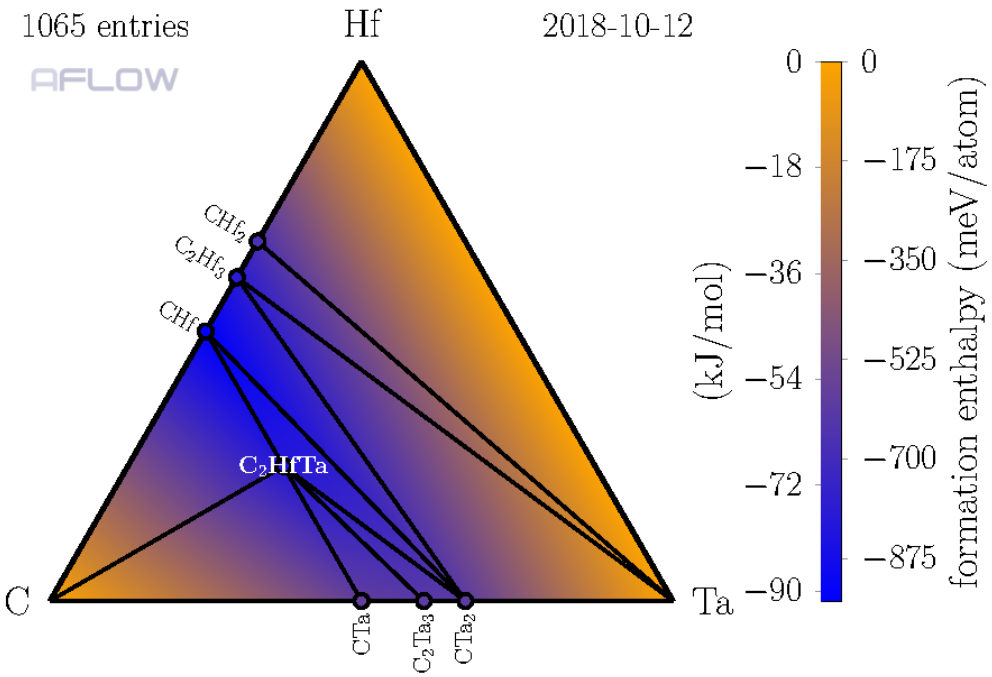

Supplementary Figure 11. CHfTa ternary hull as calculated with AFLOW-CHULL.

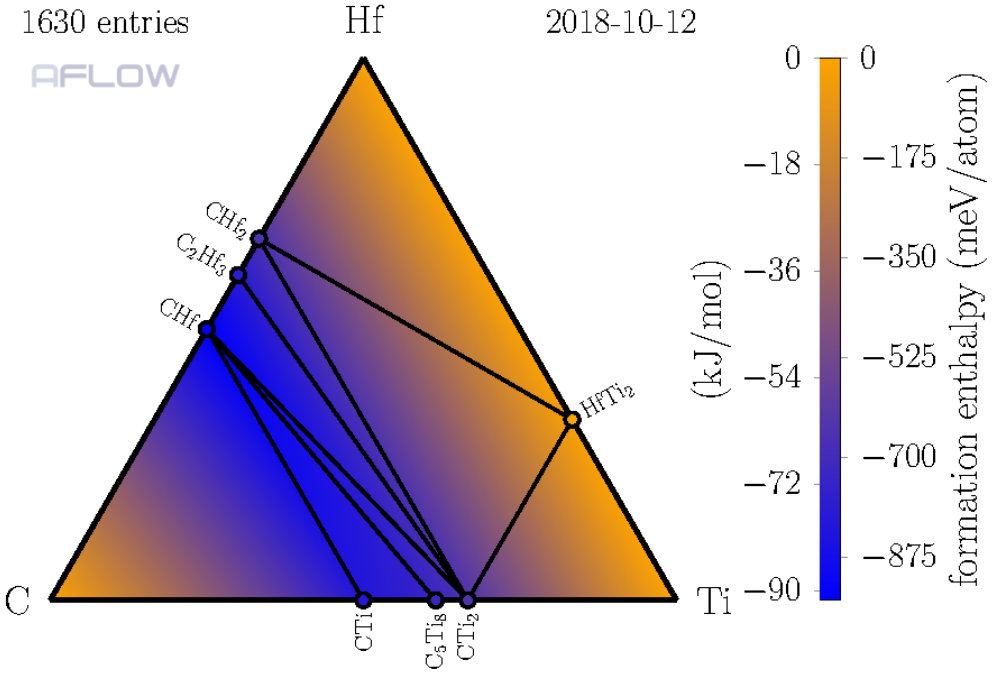

Supplementary Figure 12. CHfTi ternary hull as calculated with AFLOW-CHULL.

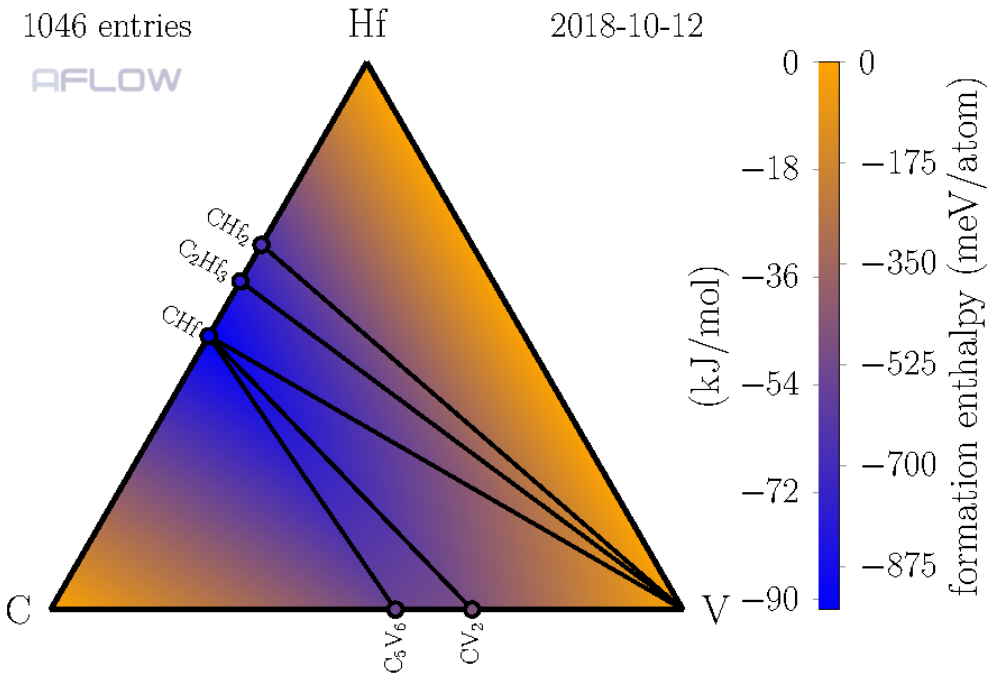

Supplementary Figure 13. CHfV ternary hull as calculated with AFLOW-CHULL.

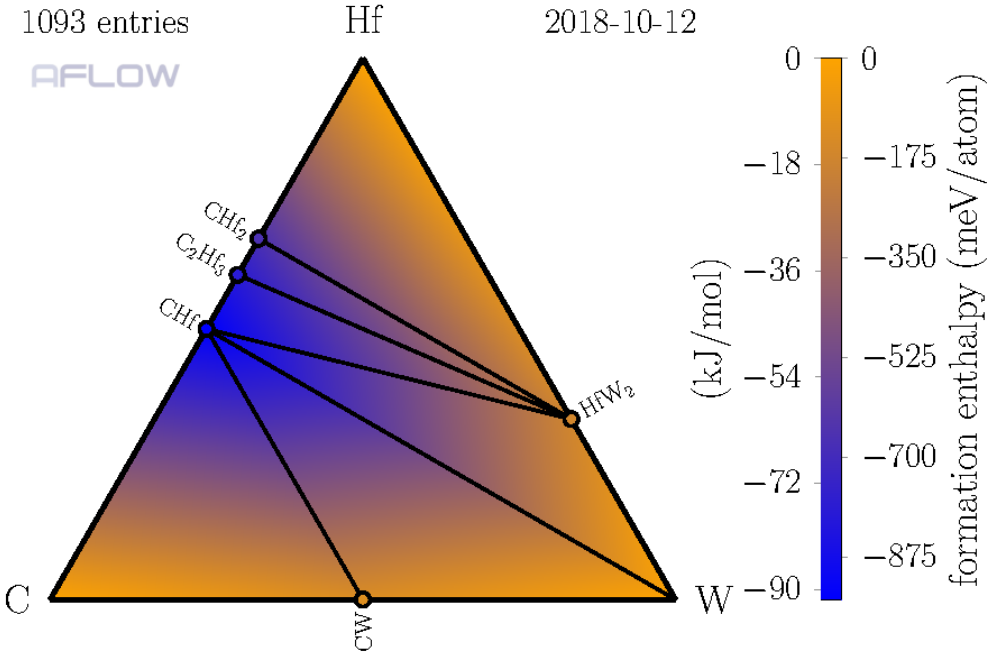

Supplementary Figure 14. CHfW ternary hull as calculated with AFLOW-CHULL.

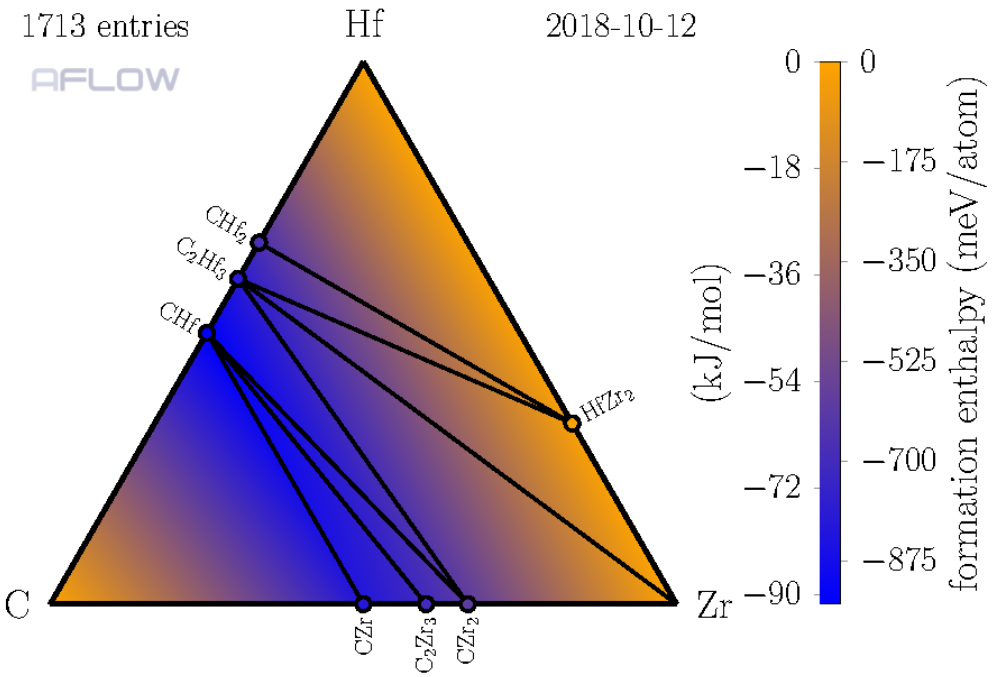

Supplementary Figure 15. CHfZr ternary hull as calculated with AFLOW-CHULL.

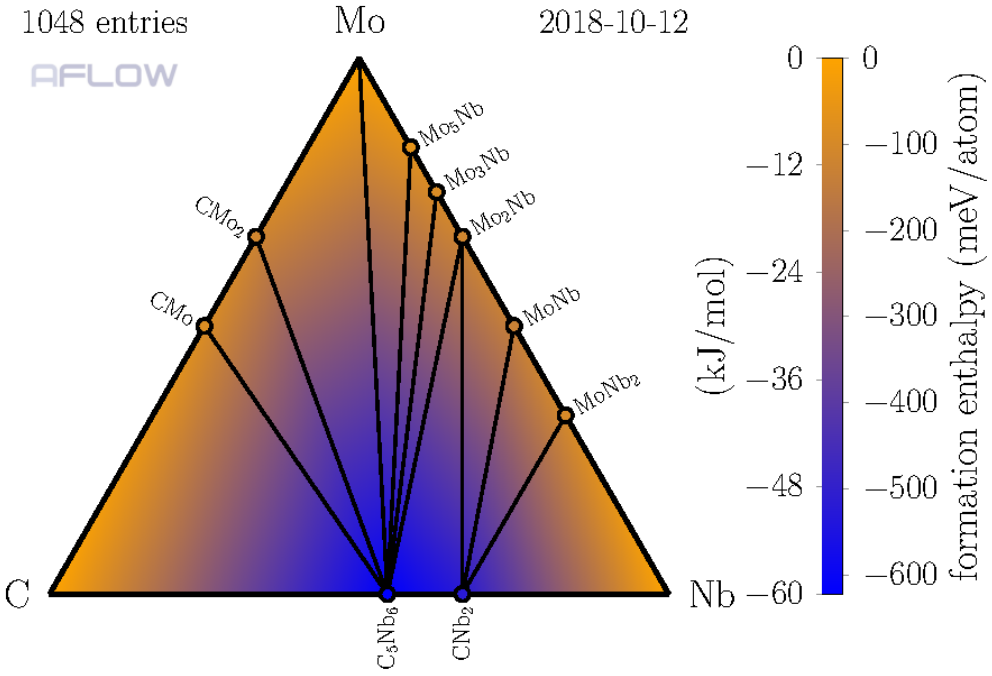

Supplementary Figure 16. CMoNb ternary hull as calculated with AFLOW-CHULL.

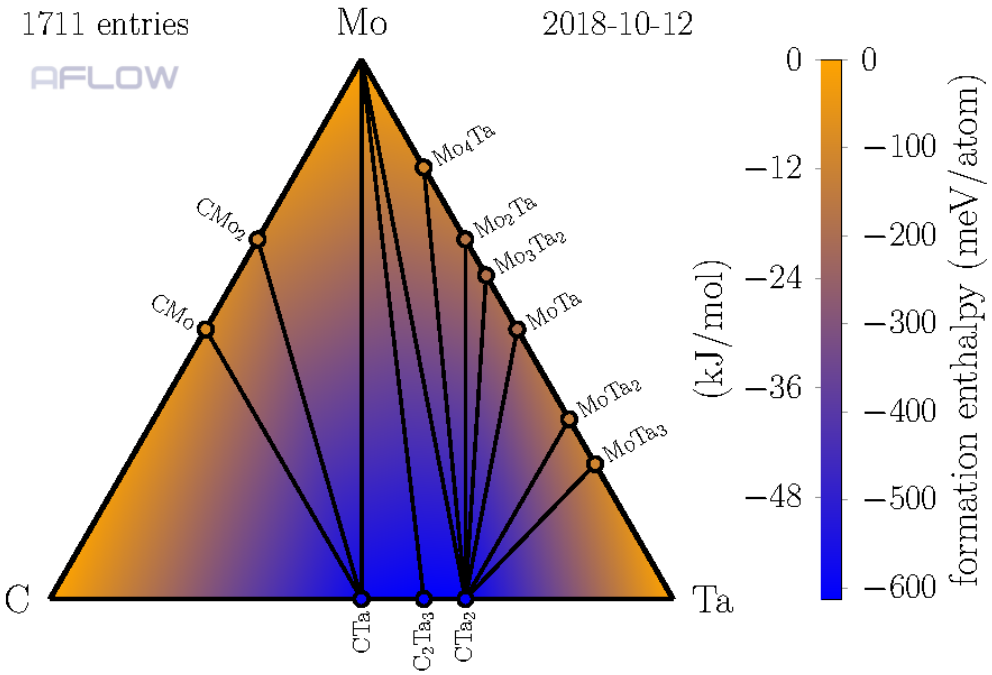

Supplementary Figure 17. CMoTa ternary hull as calculated with AFLOW-CHULL.

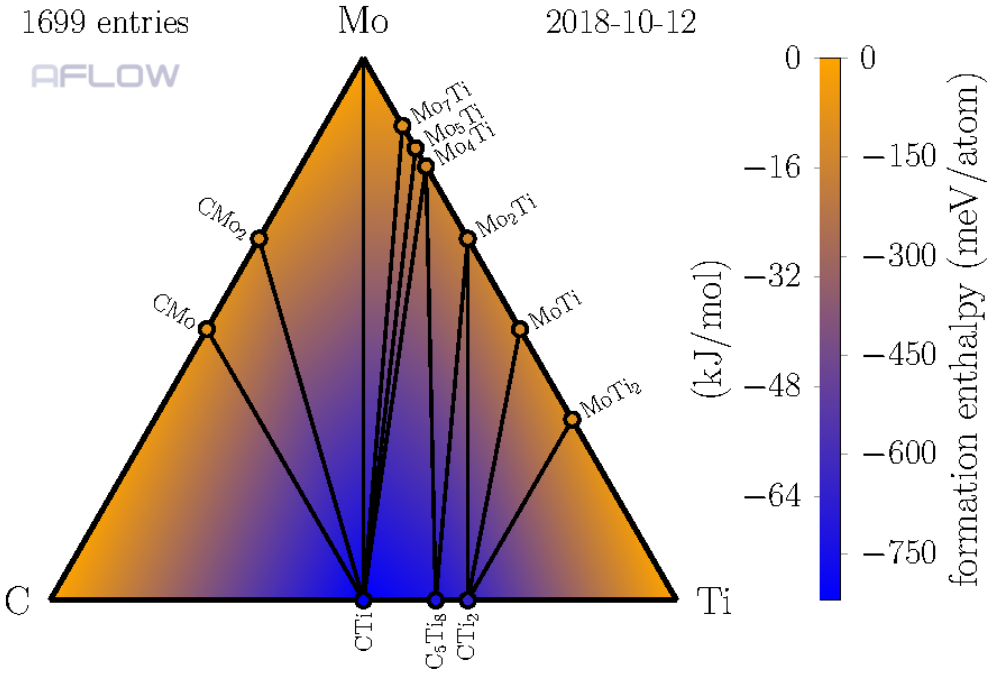

Supplementary Figure 18. CMoTi ternary hull as calculated with AFLOW-CHULL.

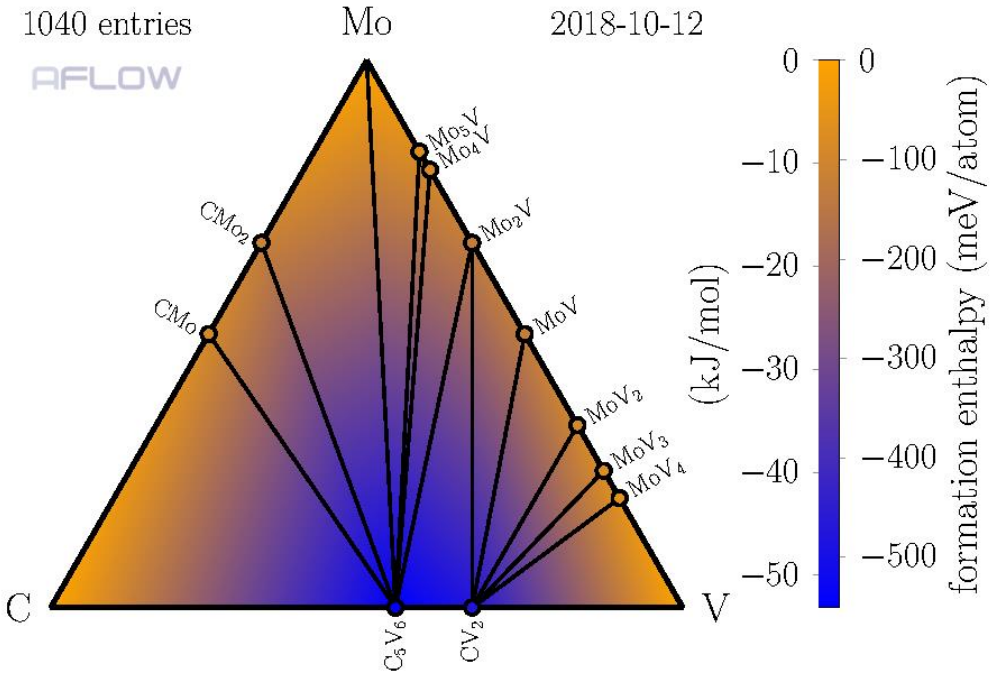

Supplementary Figure 19. CMoV ternary hull as calculated with AFLOW-CHULL.

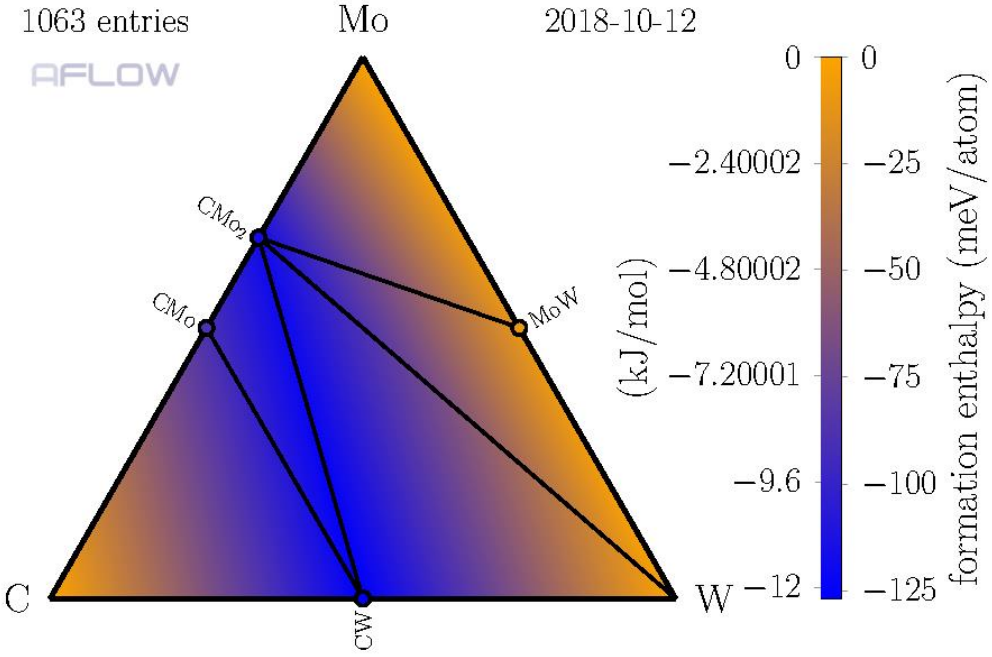

Supplementary Figure 20. CMoW ternary hull as calculated with AFLOW-CHULL.

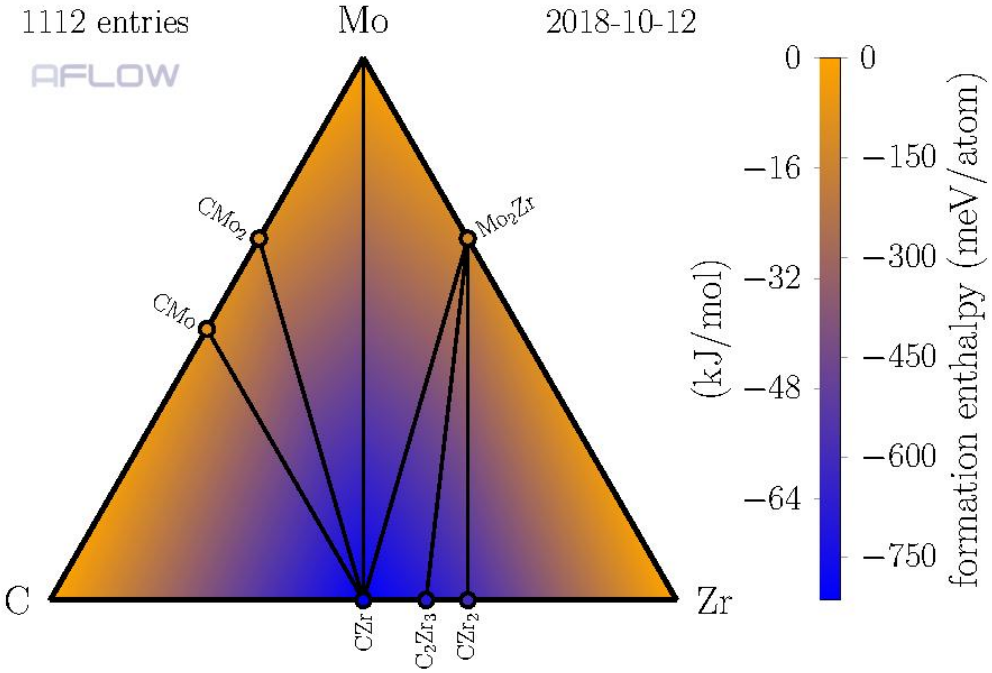

Supplementary Figure 21. CMoZr ternary hull as calculated with AFLOW-CHULL.

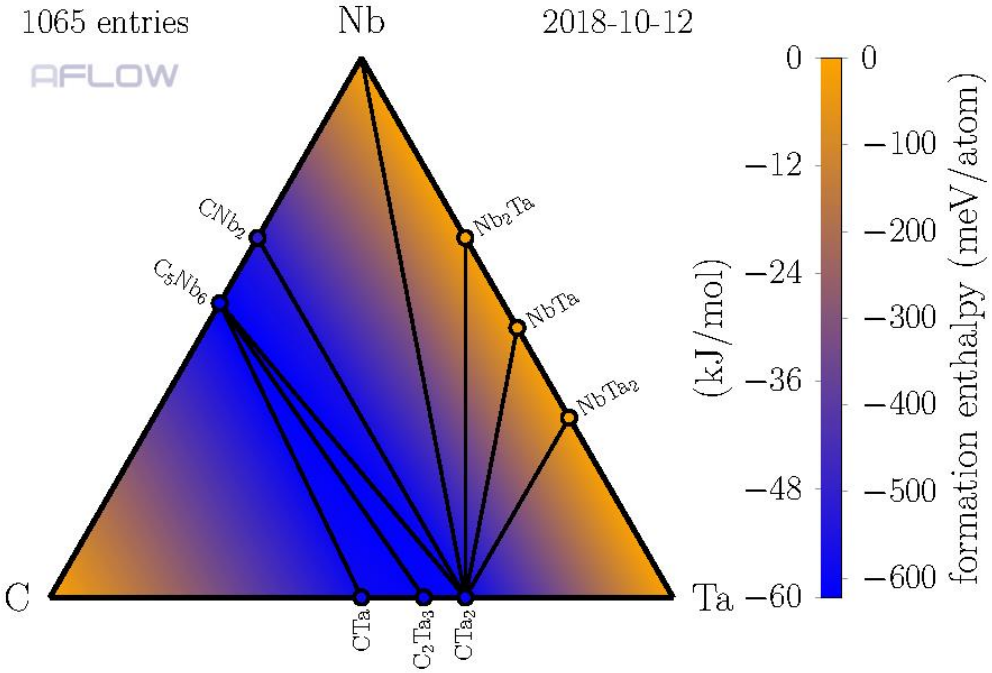

Supplementary Figure 22. CNbTa ternary hull as calculated with AFLOW-CHULL.

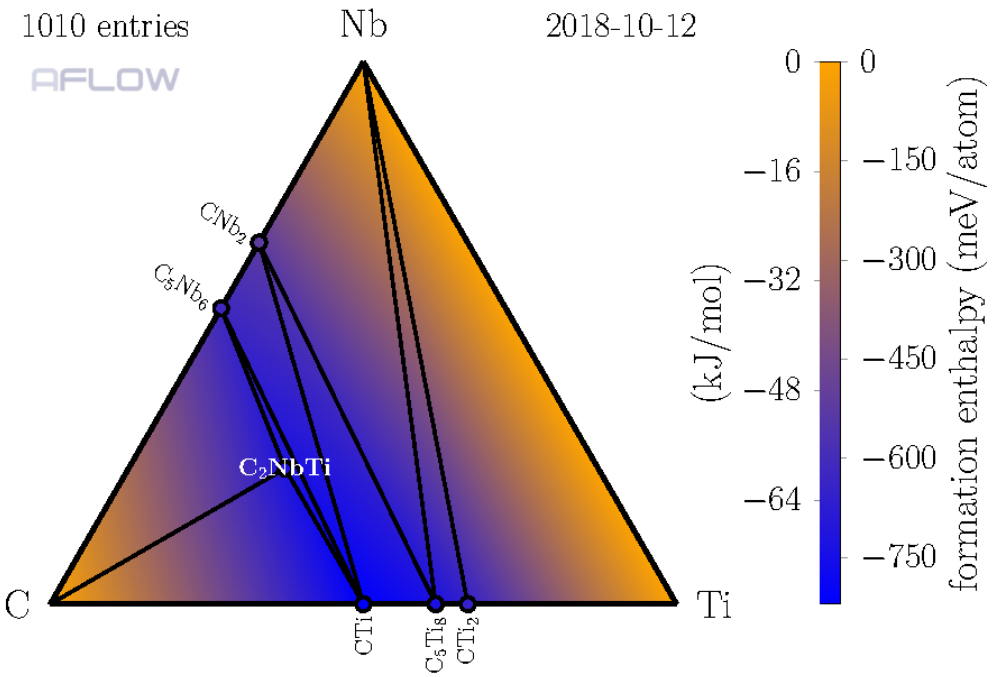

Supplementary Figure 23. CNbTi ternary hull as calculated with AFLOW-CHULL.

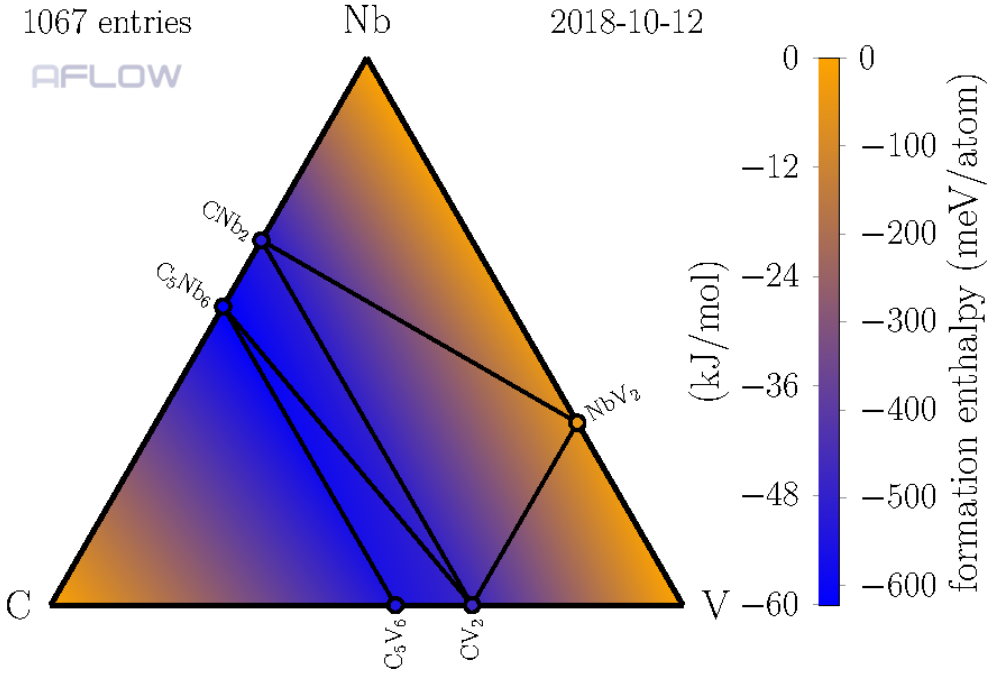

Supplementary Figure 24. CNbV ternary hull as calculated with AFLOW-CHULL.

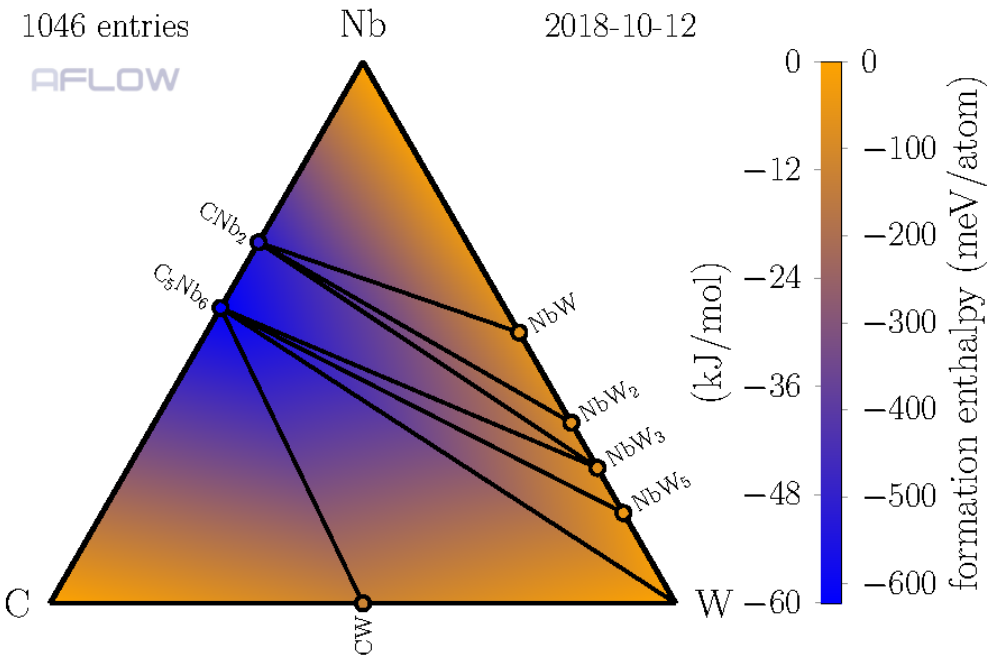

Supplementary Figure 25. CNbW ternary hull as calculated with AFLOW-CHULL.

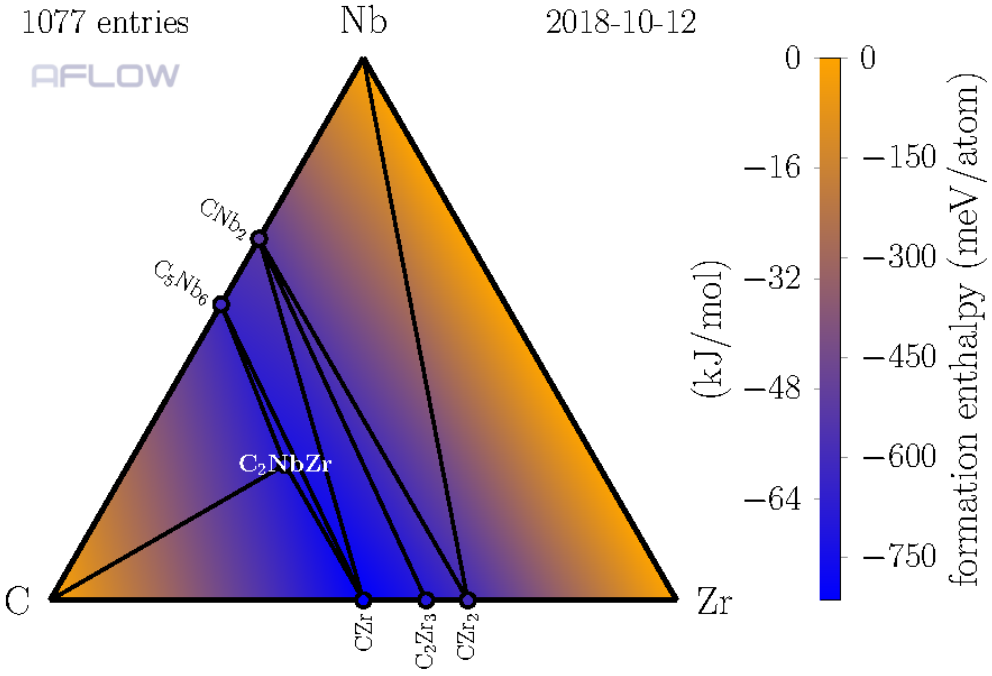

Supplementary Figure 26. CNbZr ternary hull as calculated with AFLOW-CHULL.

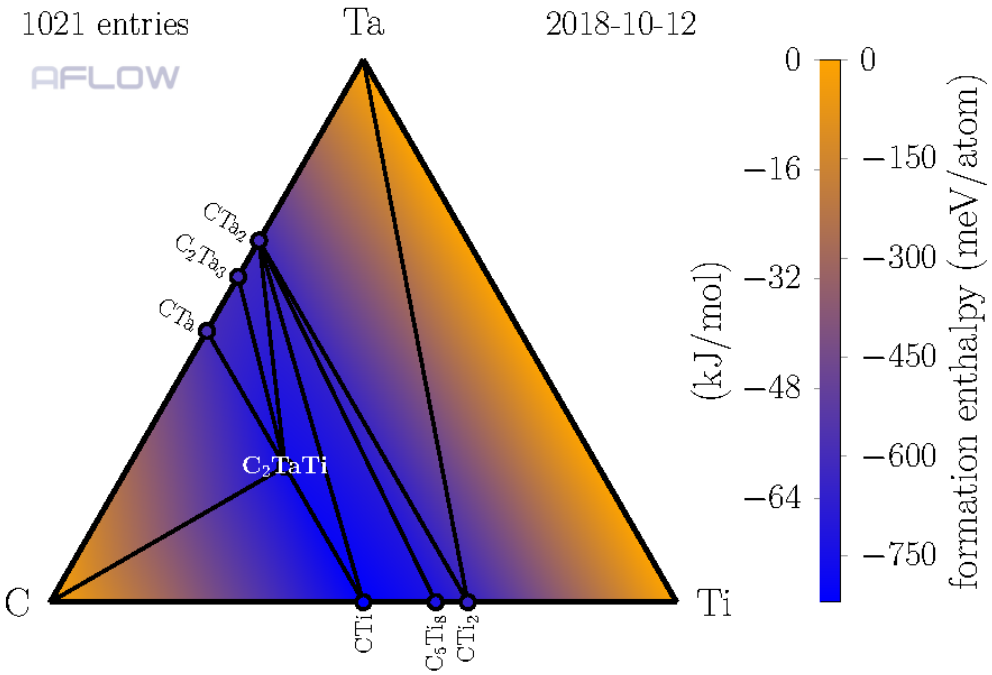

Supplementary Figure 27. CTaTi ternary hull as calculated with AFLOW-CHULL.

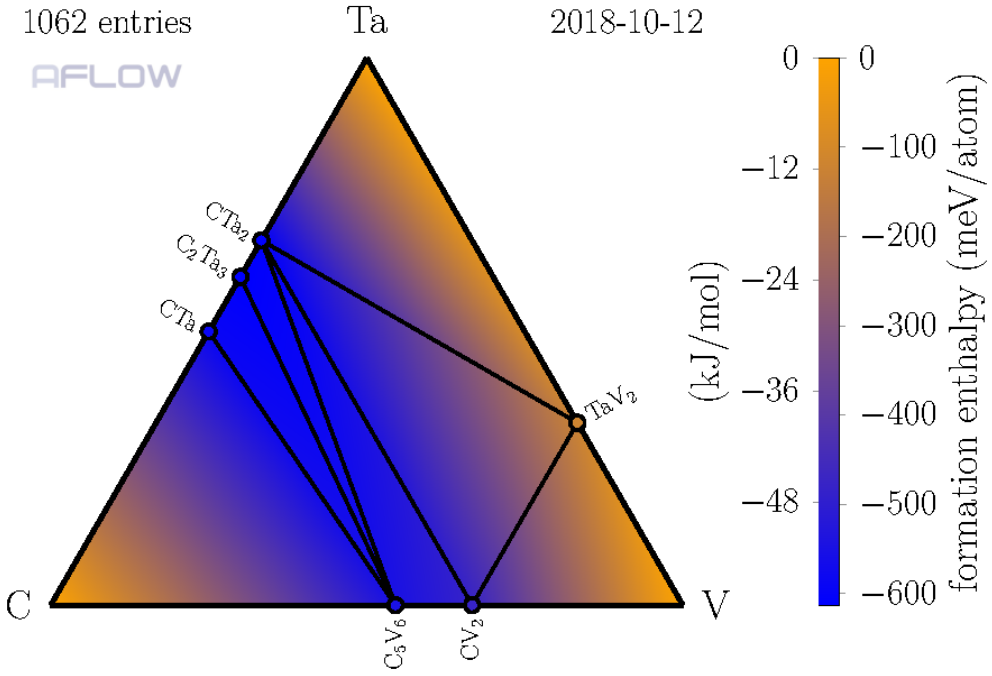

Supplementary Figure 28. CTaV ternary hull as calculated with AFLOW-CHULL.

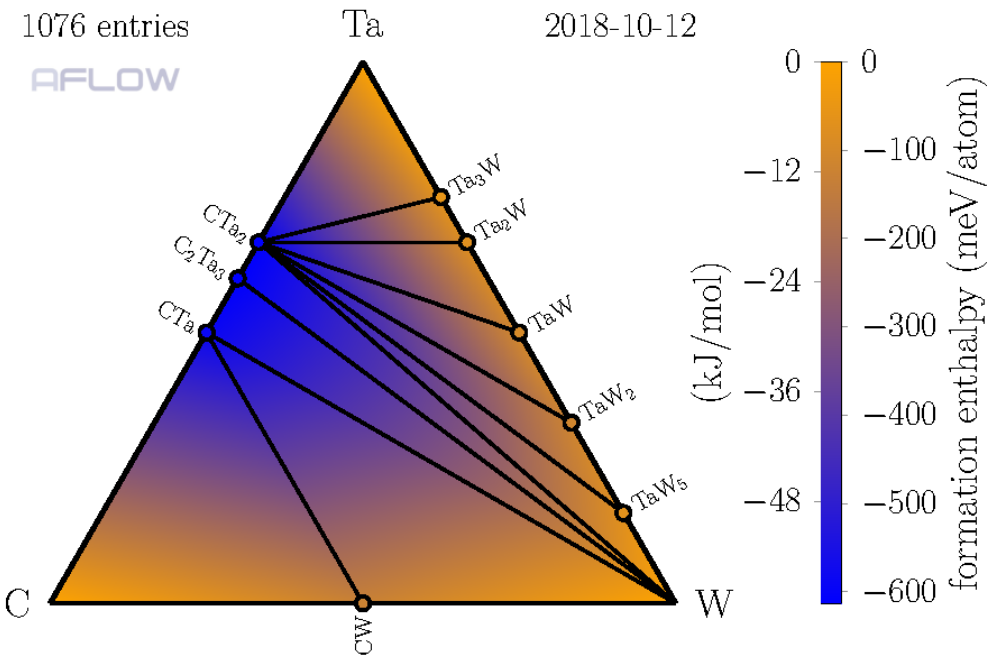

Supplementary Figure 29. CTaW ternary hull as calculated with AFLOW-CHULL.

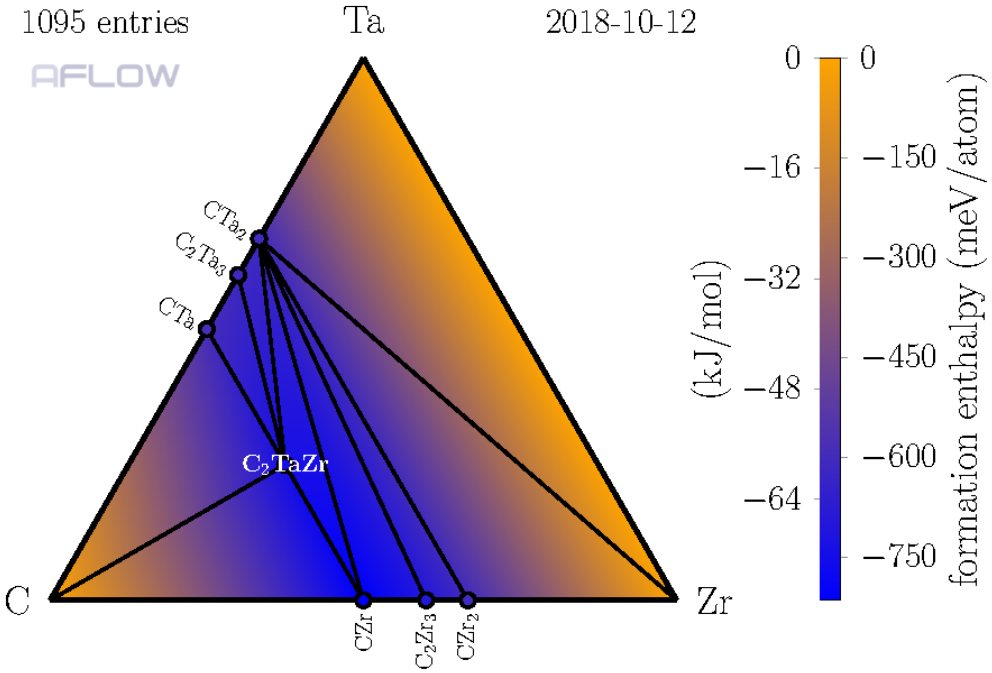

Supplementary Figure 30. CTaZr ternary hull as calculated with AFLOW-CHULL.

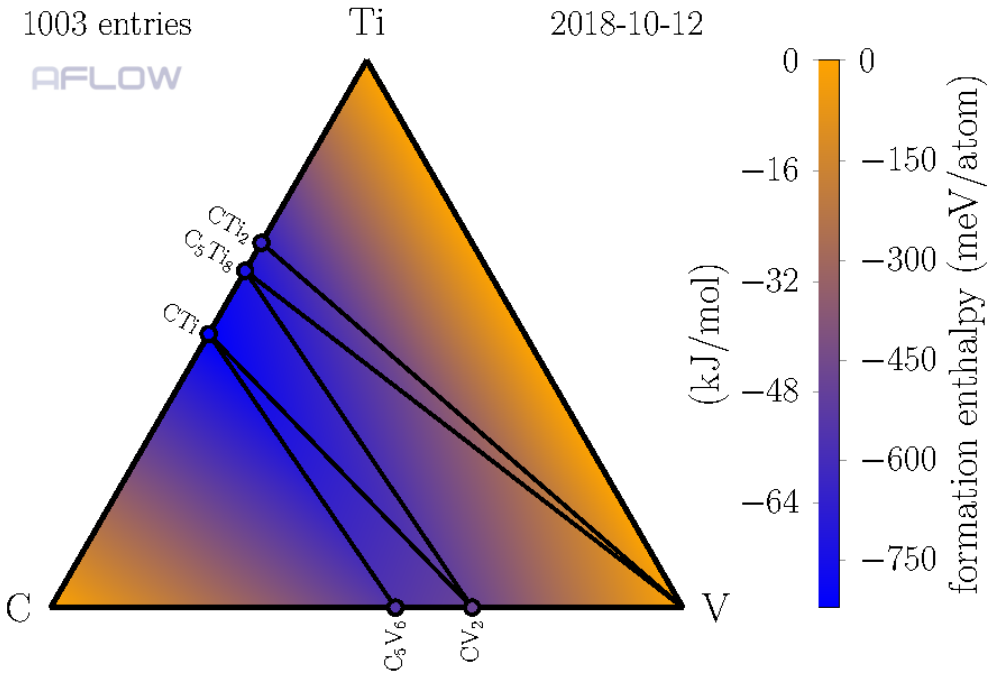

Supplementary Figure 31. CTiV ternary hull as calculated with AFLOW-CHULL.

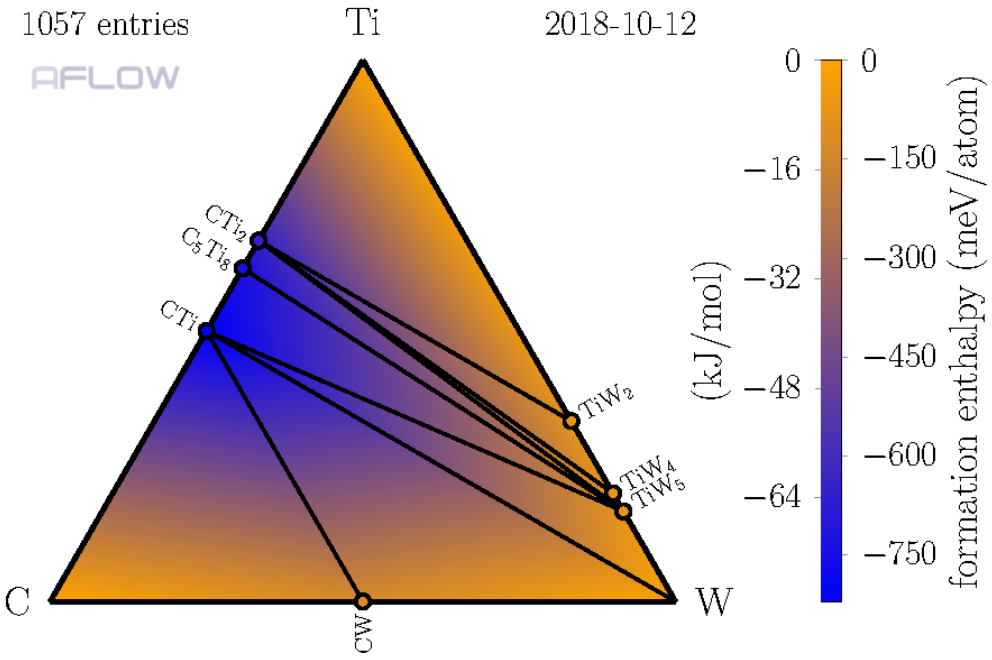

Supplementary Figure 32. CTiW ternary hull as calculated with AFLOW-CHULL.

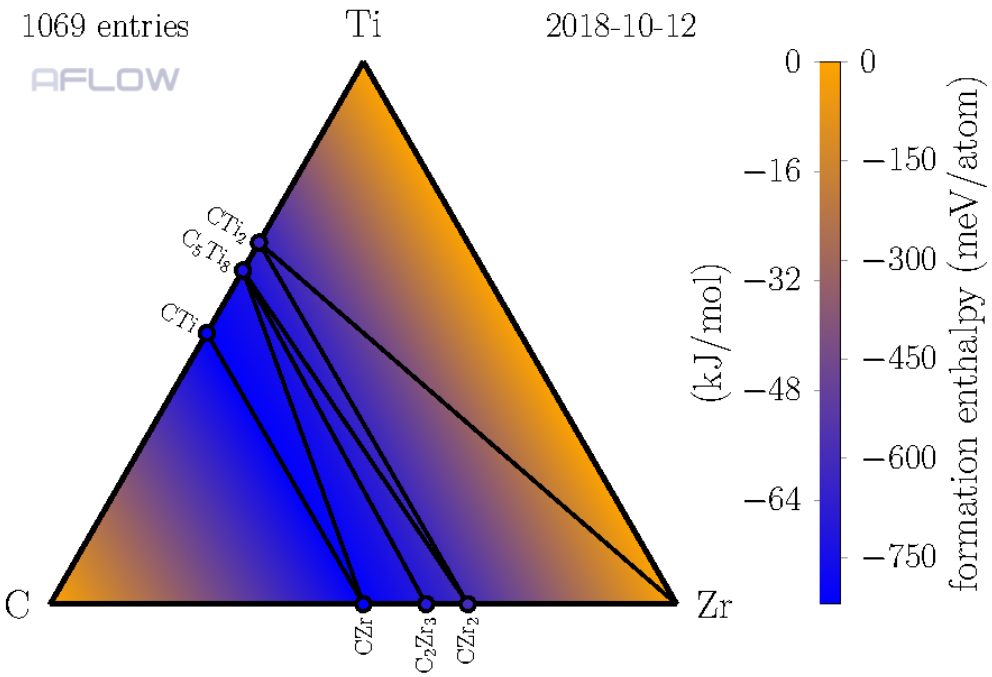

Supplementary Figure 33. CTiZr ternary hull as calculated with AFLOW-CHULL.

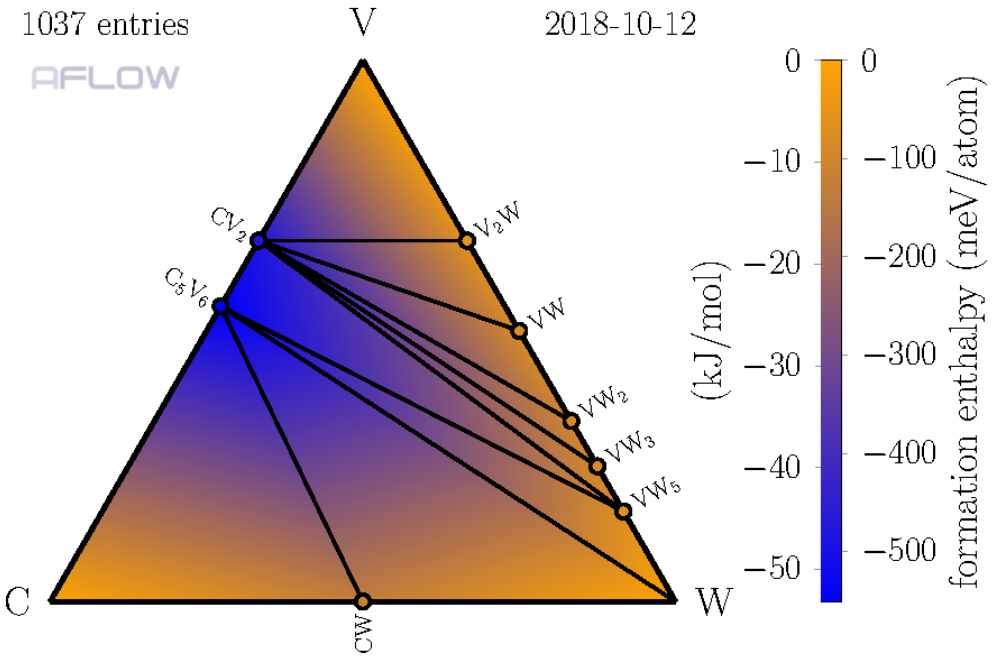

Supplementary Figure 34. CVW ternary hull as calculated with AFLOW-CHULL.

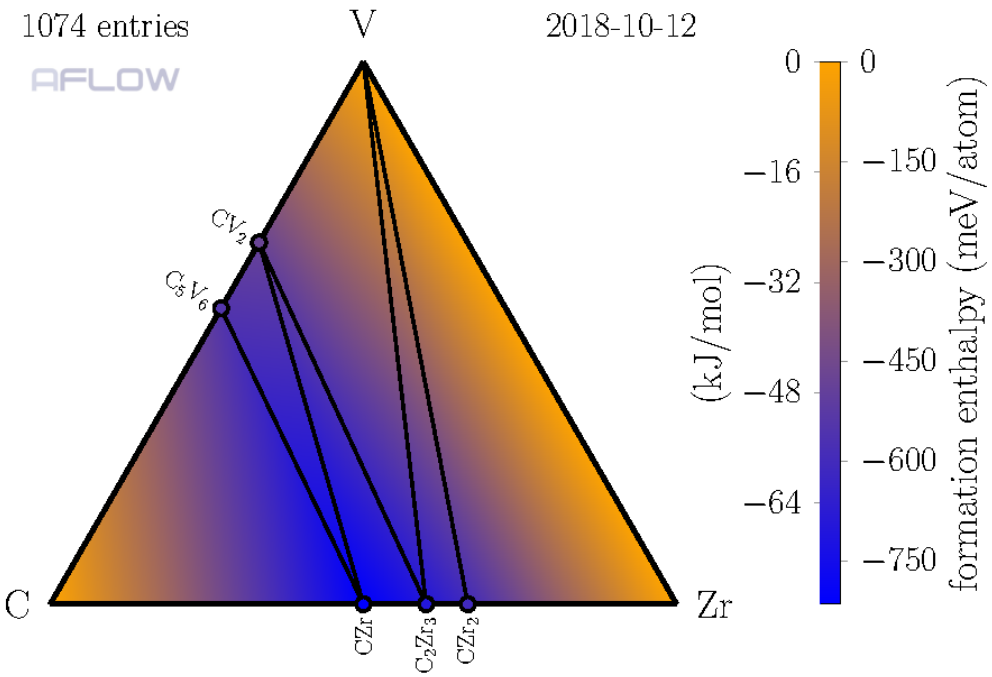

Supplementary Figure 35. CVZr ternary hull as calculated with AFLOW-CHULL.

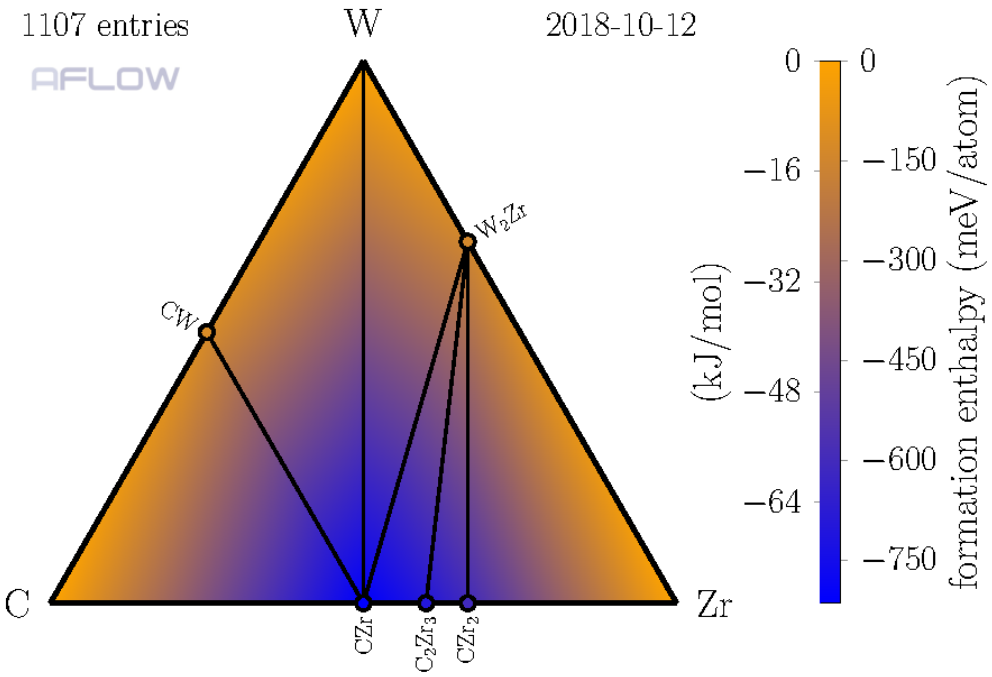

Supplementary Figure 36. CWZr ternary hull as calculated with AFLOW-CHULL.

Supplementary Table 1. Results for the calculated energetic distance from 6-dimensional convex hull, ΔH_f, and estimated synthesis temperature, T_s, for the 5-metal carbide systems, arranged in descending order of EFA. Note that the compositions listed here are nominal, and the actual synthesized compositions can vary due to the presence of carbon vacancies in the anion sublattice. Units: ΔH_f in (meV/atom) and T_s in K.

system	ΔH_f	T_s	system	ΔH_f	T_s	system	ΔH_f	T_s	system	ΔH_f	T_s
$MoNbTaVWC_5$	156	2254	$HfMoNbTaWC_5$	126	1811	$HfNbTiVWC_5$	81	1172	$HfMoNbVZrC_5$	89	1287
$HfNbTaTiZrC_5$	19	277	$HfMoNbTaVC_5$	99	1434	$HfNbTaWZrC_5$	53	764	$MoTaVWZrC_5$	148	2139
$HfNbTaTiVC_5$	56	807	$HfNbTaTiWC_5$	53	759	$NbTaVWZrC_5$	119	1718	$MoTaTiWZrC_5$	94	1359
$MoNbTaTiVC_5$	82	1185	$MoTaTiVWC_5$	128	1848	$HfTaTiVWC_5$	84	1210	$MoNbVWZrC_5$	146	2100
$NbTaTiVZrC_5$	64	922	$HfNbTaVZrC_5$	60	866	$HfMoTaVWC_5$	139	2010	$MoNbTiWZrC_5$	89	1282
$HfMoNbTaTiC_5$	48	689	$HfNbTaVWC_5$	110	1585	$HfMoNbVWC_5$	137	1977	$HfMoNbWZrC_5$	101	1452
$NbTaTiVWC_5$	92	1331	$HfMoTaTiVC_5$	82	1186	$HfNbTiWZrC_5$	56	811	$HfTiVWZrC_5$	99	1434
$MoNbTaTiWC_5$	111	1605	$HfMoNbTiZrC_5$	53	762	$HfMoTaTiWC_5$	84	1213	$HfNbVWZrC_5$	94	1359
$MoNbTiVWC_5$	122	1764	$MoNbTaWZrC_5$	133	1911	$HfMoNbTiWC_5$	81	1170	$HfMoTiVWC_5$	97	1394
$MoNbTaTiZrC_5$	57	815	$HfMoTaTiZrC_5$	55	799	$HfTaTiWZrC_5$	59	851	$HfMoTaWZrC_5$	105	1515
$HfTaTiVZrC_5$	73	1048	$NbTaTiWZrC_5$	61	879	$TaTiVWZrC_5$	96	1383	$HfTaVWZrC_5$	97	1395
$HfNbTiVZrC_5$	73	1058	$MoTaTiVZrC_5$	92	1330	$NbTiVWZrC_5$	93	1338	$MoTiVWZrC_5$	107	1541
$HfMoNbTiVC_5$	77	1112	$MoNbTiVZrC_5$	87	1259	$HfMoTiVZrC_5$	96	1380	$HfMoTiWZrC_5$	83	1192
$HfMoNbTaZrC_5$	48	690	$MoNbTaVZrC_5$	108	1562	$HfMoTaVZrC_5$	92	1326	$HfMoVWZrC_5$	141	2033

Supplementary Table 2. The predicted decomposition reaction products for the 56 5-metal carbides according to the AFLOW-CHULL module [1].

system	decomposition reaction products
$MoNbTaVWC_5$	$0.0333333\ C + 0.2\ C_{0.5}Mo_{0.5} + 0.2\ C_{0.5}Ta_{0.5} + 0.2\ C_{0.5}W_{0.5} + 0.183333\ C_{0.4545}Nb_{0.5455} + 0.183333\ C_{0.4545}V_{0.5455}$
$HfNbTaTiZrC_5$	$0.4\ C_{0.5}Hf_{0.25}Nb_{0.25} + 0.4\ C_{0.5}Ta_{0.25}Ti_{0.25} + 0.2\ C_{0.5}Zr_{0.5}$
$HfNbTaTiVC_5$	$0.0166667\ C + 0.4\ C_{0.5}Hf_{0.25}Nb_{0.25} + 0.4\ C_{0.5}Ta_{0.25}Ti_{0.25} + 0.183333\ C_{0.4545}V_{0.5455}$
$MoNbTaTiVC_5$	$0.0333333\ C + 0.2\ C_{0.5}Mo_{0.5} + 0.4\ C_{0.5}Ta_{0.25}Ti_{0.25} + 0.183333\ C_{0.4545}Nb_{0.5455} + 0.183333\ C_{0.4545}V_{0.5455}$
$NbTaTiVZrC_5$	$0.0166667\ C + 0.4\ C_{0.5}Nb_{0.25}Zr_{0.25} + 0.4\ C_{0.5}Ta_{0.25}Ti_{0.25} + 0.183333\ C_{0.4545}V_{0.5455}$
$HfMoNbTaTiC_5$	$0.4\ C_{0.5}Hf_{0.25}Nb_{0.25} + 0.2\ C_{0.5}Mo_{0.5} + 0.4\ C_{0.5}Ta_{0.25}Ti_{0.25}$
$NbTaTiVWC_5$	$0.0333333\ C + 0.4\ C_{0.5}Ta_{0.25}Ti_{0.25} + 0.2\ C_{0.5}W_{0.5} + 0.183333\ C_{0.4545}Nb_{0.5455} + 0.183333\ C_{0.4545}V_{0.5455}$
$MoNbTaTiWC_5$	$0.0166667\ C + 0.2\ C_{0.5}Mo_{0.5} + 0.4\ C_{0.5}Ta_{0.25}Ti_{0.25} + 0.2\ C_{0.5}W_{0.5} + 0.183333\ C_{0.4545}Nb_{0.5455}$
$MoNbTiVWC_5$	$0.0166667\ C + 0.2\ C_{0.5}Mo_{0.5} + 0.4\ C_{0.5}Nb_{0.25}Ti_{0.25} + 0.2\ C_{0.5}W_{0.5} + 0.183333\ C_{0.4545}V_{0.5455}$
$MoNbTaTiZrC_5$	$0.2\ C_{0.5}Mo_{0.5} + 0.4\ C_{0.5}Nb_{0.25}Zr_{0.25} + 0.4\ C_{0.5}Ta_{0.25}Ti_{0.25}$
$HfTaTiVZrC_5$	$0.0166667\ C + 0.2\ C_{0.5}Hf_{0.5} + 0.4\ C_{0.5}Ta_{0.25}Ti_{0.25} + 0.2\ C_{0.5}Zr_{0.5} + 0.183333\ C_{0.4545}V_{0.5455}$
$HfNbTiVZrC_5$	$0.0166667\ C + 0.2\ C_{0.5}Hf_{0.5} + 0.4\ C_{0.5}Nb_{0.25}Ti_{0.25} + 0.2\ C_{0.5}Zr_{0.5} + 0.183333\ C_{0.4545}V_{0.5455}$
$HfMoNbTiVC_5$	$0.0166667\ C + 0.2\ C_{0.5}Hf_{0.5} + 0.2\ C_{0.5}Mo_{0.5} + 0.4\ C_{0.5}Nb_{0.25}Ti_{0.25} + 0.183333\ C_{0.4545}V_{0.5455}$
$HfMoNbTaZrC_5$	$0.4\ C_{0.5}Hf_{0.25}Ta_{0.25} + 0.2\ C_{0.5}Mo_{0.5} + 0.4\ C_{0.5}Nb_{0.25}Zr_{0.25}$
$HfMoNbTaWC_5$	$0.0166667\ C + 0.4\ C_{0.5}Hf_{0.25}Ta_{0.25} + 0.2\ C_{0.5}Mo_{0.5} + 0.2\ C_{0.5}W_{0.5} + 0.183333\ C_{0.4545}Nb_{0.5455}$
$HfMoNbTaVC_5$	$0.0333333\ C + 0.4\ C_{0.5}Hf_{0.25}Ta_{0.25} + 0.2\ C_{0.5}Mo_{0.5} + 0.183333\ C_{0.4545}Nb_{0.5455} + 0.183333\ C_{0.4545}V_{0.5455}$
$HfNbTaTiWC_5$	$0.4\ C_{0.5}Hf_{0.25}Nb_{0.25} + 0.4\ C_{0.5}Ta_{0.25}Ti_{0.25} + 0.2\ C_{0.5}W_{0.5}$
$MoTaTiVWC_5$	$0.0166667\ C + 0.2\ C_{0.5}Mo_{0.5} + 0.4\ C_{0.5}Ta_{0.25}Ti_{0.25} + 0.2\ C_{0.5}W_{0.5} + 0.183333\ C_{0.4545}V_{0.5455}$
$HfNbTaVZrC_5$	$0.0166667\ C + 0.4\ C_{0.5}Hf_{0.25}Ta_{0.25} + 0.4\ C_{0.5}Nb_{0.25}Zr_{0.25} + 0.183333\ C_{0.4545}V_{0.5455}$
$HfNbTaVWC_5$	$0.0333333\ C + 0.4\ C_{0.5}Hf_{0.25}Ta_{0.25} + 0.2\ C_{0.5}W_{0.5} + 0.183333\ C_{0.4545}Nb_{0.5455} + 0.183333\ C_{0.4545}V_{0.5455}$
$HfMoTaTiVC_5$	$0.0166667\ C + 0.2\ C_{0.5}Hf_{0.5} + 0.2\ C_{0.5}Mo_{0.5} + 0.4\ C_{0.5}Ta_{0.25}Ti_{0.25} + 0.183333\ C_{0.4545}V_{0.5455}$
$HfMoNbTiZrC_5$	$0.2\ C_{0.5}Hf_{0.5} + 0.2\ C_{0.5}Mo_{0.5} + 0.4\ C_{0.5}Nb_{0.25}Ti_{0.25} + 0.2\ C_{0.5}Zr_{0.5}$
$MoNbTaWZrC_5$	$0.0166667\ C + 0.2\ C_{0.5}Mo_{0.5} + 0.4\ C_{0.5}Ta_{0.25}Zr_{0.25} + 0.2\ C_{0.5}W_{0.5} + 0.183333\ C_{0.4545}Nb_{0.5455}$
$HfMoTaTiZrC_5$	$0.2\ C_{0.5}Hf_{0.5} + 0.2\ C_{0.5}Mo_{0.5} + 0.4\ C_{0.5}Ta_{0.25}Ti_{0.25} + 0.2\ C_{0.5}Zr_{0.5}$
$NbTaTiWZrC_5$	$0.4\ C_{0.5}Nb_{0.25}Zr_{0.25} + 0.4\ C_{0.5}Ta_{0.25}Ti_{0.25} + 0.2\ C_{0.5}W_{0.5}$
$MoTaTiVZrC_5$	$0.0166667\ C + 0.2\ C_{0.5}Mo_{0.5} + 0.4\ C_{0.5}Ta_{0.25}Ti_{0.25} + 0.2\ C_{0.5}Zr_{0.5} + 0.183333\ C_{0.4545}V_{0.5455}$
$MoNbTiVZrC_5$	$0.0166667\ C + 0.2\ C_{0.5}Mo_{0.5} + 0.4\ C_{0.5}Nb_{0.25}Ti_{0.25} + 0.2\ C_{0.5}Zr_{0.5} + 0.183333\ C_{0.4545}V_{0.5455}$
$MoNbTaVZrC_5$	$0.0333333\ C + 0.2\ C_{0.5}Mo_{0.5} + 0.4\ C_{0.5}Ta_{0.25}Zr_{0.25} + 0.183333\ C_{0.4545}Nb_{0.5455} + 0.183333\ C_{0.4545}V_{0.5455}$
$HfNbTiVWC_5$	$0.0166667\ C + 0.2\ C_{0.5}Hf_{0.5} + 0.4\ C_{0.5}Nb_{0.25}Ti_{0.25} + 0.2\ C_{0.5}W_{0.5} + 0.183333\ C_{0.4545}V_{0.5455}$
$HfNbTaWZrC_5$	$0.4\ C_{0.5}Hf_{0.25}Ta_{0.25} + 0.4\ C_{0.5}Nb_{0.25}Zr_{0.25} + 0.2\ C_{0.5}W_{0.5}$
$NbTaVWZrC_5$	$0.0333333\ C + 0.4\ C_{0.5}Ta_{0.25}Zr_{0.25} + 0.2\ C_{0.5}W_{0.5} + 0.183333\ C_{0.4545}Nb_{0.5455} + 0.183333\ C_{0.4545}V_{0.5455}$
$HfTaTiVWC_5$	$0.0166667\ C + 0.2\ C_{0.5}Hf_{0.5} + 0.4\ C_{0.5}Ta_{0.25}Ti_{0.25} + 0.2\ C_{0.5}W_{0.5} + 0.183333\ C_{0.4545}V_{0.5455}$
$HfMoTaVWC_5$	$0.0166667\ C + 0.4\ C_{0.5}Hf_{0.25}Ta_{0.25} + 0.2\ C_{0.5}Mo_{0.5} + 0.2\ C_{0.5}W_{0.5} + 0.183333\ C_{0.4545}V_{0.5455}$
$HfMoNbVWC_5$	$0.0166667\ C + 0.4\ C_{0.5}Hf_{0.25}Nb_{0.25} + 0.2\ C_{0.5}Mo_{0.5} + 0.2\ C_{0.5}W_{0.5} + 0.183333\ C_{0.4545}V_{0.5455}$
$HfNbTiWZrC_5$	$0.2\ C_{0.5}Hf_{0.5} + 0.4\ C_{0.5}Nb_{0.25}Ti_{0.25} + 0.2\ C_{0.5}W_{0.5} + 0.2\ C_{0.5}Zr_{0.5}$
$HfMoTaTiWC_5$	$0.2\ C_{0.5}Hf_{0.5} + 0.2\ C_{0.5}Mo_{0.5} + 0.4\ C_{0.5}Ta_{0.25}Ti_{0.25} + 0.2\ C_{0.5}W_{0.5}$
$HfMoNbTiWC_5$	$0.2\ C_{0.5}Hf_{0.5} + 0.2\ C_{0.5}Mo_{0.5} + 0.4\ C_{0.5}Nb_{0.25}Ti_{0.25} + 0.2\ C_{0.5}W_{0.5}$
$HfTaTiWZrC_5$	$0.2\ C_{0.5}Hf_{0.5} + 0.4\ C_{0.5}Ta_{0.25}Ti_{0.25} + 0.2\ C_{0.5}W_{0.5} + 0.2\ C_{0.5}Zr_{0.5}$
$TaTiVWZrC_5$	$0.0166667\ C + 0.4\ C_{0.5}Ta_{0.25}Ti_{0.25} + 0.2\ C_{0.5}W_{0.5} + 0.2\ C_{0.5}Zr_{0.5} + 0.183333\ C_{0.4545}V_{0.5455}$
$NbTiVWZrC_5$	$0.0166667\ C + 0.4\ C_{0.5}Nb_{0.25}Ti_{0.25} + 0.2\ C_{0.5}W_{0.5} + 0.2\ C_{0.5}Zr_{0.5} + 0.183333\ C_{0.4545}V_{0.5455}$
$HfMoTiVZrC_5$	$0.0166667\ C + 0.2\ C_{0.5}Hf_{0.5} + 0.2\ C_{0.5}Mo_{0.5} + 0.2\ C_{0.5}Ti_{0.5} + 0.2\ C_{0.5}Zr_{0.5} + 0.183333\ C_{0.4545}V_{0.5455}$
$HfMoTaVZrC_5$	$0.0166667\ C + 0.4\ C_{0.5}Hf_{0.25}Ta_{0.25} + 0.2\ C_{0.5}Mo_{0.5} + 0.2\ C_{0.5}Zr_{0.5} + 0.183333\ C_{0.4545}V_{0.5455}$
$HfMoNbVZrC_5$	$0.0166667\ C + 0.4\ C_{0.5}Hf_{0.25}Nb_{0.25} + 0.2\ C_{0.5}Mo_{0.5} + 0.2\ C_{0.5}Zr_{0.5} + 0.183333\ C_{0.4545}V_{0.5455}$
$MoTaVWZrC_5$	$0.0166667\ C + 0.2\ C_{0.5}Mo_{0.5} + 0.4\ C_{0.5}Ta_{0.25}Zr_{0.25} + 0.2\ C_{0.5}W_{0.5} + 0.183333\ C_{0.4545}V_{0.5455}$
$MoTaTiWZrC_5$	$0.2\ C_{0.5}Mo_{0.5} + 0.4\ C_{0.5}Ta_{0.25}Ti_{0.25} + 0.2\ C_{0.5}W_{0.5} + 0.2\ C_{0.5}Zr_{0.5}$
$MoNbVWZrC_5$	$0.0166667\ C + 0.2\ C_{0.5}Mo_{0.5} + 0.4\ C_{0.5}Nb_{0.25}Zr_{0.25} + 0.2\ C_{0.5}W_{0.5} + 0.183333\ C_{0.4545}V_{0.5455}$
$MoNbTiWZrC_5$	$0.2\ C_{0.5}Mo_{0.5} + 0.4\ C_{0.5}Nb_{0.25}Ti_{0.25} + 0.2\ C_{0.5}W_{0.5} + 0.2\ C_{0.5}Zr_{0.5}$
$HfMoNbWZrC_5$	$0.4\ C_{0.5}Hf_{0.25}Nb_{0.25} + 0.2\ C_{0.5}Mo_{0.5} + 0.2\ C_{0.5}W_{0.5} + 0.2\ C_{0.5}Zr_{0.5}$
$HfTiVWZrC_5$	$0.0166667\ C + 0.2\ C_{0.5}Hf_{0.5} + 0.2\ C_{0.5}Ti_{0.5} + 0.2\ C_{0.5}W_{0.5} + 0.2\ C_{0.5}Zr_{0.5} + 0.183333\ C_{0.4545}V_{0.5455}$
$HfNbVWZrC_5$	$0.0166667\ C + 0.4\ C_{0.5}Hf_{0.25}Nb_{0.25} + 0.2\ C_{0.5}W_{0.5} + 0.2\ C_{0.5}Zr_{0.5} + 0.183333\ C_{0.4545}V_{0.5455}$
$HfMoTiVWC_5$	$0.0166667\ C + 0.2\ C_{0.5}Hf_{0.5} + 0.2\ C_{0.5}Mo_{0.5} + 0.2\ C_{0.5}Ti_{0.5} + 0.2\ C_{0.5}W_{0.5} + 0.183333\ C_{0.4545}V_{0.5455}$
$HfMoTaWZrC_5$	$0.4\ C_{0.5}Hf_{0.25}Ta_{0.25} + 0.2\ C_{0.5}Mo_{0.5} + 0.2\ C_{0.5}W_{0.5} + 0.2\ C_{0.5}Zr_{0.5}$
$HfTaVWZrC_5$	$0.0166667\ C + 0.4\ C_{0.5}Hf_{0.25}Ta_{0.25} + 0.2\ C_{0.5}W_{0.5} + 0.2\ C_{0.5}Zr_{0.5} + 0.183333\ C_{0.4545}V_{0.5455}$
$MoTiVWZrC_5$	$0.0166667\ C + 0.2\ C_{0.5}Mo_{0.5} + 0.2\ C_{0.5}Ti_{0.5} + 0.2\ C_{0.5}W_{0.5} + 0.2\ C_{0.5}Zr_{0.5} + 0.183333\ C_{0.4545}V_{0.5455}$
$HfMoTiWZrC_5$	$0.2\ C_{0.5}Hf_{0.5} + 0.2\ C_{0.5}Mo_{0.5} + 0.2\ C_{0.5}Ti_{0.5} + 0.2\ C_{0.5}W_{0.5} + 0.2\ C_{0.5}Zr_{0.5}$
$HfMoVWZrC_5$	$0.0166667\ C + 0.2\ C_{0.5}Hf_{0.5} + 0.2\ C_{0.5}Mo_{0.5} + 0.2\ C_{0.5}W_{0.5} + 0.2\ C_{0.5}Zr_{0.5} + 0.183333\ C_{0.4545}V_{0.5455}$

SUPPLEMENTARY NOTE 3: EFFECT OF PRECURSOR CHOICE ON SYNTHESIZABILITY

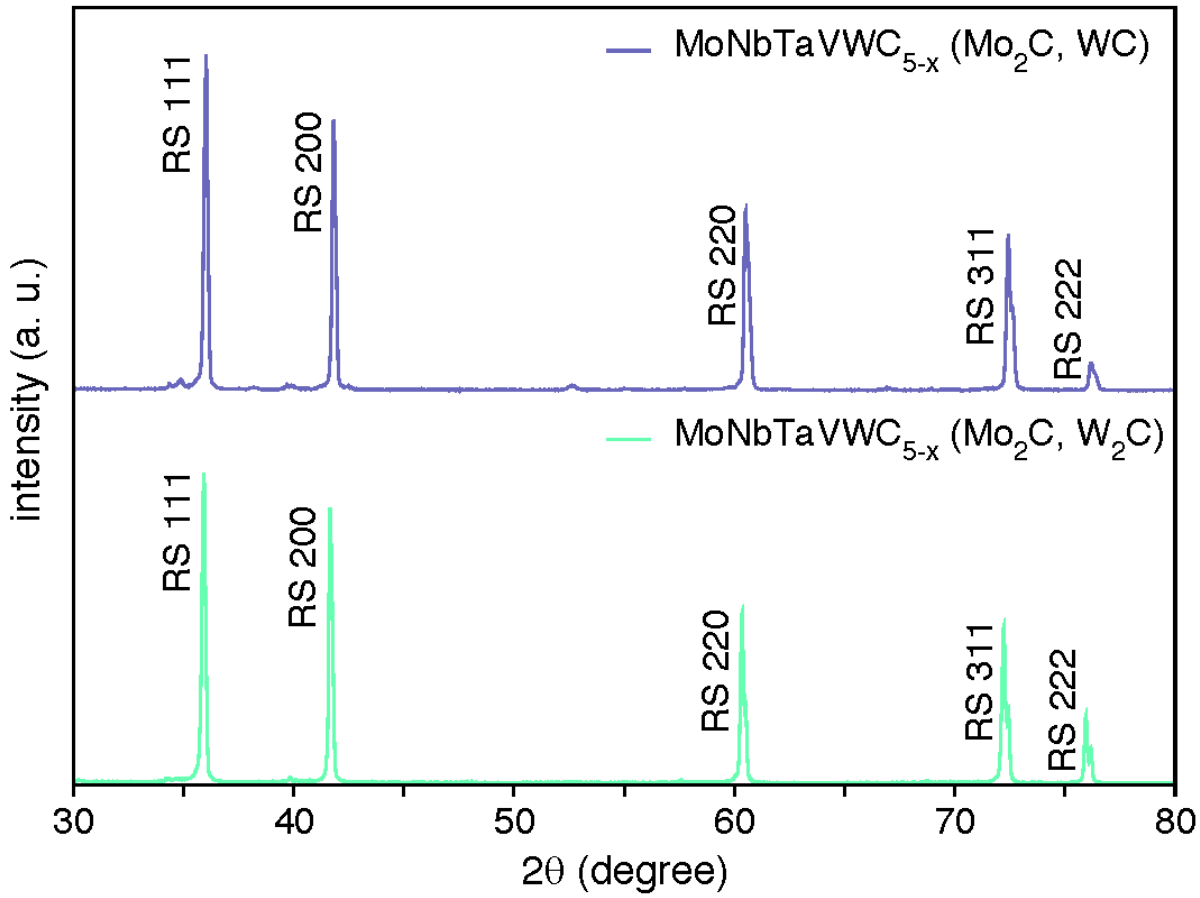

Supplementary Figure 37. **X-ray diffraction spectra for $MoNbTaVWC_{5-x}$. (Top)** Sample synthesized using Mo_2C and WC. **(Bottom)** Sample synthesized using Mo_2C and W_2C.

$MoNbTaVWC_{5-x}$ was synthesized using both hexagonal WC and W_2C precursors, to determine their impact on the homogeneity of the final sample. The x-ray diffraction spectrum for the sample synthesized using WC is displayed in the top panel of Figure 37, while the spectrum for the sample prepared with W_2C is shown in the bottom panel. Both spectra feature sharp peaks at similar values of 2θ, indicating that the choice of precursor has little effect on the structure of the high-entropy material.

SUPPLEMENTARY NOTE 4: MECHANICAL PROPERTIES

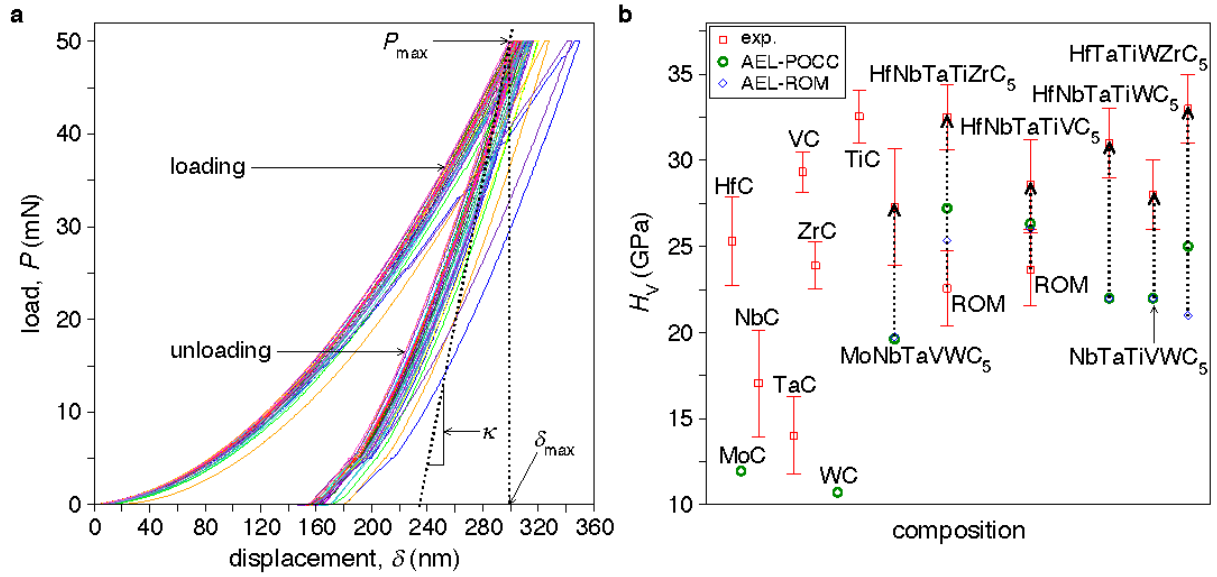

Supplementary Figure 38. **Mechanical properties.** (a) Load-displacement curves for 40 indents for $HfNbTaTiZrC_5$ at a maximum load of 50mN. This curve provides the three necessary parameters the peak load: P_{max}, the depth at peak load: δ_{max}, and the initial unloading contact stiffness: κ, (indicated by arrows for an indent) for obtaining Vickers hardness: H_V, and elastic modulus: E [2]. (b) Comparison of calculated and measured H_V for 6 single-phase 5-metal carbides. All 5-metal carbides have a higher hardness than expected from their respective ROM predictions (indicated by the dotted upward arrows), whereas the calculated H_V (green circles) are consistent with the ROM for the AFLOW-AEL results (blue diamonds). The measured H_V for the 6 rock-salt structure binary carbide samples along with the calculated H_V for rock-salt MoC and WC are also plotted. Error bars represent the standard deviations for a series of 40 indents.

The experimentally measured load-displacement indentation curves for the hardness measurements for the $HfNbTaTiZrC_5$ sample are shown in Figure 38(a). Each curve provides the three parameters necessary to obtain the Vickers hardness H_V and elastic modulus E [2, 3]: the peak load: P_{max}, the depth at peak load: δ_{max}, and the initial unloading contact stiffness: κ.

The measured and calculated H_V for 6 5-metal carbides along with 8 rock-salt binary carbides are plotted in Figure 38(b). The calculated H_V are obtained from the thermally averaged bulk (B) and shear (G) moduli, weighted according to the Boltzmann distribution at a temperature of 2200°C (the experimental sintering temperature), using the model of Chen *et al.* ($H_V = 2(k^2G)^{0.585} - 3$; $k = G/B$) [4]. The experimentally measured hardness for all 5-metal carbides exceeds the rule of mixture (ROM) predictions, whereas the calculated values are consistent with the ROM for the AFLOW-AEL (Automatic Elasticity Library) results. The atomic disorder is not accounted for in the AFLOW-AEL calculations of the AFLOW-POCC ordered-configurations, suggesting that the measured enhancement in H_V is disorder-driven. For $HfNbTaTiZrC_5$, H_V is about 50% higher than the ROM estimate. Note that the ROM predictions for Mo and/or W containing 5-metal carbides are obtained from the AFLOW-AEL calculations, since MoC and WC do not stabilize in a rock-salt phase at ambient temperature.

The values of B and G for each of the 49 configurations of 6 5-metal carbides are listed in Supplementary Table 3. These elastic moduli are calculated using the Voigt-Reuss-Hill (VRH) average within the AEL module [5] of the AFLOW framework.

Supplementary Table 3. B and G for each configuration of 6 5-metal carbides, as calculated using AFLOW-AEL. Units: B, G in GPa.

conf.	$MoNbTaVWC_5$		$HfNbTaTiZrC_5$		$HfNbTaTiVC_5$		$HfNbTaTiWC_5$		$NbTaTiVWC_5$		$HfTaTiWZrC_5$	
	B	G	B	G	B	G	B	G	B	G	B	G
1	322	166	262	189	284	193	280	188	305	189	274	189
2	317	198	259	186	270	194	290	201	340	168	269	183
3	312	191	260	190	278	191	282	201	303	189	275	193
4	308	195	262	187	281	194	283	205	307	187	270	186
5	315	199	260	192	274	193	283	197	304	200	272	187
6	313	175	260	190	271	192	286	203	314	183	275	182
7	319	189	262	192	273	199	290	201	304	201	277	190
8	310	184	261	190	278	197	293	199	330	189	276	191
9	322	194	261	194	273	196	283	196	309	201	270	187
10	313	191	261	189	273	195	287	198	307	201	271	178
11	318	192	260	195	275	194	283	200	303	202	272	189
12	307	177	262	191	276	193	291	199	304	200	280	197
13	316	188	258	189	280	200	290	203	306	200	269	181
14	305	188	260	190	277	197	291	198	303	199	273	185
15	318	186	258	192	278	197	293	203	305	170	276	196
16	316	187	260	189	274	192	290	198	304	198	273	183
17	305	188	263	195	279	198	285	200	309	189	273	183
18	316	190	262	193	280	198	283	195	346	172	272	183
19	314	196	264	194	276	194	295	204	299	201	273	189
20	318	187	261	192	277	198	296	201	303	199	272	187
21	325	188	262	195	275	193	291	203	304	200	274	189
22	321	187	262	190	279	196	294	201	305	201	272	181
23	315	171	262	194	276	195	292	205	304	200	277	191
24	321	193	262	192	283	202	296	206	312	181	273	183
25	319	189	262	191	276	197	292	199	297	201	274	190
26	314	173	262	191	274	194	292	204	293	195	276	194
27	317	186	264	193	273	194	292	201	305	205	276	193
28	316	192	264	192	274	192	292	201	304	203	275	195
29	322	188	266	196	272	191	294	205	295	199	273	191
30	314	181	262	191	273	192	291	201	299	197	273	190
31	265	169	264	194	276	196	288	203	300	200	275	194
32	277	181	265	195	276	197	293	202	296	198	274	189
33	318	190	262	190	277	194	294	204	308	206	273	192
34	277	183	263	192	276	195	291	201	305	204	274	189
35	324	189	261	189	274	194	290	202	294	199	279	196
36	318	182	262	194	276	191	294	203	301	204	279	195
37	316	182	263	192	277	196	294	203	302	180	273	187
38	315	182	262	192	276	195	292	203	298	199	272	189
39	313	188	262	192	276	196	295	208	298	199	274	194
40	270	127	262	192	282	198	291	202	306	203	272	194
41	315	174	264	191	277	197	287	201	306	203	275	193
42	319	184	263	193	276	197	291	204	304	202	275	193
43	313	171	264	195	274	192	292	204	297	198	273	192
44	312	181	263	192	275	197	295	206	307	205	274	191
45	314	180	263	194	276	194	292	196	307	204	273	191
46	317	183	263	191	277	193	294	200	305	204	274	191
47	325	190	265	194	277	198	292	203	304	204	275	193
48	320	192	266	193	279	197	292	201	304	205	278	195
49	311	177	264	193	275	196	295	204	306	203	275	195

SUPPLEMENTARY NOTE 5: ELECTRONIC DENSITY OF STATES

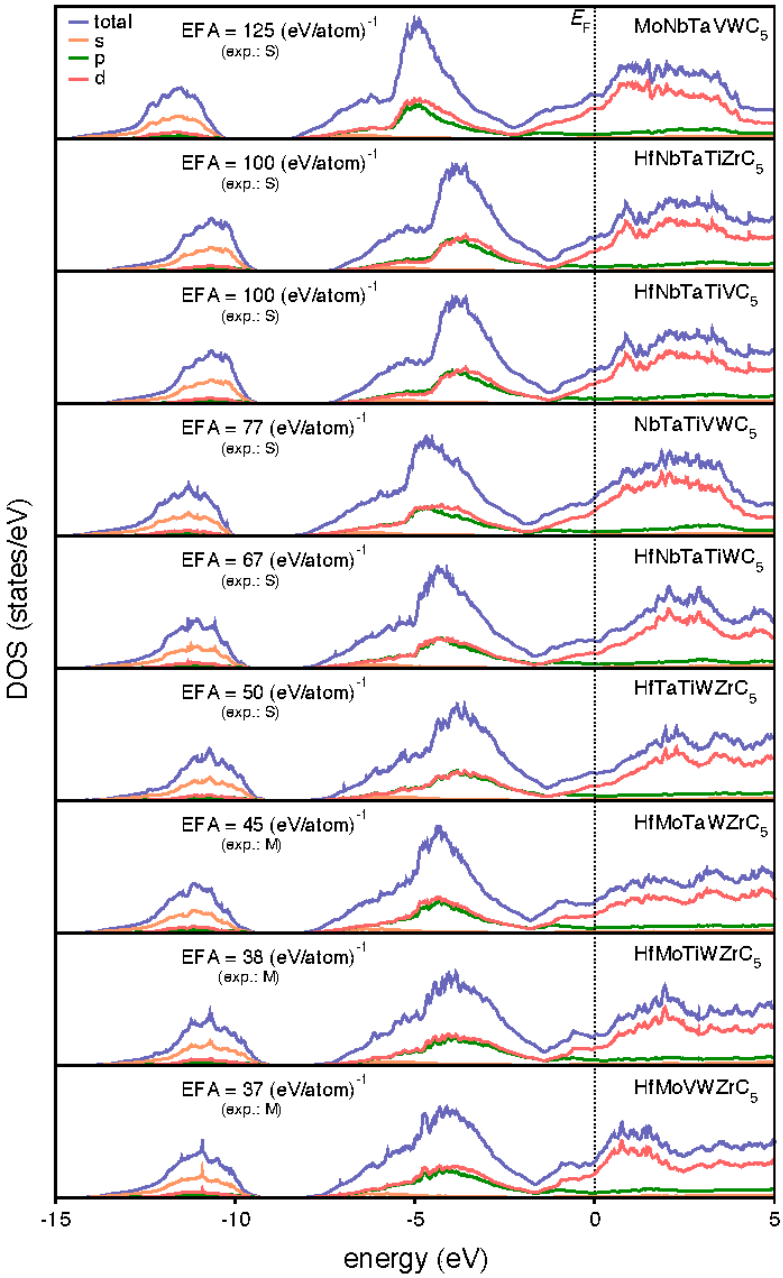

Supplementary Figure 39. **Electronic density of states (DOS).** The AFLOW-POCC ensemble averaged DOS [6] for the 9 synthesized 5-metal carbides, calculated at the experimental sintering temperature, 2200°C. "E_F": Fermi energy."S": single-phase formed; "M": multi-phase formed in experiment.

SUPPLEMENTARY NOTE 6: FORMATION ENTHALPIES

The formation enthalpies (H_f) for each of the 49 configurations of all 56 5-metal carbide compositions are listed in Supplementary Tables 4-10. Carbides are arranged from left to right in each table in descending order of EFA. Each enthalpy value also acts as a link to the AFLOW.org entry page for the corresponding composition and configuration, which contains crystallographic, thermodynamic, and electronic structure data for the system.

H_f are calculated using

$$H_\mathrm{f} = H_{\mathrm{POCC},i} - \sum_{\alpha}^{N} x_\alpha H_\alpha \tag{1}$$

where $H_{\mathrm{POCC},i}$ is the enthalpy per atom for each POCC configuration of the N-metal carbide, H_α are the enthalpies per atom for the corresponding constituent species α in their standard elemental phases, and x_α is the molar concentration of species α.

Supplementary Table 4. Formation enthalpies (H_f) with links to AFLOW.org entry pages for each calculated configuration. Units: H_f in eV/atom.

conf.	$MoNbTaVWC_5$	$HfNbTaTiZrC_5$	$HfNbTaTiVC_5$	$MoNbTaTiVC_5$	$HfMoNbTaTiC_5$	$NbTaTiVZrC_5$	$NbTaTiVWC_5$	$MoNbTaTiWC_5$
	H_f	H_f	H_f	H_f	H_f	H_f	H_f	H_f
1	-0.192	-0.754	-0.639	-0.42	-0.577	-0.601	-0.425	-0.307
2	-0.203	-0.734	-0.647	-0.43	-0.562	-0.612	-0.411	-0.329
3	-0.198	-0.757	-0.655	-0.427	-0.557	-0.62	-0.416	-0.311
4	-0.206	-0.735	-0.652	-0.432	-0.555	-0.617	-0.413	-0.331
5	-0.2	-0.736	-0.622	-0.423	-0.552	-0.578	-0.416	-0.316
6	-0.185	-0.756	-0.623	-0.423	-0.552	-0.578	-0.42	-0.31
7	-0.19	-0.736	-0.648	-0.428	-0.567	-0.613	-0.415	-0.312
8	-0.197	-0.755	-0.635	-0.424	-0.544	-0.597	-0.43	-0.326
9	-0.199	-0.734	-0.638	-0.429	-0.578	-0.595	-0.408	-0.315
10	-0.2	-0.726	-0.636	-0.428	-0.54	-0.594	-0.406	-0.317
11	-0.203	-0.737	-0.622	-0.423	-0.552	-0.577	-0.423	-0.328
12	-0.198	-0.727	-0.62	-0.422	-0.572	-0.576	-0.423	-0.315
13	-0.2	-0.753	-0.658	-0.442	-0.534	-0.623	-0.431	-0.322
14	-0.197	-0.733	-0.648	-0.438	-0.557	-0.611	-0.435	-0.306
15	-0.199	-0.756	-0.64	-0.432	-0.535	-0.6	-0.422	-0.323
16	-0.201	-0.734	-0.635	-0.437	-0.568	-0.593	-0.434	-0.321
17	-0.199	-0.746	-0.65	-0.432	-0.555	-0.602	-0.44	-0.319
18	-0.197	-0.716	-0.649	-0.44	-0.531	-0.611	-0.437	-0.308
19	-0.205	-0.744	-0.639	-0.441	-0.556	-0.609	-0.426	-0.324
20	-0.198	-0.714	-0.636	-0.436	-0.553	-0.598	-0.425	-0.319
21	-0.199	-0.735	-0.636	-0.433	-0.542	-0.594	-0.44	-0.328
22	-0.198	-0.726	-0.639	-0.432	-0.565	-0.599	-0.436	-0.326
23	-0.187	-0.737	-0.647	-0.437	-0.565	-0.61	-0.442	-0.335
24	-0.209	-0.744	-0.655	-0.436	-0.549	-0.62	-0.428	-0.31
25	-0.21	-0.743	-0.628	-0.457	-0.56	-0.582	-0.454	-0.336
26	-0.19	-0.729	-0.627	-0.449	-0.554	-0.604	-0.448	-0.334
27	-0.207	-0.746	-0.643	-0.435	-0.583	-0.611	-0.426	-0.312
28	-0.209	-0.743	-0.649	-0.447	-0.577	-0.581	-0.424	-0.331
29	-0.205	-0.757	-0.65	-0.449	-0.556	-0.612	-0.444	-0.332
30	-0.213	-0.755	-0.65	-0.457	-0.569	-0.612	-0.444	-0.341
31	-0.214	-0.749	-0.648	-0.433	-0.569	-0.609	-0.448	-0.345
32	-0.219	-0.755	-0.643	-0.449	-0.538	-0.604	-0.455	-0.352
33	-0.206	-0.733	-0.615	-0.445	-0.537	-0.567	-0.441	-0.333
34	-0.22	-0.756	-0.612	-0.43	-0.569	-0.564	-0.439	-0.352
35	-0.203	-0.732	-0.65	-0.456	-0.547	-0.612	-0.45	-0.332
36	-0.216	-0.749	-0.644	-0.455	-0.565	-0.605	-0.45	-0.344
37	-0.209	-0.754	-0.629	-0.455	-0.576	-0.607	-0.452	-0.342
38	-0.213	-0.751	-0.645	-0.451	-0.564	-0.607	-0.451	-0.342
39	-0.201	-0.754	-0.645	-0.445	-0.564	-0.584	-0.451	-0.331
40	-0.214	-0.751	-0.627	-0.444	-0.578	-0.583	-0.432	-0.343
41	-0.213	-0.755	-0.639	-0.453	-0.57	-0.596	-0.44	-0.342
42	-0.197	-0.746	-0.642	-0.454	-0.578	-0.601	-0.436	-0.328
43	-0.214	-0.749	-0.643	-0.435	-0.573	-0.604	-0.449	-0.343
44	-0.217	-0.755	-0.648	-0.437	-0.561	-0.609	-0.431	-0.345
45	-0.209	-0.749	-0.63	-0.442	-0.57	-0.586	-0.45	-0.342
46	-0.198	-0.745	-0.628	-0.437	-0.562	-0.585	-0.449	-0.33
47	-0.21	-0.747	-0.642	-0.447	-0.557	-0.597	-0.448	-0.339
48	-0.209	-0.746	-0.643	-0.442	-0.553	-0.602	-0.442	-0.338
49	-0.214	-0.748	-0.639	-0.446	-0.567	-0.597	-0.445	-0.347

Supplementary Table 5. Formation enthalpies (H_f) with links to AFLOW.org entry pages for each calculated configuration. Units: H_f in eV/atom.

conf.	$MoNbTaTiZrC_5$	$HfMoNbTaZrC_5$	$HfTaTiVZrC_5$	$HfNbTiVZrC_5$	$HfMoNbTiVC_5$	$HfMoNbTaVC_5$	$MoNbTiVWC_5$	$HfMoNbTaWC_5$
	H_f	H_f	H_f	H_f	H_f	H_f	H_f	H_f
1	-0.544	-0.563	-0.688	-0.654	-0.5	-0.448	-0.256	-0.323
2	-0.53	-0.564	-0.684	-0.666	-0.516	-0.44	-0.276	-0.33
3	-0.52	-0.527	-0.685	-0.655	-0.478	-0.439	-0.264	-0.309
4	-0.514	-0.55	-0.67	-0.665	-0.496	-0.424	-0.273	-0.335
5	-0.515	-0.526	-0.684	-0.667	-0.478	-0.434	-0.27	-0.305
6	-0.511	-0.534	-0.671	-0.664	-0.477	-0.422	-0.259	-0.338
7	-0.509	-0.548	-0.646	-0.63	-0.497	-0.443	-0.256	-0.314
8	-0.535	-0.52	-0.647	-0.632	-0.5	-0.438	-0.255	-0.315
9	-0.497	-0.519	-0.652	-0.632	-0.463	-0.448	-0.275	-0.331
10	-0.517	-0.534	-0.651	-0.634	-0.466	-0.412	-0.271	-0.325
11	-0.544	-0.518	-0.653	-0.626	-0.458	-0.442	-0.267	-0.342
12	-0.491	-0.572	-0.651	-0.627	-0.46	-0.454	-0.263	-0.327
13	-0.539	-0.518	-0.659	-0.656	-0.5	-0.407	-0.295	-0.311
14	-0.491	-0.559	-0.661	-0.653	-0.5	-0.426	-0.281	-0.309
15	-0.515	-0.541	-0.684	-0.649	-0.493	-0.405	-0.277	-0.331
16	-0.534	-0.542	-0.674	-0.646	-0.499	-0.449	-0.28	-0.309
17	-0.488	-0.573	-0.686	-0.649	-0.491	-0.424	-0.292	-0.307
18	-0.521	-0.524	-0.668	-0.649	-0.483	-0.402	-0.291	-0.329
19	-0.515	-0.546	-0.67	-0.657	-0.497	-0.443	-0.284	-0.331
20	-0.508	-0.542	-0.673	-0.664	-0.518	-0.434	-0.287	-0.323
21	-0.512	-0.522	-0.67	-0.639	-0.479	-0.42	-0.275	-0.332
22	-0.526	-0.56	-0.669	-0.641	-0.479	-0.439	-0.286	-0.35
23	-0.527	-0.545	-0.671	-0.656	-0.478	-0.441	-0.271	-0.325
24	-0.521	-0.541	-0.669	-0.667	-0.497	-0.416	-0.296	-0.327
25	-0.509	-0.524	-0.672	-0.646	-0.47	-0.432	-0.3	-0.326
26	-0.516	-0.559	-0.671	-0.651	-0.471	-0.427	-0.292	-0.352
27	-0.516	-0.56	-0.672	-0.647	-0.513	-0.423	-0.306	-0.356
28	-0.547	-0.554	-0.666	-0.65	-0.506	-0.455	-0.307	-0.35
29	-0.541	-0.545	-0.671	-0.619	-0.491	-0.457	-0.283	-0.303
30	-0.495	-0.521	-0.667	-0.619	-0.505	-0.443	-0.279	-0.304
31	-0.493	-0.547	-0.633	-0.651	-0.498	-0.407	-0.299	-0.33
32	-0.53	-0.553	-0.629	-0.65	-0.503	-0.405	-0.293	-0.33
33	-0.532	-0.544	-0.635	-0.609	-0.468	-0.448	-0.276	-0.33
34	-0.508	-0.547	-0.631	-0.612	-0.468	-0.416	-0.272	-0.345
35	-0.532	-0.539	-0.674	-0.612	-0.498	-0.445	-0.307	-0.353
36	-0.527	-0.535	-0.67	-0.615	-0.502	-0.441	-0.303	-0.351
37	-0.54	-0.563	-0.64	-0.646	-0.501	-0.457	-0.289	-0.345
38	-0.528	-0.558	-0.64	-0.645	-0.509	-0.449	-0.288	-0.353
39	-0.535	-0.563	-0.674	-0.649	-0.493	-0.435	-0.3	-0.325
40	-0.542	-0.559	-0.669	-0.653	-0.455	-0.451	-0.294	-0.344
41	-0.526	-0.537	-0.666	-0.649	-0.457	-0.448	-0.307	-0.349
42	-0.542	-0.534	-0.665	-0.653	-0.492	-0.457	-0.308	-0.313
43	-0.536	-0.514	-0.647	-0.635	-0.497	-0.45	-0.294	-0.337
44	-0.535	-0.554	-0.647	-0.637	-0.493	-0.431	-0.296	-0.353
45	-0.526	-0.553	-0.647	-0.626	-0.49	-0.448	-0.3	-0.35
46	-0.523	-0.512	-0.648	-0.626	-0.484	-0.442	-0.291	-0.326
47	-0.517	-0.544	-0.658	-0.637	-0.49	-0.422	-0.291	-0.31
48	-0.514	-0.538	-0.658	-0.628	-0.478	-0.42	-0.3	-0.327
49	-0.527	-0.537	-0.66	-0.627	-0.484	-0.433	-0.303	-0.329

Supplementary Table 6. Formation enthalpies (H_f) with links to AFLOW.org entry pages for each calculated configuration. Units: H_f in eV/atom.

conf.	$HfNbTaTiWC_5$	$HfNbTaVZrC_5$	$HfMoNbTiZrC_5$	$HfMoTaTiVC_5$	$HfNbTaVWC_5$	$MoTaTiVWC_5$	$HfMoTaTiZrC_5$	$MoNbTaWZrC_5$
	H_f	H_f	H_f	H_f	H_f	H_f	H_f	H_f
1	-0.558	-0.644	-0.599	-0.489	-0.431	-0.277	-0.615	-0.299
2	-0.578	-0.625	-0.598	-0.509	-0.445	-0.274	-0.585	-0.291
3	-0.535	-0.644	-0.573	-0.518	-0.427	-0.265	-0.619	-0.268
4	-0.554	-0.625	-0.597	-0.53	-0.431	-0.27	-0.586	-0.264
5	-0.547	-0.635	-0.574	-0.478	-0.437	-0.28	-0.617	-0.306
6	-0.546	-0.635	-0.601	-0.48	-0.423	-0.277	-0.616	-0.308
7	-0.546	-0.635	-0.574	-0.496	-0.414	-0.271	-0.582	-0.3
8	-0.554	-0.635	-0.571	-0.496	-0.422	-0.278	-0.57	-0.274
9	-0.568	-0.596	-0.574	-0.514	-0.449	-0.268	-0.586	-0.274
10	-0.565	-0.589	-0.555	-0.506	-0.436	-0.267	-0.57	-0.312
11	-0.562	-0.599	-0.602	-0.474	-0.443	-0.277	-0.588	-0.271
12	-0.52	-0.64	-0.576	-0.47	-0.39	-0.28	-0.587	-0.293
13	-0.579	-0.59	-0.556	-0.517	-0.445	-0.288	-0.594	-0.291
14	-0.522	-0.62	-0.562	-0.514	-0.392	-0.3	-0.59	-0.301
15	-0.537	-0.641	-0.604	-0.505	-0.406	-0.297	-0.619	-0.269
16	-0.53	-0.62	-0.566	-0.497	-0.4	-0.297	-0.586	-0.292
17	-0.533	-0.607	-0.576	-0.517	-0.423	-0.296	-0.622	-0.269
18	-0.553	-0.578	-0.575	-0.511	-0.441	-0.303	-0.588	-0.292
19	-0.544	-0.606	-0.549	-0.489	-0.412	-0.29	-0.557	-0.265
20	-0.539	-0.577	-0.553	-0.49	-0.407	-0.287	-0.554	-0.293
21	-0.552	-0.594	-0.557	-0.488	-0.419	-0.291	-0.601	-0.294
22	-0.555	-0.586	-0.56	-0.505	-0.423	-0.294	-0.602	-0.263
23	-0.565	-0.596	-0.59	-0.493	-0.438	-0.298	-0.603	-0.264
24	-0.568	-0.609	-0.591	-0.493	-0.442	-0.294	-0.578	-0.296
25	-0.523	-0.589	-0.586	-0.51	-0.39	-0.318	-0.601	-0.291
26	-0.55	-0.61	-0.543	-0.533	-0.415	-0.319	-0.564	-0.29
27	-0.531	-0.613	-0.541	-0.508	-0.399	-0.289	-0.58	-0.315
28	-0.546	-0.612	-0.586	-0.524	-0.412	-0.286	-0.611	-0.317
29	-0.561	-0.628	-0.582	-0.525	-0.431	-0.305	-0.609	-0.314
30	-0.574	-0.624	-0.597	-0.533	-0.449	-0.314	-0.569	-0.321
31	-0.586	-0.627	-0.597	-0.516	-0.453	-0.307	-0.615	-0.3
32	-0.556	-0.593	-0.584	-0.513	-0.426	-0.311	-0.602	-0.316
33	-0.562	-0.618	-0.584	-0.473	-0.431	-0.303	-0.615	-0.319
34	-0.563	-0.624	-0.578	-0.521	-0.442	-0.302	-0.603	-0.294
35	-0.57	-0.592	-0.585	-0.468	-0.426	-0.315	-0.614	-0.295
36	-0.559	-0.617	-0.597	-0.516	-0.444	-0.319	-0.614	-0.289
37	-0.568	-0.617	-0.597	-0.51	-0.442	-0.306	-0.584	-0.311
38	-0.567	-0.624	-0.579	-0.511	-0.44	-0.303	-0.582	-0.317
39	-0.57	-0.617	-0.572	-0.51	-0.442	-0.323	-0.607	-0.318
40	-0.579	-0.624	-0.585	-0.513	-0.454	-0.318	-0.607	-0.309
41	-0.573	-0.61	-0.585	-0.488	-0.447	-0.313	-0.617	-0.315
42	-0.574	-0.623	-0.598	-0.517	-0.449	-0.307	-0.602	-0.273
43	-0.581	-0.618	-0.598	-0.487	-0.45	-0.295	-0.616	-0.291
44	-0.57	-0.624	-0.574	-0.523	-0.443	-0.291	-0.593	-0.297
45	-0.561	-0.617	-0.588	-0.499	-0.436	-0.313	-0.602	-0.319
46	-0.57	-0.609	-0.588	-0.491	-0.444	-0.31	-0.595	-0.316
47	-0.551	-0.612	-0.567	-0.507	-0.414	-0.312	-0.593	-0.27
48	-0.552	-0.612	-0.568	-0.509	-0.417	-0.306	-0.596	-0.291
49	-0.568	-0.611	-0.59	-0.503	-0.432	-0.306	-0.609	-0.294

Supplementary Table 7. Formation enthalpies (H_f) with links to AFLOW.org entry pages for each calculated configuration. Units: H_f in eV/atom.

conf.	$NbTaTiWZrC_5$	$HfNbTaWZrC_5$	$HfNbTiVWC_5$	$MoTaTiVZrC_5$	$MoNbTiVZrC_5$	$MoNbTaVZrC_5$	$HfTaTiVWC_5$	$NbTaVWZrC_5$
	H_f	H_f	H_f	H_f	H_f	H_f	H_f	H_f
1	-0.525	-0.56	-0.516	-0.451	-0.465	-0.415	-0.482	-0.396
2	-0.545	-0.562	-0.498	-0.473	-0.479	-0.406	-0.505	-0.414
3	-0.499	-0.516	-0.492	-0.483	-0.439	-0.403	-0.515	-0.392
4	-0.517	-0.525	-0.497	-0.493	-0.46	-0.398	-0.531	-0.403
5	-0.512	-0.504	-0.473	-0.431	-0.435	-0.383	-0.508	-0.396
6	-0.509	-0.517	-0.494	-0.433	-0.434	-0.379	-0.5	-0.387
7	-0.505	-0.524	-0.479	-0.453	-0.458	-0.404	-0.47	-0.371
8	-0.513	-0.547	-0.476	-0.453	-0.464	-0.409	-0.474	-0.38
9	-0.536	-0.503	-0.453	-0.477	-0.417	-0.367	-0.494	-0.417
10	-0.476	-0.555	-0.453	-0.467	-0.419	-0.407	-0.496	-0.344
11	-0.532	-0.511	-0.458	-0.428	-0.412	-0.414	-0.466	-0.41
12	-0.529	-0.538	-0.461	-0.425	-0.413	-0.362	-0.463	-0.402
13	-0.479	-0.541	-0.5	-0.482	-0.459	-0.421	-0.518	-0.346
14	-0.546	-0.512	-0.504	-0.473	-0.464	-0.359	-0.512	-0.412
15	-0.493	-0.545	-0.495	-0.463	-0.453	-0.383	-0.498	-0.36
16	-0.487	-0.554	-0.52	-0.453	-0.46	-0.415	-0.506	-0.354
17	-0.498	-0.575	-0.482	-0.477	-0.448	-0.357	-0.521	-0.388
18	-0.519	-0.537	-0.48	-0.47	-0.439	-0.409	-0.516	-0.407
19	-0.503	-0.51	-0.498	-0.451	-0.459	-0.383	-0.482	-0.37
20	-0.499	-0.511	-0.502	-0.466	-0.481	-0.4	-0.499	-0.365
21	-0.511	-0.54	-0.485	-0.442	-0.437	-0.378	-0.493	-0.376
22	-0.515	-0.557	-0.493	-0.441	-0.436	-0.401	-0.493	-0.381
23	-0.527	-0.534	-0.493	-0.451	-0.44	-0.404	-0.508	-0.344
24	-0.479	-0.52	-0.473	-0.451	-0.457	-0.391	-0.535	-0.4
25	-0.53	-0.543	-0.522	-0.473	-0.475	-0.375	-0.511	-0.404
26	-0.511	-0.557	-0.514	-0.496	-0.468	-0.387	-0.525	-0.352
27	-0.487	-0.534	-0.503	-0.467	-0.423	-0.382	-0.492	-0.374
28	-0.507	-0.539	-0.51	-0.484	-0.424	-0.362	-0.532	-0.372
29	-0.522	-0.542	-0.496	-0.486	-0.45	-0.359	-0.492	-0.39
30	-0.518	-0.575	-0.508	-0.493	-0.466	-0.419	-0.539	-0.386
31	-0.538	-0.554	-0.468	-0.477	-0.459	-0.419	-0.522	-0.411
32	-0.55	-0.538	-0.471	-0.474	-0.466	-0.404	-0.517	-0.416
33	-0.527	-0.552	-0.475	-0.423	-0.422	-0.412	-0.465	-0.405
34	-0.535	-0.54	-0.474	-0.418	-0.422	-0.376	-0.465	-0.408
35	-0.531	-0.554	-0.508	-0.482	-0.458	-0.409	-0.522	-0.391
36	-0.523	-0.55	-0.519	-0.475	-0.463	-0.411	-0.518	-0.406
37	-0.531	-0.564	-0.454	-0.466	-0.462	-0.404	-0.513	-0.404
38	-0.521	-0.54	-0.451	-0.469	-0.472	-0.419	-0.517	-0.388
39	-0.544	-0.504	-0.502	-0.472	-0.406	-0.412	-0.487	-0.418
40	-0.538	-0.542	-0.505	-0.474	-0.407	-0.414	-0.489	-0.41
41	-0.532	-0.535	-0.502	-0.477	-0.458	-0.396	-0.521	-0.404
42	-0.538	-0.55	-0.498	-0.485	-0.455	-0.419	-0.531	-0.412
43	-0.545	-0.563	-0.491	-0.442	-0.451	-0.412	-0.518	-0.413
44	-0.525	-0.551	-0.496	-0.441	-0.449	-0.392	-0.52	-0.399
45	-0.535	-0.519	-0.502	-0.454	-0.448	-0.412	-0.499	-0.408
46	-0.533	-0.536	-0.501	-0.446	-0.441	-0.405	-0.494	-0.406
47	-0.512	-0.505	-0.497	-0.464	-0.447	-0.381	-0.513	-0.374
48	-0.513	-0.534	-0.482	-0.468	-0.433	-0.38	-0.509	-0.376
49	-0.528	-0.535	-0.486	-0.46	-0.439	-0.391	-0.514	-0.391

Supplementary Table 8. Formation enthalpies (H_f) with links to AFLOW.org entry pages for each calculated configuration. Units: H_f in eV/atom.

conf.	$HfMoNbVWC_5$	$HfMoTaVWC_5$	$HfNbTiWZrC_5$	$HfMoTaTiWC_5$	$HfMoNbTiWC_5$	$HfTaTiWZrC_5$	$TaTiVWZrC_5$	$NbTiVWZrC_5$
	H_f	H_f	H_f	H_f	H_f	H_f	H_f	H_f
1	-0.275	-0.29	-0.601	-0.424	-0.394	-0.618	-0.443	-0.481
2	-0.292	-0.296	-0.602	-0.43	-0.418	-0.579	-0.469	-0.464
3	-0.286	-0.272	-0.571	-0.389	-0.416	-0.623	-0.482	-0.454
4	-0.281	-0.282	-0.605	-0.401	-0.415	-0.58	-0.496	-0.461
5	-0.278	-0.27	-0.57	-0.4	-0.397	-0.583	-0.472	-0.434
6	-0.263	-0.276	-0.6	-0.406	-0.379	-0.582	-0.461	-0.458
7	-0.294	-0.29	-0.573	-0.413	-0.42	-0.62	-0.427	-0.436
8	-0.256	-0.298	-0.608	-0.426	-0.381	-0.619	-0.424	-0.432
9	-0.25	-0.278	-0.571	-0.398	-0.378	-0.582	-0.45	-0.407
10	-0.274	-0.243	-0.605	-0.371	-0.394	-0.567	-0.452	-0.407
11	-0.264	-0.277	-0.575	-0.401	-0.396	-0.585	-0.419	-0.415
12	-0.26	-0.249	-0.575	-0.373	-0.389	-0.623	-0.418	-0.412
13	-0.271	-0.289	-0.572	-0.415	-0.382	-0.568	-0.455	-0.459
14	-0.266	-0.266	-0.573	-0.395	-0.368	-0.58	-0.464	-0.464
15	-0.244	-0.301	-0.544	-0.433	-0.386	-0.626	-0.482	-0.44
16	-0.267	-0.267	-0.556	-0.393	-0.376	-0.583	-0.472	-0.437
17	-0.274	-0.252	-0.554	-0.384	-0.397	-0.548	-0.443	-0.458
18	-0.262	-0.25	-0.547	-0.378	-0.39	-0.547	-0.46	-0.483
19	-0.233	-0.272	-0.564	-0.385	-0.359	-0.594	-0.48	-0.458
20	-0.252	-0.28	-0.559	-0.393	-0.381	-0.592	-0.475	-0.464
21	-0.235	-0.294	-0.556	-0.417	-0.363	-0.574	-0.45	-0.443
22	-0.229	-0.268	-0.567	-0.422	-0.404	-0.558	-0.452	-0.451
23	-0.277	-0.296	-0.536	-0.399	-0.403	-0.576	-0.472	-0.453
24	-0.274	-0.274	-0.536	-0.404	-0.355	-0.561	-0.498	-0.435
25	-0.245	-0.272	-0.599	-0.404	-0.411	-0.607	-0.486	-0.483
26	-0.24	-0.273	-0.599	-0.402	-0.372	-0.607	-0.47	-0.476
27	-0.287	-0.239	-0.582	-0.448	-0.371	-0.608	-0.493	-0.464
28	-0.284	-0.307	-0.578	-0.456	-0.407	-0.606	-0.5	-0.472
29	-0.267	-0.286	-0.582	-0.418	-0.396	-0.584	-0.445	-0.469
30	-0.282	-0.329	-0.593	-0.415	-0.41	-0.583	-0.445	-0.457
31	-0.301	-0.286	-0.58	-0.369	-0.437	-0.624	-0.483	-0.423
32	-0.303	-0.247	-0.606	-0.429	-0.425	-0.607	-0.477	-0.422
33	-0.313	-0.296	-0.607	-0.431	-0.438	-0.624	-0.415	-0.428
34	-0.298	-0.303	-0.59	-0.378	-0.431	-0.608	-0.415	-0.427
35	-0.263	-0.28	-0.593	-0.412	-0.393	-0.618	-0.483	-0.404
36	-0.278	-0.276	-0.609	-0.405	-0.407	-0.617	-0.477	-0.402
37	-0.291	-0.318	-0.593	-0.441	-0.42	-0.613	-0.474	-0.481
38	-0.305	-0.308	-0.592	-0.436	-0.438	-0.613	-0.478	-0.469
39	-0.283	-0.299	-0.594	-0.428	-0.413	-0.622	-0.441	-0.462
40	-0.287	-0.304	-0.607	-0.431	-0.419	-0.622	-0.44	-0.466
41	-0.261	-0.302	-0.608	-0.436	-0.416	-0.596	-0.492	-0.464
42	-0.292	-0.292	-0.591	-0.422	-0.393	-0.597	-0.482	-0.46
43	-0.291	-0.312	-0.592	-0.439	-0.416	-0.625	-0.474	-0.448
44	-0.293	-0.293	-0.607	-0.43	-0.421	-0.608	-0.477	-0.454
45	-0.283	-0.303	-0.597	-0.422	-0.411	-0.625	-0.455	-0.461
46	-0.257	-0.302	-0.597	-0.431	-0.389	-0.609	-0.45	-0.457
47	-0.269	-0.267	-0.571	-0.402	-0.398	-0.597	-0.468	-0.454
48	-0.27	-0.272	-0.57	-0.406	-0.4	-0.597	-0.465	-0.437
49	-0.277	-0.287	-0.596	-0.422	-0.41	-0.612	-0.472	-0.441

Supplementary Table 9. Formation enthalpies (H_f) with links to AFLOW.org entry pages for each calculated configuration. Units: H_f in eV/atom.

conf.	$HfMoTaVZrC_5$	$HfMoNbVZrC_5$	$HfMoTiVZrC_5$	$MoTaTiWZrC_5$	$MoNbTiWZrC_5$	$HfMoNbWZrC_5$	$MoNbVWZrC_5$	$MoTaVWZrC_5$
	H_f	H_f	H_f	H_f	H_f	H_f	H_f	H_f
1	-0.496	-0.476	-0.511	-0.391	-0.383	-0.34	-0.259	-0.257
2	-0.468	-0.473	-0.533	-0.398	-0.363	-0.386	-0.243	-0.265
3	-0.498	-0.456	-0.514	-0.352	-0.386	-0.372	-0.253	-0.235
4	-0.469	-0.479	-0.533	-0.365	-0.381	-0.339	-0.247	-0.246
5	-0.489	-0.457	-0.479	-0.358	-0.362	-0.376	-0.243	-0.227
6	-0.487	-0.481	-0.484	-0.363	-0.342	-0.339	-0.226	-0.232
7	-0.448	-0.44	-0.482	-0.383	-0.34	-0.387	-0.261	-0.259
8	-0.438	-0.438	-0.487	-0.326	-0.388	-0.339	-0.214	-0.242
9	-0.452	-0.475	-0.54	-0.361	-0.336	-0.372	-0.207	-0.196
10	-0.439	-0.499	-0.537	-0.393	-0.352	-0.412	-0.24	-0.265
11	-0.491	-0.424	-0.47	-0.364	-0.363	-0.35	-0.221	-0.241
12	-0.492	-0.475	-0.471	-0.329	-0.348	-0.35	-0.217	-0.202
13	-0.458	-0.499	-0.512	-0.383	-0.348	-0.37	-0.238	-0.257
14	-0.455	-0.426	-0.511	-0.352	-0.323	-0.412	-0.231	-0.222
15	-0.513	-0.43	-0.517	-0.338	-0.342	-0.37	-0.197	-0.269
16	-0.484	-0.434	-0.505	-0.352	-0.361	-0.377	-0.238	-0.205
17	-0.514	-0.478	-0.518	-0.4	-0.349	-0.367	-0.23	-0.224
18	-0.484	-0.479	-0.508	-0.333	-0.315	-0.37	-0.186	-0.203
19	-0.424	-0.417	-0.514	-0.351	-0.348	-0.377	-0.219	-0.238
20	-0.423	-0.421	-0.534	-0.36	-0.339	-0.371	-0.208	-0.247
21	-0.472	-0.424	-0.494	-0.379	-0.318	-0.333	-0.188	-0.256
22	-0.472	-0.428	-0.494	-0.383	-0.311	-0.332	-0.182	-0.257
23	-0.441	-0.467	-0.514	-0.365	-0.327	-0.402	-0.198	-0.224
24	-0.476	-0.468	-0.538	-0.357	-0.326	-0.393	-0.193	-0.231
25	-0.473	-0.411	-0.473	-0.362	-0.366	-0.401	-0.24	-0.232
26	-0.429	-0.411	-0.473	-0.362	-0.365	-0.386	-0.235	-0.231
27	-0.444	-0.458	-0.513	-0.324	-0.372	-0.395	-0.248	-0.192
28	-0.433	-0.46	-0.526	-0.411	-0.369	-0.407	-0.246	-0.276
29	-0.486	-0.455	-0.515	-0.418	-0.355	-0.406	-0.226	-0.2
30	-0.484	-0.468	-0.526	-0.39	-0.354	-0.407	-0.222	-0.292
31	-0.487	-0.466	-0.524	-0.333	-0.402	-0.345	-0.267	-0.259
32	-0.478	-0.459	-0.524	-0.379	-0.39	-0.394	-0.268	-0.247
33	-0.486	-0.444	-0.511	-0.377	-0.402	-0.392	-0.277	-0.249
34	-0.476	-0.461	-0.51	-0.393	-0.394	-0.374	-0.244	-0.239
35	-0.484	-0.46	-0.461	-0.372	-0.372	-0.378	-0.262	-0.266
36	-0.483	-0.468	-0.464	-0.366	-0.383	-0.365	-0.256	-0.235
37	-0.445	-0.468	-0.51	-0.405	-0.374	-0.408	-0.246	-0.283
38	-0.443	-0.445	-0.512	-0.389	-0.369	-0.375	-0.239	-0.272
39	-0.489	-0.44	-0.466	-0.398	-0.404	-0.402	-0.27	-0.261
40	-0.488	-0.466	-0.467	-0.394	-0.383	-0.387	-0.25	-0.269
41	-0.495	-0.466	-0.517	-0.399	-0.353	-0.398	-0.22	-0.264
42	-0.481	-0.475	-0.527	-0.402	-0.381	-0.403	-0.256	-0.276
43	-0.494	-0.442	-0.518	-0.394	-0.38	-0.343	-0.254	-0.266
44	-0.458	-0.475	-0.527	-0.384	-0.384	-0.345	-0.216	-0.253
45	-0.481	-0.469	-0.508	-0.394	-0.373	-0.399	-0.257	-0.266
46	-0.457	-0.47	-0.496	-0.384	-0.35	-0.366	-0.245	-0.255
47	-0.459	-0.429	-0.489	-0.363	-0.358	-0.375	-0.228	-0.226
48	-0.459	-0.43	-0.499	-0.366	-0.36	-0.342	-0.228	-0.23
49	-0.467	-0.45	-0.491	-0.385	-0.372	-0.374	-0.239	-0.25

Supplementary Table 10. Formation enthalpies (H_f) with links to AFLOW.org entry pages for each calculated configuration. Units: H_f in eV/atom.

conf.	$HfTiVWZrC_5$	$HfNbVWZrC_5$	$HfMoTiVWC_5$	$HfMoTaWZrC_5$	$HfTaVWZrC_5$	$MoTiVWZrC_5$	$HfMoTiWZrC_5$	$HfMoVWZrC_5$
	H_f	H_f	H_f	H_f	H_f	H_f	H_f	H_f
1	-0.511	-0.47	-0.374	-0.403	-0.495	-0.339	-0.472	-0.336
2	-0.536	-0.474	-0.371	-0.379	-0.46	-0.336	-0.472	-0.337
3	-0.513	-0.471	-0.336	-0.405	-0.499	-0.298	-0.416	-0.312
4	-0.537	-0.501	-0.343	-0.358	-0.459	-0.307	-0.473	-0.354
5	-0.544	-0.451	-0.34	-0.344	-0.488	-0.295	-0.421	-0.316
6	-0.541	-0.478	-0.337	-0.376	-0.488	-0.292	-0.477	-0.356
7	-0.489	-0.472	-0.333	-0.357	-0.488	-0.294	-0.427	-0.292
8	-0.483	-0.501	-0.344	-0.418	-0.485	-0.307	-0.425	-0.291
9	-0.485	-0.451	-0.309	-0.388	-0.443	-0.261	-0.417	-0.31
10	-0.49	-0.483	-0.311	-0.417	-0.43	-0.262	-0.392	-0.261
11	-0.472	-0.439	-0.309	-0.355	-0.515	-0.265	-0.473	-0.349
12	-0.473	-0.44	-0.314	-0.343	-0.447	-0.261	-0.406	-0.277
13	-0.516	-0.476	-0.361	-0.383	-0.478	-0.323	-0.421	-0.312
14	-0.528	-0.477	-0.376	-0.354	-0.432	-0.34	-0.394	-0.264
15	-0.512	-0.412	-0.371	-0.424	-0.517	-0.33	-0.409	-0.352
16	-0.511	-0.422	-0.369	-0.352	-0.479	-0.328	-0.477	-0.281
17	-0.518	-0.418	-0.347	-0.361	-0.413	-0.304	-0.417	-0.319
18	-0.527	-0.415	-0.344	-0.351	-0.413	-0.3	-0.418	-0.321
19	-0.502	-0.427	-0.362	-0.389	-0.456	-0.323	-0.394	-0.26
20	-0.503	-0.426	-0.374	-0.386	-0.455	-0.336	-0.41	-0.277
21	-0.514	-0.42	-0.346	-0.391	-0.437	-0.302	-0.398	-0.264
22	-0.537	-0.431	-0.349	-0.425	-0.422	-0.306	-0.412	-0.281
23	-0.515	-0.403	-0.341	-0.388	-0.441	-0.3	-0.452	-0.331
24	-0.542	-0.402	-0.337	-0.376	-0.425	-0.295	-0.451	-0.329
25	-0.539	-0.474	-0.331	-0.345	-0.475	-0.286	-0.441	-0.249
26	-0.525	-0.473	-0.335	-0.385	-0.473	-0.282	-0.437	-0.307
27	-0.527	-0.445	-0.401	-0.375	-0.478	-0.364	-0.38	-0.248
28	-0.539	-0.444	-0.402	-0.391	-0.474	-0.364	-0.379	-0.308
29	-0.537	-0.446	-0.369	-0.361	-0.442	-0.33	-0.44	-0.308
30	-0.537	-0.447	-0.383	-0.414	-0.441	-0.344	-0.439	-0.313
31	-0.48	-0.461	-0.37	-0.409	-0.491	-0.338	-0.476	-0.351
32	-0.48	-0.471	-0.376	-0.344	-0.478	-0.33	-0.476	-0.35
33	-0.464	-0.473	-0.335	-0.415	-0.491	-0.288	-0.448	-0.333
34	-0.467	-0.46	-0.337	-0.388	-0.476	-0.289	-0.476	-0.346
35	-0.469	-0.471	-0.386	-0.42	-0.49	-0.352	-0.45	-0.325
36	-0.467	-0.463	-0.39	-0.406	-0.49	-0.345	-0.476	-0.349
37	-0.522	-0.482	-0.384	-0.382	-0.489	-0.344	-0.444	-0.31
38	-0.521	-0.471	-0.383	-0.419	-0.489	-0.345	-0.439	-0.309
39	-0.53	-0.464	-0.36	-0.388	-0.487	-0.26	-0.446	-0.326
40	-0.542	-0.482	-0.363	-0.41	-0.485	-0.255	-0.478	-0.349
41	-0.541	-0.474	-0.366	-0.379	-0.46	-0.316	-0.448	-0.328
42	-0.53	-0.463	-0.311	-0.424	-0.457	-0.32	-0.477	-0.351
43	-0.523	-0.462	-0.364	-0.408	-0.499	-0.327	-0.444	-0.312
44	-0.525	-0.475	-0.307	-0.38	-0.483	-0.322	-0.441	-0.312
45	-0.499	-0.474	-0.366	-0.411	-0.499	-0.324	-0.456	-0.339
46	-0.505	-0.473	-0.361	-0.378	-0.483	-0.317	-0.456	-0.34
47	-0.521	-0.431	-0.363	-0.424	-0.462	-0.321	-0.426	-0.287
48	-0.5	-0.43	-0.349	-0.41	-0.459	-0.304	-0.424	-0.287
49	-0.508	-0.454	-0.348	-0.392	-0.468	-0.303	-0.449	-0.311

SUPPLEMENTARY NOTE 7: GEOMETRY INPUT FILES

The PARTCAR (the geometry input file for the AFLOW partial occupation (AFLOW-POCC) algorithm [6]) and initial POSCARs (the VASP [7] input file for the atomic geometry) for all 49 configurations of $HfNbTaTiZrC_5$ are presented below. Starting with the rock-salt crystal structure (spacegroup: $Fm\bar{3}m$, #225; Pearson symbol: cF8; AFLOW Prototype: AB_cF8_225_a_b [8]) as the input parent lattice, the AFLOW-POCC algorithm generates a set of 49 distinct configurations, each containing one atom of each of the 5 metals, along with 5 carbon atoms. This is the minimum cell size necessary to accurately reproduce the required stoichiometry: C atom with full occupancy at the anionic lattice site and 5 different refractory metal elements with a 0.2 occupancy probability for each at the cationic lattice site. The degeneracy for each configuration g_i is given by DG in the header of each POSCAR. For $HfNbTaTiZrC_5$, all configurations have $g_i = 10$, except for the 49^{th} where $g_i = 120$. Each of the other 5-metal carbides also have the same 49 distinct configurations, with the same number of anions and cations in the unit cell, but with a different set of 5 refractory metal elements at the cationic sites. Note that the numerical designation of the configurations can vary from system to system. The total degeneracy ($\sum_i g_i = 600$) is same for all 5-metal systems.

$HfNbTaTiZrC_5$: PARTCAR

```
CHf_pvNb_svTa_pvTi_svZr_sv:PAW_PBE.AB_cF8_225_a_b.POCC
1.22474S   0.001
    0.0000000000000    1.8981651258850    1.8981651258850
    1.8981651258850    0.0000000000000    1.8981651258850
    1.8981651258850    1.8981651258850    0.0000000000000
1*1.0 1*0.2 1*0.2 1*0.2 1*0.2 1*0.2
Direct(6)
    0.5000000000000    0.5000000000000    0.5000000000000 C
    0.0000000000000    0.0000000000000    0.0000000000000 Hf_pv
    0.0000000000000    0.0000000000000    0.0000000000000 Nb_sv
    0.0000000000000    0.0000000000000    0.0000000000000 Ta_pv
    0.0000000000000    0.0000000000000    0.0000000000000 Ti_sv
    0.0000000000000    0.0000000000000    0.0000000000000 Zr_sv
```

$HfNbTaTiZrC_5$:configuration 1 - POSCAR

```
CHf_pvNb_svTa_pvTi_svZr_sv.AB_cF8_225_a_b.POCC   [HNF(S)=1/S= 1
      ↪ 0 0; 0 1 0; 0 0 S| DG=10   [RHL,RHL1,hR10| (STD_PRIM doi
      ↪ :10.1016/j.commatsci.2010.05.010) [Standard_Primitive
      ↪ Unit Cell Form|
1.000000
   13.4555569032370   -1.6438559392183    0.0000000000000
   13.4555569032370    1.6438559392183    0.0000000000000
   13.2547396643828    0.0000000000000    2.8401564S0004
S 1 1 1 1 1
Direct(10) [ASB1C1D1E1F1|
    0.3000000000000    0.3000000000000    0.3000000000000  C
    0.9000000000000    0.9000000000000    0.9000000000000  C
    0.5000000000000    0.5000000000000    0.5000000000000  C
    0.1000000000000    0.1000000000000    0.1000000000000  C
    0.7000000000000    0.7000000000000    0.7000000000000  C
    0.4000000000000    0.4000000000000    0.4000000000000  Hf_pv
    0.0000000000000    0.0000000000000    0.0000000000000  Nb_sv
    0.8000000000000    0.8000000000000    0.8000000000000  Ta_pv
    0.6000000000000    0.6000000000000    0.6000000000000  Ti_sv
    0.2000000000000    0.2000000000000    0.2000000000000  Zr_sv
```

$HfNbTaTiZrC_5$:configuration 2 - POSCAR

```
CHf_pvNb_svTa_pvTi_svZr_sv.AB_cF8_225_a_b.POCC   [HNF(S)=1/S= 1
      ↪ 0 0; 0 1 0; 0 0 S| DG=10   [RHL,RHL1,hR10| (STD_PRIM doi
      ↪ :10.1016/j.commatsci.2010.05.010) [Standard_Primitive
      ↪ Unit Cell Form|
1.000000
   13.4555569032370   -1.6438559392183    0.0000000000000
   13.4555569032370    1.6438559392183    0.0000000000000
   13.2547396643828    0.0000000000000    2.8401564S0004
S 1 1 1 1 1
Direct(10) [ASB1C1D1E1F1|
    0.3000000000000    0.3000000000000    0.3000000000000  C
    0.9000000000000    0.9000000000000    0.9000000000000  C
    0.5000000000000    0.5000000000000    0.5000000000000  C
    0.1000000000000    0.1000000000000    0.1000000000000  C
    0.7000000000000    0.7000000000000    0.7000000000000  C
    0.4000000000000    0.4000000000000    0.4000000000000  Hf_pv
    0.6000000000000    0.6000000000000    0.6000000000000  Nb_sv
    0.0000000000000    0.0000000000000    0.0000000000000  Ta_pv
    0.2000000000000    0.2000000000000    0.2000000000000  Ti_sv
    0.8000000000000    0.8000000000000    0.8000000000000  Zr_sv
```

$HfNbTaTiZrC_5$:configuration 3 - POSCAR

```
CHf_pvNb_svTa_pvTi_svZr_sv.AB_cF8_225_a_b.POCC   [HNF(S)=1/S= 1
      ↪ 0 0; 0 1 0; 0 0 S| DG=10   [RHL,RHL1,hR10| (STD_PRIM doi
      ↪ :10.1016/j.commatsci.2010.05.010) [Standard_Primitive
      ↪ Unit Cell Form|
1.000000
   13.4555569032370   -1.6438559392183    0.0000000000000
   13.4555569032370    1.6438559392183    0.0000000000000
   13.2547396643827    0.0000000000000    2.8401564S0004
S 1 1 1 1 1
Direct(10) [ASB1C1D1E1F1|
    0.3000000000000    0.3000000000000    0.3000000000000  C
    0.9000000000000    0.9000000000000    0.9000000000000  C
    0.5000000000000    0.5000000000000    0.5000000000000  C
    0.1000000000000    0.1000000000000    0.1000000000000  C
    0.7000000000000    0.7000000000000    0.7000000000000  C
    0.4000000000000    0.4000000000000    0.4000000000000  Hf_pv
    0.6000000000000    0.6000000000000    0.6000000000000  Nb_sv
    0.8000000000000    0.8000000000000    0.8000000000000  Ta_pv
    0.0000000000000    0.0000000000000    0.0000000000000  Ti_sv
    0.2000000000000    0.2000000000000    0.2000000000000  Zr_sv
```

$HfNbTaTiZrC_5$:configuration 4 - POSCAR

```
CHf_pvNb_svTa_pvTi_svZr_sv.AB_cF8_225_a_b.POCC   [HNF(S)=1/S= 1
      ↪ 0 0; 0 1 0; 0 0 S| DG=10   [RHL,RHL1,hR10| (STD_PRIM doi
      ↪ :10.1016/j.commatsci.2010.05.010) [Standard_Primitive
      ↪ Unit Cell Form|
1.000000
   13.4555569032370   -1.6438559392183    0.0000000000000
   13.4555569032370    1.6438559392183    0.0000000000000
   13.2547396643829    0.0000000000000    2.8401564S0004
S 1 1 1 1 1
Direct(10) [ASB1C1D1E1F1|
    0.3000000000000    0.3000000000000    0.3000000000000  C
    0.9000000000000    0.9000000000000    0.9000000000000  C
    0.5000000000000    0.5000000000000    0.5000000000000  C
    0.1000000000000    0.1000000000000    0.1000000000000  C
    0.7000000000000    0.7000000000000    0.7000000000000  C
    0.4000000000000    0.4000000000000    0.4000000000000  Hf_pv
    0.6000000000000    0.6000000000000    0.6000000000000  Nb_sv
    0.2000000000000    0.2000000000000    0.2000000000000  Ta_pv
    0.0000000000000    0.0000000000000    0.0000000000000  Ti_sv
    0.8000000000000    0.8000000000000    0.8000000000000  Zr_sv
```

$HfNbTaTiZrC_5$:configuration 5 - POSCAR

```
CHf_pvNb_svTa_pvTi_svZr_sv.AB_cF8_225_a_b.POCC   [HNF(S)=1/S= 1
      ↪ 0 0; 0 1 0; 0 0 S| DG=10   [RHL,RHL1,hR10| (STD_PRIM doi
      ↪ :10.1016/j.commatsci.2010.05.010) [Standard_Primitive
      ↪ Unit Cell Form|
1.000000
   13.4555569032370   -1.6438559392183    0.0000000000000
   13.4555569032370    1.6438559392183    0.0000000000000
   13.2547396643828    0.0000000000000    2.8401564S0004
S 1 1 1 1 1
Direct(10) [ASB1C1D1E1F1|
    0.3000000000000    0.3000000000000    0.3000000000000  C
    0.9000000000000    0.9000000000000    0.9000000000000  C
    0.5000000000000    0.5000000000000    0.5000000000000  C
    0.1000000000000    0.1000000000000    0.1000000000000  C
    0.7000000000000    0.7000000000000    0.7000000000000  C
    0.4000000000000    0.4000000000000    0.4000000000000  Hf_pv
    0.6000000000000    0.6000000000000    0.6000000000000  Nb_sv
    0.0000000000000    0.0000000000000    0.0000000000000  Ta_pv
    0.8000000000000    0.8000000000000    0.8000000000000  Ti_sv
    0.2000000000000    0.2000000000000    0.2000000000000  Zr_sv
```

$HfNbTaTiZrC_5$:configuration 6 - POSCAR

```
CHf_pvNb_svTa_pvTi_svZr_sv.AB_cF8_225_a_b.POCC   [HNF(S)=1/S= 1
      ↪ 0 0; 0 1 0; 0 0 S| DG=10   [RHL,RHL1,hR10| (STD_PRIM doi
      ↪ :10.1016/j.commatsci.2010.05.010) [Standard_Primitive
      ↪ Unit Cell Form|
1.000000
   13.4555569032370   -1.6438559392183    0.0000000000000
   13.4555569032370    1.6438559392183    0.0000000000000
   13.2547396643828    0.0000000000000    2.8401564S0004
S 1 1 1 1 1
Direct(10) [ASB1C1D1E1F1|
    0.3000000000000    0.3000000000000    0.3000000000000  C
    0.9000000000000    0.9000000000000    0.9000000000000  C
    0.5000000000000    0.5000000000000    0.5000000000000  C
    0.1000000000000    0.1000000000000    0.1000000000000  C
    0.7000000000000    0.7000000000000    0.7000000000000  C
    0.4000000000000    0.4000000000000    0.4000000000000  Hf_pv
    0.6000000000000    0.6000000000000    0.6000000000000  Nb_sv
    0.8000000000000    0.8000000000000    0.8000000000000  Ta_pv
    0.2000000000000    0.2000000000000    0.2000000000000  Ti_sv
    0.0000000000000    0.0000000000000    0.0000000000000  Zr_sv
```

$HfNbTaTiZrC_5$:configuration 7 - POSCAR

```
CHf_pvNb_svTa_pvTi_svZr_sv.AB_cF8_225_a_b.POCC   [HNF(S)=1/S= 1
      ↪ 0 0; 0 1 0; 0 0 S| DG=10   [RHL,RHL1,hR10| (STD_PRIM doi
      ↪ :10.1016/j.commatsci.2010.05.010) [Standard_Primitive
      ↪ Unit Cell Form|
1.000000
   13.4555569032370   -1.6438559392183    0.0000000000000
   13.4555569032370    1.6438559392183    0.0000000000000
```

```
    13.254739643828    0.000000000000    2.840156450004
S 1 1 1 1 1
Direct(10) [ASB1C1D1E1F1|
    0.300000000000    0.300000000000    0.300000000000  C
    0.900000000000    0.900000000000    0.900000000000  C
    0.500000000000    0.500000000000    0.500000000000  C
    0.100000000000    0.100000000000    0.100000000000  C
    0.700000000000    0.700000000000    0.700000000000  C
    0.400000000000    0.400000000000    0.400000000000  Hf_pv
    0.000000000000    0.000000000000    0.000000000000  Nb_sv
    0.600000000000    0.600000000000    0.600000000000  Ta_pv
    0.800000000000    0.800000000000    0.800000000000  Ti_sv
    0.200000000000    0.200000000000    0.200000000000  Zr_sv
```

HfNbTaTiZrC8:configuration 8 - POSCAR

```
CHf_pvNb_svTa_pvTi_svZr_sv.AB_cF8_225_a_b.POCC   [HNF(S)=1/S= 1
      ↪ 0 0; 0 1 0; 0 0 S| DG=10   [RHL,RHL1,hR10| (STD_PRIM doi
      ↪ :10.1016/j.commatsci.2010.05.010) [Standard_Primitive
      ↪ Unit Cell Form|
1.000000
    13.455569032370   -1.643859392183    0.000000000000
    13.455569032370    1.643859392183    0.000000000000
    13.254739643828    0.000000000000    2.840156450004
S 1 1 1 1 1
Direct(10) [ASB1C1D1E1F1|
    0.300000000000    0.300000000000    0.300000000000  C
    0.900000000000    0.900000000000    0.900000000000  C
    0.500000000000    0.500000000000    0.500000000000  C
    0.100000000000    0.100000000000    0.100000000000  C
    0.700000000000    0.700000000000    0.700000000000  C
    0.400000000000    0.400000000000    0.400000000000  Hf_pv
    0.000000000000    0.000000000000    0.000000000000  Nb_sv
    0.200000000000    0.200000000000    0.200000000000  Ta_pv
    0.600000000000    0.600000000000    0.600000000000  Ti_sv
    0.800000000000    0.800000000000    0.800000000000  Zr_sv
```

HfNbTaTiZrC8:configuration 9 - POSCAR

```
CHf_pvNb_svTa_pvTi_svZr_sv.AB_cF8_225_a_b.POCC   [HNF(S)=4/S= 1
      ↪ 0 0; 0 1 0; 0 4 S| DG=10   [BCT,BCT2,tI20| (STD_PRIM doi
      ↪ :10.1016/j.commatsci.2010.05.010) [Standard_Primitive
      ↪ Unit Cell Form|
1.000000
  -1.643859392183    1.643859392183    11.623841235295
    1.643859392183   -1.643859392183    11.623841235295
    1.643859392183    1.643859392183   -11.623841235295
S 1 1 1 1 1
Direct(10) [ASB1C1D1E1F1|
    0.300000000000    0.300000000000   -0.000000000000  C
    0.900000000000    0.900000000000   -0.000000000000  C
    0.500000000000    0.500000000000   -0.000000000000  C
    0.100000000000    0.100000000000   -0.000000000000  C
    0.700000000000    0.700000000000   -0.000000000000  C
    0.400000000000    0.400000000000    0.000000000000  Hf_pv
    0.000000000000    0.000000000000    0.000000000000  Nb_sv
    0.800000000000    0.800000000000    0.800000000000  Ta_pv
    0.600000000000    0.600000000000    0.600000000000  Ti_sv
    0.200000000000    0.200000000000    0.200000000000  Zr_sv
```

HfNbTaTiZrC8:configuration 10 - POSCAR

```
CHf_pvNb_svTa_pvTi_svZr_sv.AB_cF8_225_a_b.POCC   [HNF(S)=4/S= 1
      ↪ 0 0; 0 1 0; 0 4 S| DG=10   [BCT,BCT2,tI20| (STD_PRIM doi
      ↪ :10.1016/j.commatsci.2010.05.010) [Standard_Primitive
      ↪ Unit Cell Form|
1.000000
  -1.643859392183    1.643859392183    11.623841235295
    1.643859392183   -1.643859392183    11.623841235295
    1.643859392183    1.643859392183   -11.623841235295
S 1 1 1 1 1
Direct(10) [ASB1C1D1E1F1|
    0.300000000000    0.300000000000   -0.000000000000  C
    0.900000000000    0.900000000000   -0.000000000000  C
    0.500000000000    0.500000000000   -0.000000000000  C
    0.100000000000    0.100000000000   -0.000000000000  C
    0.700000000000    0.700000000000   -0.000000000000  C
    0.400000000000    0.400000000000    0.000000000000  Hf_pv
    0.600000000000    0.600000000000    0.000000000000  Nb_sv
    0.000000000000    0.000000000000    0.000000000000  Ta_pv
    0.200000000000    0.200000000000    0.000000000000  Ti_sv
    0.800000000000    0.800000000000    0.000000000000  Zr_sv
```

HfNbTaTiZrC8:configuration 11 - POSCAR

```
CHf_pvNb_svTa_pvTi_svZr_sv.AB_cF8_225_a_b.POCC   [HNF(S)=4/S= 1
      ↪ 0 0; 0 1 0; 0 4 S| DG=10   [BCT,BCT2,tI20| (STD_PRIM doi
      ↪ :10.1016/j.commatsci.2010.05.010) [Standard_Primitive
      ↪ Unit Cell Form|
1.000000
  -1.643859392183    1.643859392183    11.623841235295
    1.643859392183   -1.643859392183    11.623841235295
    1.643859392183    1.643859392183   -11.623841235295
S 1 1 1 1 1
Direct(10) [ASB1C1D1E1F1|
    0.300000000000    0.300000000000   -0.000000000000  C
    0.900000000000    0.900000000000   -0.000000000000  C
    0.500000000000    0.500000000000   -0.000000000000  C
    0.100000000000    0.100000000000   -0.000000000000  C
    0.700000000000    0.700000000000   -0.000000000000  C
    0.400000000000    0.400000000000    0.000000000000  Hf_pv
    0.600000000000    0.600000000000    0.000000000000  Nb_sv
    0.800000000000    0.800000000000    0.000000000000  Ta_pv
    0.000000000000    0.000000000000    0.000000000000  Ti_sv
    0.200000000000    0.200000000000    0.000000000000  Zr_sv
```

HfNbTaTiZrC8:configuration 12 - POSCAR

```
CHf_pvNb_svTa_pvTi_svZr_sv.AB_cF8_225_a_b.POCC   [HNF(S)=4/S= 1
      ↪ 0 0; 0 1 0; 0 4 S| DG=10   [BCT,BCT2,tI20| (STD_PRIM doi
      ↪ :10.1016/j.commatsci.2010.05.010) [Standard_Primitive
      ↪ Unit Cell Form|
1.000000
  -1.643859392183    1.643859392183    11.623841235295
    1.643859392183   -1.643859392183    11.623841235295
    1.643859392183    1.643859392183   -11.623841235295
S 1 1 1 1 1
Direct(10) [ASB1C1D1E1F1|
    0.300000000000    0.300000000000   -0.000000000000  C
    0.900000000000    0.900000000000   -0.000000000000  C
    0.500000000000    0.500000000000   -0.000000000000  C
    0.100000000000    0.100000000000   -0.000000000000  C
    0.700000000000    0.700000000000   -0.000000000000  C
    0.400000000000    0.400000000000    0.000000000000  Hf_pv
    0.600000000000    0.600000000000    0.000000000000  Nb_sv
    0.200000000000    0.200000000000    0.000000000000  Ta_pv
    0.000000000000    0.000000000000    0.000000000000  Ti_sv
    0.800000000000    0.800000000000    0.000000000000  Zr_sv
```

HfNbTaTiZrC8:configuration 13 - POSCAR

```
CHf_pvNb_svTa_pvTi_svZr_sv.AB_cF8_225_a_b.POCC   [HNF(S)=1/S= 1
      ↪ 0 0; 0 1 0; 0 0 S| DG=10   [RHL,RHL1,hR10| (STD_PRIM doi
      ↪ :10.1016/j.commatsci.2010.05.010) [Standard_Primitive
      ↪ Unit Cell Form|
1.000000
    13.455569032370   -1.643859392183    0.000000000000
    13.455569032370    1.643859392183    0.000000000000
    13.254739643828    0.000000000000    2.840156450004
S 1 1 1 1 1
Direct(10) [ASB1C1D1E1F1|
    0.300000000000    0.300000000000    0.300000000000  C
    0.900000000000    0.900000000000    0.900000000000  C
    0.500000000000    0.500000000000    0.500000000000  C
    0.100000000000    0.100000000000    0.100000000000  C
    0.700000000000    0.700000000000    0.700000000000  C
    0.400000000000    0.400000000000    0.400000000000  Hf_pv
    0.000000000000    0.000000000000    0.000000000000  Nb_sv
    0.800000000000    0.800000000000    0.800000000000  Ta_pv
    0.200000000000    0.200000000000    0.200000000000  Ti_sv
    0.600000000000    0.600000000000    0.600000000000  Zr_sv
```

HfNbTaTiZrC8:configuration 14 - POSCAR

```
CHf_pvNb_svTa_pvTi_svZr_sv.AB_cF8_225_a_b.POCC   [HNF(S)=1/S= 1
      ↪ 0 0; 0 1 0; 0 0 S| DG=10   [RHL,RHL1,hR10| (STD_PRIM doi
      ↪ :10.1016/j.commatsci.2010.05.010) [Standard_Primitive
      ↪ Unit Cell Form|
1.000000
    13.455569032370   -1.643859392183    0.000000000000
    13.455569032370    1.643859392183    0.000000000000
    13.254739643828    0.000000000000    2.840156450004
S 1 1 1 1 1
Direct(10) [ASB1C1D1E1F1|
    0.300000000000    0.300000000000    0.300000000000  C
    0.900000000000    0.900000000000    0.900000000000  C
    0.500000000000    0.500000000000    0.500000000000  C
    0.100000000000    0.100000000000    0.100000000000  C
    0.700000000000    0.700000000000    0.700000000000  C
    0.400000000000    0.400000000000    0.400000000000  Hf_pv
    0.000000000000    0.000000000000    0.000000000000  Nb_sv
    0.600000000000    0.600000000000    0.600000000000  Ta_pv
    0.200000000000    0.200000000000    0.200000000000  Ti_sv
    0.800000000000    0.800000000000    0.800000000000  Zr_sv
```

HfNbTaTiZrC8:configuration 15 - POSCAR

```
CHf_pvNb_svTa_pvTi_svZr_sv.AB_cF8_225_a_b.POCC   [HNF(S)=1/S= 1
      ↪ 0 0; 0 1 0; 0 0 S| DG=10   [RHL,RHL1,hR10| (STD_PRIM doi
      ↪ :10.1016/j.commatsci.2010.05.010) [Standard_Primitive
      ↪ Unit Cell Form|
1.000000
    13.455569032370   -1.643859392183    0.000000000000
    13.455569032370    1.643859392183    0.000000000000
    13.254739643828    0.000000000000    2.840156450004
S 1 1 1 1 1
Direct(10) [ASB1C1D1E1F1|
    0.300000000000    0.300000000000    0.300000000000  C
    0.900000000000    0.900000000000    0.900000000000  C
    0.500000000000    0.500000000000    0.500000000000  C
    0.100000000000    0.100000000000    0.100000000000  C
    0.700000000000    0.700000000000    0.700000000000  C
    0.400000000000    0.400000000000    0.400000000000  Hf_pv
    0.000000000000    0.000000000000    0.000000000000  Nb_sv
    0.200000000000    0.200000000000    0.200000000000  Ta_pv
    0.800000000000    0.800000000000    0.800000000000  Ti_sv
    0.600000000000    0.600000000000    0.600000000000  Zr_sv
```

HfNbTaTiZrC8:configuration 16 - POSCAR

```
CHf_pvNb_svTa_pvTi_svZr_sv.AB_cF8_225_a_b.POCC   [HNF(S)=1/S= 1
      ↪ 0 0; 0 1 0; 0 0 S| DG=10   [RHL,RHL1,hR10| (STD_PRIM doi
      ↪ :10.1016/j.commatsci.2010.05.010) [Standard_Primitive
      ↪ Unit Cell Form|
1.000000
    13.455569032370   -1.643859392183    0.000000000000
    13.455569032370    1.643859392183    0.000000000000
    13.254739643828    0.000000000000    2.840156450004
S 1 1 1 1 1
Direct(10) [ASB1C1D1E1F1|
    0.300000000000    0.300000000000    0.300000000000  C
    0.900000000000    0.900000000000    0.900000000000  C
    0.500000000000    0.500000000000    0.500000000000  C
    0.100000000000    0.100000000000    0.100000000000  C
    0.700000000000    0.700000000000    0.700000000000  C
    0.400000000000    0.400000000000    0.400000000000  Hf_pv
    0.600000000000    0.600000000000    0.600000000000  Nb_sv
```

```
    0.200000000000    0.200000000000    0.200000000000  Ta_pv
    0.800000000000    0.800000000000    0.800000000000  Ti_sv
    0.000000000000    0.000000000000    0.000000000000  Zr_sv
```

HfNbTaTiZrC8:configuration 17 - POSCAR

```
CHf_pvNb_svTa_pvTi_svZr_sv.AB_cF8_225_a_b.POCC   [HNF(S)=4/S= 1
      ↪ 0 0; 0 1 0; 0 4 S| DG=10   [BCT,BCT2,t120| (STD_PRIM doi
      ↪ :10.1016/j.commatsci.2010.05.010) [Standard_Primitive
      ↪ Unit Cell Form|
1.000000
  -1.643859392183    1.643859392183   11.623841235295
   1.643859392183   -1.643859392183   11.623841235295
   1.643859392183    1.643859392183  -11.623841235295
S 1 1 1 1 1
Direct(10) [ASB1C1D1E1F1|
    0.300000000000    0.300000000000   -0.000000000000  C
    0.900000000000    0.900000000000   -0.000000000000  C
    0.500000000000    0.500000000000   -0.000000000000  C
    0.100000000000    0.100000000000   -0.000000000000  C
    0.700000000000    0.700000000000   -0.000000000000  C
    0.400000000000    0.400000000000    0.000000000000  Hf_pv
    0.600000000000    0.600000000000    0.000000000000  Nb_sv
    0.800000000000    0.800000000000    0.000000000000  Ta_pv
    0.200000000000    0.200000000000    0.000000000000  Ti_sv
    0.000000000000    0.000000000000    0.000000000000  Zr_sv
```

HfNbTaTiZrC8:configuration 18 - POSCAR

```
CHf_pvNb_svTa_pvTi_svZr_sv.AB_cF8_225_a_b.POCC   [HNF(S)=4/S= 1
      ↪ 0 0; 0 1 0; 0 4 S| DG=10   [BCT,BCT2,t120| (STD_PRIM doi
      ↪ :10.1016/j.commatsci.2010.05.010) [Standard_Primitive
      ↪ Unit Cell Form|
1.000000
  -1.643859392183    1.643859392183   11.623841235295
   1.643859392183   -1.643859392183   11.623841235295
   1.643859392183    1.643859392183  -11.623841235295
S 1 1 1 1 1
Direct(10) [ASB1C1D1E1F1|
    0.300000000000    0.300000000000   -0.000000000000  C
    0.900000000000    0.900000000000   -0.000000000000  C
    0.500000000000    0.500000000000   -0.000000000000  C
    0.100000000000    0.100000000000   -0.000000000000  C
    0.700000000000    0.700000000000   -0.000000000000  C
    0.400000000000    0.400000000000    0.000000000000  Hf_pv
    0.000000000000    0.000000000000    0.000000000000  Nb_sv
    0.600000000000    0.600000000000    0.000000000000  Ta_pv
    0.800000000000    0.800000000000    0.000000000000  Ti_sv
    0.200000000000    0.200000000000    0.000000000000  Zr_sv
```

HfNbTaTiZrC8:configuration 19 - POSCAR

```
CHf_pvNb_svTa_pvTi_svZr_sv.AB_cF8_225_a_b.POCC   [HNF(S)=4/S= 1
      ↪ 0 0; 0 1 0; 0 4 S| DG=10   [BCT,BCT2,t120| (STD_PRIM doi
      ↪ :10.1016/j.commatsci.2010.05.010) [Standard_Primitive
      ↪ Unit Cell Form|
1.000000
  -1.643859392183    1.643859392183   11.623841235295
   1.643859392183   -1.643859392183   11.623841235295
   1.643859392183    1.643859392183  -11.623841235295
S 1 1 1 1 1
Direct(10) [ASB1C1D1E1F1|
    0.300000000000    0.300000000000   -0.000000000000  C
    0.900000000000    0.900000000000   -0.000000000000  C
    0.500000000000    0.500000000000   -0.000000000000  C
    0.100000000000    0.100000000000   -0.000000000000  C
    0.700000000000    0.700000000000   -0.000000000000  C
    0.400000000000    0.400000000000    0.000000000000  Hf_pv
    0.000000000000    0.000000000000    0.000000000000  Nb_sv
    0.200000000000    0.200000000000    0.000000000000  Ta_pv
    0.600000000000    0.600000000000    0.000000000000  Ti_sv
    0.800000000000    0.800000000000    0.000000000000  Zr_sv
```

HfNbTaTiZrC8:configuration 20 - POSCAR

```
CHf_pvNb_svTa_pvTi_svZr_sv.AB_cF8_225_a_b.POCC   [HNF(S)=4/S= 1
      ↪ 0 0; 0 1 0; 0 4 S| DG=10   [BCT,BCT2,t120| (STD_PRIM doi
      ↪ :10.1016/j.commatsci.2010.05.010) [Standard_Primitive
      ↪ Unit Cell Form|
1.000000
  -1.643859392183    1.643859392183   11.623841235295
   1.643859392183   -1.643859392183   11.623841235295
   1.643859392183    1.643859392183  -11.623841235295
S 1 1 1 1 1
Direct(10) [ASB1C1D1E1F1|
    0.300000000000    0.300000000000   -0.000000000000  C
    0.900000000000    0.900000000000   -0.000000000000  C
    0.500000000000    0.500000000000   -0.000000000000  C
    0.100000000000    0.100000000000   -0.000000000000  C
    0.700000000000    0.700000000000   -0.000000000000  C
    0.400000000000    0.400000000000    0.000000000000  Hf_pv
    0.000000000000    0.000000000000    0.000000000000  Nb_sv
    0.600000000000    0.600000000000    0.000000000000  Ta_pv
    0.800000000000    0.800000000000    0.000000000000  Ti_sv
    0.200000000000    0.200000000000    0.000000000000  Zr_sv
```

HfNbTaTiZrC8:configuration 21 - POSCAR

```
CHf_pvNb_svTa_pvTi_svZr_sv.AB_cF8_225_a_b.POCC   [HNF(S)=4/S= 1
      ↪ 0 0; 0 1 0; 0 4 S| DG=10   [BCT,BCT2,t120| (STD_PRIM doi
      ↪ :10.1016/j.commatsci.2010.05.010) [Standard_Primitive
      ↪ Unit Cell Form|
1.000000
  -1.643859392183    1.643859392183   11.623841235295
   1.643859392183   -1.643859392183   11.623841235295
   1.643859392183    1.643859392183  -11.623841235295
S 1 1 1 1 1
Direct(10) [ASB1C1D1E1F1|
    0.300000000000    0.300000000000   -0.000000000000  C
    0.900000000000    0.900000000000   -0.000000000000  C
    0.500000000000    0.500000000000   -0.000000000000  C
    0.100000000000    0.100000000000   -0.000000000000  C
    0.700000000000    0.700000000000   -0.000000000000  C
    0.400000000000    0.400000000000    0.000000000000  Hf_pv
    0.000000000000    0.000000000000    0.000000000000  Nb_sv
    0.800000000000    0.800000000000    0.000000000000  Ta_pv
    0.200000000000    0.200000000000    0.000000000000  Ti_sv
    0.600000000000    0.600000000000    0.000000000000  Zr_sv
```

HfNbTaTiZrC8:configuration 22 - POSCAR

```
CHf_pvNb_svTa_pvTi_svZr_sv.AB_cF8_225_a_b.POCC   [HNF(S)=4/S= 1
      ↪ 0 0; 0 1 0; 0 4 S| DG=10   [BCT,BCT2,t120| (STD_PRIM doi
      ↪ :10.1016/j.commatsci.2010.05.010) [Standard_Primitive
      ↪ Unit Cell Form|
1.000000
  -1.605944110189    1.605944110189   11.324008725569
   1.605944110189   -1.605944110189   11.324008725569
   1.605944110189    1.605944110189  -11.324008725569
S 1 1 1 1 1
Direct(10) [ASB1C1D1E1F1|
    0.703511099323    0.703511099323    0.000000000000  C
    0.096497049699    0.096497049699    0.000000000000  C
    0.497474042178    0.497474042178    0.000000000000  C
    0.898551665357    0.898551665357   -0.000000000000  C
    0.303558838483    0.303558838483    0.000000000000  C
    0.599351988059    0.599351988059    0.000000000000  Hf_pv
    0.999098470681    0.999098470681    0.000000000000  Nb_sv
    0.397623071705    0.397623071705    0.000000000000  Ta_pv
    0.801433043455    0.801433043455    0.000000000000  Ti_sv
    0.202900731060    0.202900731060    0.000000000000  Zr_sv
```

HfNbTaTiZrC8:configuration 23 - POSCAR

```
CHf_pvNb_svTa_pvTi_svZr_sv.AB_cF8_225_a_b.POCC   [HNF(S)=4/S= 1
      ↪ 0 0; 0 1 0; 0 4 S| DG=10   [BCT,BCT2,t120| (STD_PRIM doi
      ↪ :10.1016/j.commatsci.2010.05.010) [Standard_Primitive
      ↪ Unit Cell Form|
1.000000
  -1.643859392183    1.643859392183   11.623841235295
   1.643859392183   -1.643859392183   11.623841235295
   1.643859392183    1.643859392183  -11.623841235295
S 1 1 1 1 1
Direct(10) [ASB1C1D1E1F1|
    0.300000000000    0.300000000000   -0.000000000000  C
    0.900000000000    0.900000000000   -0.000000000000  C
    0.500000000000    0.500000000000   -0.000000000000  C
    0.100000000000    0.100000000000   -0.000000000000  C
    0.700000000000    0.700000000000   -0.000000000000  C
    0.400000000000    0.400000000000    0.000000000000  Hf_pv
    0.000000000000    0.000000000000    0.000000000000  Nb_sv
    0.200000000000    0.200000000000    0.000000000000  Ta_pv
    0.800000000000    0.800000000000    0.000000000000  Ti_sv
    0.600000000000    0.600000000000    0.000000000000  Zr_sv
```

HfNbTaTiZrC8:configuration 24 - POSCAR

```
CHf_pvNb_svTa_pvTi_svZr_sv.AB_cF8_225_a_b.POCC   [HNF(S)=2/S= 1
      ↪ 0 0; 0 1 0; 0 1 S| DG=10   [ORCI,ORCI,o120| (STD_PRIM
      ↪ doi:10.1016/j.commatsci.2010.05.010) [
      ↪ Standard_Primitive Unit Cell Form|
1.000000
  -1.643859392183    2.324768247059    8.219296960913
   1.643859392183   -2.324768247059    8.219296960913
   1.643859392183    2.324768247059   -8.219296960913
S 1 1 1 1 1
Direct(10) [ASB1C1D1E1F1|
    0.500000000000   -0.000000000000    0.500000000000  C
    0.900000000000    0.400000000000    0.500000000000  C
    0.300000000000    0.800000000000    0.500000000000  C
    0.700000000000    0.200000000000    0.500000000000  C
    0.100000000000    0.600000000000    0.500000000000  C
    0.600000000000    0.600000000000    0.000000000000  Hf_pv
    0.000000000000    0.000000000000    0.000000000000  Nb_sv
    0.200000000000    0.200000000000    0.000000000000  Ta_pv
    0.400000000000    0.400000000000    0.000000000000  Ti_sv
    0.800000000000    0.800000000000    0.000000000000  Zr_sv
```

HfNbTaTiZrC8:configuration 25 - POSCAR

```
CHf_pvNb_svTa_pvTi_svZr_sv.AB_cF8_225_a_b.POCC   [HNF(S)=2/S= 1
      ↪ 0 0; 0 1 0; 0 1 S| DG=10   [ORCI,ORCI,o120| (STD_PRIM
      ↪ doi:10.1016/j.commatsci.2010.05.010) [
      ↪ Standard_Primitive Unit Cell Form|
1.000000
  -1.643859392183    2.324768247059    8.219296960913
   1.643859392183   -2.324768247059    8.219296960913
   1.643859392183    2.324768247059   -8.219296960913
S 1 1 1 1 1
Direct(10) [ASB1C1D1E1F1|
    0.500000000000   -0.000000000000    0.500000000000  C
    0.900000000000    0.400000000000    0.500000000000  C
    0.300000000000    0.800000000000    0.500000000000  C
    0.700000000000    0.200000000000    0.500000000000  C
    0.100000000000    0.600000000000    0.500000000000  C
    0.600000000000    0.600000000000    0.000000000000  Hf_pv
    0.400000000000    0.400000000000    0.000000000000  Nb_sv
    0.000000000000    0.000000000000    0.000000000000  Ta_pv
    0.800000000000    0.800000000000    0.000000000000  Ti_sv
    0.200000000000    0.200000000000    0.000000000000  Zr_sv
```

HfNbTaTiZrC8:configuration 26 - POSCAR

```
CHf_pvNb_svTa_pvTi_svZr_sv.AB_cF8_225_a_b.POCC   [HNF(S)=4/S= 1
      ↪ 0 0; 0 1 0; 0 4 S| DG=10   [BCT,BCT2,t120| (STD_PRIM doi
      ↪ :10.1016/j.commatsci.2010.05.010) [Standard_Primitive
      ↪ Unit Cell Form|
```

```
1.000000
  -1.643859392183    1.643859392183   11.623841235295
   1.643859392183   -1.643859392183   11.623841235295
   1.643859392183    1.643859392183  -11.623841235295
S 1 1 1 1 1
Direct(10) [AsB1C1D1E1F1|
   0.300000000000   0.300000000000  -0.000000000000  C
   0.900000000000   0.900000000000  -0.000000000000  C
   0.500000000000   0.500000000000  -0.000000000000  C
   0.100000000000   0.100000000000  -0.000000000000  C
   0.700000000000   0.700000000000  -0.000000000000  C
   0.400000000000   0.400000000000   0.000000000000  Hf_pv
   0.600000000000   0.600000000000   0.000000000000  Nb_sv
   0.200000000000   0.200000000000   0.000000000000  Ta_pv
   0.800000000000   0.800000000000   0.000000000000  Ti_sv
   0.000000000000   0.000000000000   0.000000000000  Zr_sv
```

HfNbTaTiZrC$_5$:configuration 27 - POSCAR

```
CHf_pvNb_svTa_pvTi_svZr_sv.AB_cFS_225_a_b.POCC   [HNF(S)=2/S= 1
      ↪ 0 0; 0 1 0; 0 1 S| DG=10   [ORCI,ORCI,o120| (STD_PRIM
      ↪ doi:10.1016/j.commatsci.2010.05.010) [
      ↪ Standard_Primitive Unit Cell Form|
1.000000
  -1.643859392183    2.324768247059    8.219296960913
   1.643859392183   -2.324768247059    8.219296960913
   1.643859392183    2.324768247059   -8.219296960913
S 1 1 1 1 1
Direct(10) [AsB1C1D1E1F1|
   0.500000000000  -0.000000000000   0.500000000000  C
   0.900000000000   0.400000000000   0.500000000000  C
   0.300000000000   0.800000000000   0.500000000000  C
   0.700000000000   0.200000000000   0.500000000000  C
   0.100000000000   0.600000000000   0.500000000000  C
   0.600000000000   0.600000000000   0.000000000000  Hf_pv
   0.400000000000   0.400000000000   0.000000000000  Nb_sv
   0.200000000000   0.200000000000   0.000000000000  Ta_pv
   0.000000000000   0.000000000000   0.000000000000  Ti_sv
   0.800000000000   0.800000000000   0.000000000000  Zr_sv
```

HfNbTaTiZrC$_5$:configuration 28 - POSCAR

```
CHf_pvNb_svTa_pvTi_svZr_sv.AB_cFS_225_a_b.POCC   [HNF(S)=2/S= 1
      ↪ 0 0; 0 1 0; 0 1 S| DG=10   [ORCI,ORCI,o120| (STD_PRIM
      ↪ doi:10.1016/j.commatsci.2010.05.010) [
      ↪ Standard_Primitive Unit Cell Form|
1.000000
  -1.643859392183    2.324768247059    8.219296960913
   1.643859392183   -2.324768247059    8.219296960913
   1.643859392183    2.324768247059   -8.219296960913
S 1 1 1 1 1
Direct(10) [AsB1C1D1E1F1|
   0.500000000000  -0.000000000000   0.500000000000  C
   0.900000000000   0.400000000000   0.500000000000  C
   0.300000000000   0.800000000000   0.500000000000  C
   0.700000000000   0.200000000000   0.500000000000  C
   0.100000000000   0.600000000000   0.500000000000  C
   0.600000000000   0.600000000000   0.000000000000  Hf_pv
   0.400000000000   0.400000000000   0.000000000000  Nb_sv
   0.800000000000   0.800000000000   0.000000000000  Ta_pv
   0.000000000000   0.000000000000   0.000000000000  Ti_sv
   0.200000000000   0.200000000000   0.000000000000  Zr_sv
```

HfNbTaTiZrC$_5$:configuration 29 - POSCAR

```
CHf_pvNb_svTa_pvTi_svZr_sv.AB_cFS_225_a_b.POCC   [HNF(S)=2/S= 1
      ↪ 0 0; 0 1 0; 0 1 S| DG=10   [ORCI,ORCI,o120| (STD_PRIM
      ↪ doi:10.1016/j.commatsci.2010.05.010) [
      ↪ Standard_Primitive Unit Cell Form|
1.000000
  -1.643859392183    2.324768247059    8.219296960913
   1.643859392183   -2.324768247059    8.219296960913
   1.643859392183    2.324768247059   -8.219296960913
S 1 1 1 1 1
Direct(10) [AsB1C1D1E1F1|
   0.500000000000  -0.000000000000   0.500000000000  C
   0.900000000000   0.400000000000   0.500000000000  C
   0.300000000000   0.800000000000   0.500000000000  C
   0.700000000000   0.200000000000   0.500000000000  C
   0.100000000000   0.600000000000   0.500000000000  C
   0.600000000000   0.600000000000   0.000000000000  Hf_pv
   0.400000000000   0.400000000000   0.000000000000  Nb_sv
   0.200000000000   0.200000000000   0.000000000000  Ta_pv
   0.800000000000   0.800000000000   0.000000000000  Ti_sv
   0.000000000000   0.000000000000   0.000000000000  Zr_sv
```

HfNbTaTiZrC$_5$:configuration 30 - POSCAR

```
CHf_pvNb_svTa_pvTi_svZr_sv.AB_cFS_225_a_b.POCC   [HNF(S)=3/S= 1
      ↪ 0 0; 0 1 0; 0 2 S| DG=10   [MCLC,MCLC1,mS20| (STD_PRIM
      ↪ doi:10.1016/j.commatsci.2010.05.010) [
      ↪ Standard_Primitive Unit Cell Form|
1.000000
   1.643859392183    5.452064811971    0.000000000000
  -1.643859392183    5.452064811971    0.000000000000
   0.000000000000    3.965138045070    7.009440000025
S 1 1 1 1 1
Direct(10) [AsB1C1D1E1F1|
   0.200000000000   0.200000000000   0.700000000000  C
   0.600000000000   0.600000000000   0.100000000000  C
  -0.000000000000   0.000000000000   0.500000000000  C
   0.400000000000   0.400000000000   0.900000000000  C
   0.800000000000   0.800000000000   0.300000000000  C
   0.600000000000   0.600000000000   0.600000000000  Hf_pv
   0.400000000000   0.400000000000   0.400000000000  Nb_sv
   0.800000000000   0.800000000000   0.800000000000  Ta_pv
   0.200000000000   0.200000000000   0.200000000000  Ti_sv
   0.000000000000   0.000000000000   0.000000000000  Zr_sv
```

HfNbTaTiZrC$_5$:configuration 31 - POSCAR

```
CHf_pvNb_svTa_pvTi_svZr_sv.AB_cFS_225_a_b.POCC   [HNF(S)=3/S= 1
      ↪ 0 0; 0 1 0; 0 2 S| DG=10   [MCLC,MCLC1,mS20| (STD_PRIM
      ↪ doi:10.1016/j.commatsci.2010.05.010) [
      ↪ Standard_Primitive Unit Cell Form|
1.000000
   1.643859392183    5.452064811971    0.000000000000
  -1.643859392183    5.452064811971    0.000000000000
   0.000000000000    3.965138045070    7.009440000025
S 1 1 1 1 1
Direct(10) [AsB1C1D1E1F1|
   0.200000000000   0.200000000000   0.700000000000  C
   0.600000000000   0.600000000000   0.100000000000  C
  -0.000000000000   0.000000000000   0.500000000000  C
   0.400000000000   0.400000000000   0.900000000000  C
   0.800000000000   0.800000000000   0.300000000000  C
   0.600000000000   0.600000000000   0.600000000000  Hf_pv
   0.000000000000   0.000000000000   0.000000000000  Nb_sv
   0.800000000000   0.800000000000   0.800000000000  Ta_pv
   0.200000000000   0.200000000000   0.200000000000  Ti_sv
   0.400000000000   0.400000000000   0.400000000000  Zr_sv
```

HfNbTaTiZrC$_5$:configuration 32 - POSCAR

```
CHf_pvNb_svTa_pvTi_svZr_sv.AB_cFS_225_a_b.POCC   [HNF(S)=2/S= 1
      ↪ 0 0; 0 1 0; 0 1 S| DG=10   [ORCI,ORCI,o120| (STD_PRIM
      ↪ doi:10.1016/j.commatsci.2010.05.010) [
      ↪ Standard_Primitive Unit Cell Form|
1.000000
  -1.643859392183    2.324768247059    8.219296960913
   1.643859392183   -2.324768247059    8.219296960913
   1.643859392183    2.324768247059   -8.219296960913
S 1 1 1 1 1
Direct(10) [AsB1C1D1E1F1|
   0.500000000000  -0.000000000000   0.500000000000  C
   0.900000000000   0.400000000000   0.500000000000  C
   0.300000000000   0.800000000000   0.500000000000  C
   0.700000000000   0.200000000000   0.500000000000  C
   0.100000000000   0.600000000000   0.500000000000  C
   0.600000000000   0.600000000000   0.000000000000  Hf_pv
   0.000000000000   0.000000000000   0.000000000000  Nb_sv
   0.800000000000   0.800000000000   0.000000000000  Ta_pv
   0.400000000000   0.400000000000   0.000000000000  Ti_sv
   0.200000000000   0.200000000000   0.000000000000  Zr_sv
```

HfNbTaTiZrC$_5$:configuration 33 - POSCAR

```
CHf_pvNb_svTa_pvTi_svZr_sv.AB_cFS_225_a_b.POCC   [HNF(S)=2/S= 1
      ↪ 0 0; 0 1 0; 0 1 S| DG=10   [ORCI,ORCI,o120| (STD_PRIM
      ↪ doi:10.1016/j.commatsci.2010.05.010) [
      ↪ Standard_Primitive Unit Cell Form|
1.000000
  -1.643859392183    2.324768247059    8.219296960913
   1.643859392183   -2.324768247059    8.219296960913
   1.643859392183    2.324768247059   -8.219296960913
S 1 1 1 1 1
Direct(10) [AsB1C1D1E1F1|
   0.500000000000  -0.000000000000   0.500000000000  C
   0.900000000000   0.400000000000   0.500000000000  C
   0.300000000000   0.800000000000   0.500000000000  C
   0.700000000000   0.200000000000   0.500000000000  C
   0.100000000000   0.600000000000   0.500000000000  C
   0.600000000000   0.600000000000   0.000000000000  Hf_pv
   0.400000000000   0.400000000000   0.000000000000  Nb_sv
   0.000000000000   0.000000000000   0.000000000000  Ta_pv
   0.200000000000   0.200000000000   0.000000000000  Ti_sv
   0.800000000000   0.800000000000   0.000000000000  Zr_sv
```

HfNbTaTiZrC$_5$:configuration 34 - POSCAR

```
CHf_pvNb_svTa_pvTi_svZr_sv.AB_cFS_225_a_b.POCC   [HNF(S)=3/S= 1
      ↪ 0 0; 0 1 0; 0 2 S| DG=10   [MCLC,MCLC1,mS20| (STD_PRIM
      ↪ doi:10.1016/j.commatsci.2010.05.010) [
      ↪ Standard_Primitive Unit Cell Form|
1.000000
   1.643859392183    5.452064811971    0.000000000000
  -1.643859392183    5.452064811971    0.000000000000
   0.000000000000    3.965138045070    7.009440000025
S 1 1 1 1 1
Direct(10) [AsB1C1D1E1F1|
   0.200000000000   0.200000000000   0.700000000000  C
   0.600000000000   0.600000000000   0.100000000000  C
  -0.000000000000   0.000000000000   0.500000000000  C
   0.400000000000   0.400000000000   0.900000000000  C
   0.800000000000   0.800000000000   0.300000000000  C
   0.600000000000   0.600000000000   0.600000000000  Hf_pv
   0.000000000000   0.000000000000   0.000000000000  Nb_sv
   0.400000000000   0.400000000000   0.400000000000  Ta_pv
   0.800000000000   0.800000000000   0.800000000000  Ti_sv
   0.200000000000   0.200000000000   0.200000000000  Zr_sv
```

HfNbTaTiZrC$_5$:configuration 35 - POSCAR

```
CHf_pvNb_svTa_pvTi_svZr_sv.AB_cFS_225_a_b.POCC   [HNF(S)=2/S= 1
      ↪ 0 0; 0 1 0; 0 1 S| DG=10   [ORCI,ORCI,o120| (STD_PRIM
      ↪ doi:10.1016/j.commatsci.2010.05.010) [
      ↪ Standard_Primitive Unit Cell Form|
1.000000
  -1.643859392183    2.324768247059    8.219296960913
   1.643859392183   -2.324768247059    8.219296960913
   1.643859392183    2.324768247059   -8.219296960913
S 1 1 1 1 1
Direct(10) [AsB1C1D1E1F1|
   0.500000000000  -0.000000000000   0.500000000000  C
   0.900000000000   0.400000000000   0.500000000000  C
   0.300000000000   0.800000000000   0.500000000000  C
   0.700000000000   0.200000000000   0.500000000000  C
   0.100000000000   0.600000000000   0.500000000000  C
```

```
    0.6000000000000    0.6000000000000    0.0000000000000   Hf_pv
    0.0000000000000    0.0000000000000    0.0000000000000   Nb_sv
    0.4000000000000    0.4000000000000    0.0000000000000   Ta_pv
    0.2000000000000    0.2000000000000    0.0000000000000   Ti_sv
    0.8000000000000    0.8000000000000    0.0000000000000   Zr_sv
```

HfNbTaTiZrC$_8$:configuration 36 - POSCAR

```
CHf_pvNb_svTa_pvTi_svZr_sv.AB_cF8_225_a_b.POCC   [HNF(S)=3/S= 1
      ↪ 0 0; 0 1 0; 0 2 S| DG=10   [MCLC,MCLC1,mS20] (STD_PRIM
      ↪ doi:10.1016/j.commatsci.2010.05.010) [
      ↪ Standard_Primitive Unit Cell Form|
1.000000
    1.6438859392183    5.4520648111971    0.0000000000000
   -1.6438859392183    5.4520648111971    0.0000000000000
    0.0000000000000    3.9651380450070    7.0094400000025
S 1 1 1 1 1
Direct(10) [ASB1C1D1E1F1|
    0.2000000000000    0.2000000000000    0.7000000000000   C
    0.6000000000000    0.6000000000000    0.1000000000000   C
   -0.0000000000000    0.0000000000000    0.5000000000000   C
    0.4000000000000    0.4000000000000    0.9000000000000   C
    0.8000000000000    0.8000000000000    0.3000000000000   C
    0.6000000000000    0.6000000000000    0.6000000000000   Hf_pv
    0.0000000000000    0.0000000000000    0.0000000000000   Nb_sv
    0.2000000000000    0.2000000000000    0.2000000000000   Ta_pv
    0.8000000000000    0.8000000000000    0.8000000000000   Ti_sv
    0.4000000000000    0.4000000000000    0.4000000000000   Zr_sv
```

HfNbTaTiZrC$_8$:configuration 37 - POSCAR

```
CHf_pvNb_svTa_pvTi_svZr_sv.AB_cF8_225_a_b.POCC   [HNF(S)=3/S= 1
      ↪ 0 0; 0 1 0; 0 2 S| DG=10   [MCLC,MCLC1,mS20] (STD_PRIM
      ↪ doi:10.1016/j.commatsci.2010.05.010) [
      ↪ Standard_Primitive Unit Cell Form|
1.000000
    1.6438859392183    5.4520648111971    0.0000000000000
   -1.6438859392183    5.4520648111971    0.0000000000000
    0.0000000000000    3.9651380450070    7.0094400000025
S 1 1 1 1 1
Direct(10) [ASB1C1D1E1F1|
    0.2000000000000    0.2000000000000    0.7000000000000   C
    0.6000000000000    0.6000000000000    0.1000000000000   C
   -0.0000000000000    0.0000000000000    0.5000000000000   C
    0.4000000000000    0.4000000000000    0.9000000000000   C
    0.8000000000000    0.8000000000000    0.3000000000000   C
    0.6000000000000    0.6000000000000    0.6000000000000   Hf_pv
    0.0000000000000    0.0000000000000    0.0000000000000   Nb_sv
    0.2000000000000    0.2000000000000    0.2000000000000   Ta_pv
    0.8000000000000    0.8000000000000    0.8000000000000   Ti_sv
    0.4000000000000    0.4000000000000    0.4000000000000   Zr_sv
```

HfNbTaTiZrC$_8$:configuration 38 - POSCAR

```
CHf_pvNb_svTa_pvTi_svZr_sv.AB_cF8_225_a_b.POCC   [HNF(S)=3/S= 1
      ↪ 0 0; 0 1 0; 0 2 S| DG=10   [MCLC,MCLC1,mS20] (STD_PRIM
      ↪ doi:10.1016/j.commatsci.2010.05.010) [
      ↪ Standard_Primitive Unit Cell Form|
1.000000
    1.6438859392183    5.4520648111971    0.0000000000000
   -1.6438859392183    5.4520648111971    0.0000000000000
    0.0000000000000    3.9651380450070    7.0094400000025
S 1 1 1 1 1
Direct(10) [ASB1C1D1E1F1|
    0.2000000000000    0.2000000000000    0.7000000000000   C
    0.6000000000000    0.6000000000000    0.1000000000000   C
   -0.0000000000000    0.0000000000000    0.5000000000000   C
    0.4000000000000    0.4000000000000    0.9000000000000   C
    0.8000000000000    0.8000000000000    0.3000000000000   C
    0.6000000000000    0.6000000000000    0.6000000000000   Hf_pv
    0.0000000000000    0.0000000000000    0.0000000000000   Nb_sv
    0.8000000000000    0.8000000000000    0.8000000000000   Ta_pv
    0.4000000000000    0.4000000000000    0.4000000000000   Ti_sv
    0.2000000000000    0.2000000000000    0.2000000000000   Zr_sv
```

HfNbTaTiZrC$_8$:configuration 39 - POSCAR

```
CHf_pvNb_svTa_pvTi_svZr_sv.AB_cF8_225_a_b.POCC   [HNF(S)=3/S= 1
      ↪ 0 0; 0 1 0; 0 2 S| DG=10   [MCLC,MCLC1,mS20] (STD_PRIM
      ↪ doi:10.1016/j.commatsci.2010.05.010) [
      ↪ Standard_Primitive Unit Cell Form|
1.000000
    1.6438859392183    5.4520648111971    0.0000000000000
   -1.6438859392183    5.4520648111971    0.0000000000000
    0.0000000000000    3.9651380450070    7.0094400000025
S 1 1 1 1 1
Direct(10) [ASB1C1D1E1F1|
    0.2000000000000    0.2000000000000    0.7000000000000   C
    0.6000000000000    0.6000000000000    0.1000000000000   C
   -0.0000000000000    0.0000000000000    0.5000000000000   C
    0.4000000000000    0.4000000000000    0.9000000000000   C
    0.8000000000000    0.8000000000000    0.3000000000000   C
    0.6000000000000    0.6000000000000    0.6000000000000   Hf_pv
    0.4000000000000    0.4000000000000    0.4000000000000   Nb_sv
    0.0000000000000    0.0000000000000    0.0000000000000   Ta_pv
    0.2000000000000    0.2000000000000    0.2000000000000   Ti_sv
    0.8000000000000    0.8000000000000    0.8000000000000   Zr_sv
```

HfNbTaTiZrC$_8$:configuration 40 - POSCAR

```
CHf_pvNb_svTa_pvTi_svZr_sv.AB_cF8_225_a_b.POCC   [HNF(S)=3/S= 1
      ↪ 0 0; 0 1 0; 0 2 S| DG=10   [MCLC,MCLC1,mS20] (STD_PRIM
      ↪ doi:10.1016/j.commatsci.2010.05.010) [
      ↪ Standard_Primitive Unit Cell Form|
1.000000
    1.6438859392183    5.4520648111971    0.0000000000000
   -1.6438859392183    5.4520648111971    0.0000000000000
    0.0000000000000    3.9651380450070    7.0094400000025
S 1 1 1 1 1
Direct(10) [ASB1C1D1E1F1|
    0.2000000000000    0.2000000000000    0.7000000000000   C
    0.6000000000000    0.6000000000000    0.1000000000000   C
   -0.0000000000000    0.0000000000000    0.5000000000000   C
    0.4000000000000    0.4000000000000    0.9000000000000   C
    0.8000000000000    0.8000000000000    0.3000000000000   C
    0.6000000000000    0.6000000000000    0.6000000000000   Hf_pv
    0.4000000000000    0.4000000000000    0.4000000000000   Nb_sv
    0.8000000000000    0.8000000000000    0.8000000000000   Ta_pv
    0.0000000000000    0.0000000000000    0.0000000000000   Ti_sv
    0.2000000000000    0.2000000000000    0.2000000000000   Zr_sv
```

HfNbTaTiZrC$_8$:configuration 41 - POSCAR

```
CHf_pvNb_svTa_pvTi_svZr_sv.AB_cF8_225_a_b.POCC   [HNF(S)=3/S= 1
      ↪ 0 0; 0 1 0; 0 2 S| DG=10   [MCLC,MCLC1,mS20] (STD_PRIM
      ↪ doi:10.1016/j.commatsci.2010.05.010) [
      ↪ Standard_Primitive Unit Cell Form|
1.000000
    1.6438859392183    5.4520648111971    0.0000000000000
   -1.6438859392183    5.4520648111971    0.0000000000000
    0.0000000000000    3.9651380450070    7.0094400000025
S 1 1 1 1 1
Direct(10) [ASB1C1D1E1F1|
    0.2000000000000    0.2000000000000    0.7000000000000   C
    0.6000000000000    0.6000000000000    0.1000000000000   C
   -0.0000000000000    0.0000000000000    0.5000000000000   C
    0.4000000000000    0.4000000000000    0.9000000000000   C
    0.8000000000000    0.8000000000000    0.3000000000000   C
    0.6000000000000    0.6000000000000    0.6000000000000   Hf_pv
    0.4000000000000    0.4000000000000    0.4000000000000   Nb_sv
    0.8000000000000    0.8000000000000    0.8000000000000   Ta_pv
    0.0000000000000    0.0000000000000    0.0000000000000   Ti_sv
    0.2000000000000    0.2000000000000    0.2000000000000   Zr_sv
```

HfNbTaTiZrC$_8$:configuration 42 - POSCAR

```
CHf_pvNb_svTa_pvTi_svZr_sv.AB_cF8_225_a_b.POCC   [HNF(S)=2/S= 1
      ↪ 0 0; 0 1 0; 0 1 S| DG=10   [ORCI,ORCI,o12] (STD_PRIM
      ↪ doi:10.1016/j.commatsci.2010.05.010) [
      ↪ Standard_Primitive Unit Cell Form|
1.000000
   -1.6438859392183    2.3247682470759    8.2192969609013
    1.6438859392183   -2.3247682470759    8.2192969609013
    1.6438859392183    2.3247682470759   -8.2192969609013
S 1 1 1 1 1
Direct(10) [ASB1C1D1E1F1|
    0.5000000000000   -0.0000000000000    0.5000000000000   C
    0.9000000000000    0.4000000000000    0.5000000000000   C
    0.3000000000000    0.8000000000000    0.5000000000000   C
    0.7000000000000    0.2000000000000    0.5000000000000   C
    0.1000000000000    0.6000000000000    0.5000000000000   C
    0.6000000000000    0.6000000000000    0.0000000000000   Hf_pv
    0.0000000000000    0.0000000000000    0.0000000000000   Nb_sv
    0.2000000000000    0.2000000000000    0.0000000000000   Ta_pv
    0.8000000000000    0.8000000000000    0.0000000000000   Ti_sv
    0.4000000000000    0.4000000000000    0.0000000000000   Zr_sv
```

HfNbTaTiZrC$_8$:configuration 43 - POSCAR

```
CHf_pvNb_svTa_pvTi_svZr_sv.AB_cF8_225_a_b.POCC   [HNF(S)=3/S= 1
      ↪ 0 0; 0 1 0; 0 2 S| DG=10   [MCLC,MCLC1,mS20] (STD_PRIM
      ↪ doi:10.1016/j.commatsci.2010.05.010) [
      ↪ Standard_Primitive Unit Cell Form|
1.000000
    1.6438859392183    5.4520648111971    0.0000000000000
   -1.6438859392183    5.4520648111971    0.0000000000000
    0.0000000000000    3.9651380450070    7.0094400000025
S 1 1 1 1 1
Direct(10) [ASB1C1D1E1F1|
    0.2000000000000    0.2000000000000    0.7000000000000   C
    0.6000000000000    0.6000000000000    0.1000000000000   C
   -0.0000000000000    0.0000000000000    0.5000000000000   C
    0.4000000000000    0.4000000000000    0.9000000000000   C
    0.8000000000000    0.8000000000000    0.3000000000000   C
    0.6000000000000    0.6000000000000    0.6000000000000   Hf_pv
    0.4000000000000    0.4000000000000    0.4000000000000   Nb_sv
    0.2000000000000    0.2000000000000    0.2000000000000   Ta_pv
    0.0000000000000    0.0000000000000    0.0000000000000   Ti_sv
    0.8000000000000    0.8000000000000    0.8000000000000   Zr_sv
```

HfNbTaTiZrC$_8$:configuration 44 - POSCAR

```
CHf_pvNb_svTa_pvTi_svZr_sv.AB_cF8_225_a_b.POCC   [HNF(S)=3/S= 1
      ↪ 0 0; 0 1 0; 0 2 S| DG=10   [MCLC,MCLC1,mS20] (STD_PRIM
      ↪ doi:10.1016/j.commatsci.2010.05.010) [
      ↪ Standard_Primitive Unit Cell Form|
1.000000
    1.6438859392183    5.4520648111971    0.0000000000000
   -1.6438859392183    5.4520648111971    0.0000000000000
    0.0000000000000    3.9651380450070    7.0094400000025
S 1 1 1 1 1
Direct(10) [ASB1C1D1E1F1|
    0.2000000000000    0.2000000000000    0.7000000000000   C
    0.6000000000000    0.6000000000000    0.1000000000000   C
   -0.0000000000000    0.0000000000000    0.5000000000000   C
    0.4000000000000    0.4000000000000    0.9000000000000   C
    0.8000000000000    0.8000000000000    0.3000000000000   C
    0.6000000000000    0.6000000000000    0.6000000000000   Hf_pv
    0.4000000000000    0.4000000000000    0.4000000000000   Nb_sv
    0.0000000000000    0.0000000000000    0.0000000000000   Ta_pv
    0.8000000000000    0.8000000000000    0.8000000000000   Ti_sv
    0.2000000000000    0.2000000000000    0.2000000000000   Zr_sv
```

HfNbTaTiZrC$_8$:configuration 45 - POSCAR

```
HfPvNbSvTaPvTiSvZrSv.AB_cF8_225_a_b.POCC   [HNF(5)=3/5= 1
      ↪ 0 0; 0 1 0; 0 2 5| DG=10   [MCLC,MCLC1,mS20|  (STD_PRIM
      ↪ doi:10.1016/j.commatsci.2010.05.010) [
      ↪ Standard_Primitive Unit Cell Form|
1.000000
    1.643859392183    5.452064811971    0.000000000000
   -1.643859392183    5.452064811971    0.000000000000
    0.000000000000    3.965138045070    7.009440000025
5 1 1 1 1 1
Direct(10) [AsB1C1D1E1F1|
    0.200000000000    0.200000000000    0.700000000000  C
    0.600000000000    0.600000000000    0.100000000000  C
   -0.000000000000    0.000000000000    0.500000000000  C
    0.400000000000    0.400000000000    0.900000000000  C
    0.800000000000    0.800000000000    0.300000000000  C
    0.600000000000    0.600000000000    0.600000000000  Hf_pv
    0.000000000000    0.000000000000    0.000000000000  Nb_sv
    0.200000000000    0.200000000000    0.200000000000  Ta_pv
    0.400000000000    0.400000000000    0.400000000000  Ti_sv
    0.800000000000    0.800000000000    0.800000000000  Zr_sv
```

HfNbTaTiZrC$_3$:configuration 46 - POSCAR

```
HfPvNbSvTaPvTiSvZrSv.AB_cF8_225_a_b.POCC   [HNF(5)=2/5= 1
      ↪ 0 0; 0 1 0; 0 1 5| DG=10   [ORCI,ORCI,o120|  (STD_PRIM
      ↪ doi:10.1016/j.commatsci.2010.05.010) [
      ↪ Standard_Primitive Unit Cell Form|
1.000000
   -1.643859392183    2.324768247059    8.219296960913
    1.643859392183   -2.324768247059    8.219296960913
    1.643859392183    2.324768247059   -8.219296960913
5 1 1 1 1 1
Direct(10) [AsB1C1D1E1F1|
    0.500000000000   -0.000000000000    0.500000000000  C
    0.900000000000    0.400000000000    0.500000000000  C
    0.300000000000    0.800000000000    0.500000000000  C
    0.700000000000    0.200000000000    0.500000000000  C
    0.100000000000    0.600000000000    0.500000000000  C
    0.600000000000    0.600000000000    0.000000000000  Hf_pv
    0.000000000000    0.000000000000    0.000000000000  Nb_sv
    0.400000000000    0.400000000000    0.000000000000  Ta_pv
    0.800000000000    0.800000000000    0.000000000000  Ti_sv
    0.200000000000    0.200000000000    0.000000000000  Zr_sv
```

HfNbTaTiZrC$_3$:configuration 47 - POSCAR

```
HfPvNbSvTaPvTiSvZrSv.AB_cF8_225_a_b.POCC   [HNF(5)=2/5= 1
      ↪ 0 0; 0 1 0; 0 1 5| DG=10   [ORCI,ORCI,o120|  (STD_PRIM
      ↪ doi:10.1016/j.commatsci.2010.05.010) [
      ↪ Standard_Primitive Unit Cell Form|
1.000000
   -1.643859392183    2.324768247059    8.219296960913
    1.643859392183   -2.324768247059    8.219296960913
    1.643859392183    2.324768247059   -8.219296960913
5 1 1 1 1 1
Direct(10) [AsB1C1D1E1F1|
    0.500000000000   -0.000000000000    0.500000000000  C
    0.900000000000    0.400000000000    0.500000000000  C
    0.300000000000    0.800000000000    0.500000000000  C
    0.700000000000    0.200000000000    0.500000000000  C
    0.100000000000    0.600000000000    0.500000000000  C
    0.600000000000    0.600000000000    0.000000000000  Hf_pv
    0.000000000000    0.000000000000    0.000000000000  Nb_sv
    0.800000000000    0.800000000000    0.000000000000  Ta_pv
    0.200000000000    0.200000000000    0.000000000000  Ti_sv
    0.400000000000    0.400000000000    0.000000000000  Zr_sv
```

HfNbTaTiZrC$_3$:configuration 48 - POSCAR

```
HfPvNbSvTaPvTiSvZrSv.AB_cF8_225_a_b.POCC   [HNF(5)=2/5= 1
      ↪ 0 0; 0 1 0; 0 1 5| DG=10   [ORCI,ORCI,o120|  (STD_PRIM
      ↪ doi:10.1016/j.commatsci.2010.05.010) [
      ↪ Standard_Primitive Unit Cell Form|
1.000000
   -1.643859392183    2.324768247059    8.219296960913
    1.643859392183   -2.324768247059    8.219296960913
    1.643859392183    2.324768247059   -8.219296960913
5 1 1 1 1 1
Direct(10) [AsB1C1D1E1F1|
    0.500000000000   -0.000000000000    0.500000000000  C
    0.900000000000    0.400000000000    0.500000000000  C
    0.300000000000    0.800000000000    0.500000000000  C
    0.700000000000    0.200000000000    0.500000000000  C
    0.100000000000    0.600000000000    0.500000000000  C
    0.600000000000    0.600000000000    0.000000000000  Hf_pv
    0.000000000000    0.000000000000    0.000000000000  Nb_sv
    0.400000000000    0.400000000000    0.000000000000  Ta_pv
    0.800000000000    0.800000000000    0.000000000000  Ti_sv
    0.200000000000    0.200000000000    0.000000000000  Zr_sv
```

HfNbTaTiZrC$_3$:configuration 49 - POSCAR

```
HfPvNbSvTaPvTiSvZrSv.AB_cF8_225_a_b.POCC   [HNF(5)=5/5= 1
      ↪ 0 0; 0 1 0; 1 2 5| DG=120   [MCLC,MCLC3,mS20|  (STD_PRIM
      ↪ doi:10.1016/j.commatsci.2010.05.010) [
      ↪ Standard_Primitive Unit Cell Form|
1.000000
    5.198339832357    2.324768247059    0.000000000000
   -5.198339832357    2.324768247059    0.000000000000
    0.000000000000    2.324768247059    5.198339832357
5 1 1 1 1 1
Direct(10) [AsB1C1D1E1F1|
    0.500000000000    0.500000000000    0.000000000000  C
    0.300000000000    0.100000000000    0.600000000000  C
    0.100000000000    0.700000000000    0.200000000000  C
    0.900000000000    0.300000000000    0.800000000000  C
    0.700000000000    0.900000000000    0.400000000000  C
    0.200000000000    0.400000000000    0.400000000000  Hf_pv
    0.000000000000    0.000000000000    0.000000000000  Nb_sv
    0.400000000000    0.800000000000    0.800000000000  Ta_pv
    0.800000000000    0.600000000000    0.600000000000  Ti_sv
    0.600000000000    0.200000000000    0.200000000000  Zr_sv
```

SUPPLEMENTARY REFERENCES

* These authors contributed equally to the work
† kvecchio@eng.ucsd.edu
‡ stefano@duke.edu

[1] Oses, C. *et al.* AFLOW-CHULL: Cloud-oriented platform for autonomous phase stability analysis. *J. Chem. Inf. Model.* **in press**, doi:10.1021/acs.jcim.8b00393 (2018).

[2] Oliver, W. C. & Pharr, G. M. An improved technique for determining hardness and elastic modulus using load and displacement sensing indentation experiments. *J. Mater. Res.* **7**, 1564 1583 (1992).

[3] Oliver, W. C. & Pharr, G. M. Measurement of hardness and elastic modulus by instrumented indentation: Advances in understanding and refinements to methodology. *J. Mater. Res.* **19**, 3 20 (2004).

[4] Chen, X.-Q., Niu, H., Li, D. & Li, Y. Modeling hardness of polycrystalline materials and bulk metallic glasses. *Intermetallics* **19**, 1275 1281 (2011).

[5] Toher, C. *et al.* Combining the AFLOW GIBBS and elastic libraries to efficiently and robustly screen thermomechanical properties of solids. *Phys. Rev. Materials* **1**, 015401 (2017).

[6] Yang, K., Oses, C. & Curtarolo, S. Modeling off-stoichiometry materials with a high-throughput *ab-initio* approach. *Chem. Mater.* **28**, 6484 6492 (2016).

[7] Kresse, G. & Furthmüller, J. Efficient iterative schemes for *ab initio* total-energy calculations using a plane-wave basis set. *Phys. Rev. B* **54**, 11169 11186 (1996).

[8] Mehl, M. J. *et al.* The AFLOW library of crystallographic prototypes: Part 1. *Comput. Mater. Sci.* **136**, S1 S828 (2017).

SUPPLEMENTARY INFORMATION PART 3

Phase stability and mechanical properties of novel high entropy transition metal carbides

Tyler J. Harrington,[1,2] Joshua Gild,[2] Pranab Sarker,[3] Cormac Toher,[3] Christina M. Rost,[4] Olivia F. Dippo,[2] Cameron McElfresh[1], Kevin Kaufmann,[1] Eduardo Marin,[1] Lucas Borowski,[1] Patrick E. Hopkins[4], Jian Luo,[1,2] Stefano Curtarolo,[5] Donald W. Brenner,[6] Kenneth S. Vecchio[1,2,*]

[1]*Department of NanoEngineering, University of California San Diego, La Jolla, CA 92093, USA*
[2]*Materials Science and Engineering Program, University of California San Diego, La Jolla, CA 92093, USA*
[3]*Department of Mechanical Engineering and Materials Science, Duke University, Durham, NC 27708, USA*
[4]*Department of Mechanical and Aerospace Engineering, University of Virginia, Charlottesville, VA 22904, USA*
[5]*Materials Science, Electrical Engineering, Physics and Chemistry, Duke University, Durham, NC 27708, USA*
[6]*Department of Materials Science and Engineering, North Carolina State University, Raleigh, NC 27695, USA*

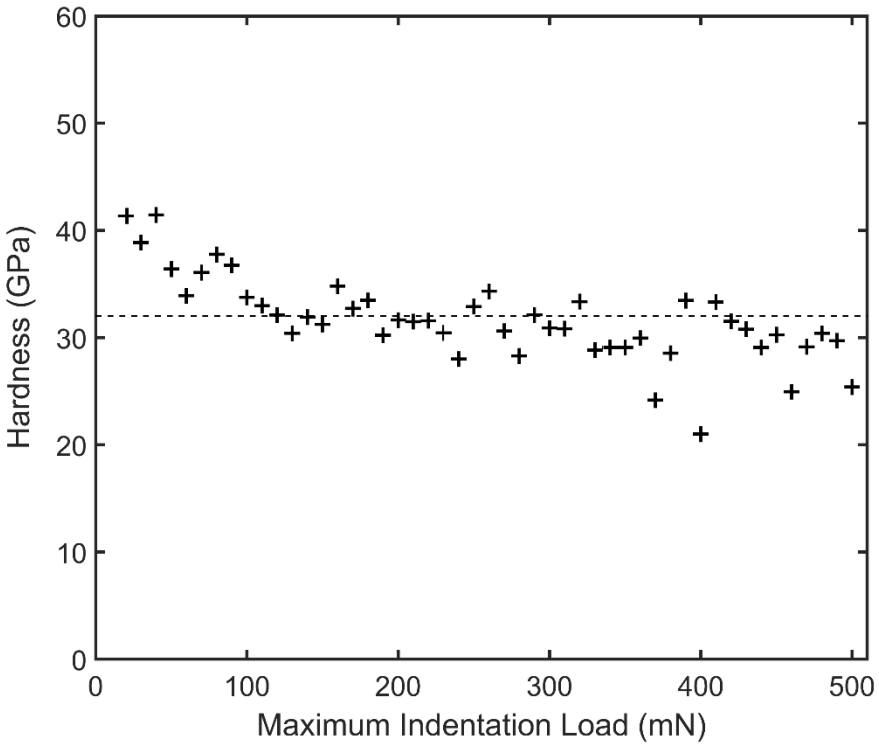

Supplementary Figure 40. Results from nanoindentation testing of a 99% dense sample of $(Ti_{0.2}Zr_{0.2}Hf_{0.2}Nb_{0.2}Ta_{0.2})C$ at varying loads from 10 mN to 500 mN where the dotted line represents the hardness value of 32 GPa, reported for the composition for 100 indents at 300 mN load.

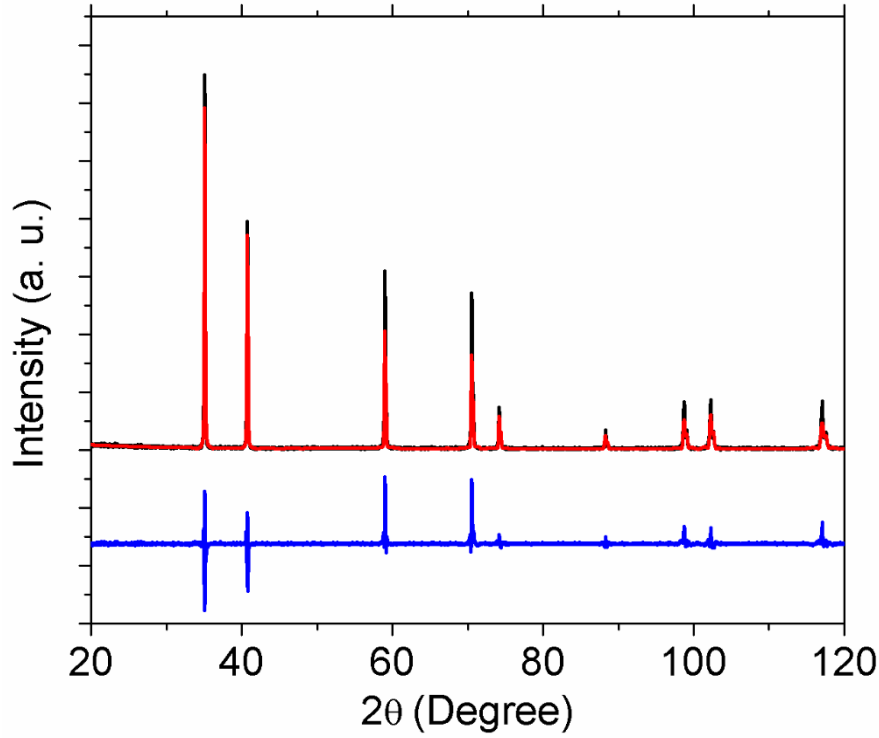

Supplementary Figure 41. Reitveld refinement (Fullprof) of example composition $(Ti_{0.2}Hf_{0.2}Nb_{0.2}V_{0.2}Ta_{0.2})C$ with a calculated lattice parameter of a = 4.42(1) Å and χ^2 of 3.3.

Supplementary Table 11. Results from nanoindentation testing of seven of the single-phase carbides along with the prediction from a rule of mixtures (RoM) from the binaries, which were synthesized and tested in the same manner. RoM values for compositions containing WC or MoC were calculated using experimental or calculated reference values, as neither are stable as rocksalt monocarbides down to room temperature.

Composition	Elastic Modulus (GPa)	Exp. Hardness (GPa)	RoM Modulus (GPa)	RoM Hardness (GPa)	VEC
$(Ti_{0.2}Zr_{0.2}Hf_{0.2}Nb_{0.2}Ta_{0.2})C$	443 ± 40	32 ± 2	436	22	8.4
$(Ti_{0.2}Hf_{0.2}V_{0.2}Nb_{0.2}Ta_{0.2})C$	503 ± 30	29 ± 3	448	23	8.6
$(Ti_{0.2}V_{0.2}Nb_{0.2}Ta_{0.2}W_{0.2})C$	485 ± 36	28 ± 2	459	24	9
$(Ti_{0.2}Zr_{0.2}Hf_{0.2}Ta_{0.2}W_{0.2})C$	473 ± 26	33 ± 2	446	24	8.6
$(Ti_{0.2}Hf_{0.2}Nb_{0.2}Ta_{0.2}W_{0.2})C$	483 ± 24	31 ± 2	451	23	8.8
$(V_{0.2}Nb_{0.2}Ta_{0.2}Mo_{0.2}W_{0.2})C$	533 ± 32	27 ± 3	440	22	9.4
$(Ti_{0.2}Hf_{0.2}Nb_{0.2}Ta_{0.2}Mo_{0.2})C$	481 ± 37	27 ± 3	434	22	9
TiC	489	31	-	-	8.0
ZrC	402	24	-	-	8.0
HfC	428	25	-	-	8.0
VC	465	29	-	-	9.0
NbC	429	17	-	-	9.0
TaC	431	14	-	-	9.0
MoC	396 [*, a]	21 [*, a]	-	-	10.0
WC	480 [b]	27 [c,d]	-	-	10.0

* First principles calculations.
[a] Ref. [41]
[b] Ref. [42]
[c] Ref. [43]
[d] Ref. [44]

Supplementary Table 12. Results from a carbon combustion analysis for four of the compositions. The expected carbon content is based on calculation from some carbon deficient precursors used (i.e. W_2C, Mo_2C, and $VC_{0.88}$). The results suggest that, at a high processing temperature of 2200°C in a carbon rich environment, the compositions approach an equilibrium substoichiometric carbon content that is not heavily dependent on the amount of carbon in the initial precursors.

Composition	x (results)	x (expected)	HV (GPa)
$(Ti_{0.2}Hf_{0.2}V_{0.2}Nb_{0.2}Ta_{0.2})C_{1-x}$	0.12	0.025	29 ± 3
$(Ti_{0.2}V_{0.2}Nb_{0.2}Ta_{0.2}W_{0.2})C_{1-x}$	0.15	0.125	28 ± 2
$(Ti_{0.2}Zr_{0.2}Hf_{0.2}Ta_{0.2}W_{0.2})C_{1-x}$	0.13	0.100	33 ± 2
$(Ti_{0.2}Hf_{0.2}Nb_{0.2}Ta_{0.2}W_{0.2})C_{1-x}$	0.09	0.100	31 ± 2

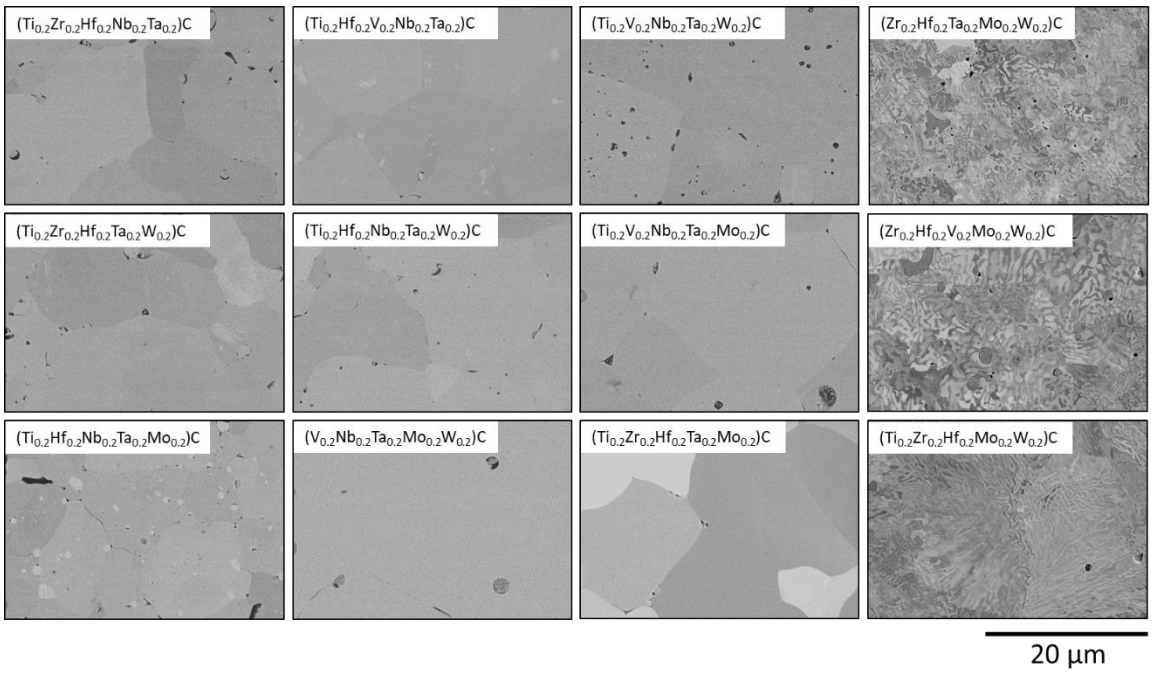

Supplementary Figure 42. SEM microstructure images for all twelve high entropy carbide compositions.

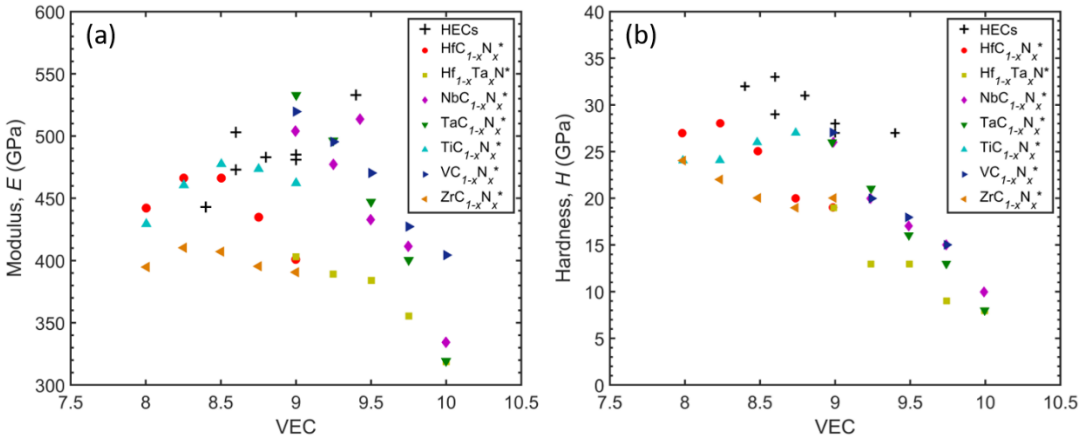

Supplementary Figure 43. Comparison of HEC elastic moduli (a) and hardness (b) in this study with calculated results from Ref. [48] with respect to VEC.

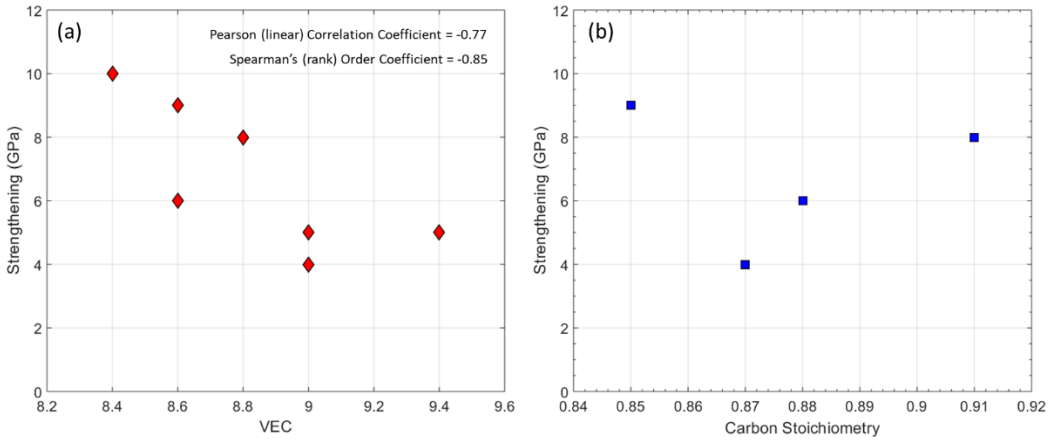

Supplementary Figure 44. Comparison of (a) the strengthening (HV – RoM) and VEC for each of the carbide compositions and (b) strengthening vs carbon content for four of the compositions.

SUPPLEMENTARY INFORMATION PART 4

Fermi level engineering of tunable and ultra-tough entropy stabilized carbides

Tyler J. Harrington[1,2,†], Corey Oses[3,†], Cormac Toher[3], Joshua Gild[2], William Mellor[2], Kevin Kaufmann[1], Andrew Wright[2], Jian Luo[1,2], Stefano Curtarolo[4,*], Kenneth Vecchio[1,2,*]

[1]Department of NanoEngineering, University of California San Diego, La Jolla, CA 92093, USA
[2]Materials Science and Engineering Program, University of California San Diego, La Jolla, CA 92093, USA
[3]Department of Mechanical Engineering and Materials Science, Duke University, Durham, NC 27708, USA
[4]Materials Science, Electrical Engineering, Physics and Chemistry, Duke University, Durham, NC 27708, USA
† These authors contributed equally
** Corresponding author(s)*

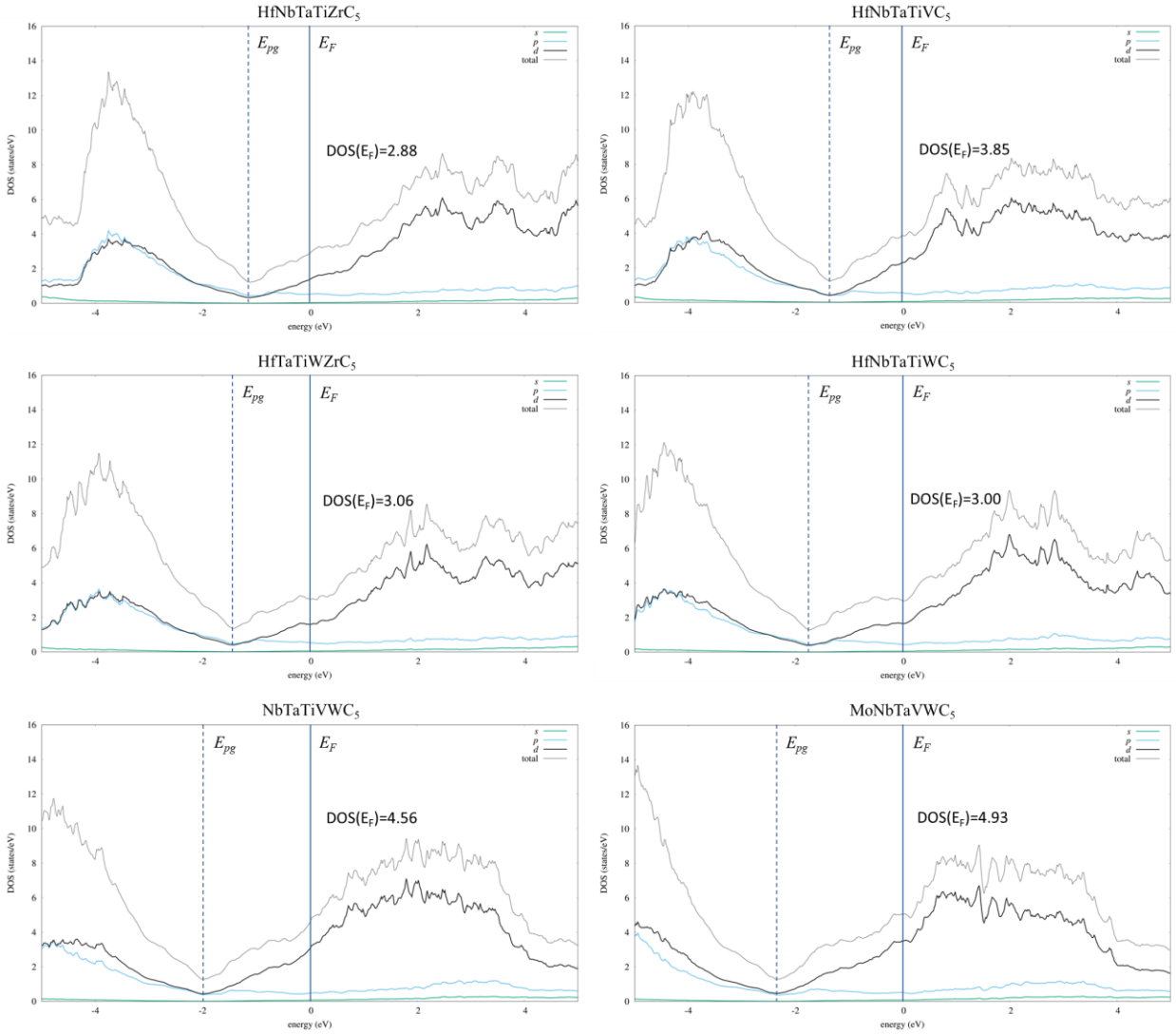

Supplementary Figure 45: Complete electronic density of states for each of the high entropy carbide compositions, showing the DOS(E_F), Fermi level, E_F, and pseudo-gap energy, E_{pg}.

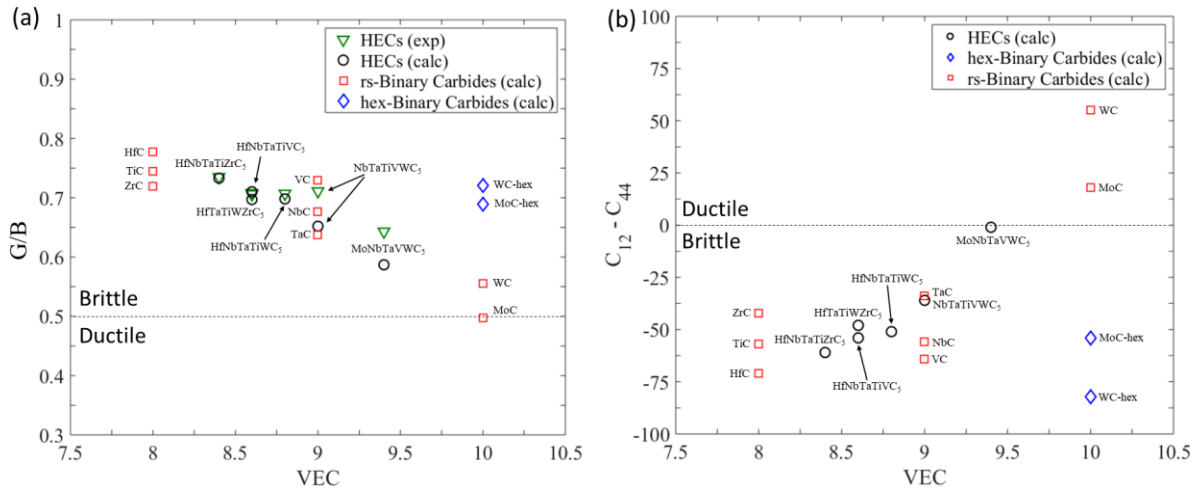

Supplementary Figure 46: (a) The modeled and experimental Pugh's Modulus ratio (G/B) for each of the HECs along with the calculated values for the rocksalt (rs) binary carbides and hexagonal (hex) binary carbides and **(b)** the calculated Cauchy pressures for each of the HECs and rs and hex binary carbides. Note that the lowest Pugh's modulus ratio and highest Cauchy pressure is attained with $MoNbTaVWC_5$ when considering that rocksalt structured WC and MoC are not stable at room temperature.

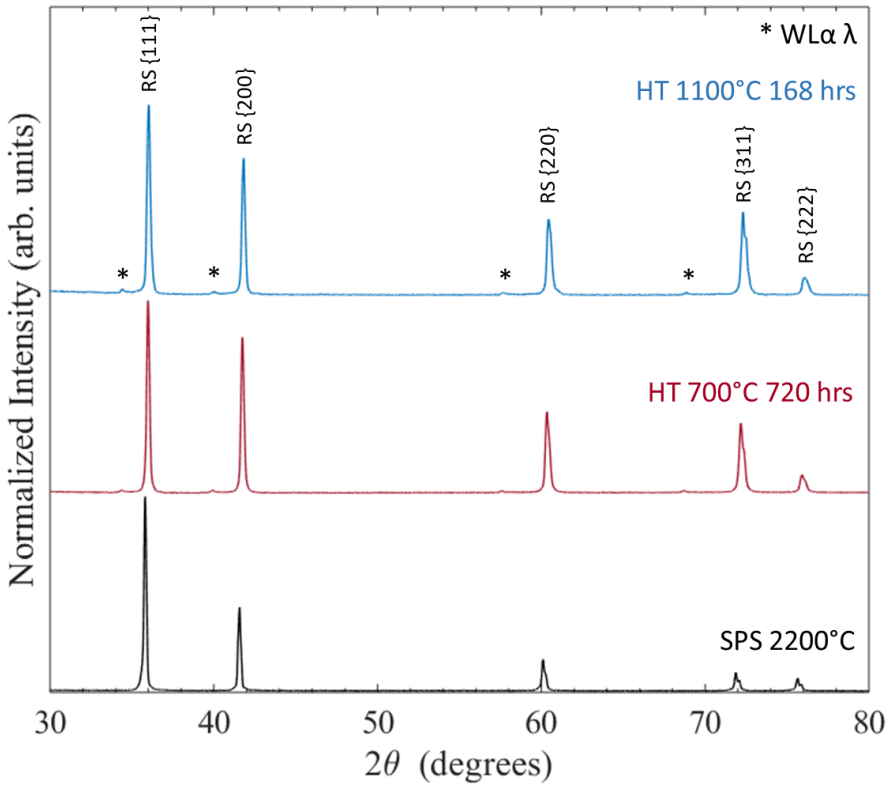

Supplementary Figure 47: XRD patterns from a sample of $MoNbTaVWC_5$ after high temperature sintering at 2200°C (bottom), heat treatment at 700°C for 720 hours (middle), and heat treatment at 1100°C for 168 hours. Note that only the single-phase rocksalt (RS) structure is maintained after all heat treatments.